Application of Topological Data Analysis to TEM Images of Metal/Oxide Nanocomposites for Quantitative Structural Description

Yu Wen

February 2022

Application of Topological Data Analysis to TEM Images of Metal/Oxide Nanocomposites for Quantitative Structural Description

Yu Wen
Doctoral Program in Materials Science and Engineering

Submitted to the Graduate School of
Pure and Applied Sciences
in Partial Fulfillment of the Requirements
for the Degree of Doctor of Philosophy in
Engineering

at the
University of Tsukuba

Table of Contents

Abstract

Noble metal/metal oxide (NM/MO) nanostructured composites are attractive catalysts for accelerating ecofriendly chemical reactions and ionic–electronic transportation due to the strong interaction between NMs and MOs. Oxygen ionic conductivity is essential in applying NM/MO, especially CeO_2-based nanocomposites (NCs). In addition to the interfacial effect for the improved ionic conductivity, conductive phase (CeO_2) connectivity is important for providing the transportation pathway. However, it is difficult to evaluate the phase connectivity of the complicated interwoven structure. Topological data analysis (TDA) is suitable for studying the data shape from topology in multiscale and multidimensions. Homology, an algorithmic method, which is one of the TDA tools, has been widely applied in materials science for distinguishing and classifying the complicated structures of various materials and therefore can be applied for evaluating phase connectivity. This thesis aims to apply homology to TEM images of Pt/CeO_2 NCs for structural description, which helps understand the structure–ionic conductivity relationship.

This thesis comprises three parts. First, atomic-scale TEM was conducted to structurally engineer Pt/CeO_2, which provides hints to prepare different structures for the homology analysis. Pt/CeO_2 NCs were prepared by annealing Pt_5Ce alloys through an oxidation-induced phase separation behavior. The oxygen partial pressure and annealing temperature are the two main factors affecting the Pt/CeO_2 structure because they influence the counter diffusion of Pt and Ce atoms in the Pt_5Ce alloy for phase separation and oxygen inward diffusion through CeO_2. Second, a homology descriptor, Betti numbers, was applied to the TEM images for quantitative phase connectivity evaluation. For different structures varying from lamellar to maze patterns prepared using different oxygen partial pressure, the two-dimensional (2D) phase connectivities of CeO_2 phases were described, and their positive effects on ionic conductivity were demonstrated by the zeroth Betti number (β_0). For different structures varying from stripy to network patterns prepared at different annealing temperatures, the 3D phase connectivities were quantified since the network structure cannot be accurately interpreted by 2D structural characterization. It was also demonstrated that 3D CeO_2 phase connectivities are decisive for oxygen-ion conduction. Third, the various structures mentioned above were analyzed using the persistence diagram, another homology descriptor, for structural classification. As the persistence diagram provides both homological and geometric information about the TEM structural images, the differences among various structures were identified. The structures were classified combing the persistence diagram and machining learning model.

In summary, this study successfully applied TDA to the TEM images of Pt/CeO_2 NCs for structural description. Long-striped pattern with high phase connectively (low value of β_0) is ideal for the oxygen-transportation in Pt/CeO_2 NCs. Therefore, these findings give sights for the structural design and property prediction of many other nanomaterials. It is expected to be applicable in estimating the oxygen-ion transport properties, and other transport phenomena, such as magnetic and electronic transportation. The feasibility of applying machine learning to the computed homology provides us a way to analyze material structure automatically and efficiently.

Chapter 1 Introduction

The strong interaction at the interface between nanoscale noble metals (NM) and metal oxides (MO) makes it very attractive in various applications, such as catalysis, environmental remediation, and fuel cells. Owing to the importance of configuration in composites to the corresponding properties, tailored heterostructures by processing adjustment have been studied extensively for designing excellent NM/MO nanocomposites (NM/MO NCs). Based on the NM MO combines, various synthesis methods were developed, such as the sol–gel method, deposition−precipitation methods. Self-assembled NM/MO NCs from binary alloys are of interest because of their easy control and structural diversity.

CeO_2-based NCs have received much attention because of the strong oxygen storage ability of the CeO_2 phase. The interfacial effects between NM, such as Pt, cause charge perturbation and oxygen vacancies (Vo) formation. Consequently, the properties of the CeO_2-based NCs are significantly improved. Specifically, the excellent ionic conductivity, an essential function in the fuel cells, of CeO_2-based NCs makes it suitable as an electrolyte or electrode material. As the ion transportation pathway is critical for ionic conductivity, the structure–ionic conductivity relationship should be studied to design desired ionic conductors. Quantifying this relationship will further provide hints for the materials' design.

Mathematical tools help quantify data. Computational homology, one of the TDA methods, meets the requirements for extracting features from structural data. It has recently been gradually applied to materials science, such as the atomic configuration of metallic glass and ceramics. Using homology analysis to link the structure–ionic conductivity is interesting and promising in materials science.

1.1 Metal/oxide nanocomposites

1.1.1 Theoretical studies on metal-oxide interface

Metals and oxides show extremely different properties because of their different metallic and ionic bonding characteristics, respectively. The combination of metals and oxides, while exceeding the component performance, is the most interesting object for materials science. Fast-developed MO composites with superior properties, such as catalytic and electronic transportation, are attributed to the synergetic effect at the MO interface. Both theoretical and experimental studies on model systems (Pt/CeO_2, Pd/CeO_2, and Ni/ZrO_2) verified the important roles of the interfacial effect, establishing fundamentals for designing unique systems with new functionalities. This subsection summarizes theoretical studies by the first-principles mechanism on the interfacial effect between metals and oxides. The experimental studies on the application of the interfacial effect will be introduced in the next subsection.

Before understanding the strong interfacial effect between the metal and oxide surfaces, the bonding nature of MO interfaces must be clarified. Although a large atomic structure mismatch exists at the heterointerface between the metal and the oxide, an effective chemical bonding transition stabilizes the

interface [1]. It favors specific parallel alignment at the interfacial plane; that is, a preferred orientation relationship forms. For face-centered cubic (fcc) metals and oxides, {111} and {100} paralleled interfaces are usually concerned. Owing to the most stable (111) surface in the fcc structure, NMs absorbed on CeO_2 (111) and oxides on (111) Pt planes have been heavily studied. For the NM atoms, several O sites are possible for adsorption on the CeO_2 (111) surface. Figure 1.1a shows the top view of the CeO_2 (111) surface, where NM adatoms can be stable on top of the surfaces by adsorption. Obviously, the surface O-bridge sites (Figure 1.1b) are the most preferable adsorption sites for Pt atoms because of the lowest adsorption energy [2, 3]. Different adatoms have different preferable adsorption sites, as shown in Figure 1.1c, where the O-hollow sites are preferable for Rh atoms. Due to the strong covalent bonds between atomic-specie pairs, such as Pt–Ce and Pt–O, the physical and chemical properties are consequently changed at the interfaces.

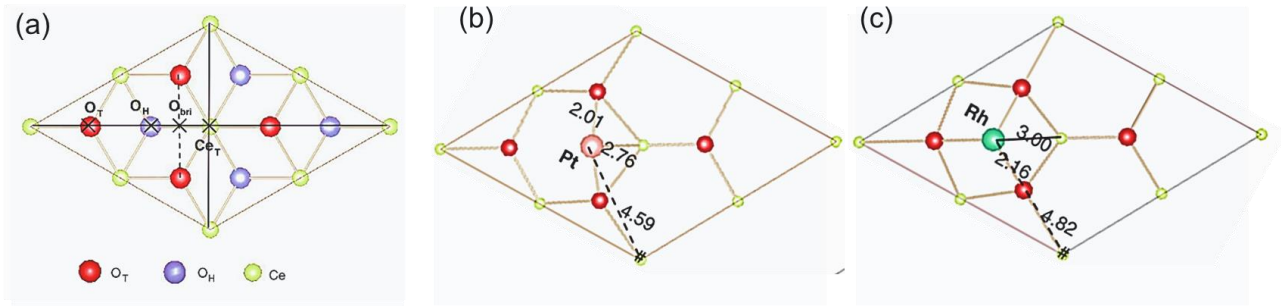

Figure 1.1. Bonding structure of NM on CeO_2(111) plane. (a) Model of CeO_2 surface for NM adsorption from the top view of CeO_2(111). 'O_T', 'O_H' and 'O_{bri}' are related to the top, hollow and bridge sites of surface oxygen atoms, respectively. The most stable position for (b) Pt and (c) Rh absorbed on CeO_2(111) plane [3].

The charge density difference and spin densities for the NM–CeO_2(111) interface were frequently used to characterize the changes in the electronic properties due to the NM adatoms. Z. Lu *et al.* discovered the significant electron depletion around the NM atoms and electron accumulation on their near next surface Ce ion. As shown in Figure 1.2a–c, the thin (blue) and thick (yellow) could around the atoms in Figure 1.2 indicate the positive and negative charges, respectively. Such localized charge redistribution indicates electrons' transfer from the NM adatoms to their nearest-neighbor Ce ion. Consequently, Ce ions were reduced, and oxygen vacancies formed by getting excess electrons. The spin densities of the NM–CeO_2 interfaces shown in Figure 1.2d and e confirmed that the surface reduced Ce^{3+} ions by the reaction ($NM/Ce^{4+} \rightarrow NM^{+}/Ce^{3+}$) because the spin densities are mainly localized on NM adatoms and their next near reduced Ce ions. The above changed electronic properties have also been verified by many other studies, such as Pt cluster on CeO_2(111) surface by C. Campbell [4] and G. Vayssilov *et al.* [5], Ag islands on CeO_2(111) by P. Luches *et al.* [6], and Cu and Au atoms on Ce(111) surface by M. Branda *et al.* [7]. Since the bonding strength of NM-Ce varies with the metals, the interface effect differs: Rh > Pt > Pd [3]. Besides, the interfacial effect of the metal cluster is stronger than that of single atoms [2].

Using the spin-polarized density-functional theory (DFT) with the Hubbard U term, in which an onsite Coulomb correction potential (U) is introduced as an energy penalty on the delocalization of electrons, many

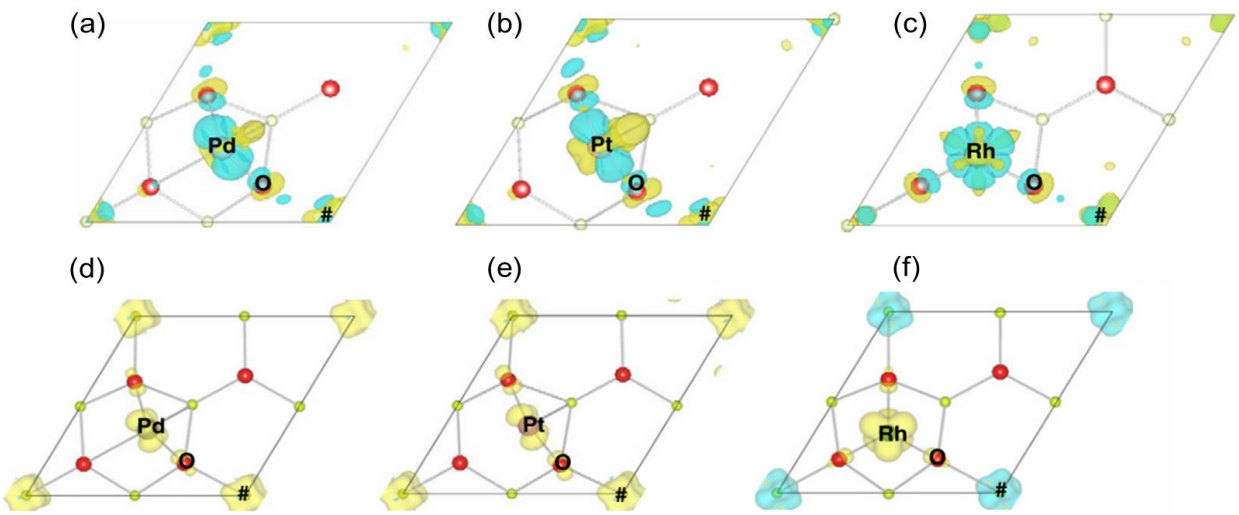

Figure 1.2. The charge density difference (CDD) maps and spin densities for the most stable optimized configurations of the NM/CeO_2(111) interfaces: (a) and (d) Pd/CeO_2(111); (b) and (e) Pt/CeO_2(111), and (c) and (f) for the Rh/CeO_2(111) interface. Here and onwards, blue and yellow clouds represent positive and negative charges, respectively [3].

researchers found that due to the electronic perturbation and oxygen vacancies' formation, the interfacial effect facilitates the adsorption and oxidation of gas molecules and thus improves the catalytic properties. Figure 1.3 illustrates that the interfacial effect between TiO_2 and Pt(111) activates CO_2 reduction using the $Ti_3O_6H_6$/Pt(111) model [8]. The optimized configuration of CO_2 adsorption on Pt(111) and $Ti_3O_6H_6$–Pt(111) interface are shown in Figure 1.3a and b, respectively. The original linear configuration remained on the Pt(111) surface. However, it changed to a V-shape on the $Ti_3O_6H_6$–Pt(111) because of the strong CO_2 interaction with the interface forming C–O bonds. The differential charge density around the interface is shown in Figure 1.3c, where blue and yellow clouds represent depletion (positive) and cumulation (negative) of electronic charge, respectively. The charge density redistribution, that is, electron depletion and accumulation around Ti and O_2 atoms in CO_2, respectively, suggests a substantial transfer of electrons from the interface to the CO_2 molecule, resulting in enhanced CO_2 reduction activity. DFT calculations for the reaction energy of CO_2 reduction shown in Figure 1.3d indicates that the $Ti_3O_6H_6$–Pt(111) interface facilitates CO_2 reduction due to the strong binding to the interfacial sites. Similarly, Single Pd atoms embedded in CeO_2(111) are active for NO reduction with CO because of the Pd–oxygen vacancy pair and interfacial effect [9]. The interface of the Ni atoms, which builds tetrahedral Ni_4 clusters supported on the CeO_2(111) surface is promising for methane reforming reactions because CH_3 is stably adsorbed at the interfacial O site [10]. Oxygen vacancies Vo on CeO_2 (111) facilitate H and OH incorporation below the surface, which helps understand the CeO_2 reactivity in selective alkyne hydrogenation and water-gas shift reactions [11, 12]. The Pt/CeO_2(111) interface has been exclusively studied and was found to be potent for various catalysts, such as water-gas shift processes [13, 14], methanol oxidation [15], and selective hydrogenation of quinolines [16].

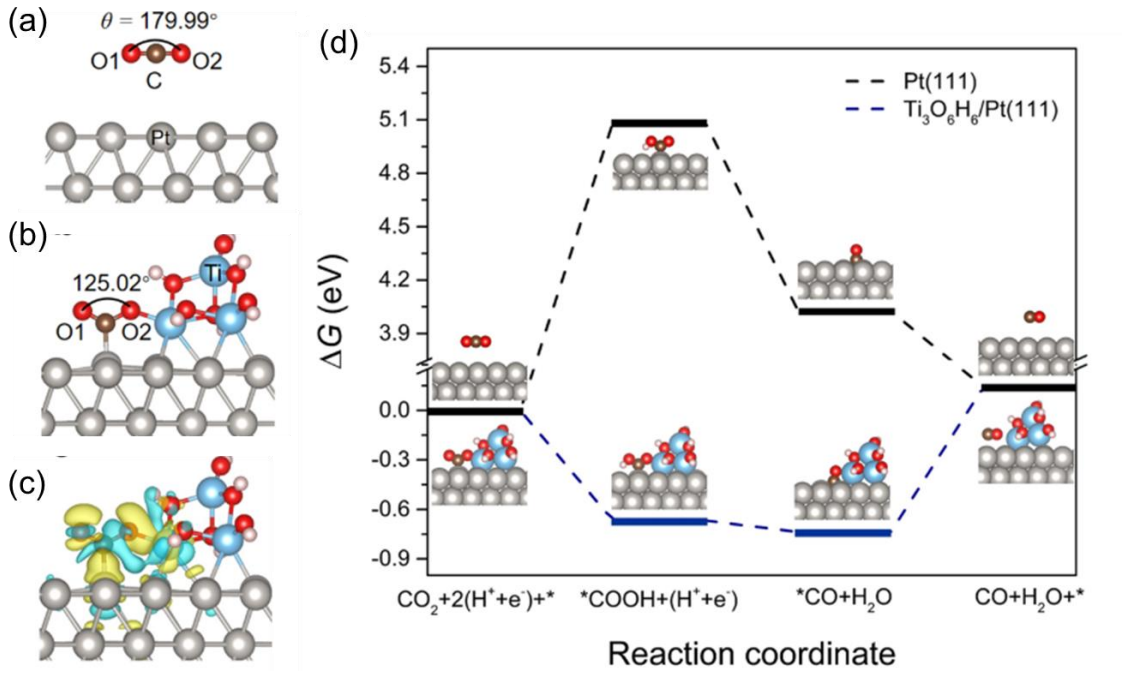

Figure 1.3. Side views of optimized configurations of CO_2 adsorbed on (a) Pt(111) and (b) $Ti_3O_6H_6$/Pt(111) surface. (c) Differential charge density of CO_2 adsorbed at the $Ti_3O_6H_6$/Pt(111) interface. (d) Calculated free energy diagrams for CO_2 reduction to CO on Pt(111) and $Ti_3O_6H_6$/Pt(111) surfaces at 0 V *vs.* reversible hydrogen electrode [8].

1.1.2 Structure and properties of metal-oxide nanocomposite

According to the abovementioned theoretical studies, a strong interfacial effect between metals and oxides increases the oxygen vacancies and electronic perturbation, which provides numerous active sites. Consequently, many applications have been studied for MO NCs, such as catalysts, fuel cells, and sensors. One of the interesting objectives is the configuration control of MO NCs to tune the interfacial effect for superior functionalities. Concerning NM or MO nanoparticles (NPs) as catalysts, NM–MOs can be divided into five categories based on the configuration shown in Figure 1.4: (1) NM-decorated MO NPs; (2) NM-decorated MO nanoarrays; (3) core–shell structures; (4) yolk–shell nanostructures; (5) Janus NM–MO nanostructure [17].

The structure of NM-decorated MO NPs has a high surface area, but is unsuitable for charge separation and transfer [18, 19]. The shape of MOs has been changed to increase the active sites for interface bonding and further improve catalytical properties, such as Au-decorated TiO_2 hollow nanospheres [20] for enhanced visible-light-driven photocatalyst, Ag-decorated ZnO nanorods [21] showing obvious photocurrent multiplication effect, and ZnO/Au nanoneedles as robust substrates for food safety monitoring [22]. These configurations are summarized as the second category, NM-decorated MO nanoarrays. Core–shell nanostructure is useful for preventing aggregation and deterioration of metal NPs. The most common Au@TiO_2 core–shell structure with a controlled core diameter and shell thickness makes it a candidate for several applications in catalysis and sensors [23]. The yolk–shell nanostructure shown in Figure1.4 comprises

a hollow MO shell with an NM core, like the core–shell structure. The structural features are the void between the core and the shell and the movable NM core. This kind of structure can advantageously reduce the NM aggregation and thermal stability. Yolk–shell structures with unique large hollow spaces and good biocompatibility are suitable for drug delivery vehicles, nanoreactors, and lithium-ion battery electrodes [24]. The Janus NM–MO nanostructure combines two components at a small junction point, whereas other regions are exposed to high catalytic activity. Due to this special configuration, it possesses excellent performance in electric, magnetic, optical, and biological applications [25].

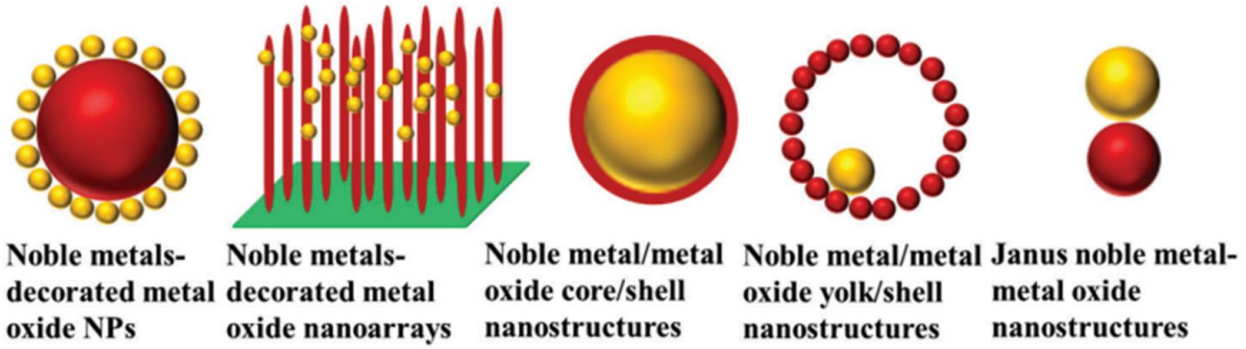

Figure 1.4. Schematic representation of different structures of NM/MO NCs [17].

The configuration between NM and MO in the form of thin films is another important part of the abovementioned configuration, which is mainly used in sensors and solid oxide fuel cells (SOFCs) for electrical conduction. Concerning the NM–MO interface within thin films, interwoven nanostructures are promising for mixed electronic and ionic conductors, which are usually applied in SOFCs as anodes (Figure 1.5), such as Pt-CGO (gadolinia-doped CeO_2) [26-28] and Pt-YSZ (yttria-stabilized zirconia) [29-32]. Oxygen-ion conductors, such as YSZ, are generally deposited on the porous metal films, resulting in a mesoporous NM–MO structure. The basic requirements for excellent electrodes in SOFCs are the high electronic–ionic conductivity, high electrocatalytic activity for the electrode reaction, and porous microstructure for gaseous diffusion. Therefore, the combination of NM-catalyzing reduction reaction and MO-favorable ionic transportation makes it exhibit good electrochemical properties and is promising for SOFC applications (magnified schematic in Figure 1.5).

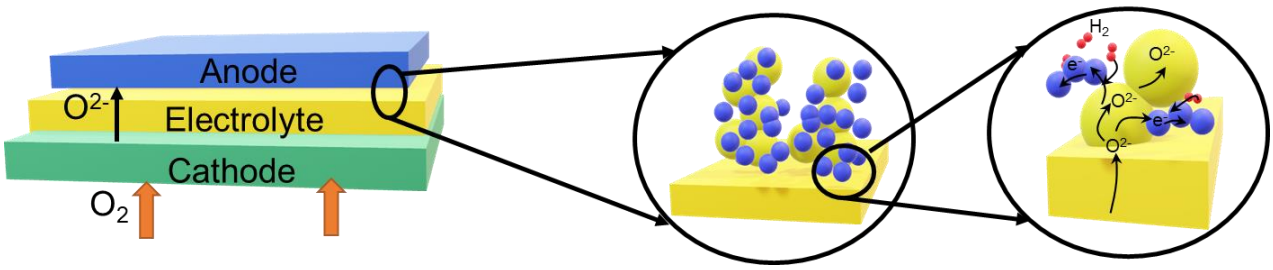

Figure 1.5. Summary of the schematic of different structures of NM–MO NCs.

1.1.3 Synthesis of metal-oxide nanocomposites

According to the expected configuration of NM–MOs, different preparation methods have been applied, including the deposition–precipitation method [33], sol–gel method [34], chemical reduction [35], and alloy oxidation [36-38]. Deposition–precipitation methods have commonly been used to synthesize Au NPs on ZnO_2 or TiO_2 templates. The advantages of this method include fine Au NPs and well-defined coupling between Au and the template [39, 40]. The sol–gel method is good for preparing core–shell structures by introducing ligand or surfactant molecules. It is easy to control the core diameter and shell thickness using the sol–gel method [41]. Chemical reduction methods are frequently used to prepare NM-decorated MO nanoarrays. It is the simplest way to integrate NM NPs onto the surface of MO nanoarrays. The selection of a reducing agent is critical for the nucleation and growth of NMs. In the following part, we will focus on the oxidation of binary alloys as we used in experiments.

In the case of a binary alloy A_xB_y comprising two components with totally different oxygen affinities (example, B >A), the oxidation of the binary alloy precipitates the oxide of B in the metal matrix A. The oxygen partial pressure in the surface is sufficient to oxidize B, but too low for the A oxide formation. Oxygen dissolves into the alloy and oxidizes B internally because of the faster inward oxygen diffusion than B outward diffusion in the alloy. When the concentration of oxide molecules exceeds the solubility limit in matrix A, the oxide of B precipitates from A. Oxygen-ion diffusion through the B oxide to the alloy interface further oxidizes the alloy. Note that such an oxidation process leading to phase separation is known as internal oxidation, where the process is kinetically diffusion-limited. Therefore, the depth of the oxidized area (X_i) increases with time (t) following the parabolic kinetics:

$$X_{(i)}^2 = 2k_p^{(i)}t \quad (1-1)$$

where $k_p^{(i)}$ is the oxidation rate constant. The constant $k_p^{(i)}$ as a function of temperature T is written by

$$k_p^{(i)} = k_0 \exp\left(-\frac{E}{RT}\right) \text{ or } lnk_p^{(i)} = lnk_0 - \frac{E}{RT} \quad (1-2)$$

where E is the activation energy for the oxidation, k_0 is a parameter related to the oxide properties, and R is the Boltzmann constant. Combining Equations (1-1) and (1-2), E can be deduced from the oxidation experiments. Oxidation kinetics of Pb–Sn [42], Pb–In [43, 44], and Mo–Pt [45, 46] alloys have been studied and showed parabolic oxidation in good approximation. Since various structures of NM–MO two-phase composites can be obtained depending on the competition between precipitates' nucleation and growth, the outcomes are termed self-assembled structures.

The self-assembled structures of the NM–MO composites form binary alloys, which are influenced by the alloy structure, alloy composition, oxygen partial pressure, and temperature. For nanoalloys, MOs-decorated NMs and NM-core–MO-shell structures can be obtained. X. Wang *et al.* [47] prepared Pt–MO (M = Ni, Fe, Co) catalysts from Pt–M alloy NPs (Figure 1.6a), which showed high catalytic activities for p-

chloronitrobenzene hydrogenation reaction because of the strong Pt–M_xO_y interaction. Amorphous oxides surrounding a crystalline alloy core from Au–Sn alloys have been prepared (see Figure 1.6b) and showed high activity in a CO-oxidation prone action [48, 49]. More recently, the growth process of a core–shell structure driven by oxygen was observed in Pt–Co NPs via *in situ* atomic-scale transmission electron microscopy (TEM) technique [50]. For bulk alloys, the shape of MO precipitates varies from particles to needle-like shapes depending on the concentration of nonNMs in the alloy. Figure 1.6c shows that composites of nanocrystalline ZrO_2 coupled with nanogold particles were prepared by oxidizing $AuZr_3$ metallic compound and exhibited high catalytic activities for CO oxidation reaction [51]. H. Abe's group formed an entangled network structure of metal and MO composite (N#MO) catalysis, such as Ni#Y_2O_3 [52], Ni#NbO_x [53], Rh#NbO_x [54], and Rh#Y_2O_3 [55]) with excellent catalytical properties. The left panel of Figure 1.6d illustrates the formation of Ni/NbO_x precipitated from the Ni_3Nb alloy, and the right panels show the stable Ni/NbO_x structure after a 550-h catalytic process. Usually, it is difficult to control the crystallography of the interface between self-assembly NM and MO phases. Nevertheless, atomically flat interfaces with a unique orientation relationship, i.e., epitaxial relationship, between precipitated NM and MO was found in many systems [56]. This kind of precipitation can be collectively referred to as cellular precipitation. For the cellular precipitation, the precipitates are constrained in the normal direction to the alloy surface for fast oxygen diffusion. Consequently, lamellae patterns can be obtained. As a large internal surface area for the lamellae pattern, an energetically favorable orientation relationship between the precipitates and alloy or between the two precipitates is accommodated to decrease the energy.

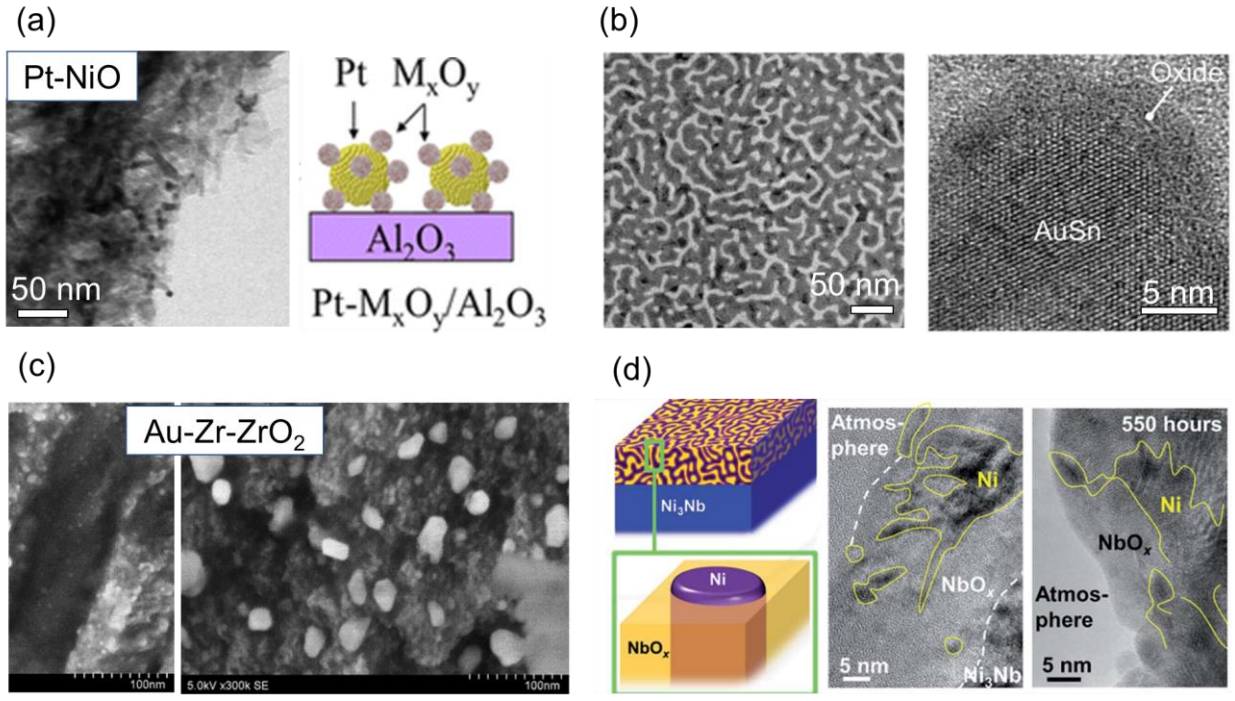

Figure 1.6. Various structures of metal/oxide composites through the oxidation of binary alloy:(a) NiO-decorated Pt NPs [47], (b) crystalline AuSn core-amorphous Sn oxide shell structure [48], (c) ZrO_2 NPs'-decorated Au–Zn alloy [51], and (d) Interwoven Ni#NbO_x structure [53].

1.2 Nanostructured CeO_2- based materials as ionic conductors

Oxygen ionic conductors are widely used in oxygen-permeating membranes, catalysts, and SOFCs. CeO_2-based materials are one of the main ionic conductor candidates with oxygen-vacancy-mediated transport mechanisms owing to their excellent ability to store and release oxygen. Pure stoichiometric CeO_2 is unsuitable as an ionic conductor because of the low concentration of oxygen vacancies. NM-doped CeO_2 and NM–CeO_2 composites are of interest because of the increased oxygen vacancies and the strong interfacial effect.

1.2.1 CeO_2- based materials

Cerium, as the most abundant member of the rare earth family, has a configuration of $[Xe]4f^2 5d^1 6s^2$ with a partially occupied *f* orbital. Ce formally has two oxidation states: +4 in CeO_2 and +3 in Ce_2O_3. CeO_2 is an fcc crystal structure with face group Fm-3 m, also called a fluorite structure (Figure 1.7a). In the unit cell, Ce and O occupy the octahedral interstitial sites, where each Ce cation is coordinated by eight nearest-neighbor oxygen anions, and each oxygen anion is coordinated by four nearest-neighbor cerium cations [57]. Depending on the oxygen partial pressure, structural defects exist in fluorite CeO_2 (Figure 1.7b). Under relatively lower oxygen partial pressure, oxygen atoms in the crystal diffuse toward the surface, and oxygen vacancies move into the crystal (Figure 1.8a [58]). Simultaneously, two electrons condense into the localized *f*-level traps on two Ce atoms and thus convert Ce^{4+} to Ce^{3+}. Oxygen vacancy formation on the CeO_2 surface accompanies the reduction of adjacent Ce^{4+} to Ce^{3+}, and the concentration of Ce^{3+} ions is proportional to that of oxygen vacancies [59]. Therefore, the valence state ratio (Ce^{3+}/Ce^{4+}) assesses the concentration of oxygen vacancies. Figure 1.8b shows the vacancy formation process [60], and it can be described by the reaction:

$$O_O^x + 2Ce_{Ce}^x \rightarrow V_o^{\cdot\cdot} + 2Ce_{Ce}^{\prime} + 1/2O_2 \quad (1-3)$$

Conversely, the transformation from Ce^{3+} to Ce^{4+} occurs when the surface oxygen pressure is relatively higher. Since the oxygen vacancy defects in the CeO_2 structure importantly affect the physical and chemical properties, applying the nanoscale scope, doping with other trivalent ions, and compositing with NMs have been largely studied to further introduce oxygen vacancies.

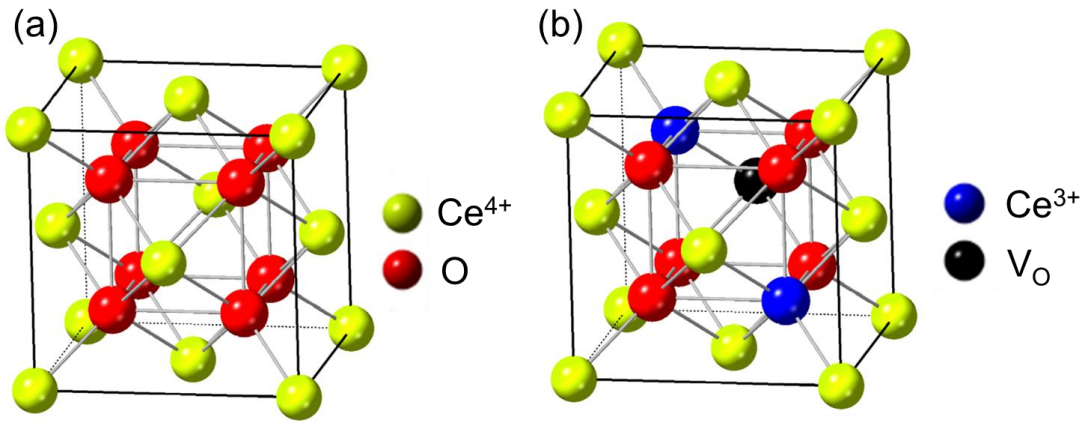

Figure 1.7. Crystal structure of (a) pure CeO_2 and vacancy-defected CeO_2.

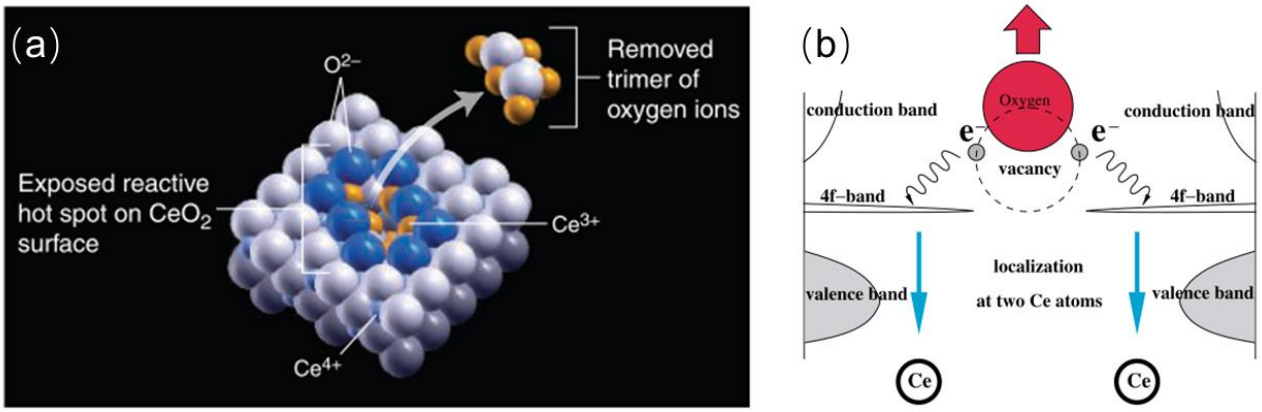

Figure1.8. (a) Ce^{4+} in a dimeric surface vacancy cluster are reduced to reactive Ce^{3+} when the trimer of oxygen ions is removed [58]. (b) Process of Vo formation in CeO_2 [60].

With the decreasing particle size down to the nanometer range, the large surface-area-to-volume ratio produces more oxygen vacancies in the CeO_2 particles [61, 62], thus resulting in unique properties. The high concentration of oxygen vacancy defects in CeO_2 nanotubes or nanorods significantly affects the photocatalytic oxidation of water [63], oxidative dehydrogenation of methanol [64], and electrochemical performance characteristics [65]. Furthermore, the induction of $Ce3^+$ caused by the formation of oxygen vacancies leads to variation in the lattice parameters. Consequently, lattice strain exits in the structure [61, 66]. Enhanced electronic conductivity and lattice relaxation have been found in the nanocrystalline CeO_2 materials [67, 68].

Doping of CeO_2 with trivalent rear-earth (RE) ions, such as Sm, Dy, Gd, and Y, form oxygen vacancies following the reaction:

$$RE_2O_3 \rightarrow 2RE'_{Ce} + 3O_O^x + V_{\ddot{O}} \quad (1-4)$$

Using the first-principles DFT calculation, Y. Tang *et al.* [69] found that two different mechanisms contribute to the oxygen vacancy formation in doped CeO_2. Compared with pure CeO_2, the structural distortion in Zr-doped CeO_2 reduces the $V_{\dot{O}}$ formation energy. However, for Mn-, Pr-, or Sn-doped CeO_2, structural distortion coupled with electronic modification facilitate the $V_{\dot{O}}$ formation. Equation (1-4) shows that the concentration of vacancy defects is controlled by the dopant fraction according to $[RE'_{Ce}] = 2[V_{\dot{O}}]$. Usually, the dopants substitute the Ce atoms in the lattice, while maintaining the fluorite structure. A limitation exists in the concentration of dopants (x_{max}) (Figure 1.9 adopted from Ref. [70]). For most dopants, the suitable solubility (x) is ~$0.2 < x < 0.6$. Doped CeO_2 materials, such as CGO, are good commercial electrolytes because of their high ionic conductivity. The connection between the dopant element and ionic conductivity was clarified using a quantum-mechanical first-principles study by D. A. Andersson *et al.* [71]. It was demonstrated that the factors including migration barriers and vacancy-dopant interactions should be balanced for an optical electrolyte.

Due to the strong MO interaction in NM–CeO_2 composites as described in Subsection 1.1.1, rich vacancies are favored to be generated at the NM–CeO_2 interface. Owing to the strong oxygen storage and release capacity and favored oxygen vacancy formation, CeO_2 has been thought to be the best supporting material for catalysis at Au and Pt NPs. The atomic columns of Au particles on CeO_2 were revealed by T.

Akita *et al.*, [72], which explain the high catalytic activity for the low-temperature water–gas shift reaction. Through the characterization of atomic-scale structure of the Pt/CeO_2(111) interface by aberration-corrected scanning TEM (STEM) imaging and electron energy loss spectroscopy (EELS) technique, local modifications of the registry between Pt and O were detected, and the formation of Ce^{3+} at the MO interface was found [73]. Via the interfacial Pt–O–Ce formation, the amount of oxygen vacancy, thereby accelerating oxygen mobility, promoted the CO oxidation over Pt/CeO_2 catalysts [74]. The Pt/CeO_2 interface is usually engineered to be an epitaxial relationship, exhibiting high catalytic activity for CO oxidation near room temperature [75].

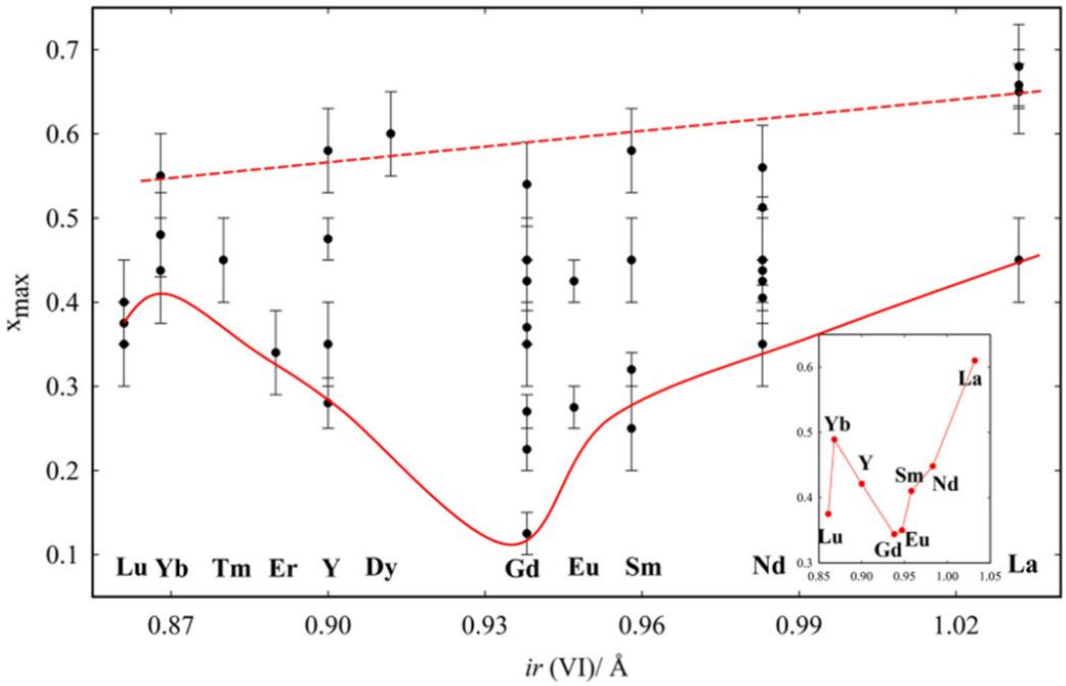

Figure 1.9. Summarized maximum values x_{max}, i.e., the limitation reported for the dopant concentration. Red and dashed lines represent the largest and smallest x_{max} for each dopant, respectively. The insert displays the average x_{max} values based on at least two entries [68].

1.2.2 Oxygen-ion conductivity in CeO_2-based materials

In SOFCs, high oxygen-ion conductivity is required for both the electrode and electrolyte, which is promising for future energy applications. CeO_2-based materials with vacancy jump transportation are attractive because of their abundant vacancy defects [76]. For polycrystalline materials, the total ion conductivity comprises the bulk and grain-boundary (GB) transportations. For bulk transportation (Figure 1.10a), the oxygen ion in the crystal lattice site hops into the adjacent tetrahedral oxygen vacancies by overcoming the energy landscape. There are three pathways: along the <100>, <110>, and <111> directions. Computational results of the energy profiles show that pathway 1 along the <100> direction possesses relatively lower activation energy [77] for the pure CeO_2. However, for the RE-doped CeO_2, five oxygen vacancy-hopping models are possible for transportation (Figure 1.10b). Owing to the emerged lattice strain and dislocations caused by the doped atoms, the type and radius of RE^{3+} influence the hopping energy barrier and trapping

effect, consequently affecting the ionic conductivity [77]. Doping with smaller RE^{3+} reduces the hopping energy barrier, but traps oxygen vacancies at the nearest-neighbor site. In contrast, increased energy barriers and decreased vacancy trapping occur when doping with larger RE^{3+}. Concerning the GB transportation, structural disorder and edge dislocation at the GBs facilitate ionic transport, whereas precipitates and oxygen vacancy depletion block ionic migration, such as SiO_2 precipitates, at the GBs of YSZ conductors [78, 79]. However, in the case of heterointerfaces, ion redistribution in a space-charge region or the abovementioned interfacial effect provides a fast conductive pathway along the interface [80].

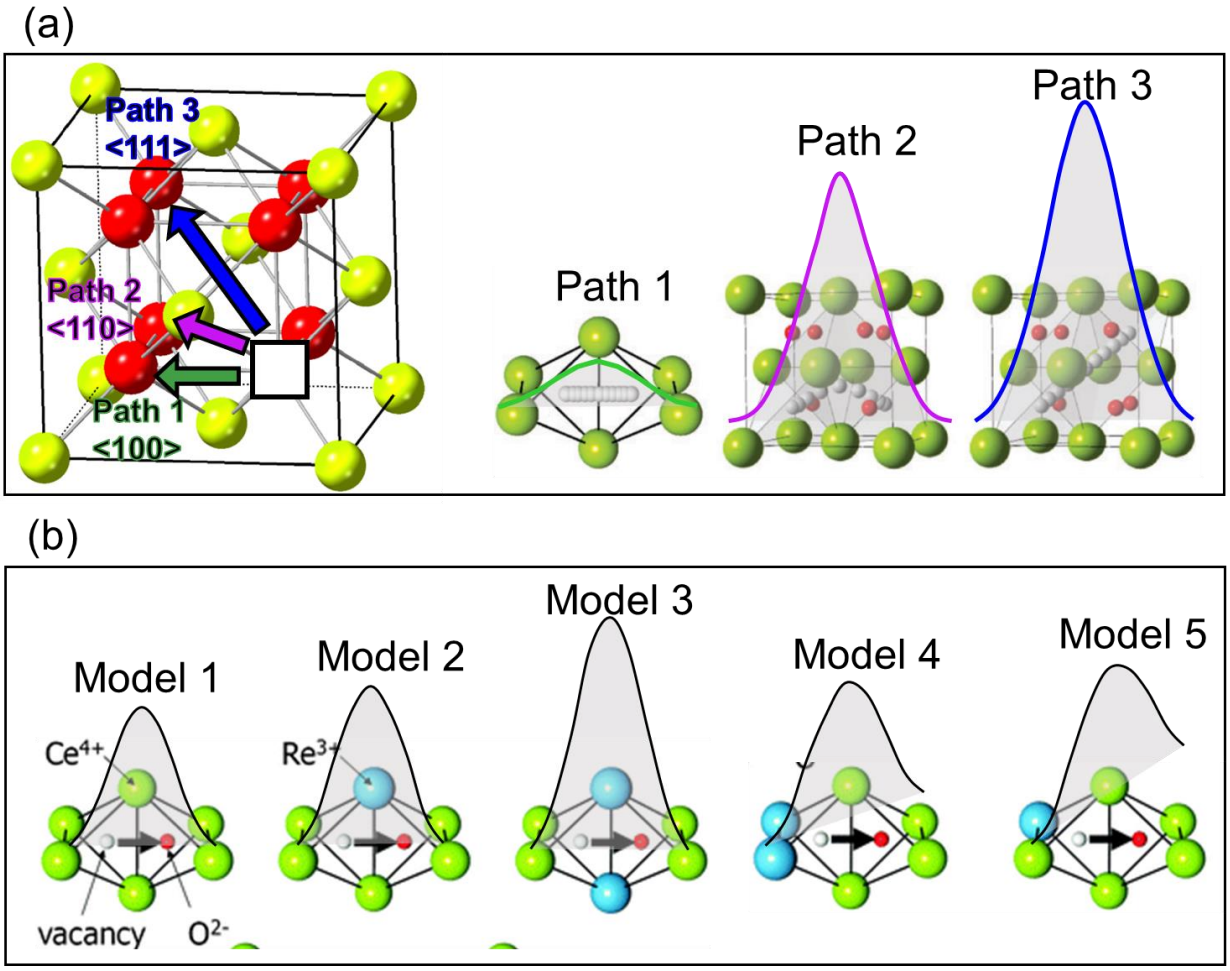

Figure 1.10. (a) Three possible oxygen-hopping pathways and energy profiles for fluorite CeO_2. (b) Five models and energy profiles for the oxygen hopping along the path 1, <100>, for the RE-doped CeO_2 [77].

For oxide-based heterostructures, oxygen transportation along the heterointerface is more dominant than bulk transport [81]. The origin of fast oxygen transportation in the multilayered heterointerfaces has been studied, and the influential factors, including edge dislocations, epitaxial strain, and space-charge regions, have been elucidated [82-84]. Due to the mismatched lattice between the two different phases, the defects certainly exceed that in the bulk crystals that facilitate the oxygen-ion hopping. As indicated by the density-functional calculations, the lattice-mismatch strain and oxygen-sublattice incompatibility in multilayers of YSZ and $SrTiO_3$ induce extreme disorder, even at room temperature [83].

Depending on the mismatch degree of the lattice parameter, the heterointerfaces can be classified into three groups: incoherent, semicoherent, and coherent interfaces (Figure 1.11). For a large mismatch degree, a large strain at the interface cannot be accommodated by the elastic strain. To reduce the interfacial strain, misfit dislocations are introduced in the incoherent and semicoherent interfaces. Rich oxygen vacancies in these interfaces provide a fast conduction pathway for oxygen ions [85]. However, no misfit dislocations occur in the coherent interfaces because of the small mismatch degree, resulting in a stained field around the interface. The phases with larger and smaller lattice parameters are compressed and tensed, respectively. For heterostructures coupling an ionic conductor with an insulator, the elastic strain influence on the oxygen-ion transportation has attracted great attention. Generally, tensile strain in the conductive phase positively affects the interfacial conductivity, such as YSZ–STO multilayers [86], YSZ–Y_2O_3 [87], and $SrZrO_3$–RE_2O_3 (RE = Sm, Eu, Gd, Dy, and Er) [88]. However, compressive strain negatively influences the ionic conductivity, such as the case in YSZ–Sc_2O_3 multilayers [89]. Without considering the anisotropies and stress relaxation in heterostructures, Korte *et al.* found a linear dependence of the interfacial conductivity on the lattice misfit [87].

As explained in the interfacial effect between metals and oxides, charge transfer appears in the heterointerface because of the free energy discontinuity. The redistribution of ionic and electronic defects causes a local space-charge region where mobile charges deplete or accumulate [89]. In the YSZ and CGO polycrystalline materials with many oxygen vacancies, oxygen vacancies and electrons accumulate at the space-charge region [67, 90]. The characteristic length scale of the space-charge region is of the same order as the Debye length, and the space-charge effects are remarkable when this region is comparable to the thickness of the individual layer. However, the space-charge effects should minimally affect the conduction properties because of the high concentration of defects with a narrowed Debye length.

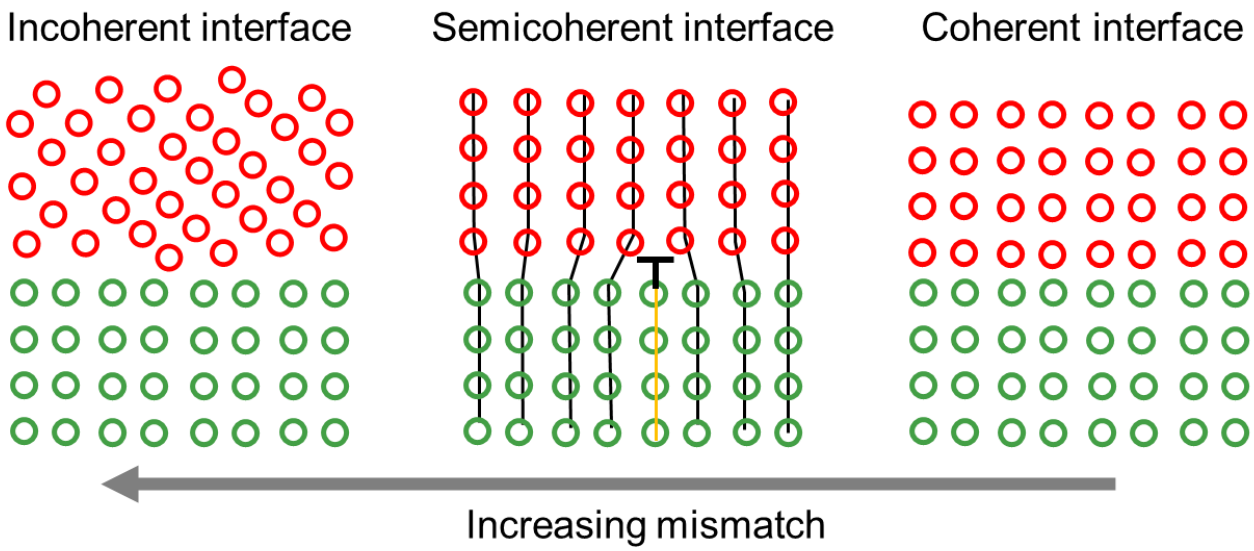

Figure 1.11. Three kinds of interfaces between different phases: incoherent, semicoherent, and coherent interface with decreasing mismatch.

1.2.3 Importance of conductive phase connectivity to the ionic transportation

The local structural effect on the oxygen ionic conductivity has been well studied and made great application progress. It is reasonable to expect a high ionic conductivity in the NM–CeO_2 heterostructures. Nevertheless, studies about the effects of the transportation pathway in a long-range distance (>100 nm) on the ionic conductivity of the oxide NCs are limited. The relationship between morphology and ionic conductivity (Li^+) has been studied severally for polymers [91-93]. Compared with NPs, the lamellae or aligned nanowire-filled conductive polymers supply a more continuous fast pathway for Li^+ transportation

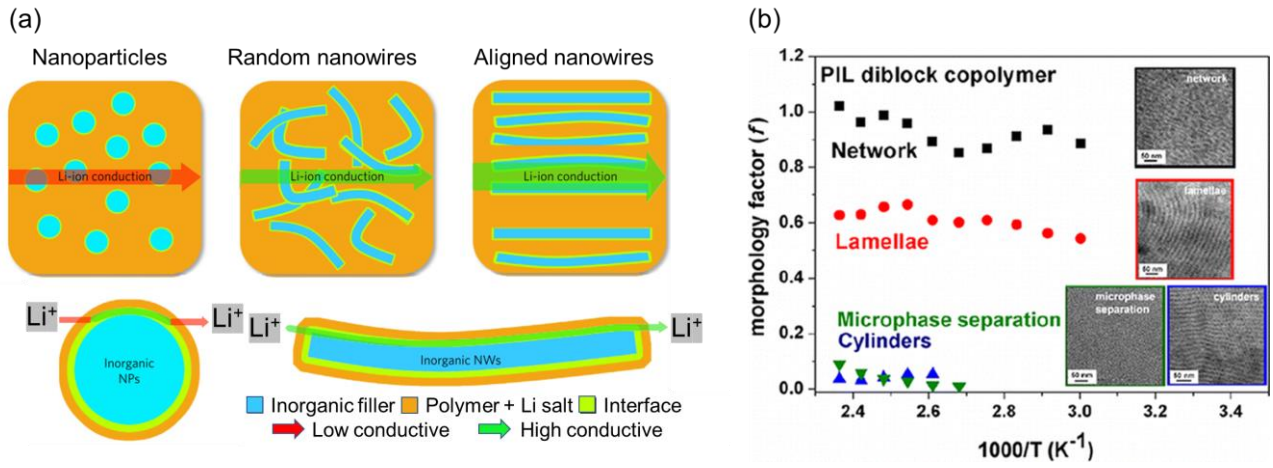

Figure 1.12. Influence of morphology of conductive phase on Li^+ transpiration. (a) Fast ion-conducting pathway without crossing junctions contributes to enhanced ionic conductivity, as reported by Liu *et. al.* [94]. (b) Network conductive phase showed the highest conductivity than lamellar and cylinders structures, as demonstrated by J. H. Choi *et al*. [96].

without crossing junctions, contributing to slow transportation (Figure 1.12a) [94, 95]. Furthermore, Figure 1.12b shows that the network structure was demonstrated to have a higher conductive property than the lamellae structure for the phase-separated block copolymers because of the highly connective conductive phase [96]. For CeO_2-based NCs, the interaction effects between NM and CeO_2 dominate the transportation along the interface. The interface region enriched with oxygen vacancies allows fast oxygen-ion hopping from one vacancy to another. Also, the bonding states between the Ce atoms could be changed to facilitate oxygen-ion hopping. Consequently, enhanced oxygen-ion mobility and reduced activation energy are expected for the composites with high connectivity of CeO_2 phases. Another influence of the different phase connectivities on NCs is the interface area between the NM and CeO_2 in the case of the same volume of CeO_2 in the composites. The higher the connectivity of the CeO_2 phase, the lower the interface area. Since the strain remains around the interface, the interfacial area affects the activation energy of the oxygen-ion transportation. Therefore, it is important to quantitatively identify the phase connectivities to understand the relationship between the structure and ionic conductivity of CeO_2-based NCs.

However, it is difficult and time-consuming to visually distinguish the two similar lamellar structures and evaluate the phase connectivities quantitatively via a conventional method. As more complicated structures

are supposed to be obtained with the development of engineered NM–CeO_2 NCs, quantitative description of the structures helps clarify the relationship between the morphology and properties, which accelerates the design of ideal textures with superior transportation properties. Thus, a mathematical tool-TDA extracting the feature of textures is needed.

1.3 Topological data analysis

Topological data analysis (TDA), a subarea of computational topology, is an emerging mathematical tool for the robust analysis of statistical data. Using TDA, we can extract the topological features (components, rings, and cavities) from the scientific data. Various fields, including biology [97, 98], brain science [99, 100], and materials science [101, 102] have successfully applied TDA for describing data shape. Different from the conventional data geometry, which focuses on the size and unique shape, topology concentrates on the data continuity, i.e., the connection and existence of a hole. For example, we naturally think about a cup and a donut (Figure 1.13) by describing their heights, radii, and colors. These descriptions are entirely different from the geometric and statistic viewpoints. Actually, they can be the same in the topological world since they can

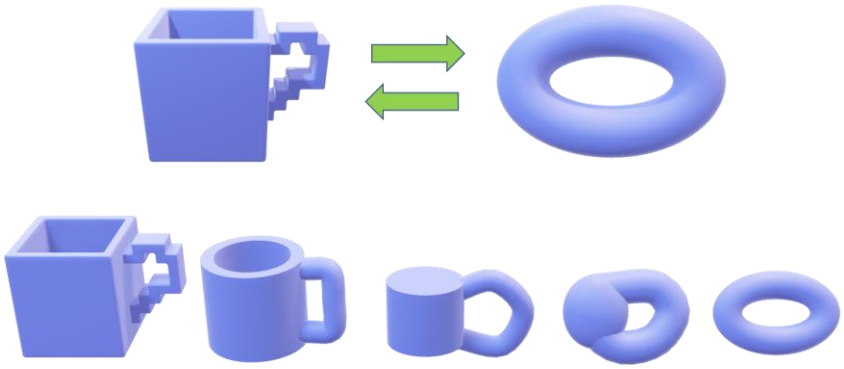

Figure 1.13. A cup and a donut are topologically equivalent since they can be continuously transformed to each other. The continuous transformation includes the stretching, twisting, crumpling, and bending without tearing and gluing.

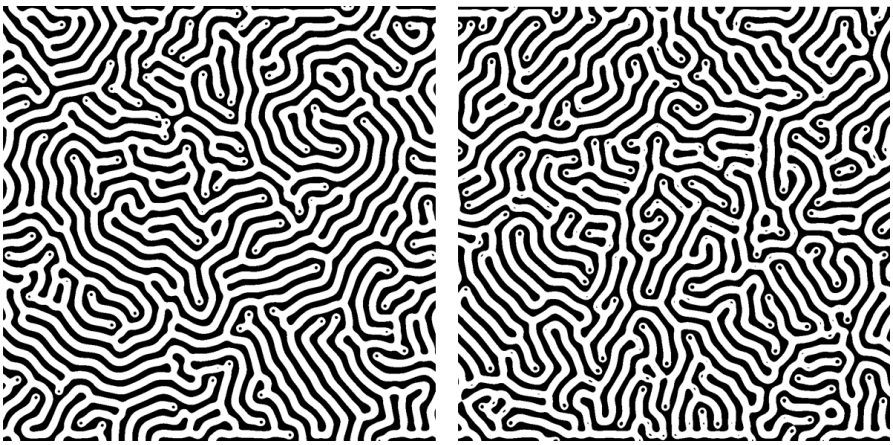

Figure 1.14. Two maze patterns generated by the reaction diffusion system (Gray-scott) model with different feed and death rates. Software is available in https://pmneila.github.io/jsexp/grayscott/.

transform into each other continuously without tearing and gluing. Therefore, TDA is a complementary tool that aids structural recognition from a different viewpoint. Importantly, for the complicated structures that are difficult to identify by geometric description (Figure 1.14), TDA analysis is significantly useful in such classification. Furthermore, homology is an important tool in TDA that describes the data structure quantitatively. The phase connectivity can be quickly identified through algorism-based computations.

1.3.1 Homology and Betti numbers

Considering the abovementioned example, a cup and a donut are identical in the homological sense because they can be continuously transformed into each other. Therefore, homology measures the features related to the different dimensions, rather than the statistical data from a specific dimension. Figure 1.15a shows the homological features for commonly studied dimensions. In the 0-dimension (0D), homology measures the connected component, tunnels or loops from 1D, and cavities or voids from 2D. For higher k-dimensional (kD, k > 2) features, it is difficult to visualize them intuitively, but they exist in higher-dimensional objects. The rank of the *i*-dimensional (*i*D) homological group is called the Betti numbers (β_i), which counts the number of *i*D features. Two-dimensional objects have two values: β_0 and β_1, and 3D objects have three values: β_0, β_1, and β_2.

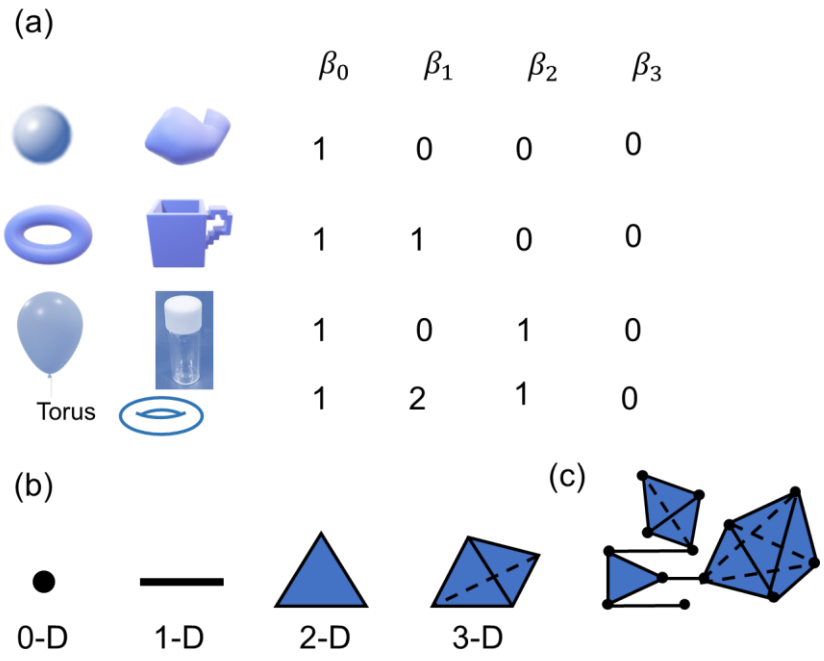

Figure 1.15. (a) Betti numbers for different objects. The k-th Betti number measures the kD holes, i.e., Betti number 1 for connectivity, Betti number 2 for loops, and Betti 3 for enclosed holes. (b) Simplexes with increasing dimensions: a vertex in 0-D, an edge in 1-D, a triangle in 2-D, and a triangular pyramid in 3-D. (c) Simplicial complex containing different dimensional simplexes.

A basic item for understanding computational homology is the simplicial complex. The i-simplex is the convex hull of $i + 1$ affinely independent points $x_0, x_1, \ldots, x_i \in R^d$. Denoting $\sigma = \text{conv}\{x_0, x_1, \ldots, x_i\}$, the

dimension of σ is i. Figure 1.15b shows the different simplex with increasing dimensions. Specifically, a point is a 0D object, an edge ended with two vertices is a 1D object, a face comprising three edges is a 2D object, a 3D simplex comprises four edge-connected faces forming a closed cycle. A simplicial complex X is a finite collection of simplices; they can be seen as a higher-dimensional generalization of graphs (Figure 1.15c). An object can be separated into several groups according to different dimensions. For example, $C_0(X)$ is the class of all vertices, $C_1(X)$ is the class of all edges, and $C_2(X)$ is the group of all triangle faces. Each group has a module of 2, i.e., $Z_2 := \{0, 1\}(2n = 0, 2n + 1 = 1, for\ n > 0)$. To calculate the holes in iD, it is important to know the boundary of a complex. The boundary operator (∂_i) connects the simplicial groups into a chain complex C_i:

$$\dots \to C_{k+1} \xrightarrow{\partial_{k+1}} C_k \xrightarrow{\partial_k} C_{k-1} \to \cdots$$

The boundary of an iD group is the degraded $i - 1$ subgroup. For example, the boundaries of an edge and a triangle comprises two vertices and three edges, respectively. However, the boundary of a triangle with three edges is empty. An iD hole exists when the boundary of C_i, i.e., the boundary of C_{i+1}, is empty. Figure 1.16a lists several simplicial complexes with a spatial hole or not. Two groups must be defined: the cycle ($Z_k = ker\partial_k$)and the boundary group ($B_k = im\partial_{k+1}$). The k-th homology group is $H_k = Z_k/B_k$. Figure 1.6b shows the calculation process with a simplicial complex. The results demonstrate that a loop comprising three edges (24, 23, 34) exists in this component.

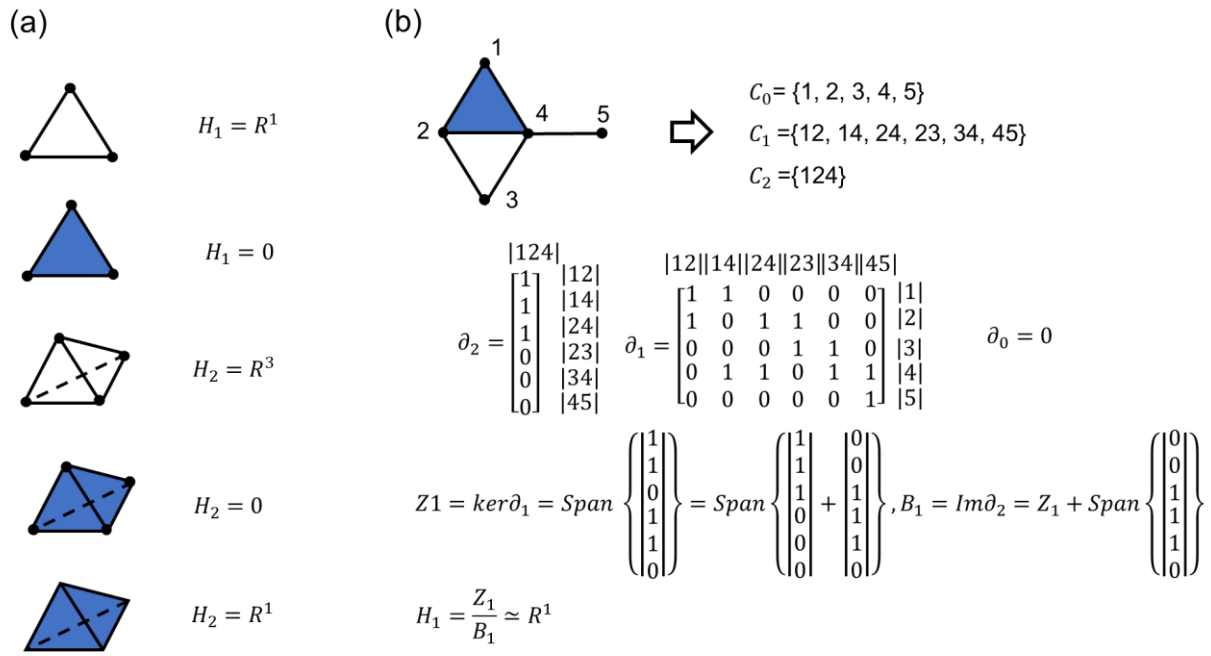

Figure 1.16. (a) Several examples showing the exitance of homology groups or not. (b) Calculation process for homology groups. A loop comprising (23, 24, 34) is detected in this complex.

To clearly understand what features and how homology measures, digital images will be introduced since images from experiments or simulations are commonly used data in materials science. Figure 1.17 shows the workflow for analyzing a grayscale image with five coins on a desk. Figure 1.17a is a grayscale image with

the histogram on top of Figure 1.17b. The coins from the desk background must be extracted through the image binarization (Figure 1.15c). The corresponding histogram indicates that only 0 and 255 gray values are shown at the bottom of Figure 1.15b. Then, β_0 and β_1 are counted by counting the black and enclosed white domains, respectively. Since the top coin is not totally enclosed by the black background, it does not contribute to β_1. Therefore, β_0 = 3 and β_1 = 4. Interestingly, β_0 and β_1 here can be used to recognize the number of coins with a hole and the total number of coins.

Based on how homology works for data analysis, several descriptors, such as Euler characteristic, Betti curve, Euler characteristic graph, persistence diagram, and persistence image, are used for applications except for the basic descriptor (β_0 and β_1), as explained above. The Euler characteristic (χ) is also a descriptor based only on a relationship between the number of topological features. χ is the alternating sum of Betti numbers, $\chi = \sum_{i=0}^{\infty}(-1)^i\beta_i$. The Betti numbers and Euler characteristic are invariants for certain static data. The Betti curves and the Euler characteristic graph are the descriptors that track the changes in Betti numbers and χ when the data is changed by a filtration, respectively. Additionally, persistence diagrams and images are recently developed descriptors that investigate the persistence of the topological features during the data change. These nonstatic descriptors are classified as persistence homology, which is an advanced homology tool. The next subsections will introduce the application of Betti numbers and persistence diagrams as descriptors in materials science.

1.3.2 Betti numbers for describing the structure of materials

Betti numbers are useful indices to represent material structures and have been used to correlate the structure and property in various materials quantitatively. Gamerio *et al.* used Betti numbers on simulated images to clarify the differences between the deterministic and stochastic models in the structural evolution during spinodal decomposition [103]. Ishida *et al.* analyzed the fracture surfaces of low-carbon steel using the homology method and found that β_1 is strongly related to the stress intensity factor [104]. Wanner *et al.* quantitatively characterized the simulated thermal–elastic response of a calcite-based polycrystal. They demonstrated that the Betti numbers could distinguish different GB misorientations and the corresponding response fields [105]. Besides, β_1/β_0 can further distinguish the data shape. K. Nakane *et al.* successfully used β_1/β_0 as indices for tumor tissues from normal tissue from a digital image of colon tissue [106]. A decreased value of β_1/β_0 representing a reduced electrical conductivity in Ni–polymer NCs was reported by Hansen *et al.* using SEM images [107]. Also, several researchers analyzed 2D and 3D structures using Betti numbers to build structure–property relationships. Different types of bone trabecular structures in 3D revealed by the microcomputed tomography were classified by β_1/β_0, and β_2/β_0 with high accuracy [108]. Homology is also suitable for discriminating 3D chondritic meteorites, which were reconstructed by X-ray computed tomography [109].

The phase connectivity of structures can be easily represented by the number of domains inside the projected image. Thus, the higher the value of β_0, the lower the phase connectivity. The relation applies to

different structures with similar total phase proportions. Considering Figure 1.14 as an example, it is easy to count the number of black domains (β_0) to evaluate the connectivity of the black phase. The results are β_0 = 163 and β_0 = 224 for the left and right panels of Figure 1.14, respectively, suggesting that the left pattern has higher connectivity than the right pattern. Comparing the two patterns carefully reveals more short stripes and dots on the right pattern, confirming the lower connectivity. If the white domains are the interesting phase and the influence of picture edge is excluded, β_1 can also reflect the connectivity of white parts. Therefore, Betti numbers are suitable descriptors for quantitatively evaluating the phase connectivities of structures.

1.3.3 Persistence diagram for structural description

Homology measures the existence of iD holes for a specific structure. In contrast, persistence homology tracks when the holes appear and disappear as a function of continuous changeable factors, such as point radius, watermark, and binary threshold. Persistent homology records the number of homological features, iD holes, and their lifetime from birth (b) to death (d) time. It allows for a multiscale approach to get more information

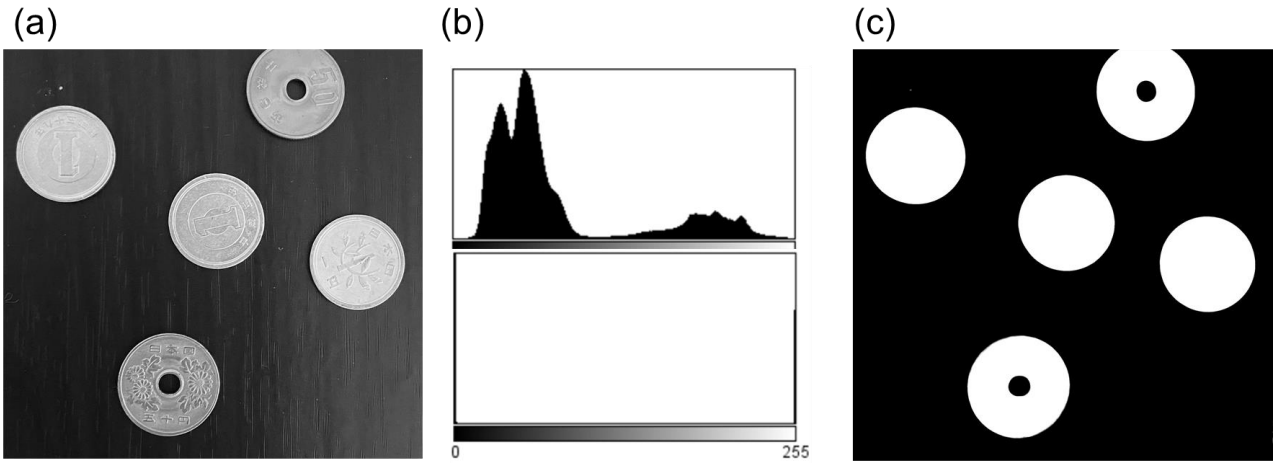

Figure 1.17. Calculation process of homology groups for a grayscale image. (a) An image displaying 5 coins on a desk. (b) Top and bottom panel histograms of grayscale image (a) and corresponding binary image (c), respectively.

from the data. An important graphical representation of the persistent homology is the persistence diagram (PD). The pairs (b, d) are represented as points on the coordinate axis, with the birth and death times as the horizontal and vertical axes, respectively. Through additional filtration, the geometric information of the iD holes can be obtained.

Figure 1.18a shows a typical example of computational persistent homology by constructing the Rips complex of point cloud data. As each point's radius increases, the points touch each other. Consequently, two touched points are connected by an edge, three touched points form a triangle face, and four touched points form a tetrahedron 4D simplex. Rips simplicial complex includes every finite set of balls that has a radius, at most r. As new simplices appear, the Betti numbers change. Tracking the appearance and disappearance of holes by changing a parameter is termed filtration. The PD in Figure 1.18a draws pairs (birth, death) of Betti

1 (loops) as the radius increases. Initially, each ball with r = 0.3 distributes dependently, contributing to no loops among the balls. When r increases to 0.6, five balls form a loop, as indicated by a red arrow. This loop disappears when the five balls connect to each other (r = 0.8), as indicated by a blue arrow. Consequently, the birth and death times of this loop are recorded as a pair (0.6, 0.8). Similarly, the loop formed (marked by red arrow) at r = 0.8 and 0.9 disappeared (marked by the blue arrow) at 1.8 and 1.6 leading to pairs of (0.8, 1.8) and (0.9, 1.6) in PD, respectively. Since the death time is always later than the death time, all pairs must be located above the diagonal line of the figure. Moreover, the pairs located near the diagonal line indicate that the corresponding holes cannot remain persistent for long during filtration, and thus are likely to be considered as noise.

The applications of the persistent homology with point clouds data are the atomic configuration in amorphous solids (glass, Figure 1.18b) [110, 111] and organic molecular structures (Figure 1.18c) [112]. The hierarchical structure of shapes in the amorphous system can be characterized by the point distributions in PDs. Specific molecules with embedded chemical bonding information can be identified through PDs, which helps predict the interaction energy with CO_2. In addition to the point cloud data, digital images are common cases for computational persistent homology. Trigger sites and hepatic tumor classification have been studied using PDs [113, 114]. Furthermore, with the help of PD for discerning different structures, big data processing becomes possible using machine-learning models. The combination of PD and machine-learning models has been used in various areas, including image analysis [115], shape analysis [116], and the biology filed [114].

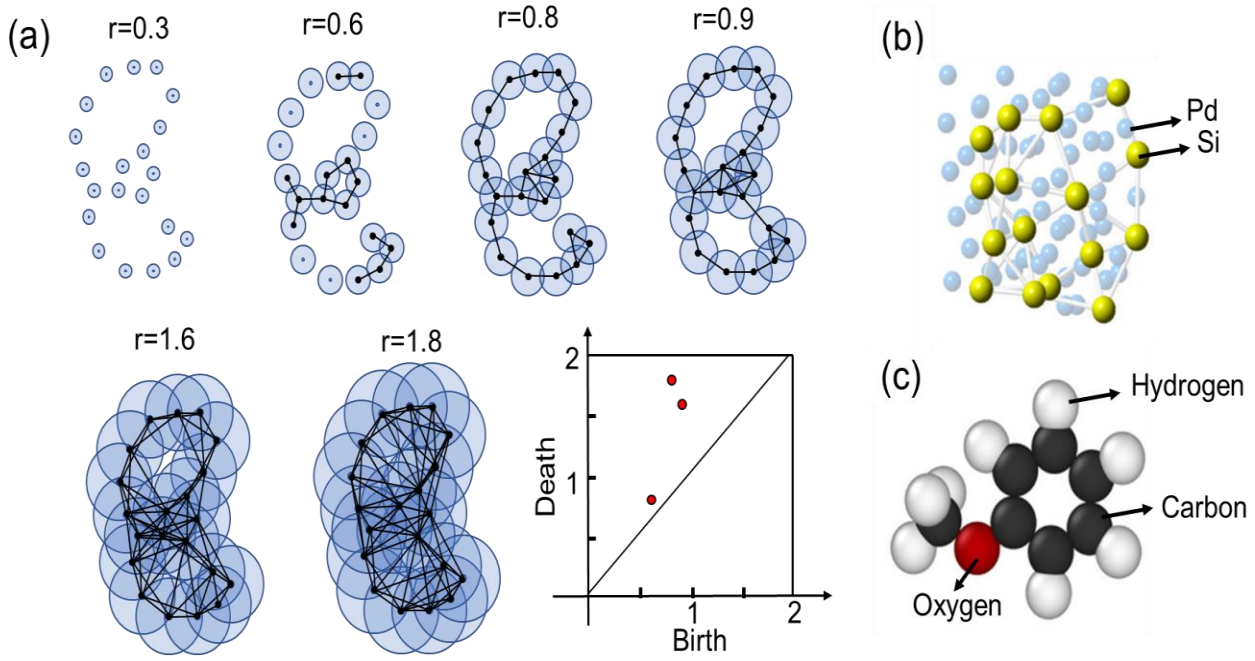

Figure 1.18. (a) Example of a point cloud data for persistent homology analysis. As *r* of each point increases, the two points with distance of < 2*r* are connected with an edge. By constructing the Rips complex, the appearance and disappearance of loops, i.e., Betti 1, are tracked and recorded as red points in the persistence diagram. (b) Application of persistent homology on glass [109] and the molecular structure [110].

1.4 Goals of this study

It is well known that homology for stationary structural analysis helps recognize differences that are difficult to discern visually, and the conventional geometrical measurements, TDA, enable to determine the look-alike features and locate the topological features based on connectivity. As a powerful and functional tool in materials science, TDA is important in classifying different structural data and predicting the corresponding properties, accelerating the materials' design in the future. Computed homology for material structures convenient us to apply the machining learning to the structure analysis, which will be the mainstream of material characterization.

Although digital images can be obtained from simulated mappings, optical and scanning electron microscopy were already used for homological structure analysis, and TEM images have rarely been applied before, which are common techniques for characterizing the nanostructures, especially phase-separated NCs with clear contrast for identification. The transportation behavior along one conductive nanophase of two-phase composites is strongly related to the configuration of NCs, which can be uncovered by TEM imaging. Therefore, applying the homology method to classify various structures and relating the structure to the transport properties is feasible and worth using STEM image data, which is scanning-type TEM imaging. Nevertheless, the 2D information about nanostructures contained in the STEM images is difficult to correctly describe the real 3D object. Much information along the depth dimension is excluded and must be revealed. STEM tomography, with its mature reconstruction process, does allow the visualization of the 3D compositional structure of NCs. The relationship between the 3D structure and physical property paves a longer way to practical issues.

As mentioned in Subsection 1.1.2, Pt/CeO_2 NCs are a mixture of ionic and electronic conductors with potential applications as the electrodes of SOFCs. Self-assembled Pt/CeO_2 from Pt_5Ce alloy with various structures is suitable for fundamentally studying the homological linkage between the structure and the ionic conduction along the CeO_2 phase. Since the self-assembly process via annealing of the binary alloy introduces internal oxidation, which negatively affects the performance in applications, most studies concentrated on avoiding the oxidation behavior. Therefore, the kinetic of which has been extensively studied for various materials and shown a parabolic law, while the questions concerning the nucleation and growth of the precipitate, orientation relationship between the two separated phases, and the factors affecting the precipitate morphologies or distributions are limited identified. Understanding the oxidation-induced self-assembly process mechanism is critical to answer such questions and control the MO interface and the configuration of NCs.

Therefore, the study aims at applying TDA to TEM structural images to study the structure–ionic conductivity relationship of Pt/CeO_2 NCs. To achieve this goal, the following objectives must be accomplished: (1) Understand the phase separation behavior at the atomic scale during the oxidation of the precursor (Pt_5Ce) to control the Pt/CeO_2 interface.

(2) Apply the Betti number for describing the 2D phase connectivity of Pt/CeO_2 NCs to understand the quantitative 2D structure–ionic conductivity relationship.

(3) Apply the Betti number for describing the 3D phase connectivity of Pt/CeO_2 NCs to understand the quantitative 3D structure–ionic conductivity relationship.

(4) Describe the Pt/CeO_2 structures using a persistence diagram for structural classification.

To this end, this thesis comprises seven chapters. Chapter 1 introduces the research background in MO composites and basic knowledge of homology analysis, leading to the purposes of this thesis. Chapter 2 contains the experimental section for the sample fabrication and subsequent characterization methods. Chapter 3 reveals the mechanism of the oxidation-induced self-assembly phase separation process at the atomic scale. Chapters 4 and 5 study the 2D- and 3D-reconstructed structure–oxygen-ion-conductivity quantitative relationships using Betti numbers, respectively. Chapter 6 applies the persistence diagram to identify the topological features in each structure, and finally, Chapter 7 summarizes the study and provides future prospects.

References

[1] Matsunaga, K.; Sasaki, T.; Shibata, N.; Mizoguchi, T.; Yamamoto, T.; Ikuhara, Y. Bonding Nature of Metal/Oxide Incoherent Interfaces by First-Principles Calculations. Phys. Rev. B - Condens. Matter Mater. Phys. 2006, 74 (12), 2–9.

[2] Yang, Z.; Lu, Z.; Luo, G. First-Principles Study of the Pt/CeO_2 (111) Interface. Phys. Rev. B - Condens. Matter Mater. Phys. 2007, 76 (7).

[3] Lu, Z.; Yang, Z. Interfacial Properties of $NM/CeO_2(111)$ (NM = Noble Metal Atoms or Clusters of Pd, Pt and Rh): A First Principles Study. J. Phys. Condens. Matter 2010, 22 (47).

[4] Campbell, C. T. Catalyst-Support Interactions: Electronic Perturbations. Nat. Chem. 2012, 4 (8), 597–598.

[5] Vayssilov, G. N.; Lykhach, Y.; Migani, A.; Staudt, T.; Petrova, G. P.; Tsud, N.; Skála, T.; Bruix, A.; Illas, F.; Prince, K. C.; Matolín, V.; Neyman, K. M.; Libuda, J. Support Nanostructure Boosts Oxygen Transfer to Catalytically Active Platinum Nanoparticles. Nat. Mater. 2011, 10 (4), 310–315.

[6] Luches, P.; Pagliuca, F.; Valeri, S.; Illas, F.; Preda, G.; Pacchioni, G. Nature of Ag Islands and Nanoparticles on the $CeO_2(111)$ Surface. J. Phys. Chem. C 2012, 116 (1), 1122–1132.

[7] Branda, M. M.; Hernández, N. C.; Sanz, J. F.; Illas, F. Density Functional Theory Study of the Interaction of Cu, Ag, and Au Atoms with the Regular CeO_2 (111) Surface. J. Phys. Chem. C 2010, 114 (4), 1934–1941.

[8] Chu, S.; Ou, P.; Ghamari, P.; Vanka, S.; Zhou, B.; Shih, I.; Song, J.; Mi, Z. Photoelectrochemical CO_2 Reduction into Syngas with the Metal/Oxide Interface. J. Am. Chem. Soc. 2018, 140 (25), 7869–7877.

[9] Ding, W. C.; Gu, X. K.; Su, H. Y.; Li, W. X. Single Pd Atom Embedded in $CeO_2(111)$ for NO Reduction with CO: A First-Principles Study. J. Phys. Chem. C 2014, 118 (23), 12216–12223.

[10] Singha, R. K.; Tsuji, Y.; Mahyuddin, M. H.; Yoshizawa, K. Methane Activation at the Metal-Support Interface of Ni_4-CeO_2(111) Catalyst: A Theoretical Study. J. Phys. Chem. C 2019, 123 (15), 9788–9798.

[11] Werner, K.; Weng, X.; Calaza, F.; Sterrer, M.; Kropp, T.; Paier, J.; Sauer, J.; Wilde, M.; Fukutani, K.; Shaikhutdinov, S.; Freund, H. J. Toward an Understanding of Selective Alkyne Hydrogenation on Ceria: On the Impact of O Vacancies on H_2 Interaction with CeO_2(111). J. Am. Chem. Soc. 2017, 139 (48), 17608–17616.

[12] Chen, B.; Ma, Y.; Ding, L.; Xu, L.; Wu, Z.; Yuan, Q.; Huang, W. Reactivity of Hydroxyls and Water on a CeO_2(111) Thin Film Surface: The Role of Oxygen Vacancy. J. Phys. Chem. C 2013, 117 (11), 5800–5810.

[13] Fu, Q.; Saltsburg, H.; Flytzani-Stephanopoulos, M. Active Nonmetallic Au and Pt Species on Ceria-Based Water-Gas Shift Catalysts. Science. 2003, 301 (5635), 935–938.

[14] Bruix, A.; Rodriguez, J. A.; Ramírez, P. J.; Senanayake, S. D.; Evans, J.; Park, J. B.; Stacchiola, D.; Liu, P.; Hrbek, J.; Illas, F. A New Type of Strong Metal-Support Interaction and the Production of H_2 through the Transformation of Water on Pt/CeO_2(111) and Pt/CeO_x/TiO_2(110) Catalysts. J. Am. Chem. Soc. 2012, 134 (21), 8968–8974.

[15] Tao, L.; Shi, Y.; Huang, Y.; Zhang, Y.; Huo, J.; Zou, Y.; Luo, J.; Dong, C.; Wang, S. Interface Engineering of Pt and CeO_2 Nanorods with Unique Interaction for Methanol Oxidation. Nano Energy 2018, 53, 604–612.

[16] Zhang, S.; Xia, Z.; Ni, T.; Zhang, Z.; Ma, Y.; Qu, Y. Strong Electronic Metal-Support Interaction of Pt/CeO_2 Enables Efficient and Selective Hydrogenation of Quinolines at Room Temperature. J. Catal. 2018, 359, 101–111.

[17] Liu, X.; Iocozzia, J.; Wang, Y.; Cui, X.; Chen, Y.; Zhao, S.; Li, Z.; Lin, Z. Noble Metal-Metal Oxide Nanohybrids with Tailored Nanostructures for Efficient Solar Energy Conversion, Photocatalysis and Environmental Remediation. Energy Environ. Sci. 2017, 10 (2), 402–434.

[18] Jing, L.; Zhou, W.; Tian, G.; Fu, H. Surface Tuning for Oxide-Based Nanomaterials as Efficient Photocatalysts. Chem. Soc. Rev. 2013, 42 (24), 9509–9549.

[19] Yu X.; Kim B.; Kim Y. K. Highly Enhanced Photoactivity of anatase TiO_2 nanocrystals by controlled hydrogenation-induced surface defects[J]. ACS Catal., 2013, 3(11), 2479–2486.

[20] Dinh, C. T.; Yen, H.; Kleitz, F.; Do, T. O. Three-Dimensional Ordered Assembly of Thin-Shell Au/TiO_2 Hollow Nanospheres for Enhanced Visible-Light-Driven Photocatalysis. Angew. Chemie - Int. Ed. 2014, 53 (26), 6618–6623.

[21] Liu, X.; Li, F.; Wang, Y.; Jin, H.; Wang, H.; Li, Z. Surface-Enhanced Raman Scattering and Photocurrent Multiplication Phenomenon of ZnO/Ag Nanoarrays. Mater. Lett. 2013, 94, 19–22.

[22] Chen, L.; Luo, L.; Chen, Z.; Zhang, M.; Zapien, J. A.; Lee, C. S.; Lee, S. T. ZnO/Au Composite Nanoarrays as Substrates for Surface-Enhanced Raman Scattering Detection. J. Phys. Chem. C 2010, 114 (1), 93–100.

[23] Wang, M.; Pang, X.; Zheng, D.; He, Y.; Sun, L.; Lin, C.; Lin, Z. Nonepitaxial Growth of Uniform and Precisely Size-Tunable Core/Shell Nanoparticles and Their Enhanced Plasmon-Driven Photocatalysis. J. Mater. Chem. A 2016, 4 (19), 7190–7199.

[24] (1) Liu, J.; Qiao, S. Z.; Chen, J. S.; Lou, X. W.; Xing, X.; Lu, G. Q. Yolk/Shell Nanoparticles: New Platforms for Nanoreactors, Drug Delivery and Lithium-Ion Batteries. Chem. Commun. 2011, 47 (47), 12578–12591.

[25] Walther A, Muller A H E. Janus Particles: Synthesis, Self-assembly, Physical Properties, and Applications. Chemical reviews, 2013, 113(7), 5194-5261.

[26] Bieberle-Hütter, A.; Hertz, J. L.; Tuller, H. L. Fabrication and Electrochemical Characterization of Planar Pt-CGO Microstructures. Acta Mater. 2008, 56 (2), 177–187.

[27] Price, R.; Cassidy, M.; Grolig, J. G.; Mai, A.; Irvine, J. T. S. Preparation and Testing of Metal/$Ce_{0.80}Gd_{0.20}O_{1.90}$ (Metal: Ni, Pd, Pt, Rh, Ru) Co-Impregnated $La_{0.20}Sr_{0.25}Ca_{0.45}TiO_3$ Anode Microstructures for Solid Oxide Fuel Cells. J. Electrochem. Soc. 2019, 166 (4), F343–F349.

[28] Choi, S.; Bae, J.; Lee, J., Cha, J. Exhaust Gas Fuel Reforming for Hydrogen Production with CGO-based Precious Metal Catalysts. Chem. Eng. Sci. 2017, 163, 206-214.

[29] Barbucci, A.; Bozzo, R.; Cerisola, G.; Costamagna, P. Characterisation of Composite SOFC Cathodes Using Electrochemical Impedance Spectroscopy. Analysis of Pt/YSZ and LSM/YSZ Electrodes. Electrochim. Acta 2002, 47 (13–14), 2183–2188.

[30] Fóti, G.; Jaccoud, A.; Falgairette, C.; Comninellis, C. Charge Storage at the Pt/YSZ Interface. J. Electroceramics 2009, 23 (2–4), 175–179.

[31] Opitz, A. K.; Fleig, J. Investigation of O_2 Reduction on Pt/YSZ by Means of Thin Film Microelectrodes: The Geometry Dependence of the Electrode Impedance. Solid State Ionics 2010, 181 (15–16), 684–693.

[32] Luerßen, B.; Janek, J.; Imbihl, R. Electrocatalysis on Pt/YSZ Electrodes. Solid State Ionics 2001, 142, 701–707.

[33] Ohyama, J.; Koketsu, T.; Yamamoto, Y.; Arai, S.; Satsuma, A. Preparation of TiO_2-Supported Twinned Gold Nanoparticles by CO Treatment and Their CO Oxidation Activity. Chem. Commun. 2015, 51 (87), 15823–15826.

[34] Gao, C.; Vuong, J.; Zhang, Q.; Liu, Y.; Yin, Y. One-Step Seeded Growth of Au Nanoparticles with Widely Tunable Sizes. Nanoscale 2012, 4 (9), 2875–2878.

[35] Lim, S. P.; Pandikumar, A.; Huang, N. M.; Lim, H. N. Facile Synthesis of Au@TiO_2 Nanocomposite and Its Application as a Photoanode in Dye-Sensitized Solar Cells. RSC Adv. 2015, 5 (55), 44398–44407.

[36] Yu, K.; Wu, Z.; Zhao, Q.; Li, B.; Xie, Y. High-Temperature-Stable Au@SnO_2 Core/Shell Supported Catalyst for CO Oxidation. J. Phys. Chem. C 2008, 112 (7), 2244–2247.

[37] Nesterenko, S. N.; Meshkov, L. L.; Zosimova, P. A.; Nesterenko, N. S. Structure and Morphology of Catalysts Produced via Oxidation of Mo-Pt Alloys. Inorg. Mater. 2009, 45 (3), 264–270.

[38] Lomello-Tafin, M.; Chaou, A. A.; Morfin, F.; Caps, V.; Rousset, J. L. Preferential Oxidation of CO in H_2 over Highly Loaded Au/ZrO_2 Catalysts Obtained by Direct Oxidation of Bulk Alloy. Chem. Commun. 2005, No. 3, 388–390.

[39] Haruta, M.; Tsubota, S.; Kobayashi, T.; Kageyama, H.; Genet, M. J.; Delmon, B. Low-Temperature Oxidation of CO over Gold Supported on TiO_2, α-Fe_2O_3, and Co_3O_4. Journal of Catalysis. 1993, 144, 175–192.

[40] Yazid, H.; Adnan, R.; Hamid, S. A.; Farrukh, M. A. Synthesis and Characterization of Gold Nanoparticles Supported on Zinc Oxide via the Deposition-Precipitation Method. Turkish J. Chem. 2010, 34 (4), 639–650.

[41] Goebl, J.; Joo, J. B.; Dahl, M.; Yin, Y. Synthesis of Tailored Au@TiO_2 Core-Shell Nanoparticles for Photocatalytic Reforming of Ethanol. Catal. Today 2014, 225, 90–95.

[42] Konetzki, R. A.; Chang, Y. A. Oxidation Kinetics of Pb-Sn Alloys. 1989, 4(6), 1421–1426.

[43] Zhang, M.; Chang, Y. A.; Marcottet, V. C. Oxidation Kinetics of a Pb-64 at. % In Single-Phase Alloy. 1991, 36, 465–474.

[44] Zhang, M.; Chang, Y. A.; Marcottet, V. C. Oxidation of Single-Phase Pb-In Alloys. 1990, 33, 301–308.

[45] Nesterenko, S. N.; Meshkov, L. L.; Zosimova, P. A.; Nesterenko, N. S. Composition and Structure of the Oxidation Products of Mo-Pt Alloys. Inorg. Mater. 2009, 45 (2), 145–150.

[46] Nesterenko, S. N.; Meshkov, L. L.; Zosimova, P. A.; Nesterenko, N. S. Structure and Morphology of Catalysts Produced via Oxidation of Mo-Pt Alloys. Inorg. Mater. 2009, 45 (3), 264–270.

[47] Wang, X.; Yu, H.; Hua, D.; Zhou, S. Enhanced Catalytic Hydrogenation Activity and Selectivity of Pt-M XO_y/Al_2O_3 (M = Ni, Fe, Co) Heteroaggregate Catalysts by in Situ Transformation of PtM Alloy Nanoparticles. J. Phys. Chem. C 2013, 117 (14), 7294–7302.

[48] Sutter, E. A.; Tong, X.; Jungjohann, K.; Sutter, P. W. Oxidation of Nanoscale Au-In Alloy Particles as a Possible Route toward Stable Au-Based Catalysts. Proc. Natl. Acad. Sci. U. S. A. 2013, 110 (26), 10519–10524.

[49] Sutter, P.; Tenney, S. A.; Ivars-Barcelo, F.; Wu, L.; Zhu, Y.; Sutter, E. Alloy Oxidation as a Route to Chemically Active Nanocomposites of Gold Atoms in a Reducible Oxide Matrix. Nanoscale Horizons 2016, 1 (3), 212–219.

[50] Dai, S.; You, Y.; Zhang, S.; Cai, W.; Xu, M.; Xie, L.; Wu, R.; Graham, G. W.; Pan, X. In Situ Atomic-Scale Observation of Oxygen-Driven Core-Shell Formation in Pt_3Co Nanoparticles. Nat. Commun. 2017, 8 (1), 1–8.

[51] Endo, N.; Kameoka, S.; Tsai, A. P.; Hirata, T.; Nishimura, C. Preparation of Nano-Composited Catalyst from the Bulk Intermetallic Compound $AuZr_3$ with Hydrogen Absorption. Catal. Letters 2010, 139 (1–2), 67–71.

[52] Shoji, S.; Peng, X.; Imai, T.; Murphin Kumar, P. S.; Higuchi, K.; Yamamoto, Y.; Tokunaga, T.; Arai, S.; Ueda, S.; Hashimoto, A.; Tsubaki, N.; Miyauchi, M.; Fujita, T.; Abe, H. Topologically Immobilized

Catalysis Centre for Long-Term Stable Carbon Dioxide Reforming of Methane. Chem. Sci. 2019, 10 (13), 3701–3705.

[53] Tanabe, T.; Imai, T.; Tokunaga, T.; Arai, S.; Yamamoto, Y.; Ueda, S.; Ramesh, G. V.; Nagao, S.; Hirata, H.; Matsumoto, S. I.; Fujita, T.; Abe, H. Nanophase-Separated Ni_3Nb as an Automobile Exhaust Catalyst. Chem. Sci. 2017, 8 (5), 3374–3378.

[54] Imai, T.; Ueda, S.; Nagao, S.; Hirata, H.; Deepthi, K. R.; Abe, H. N_2O-Emission-Free Exhaust Remediation by Rh-NbO_x Nanocomposites Developed from Rh_3Nb Alloy Precursor. RSC Adv. 2017, 7 (16), 9628–9631.

[55] Najib, A. S. B. M.; Peng, X.; Hashimoto, A.; Shoji, S.; Iida, T.; Bai, Y.; Abe, H. Mesoporous Rh Emerging from Nanophase‐separated Rh‐Y Alloy. Chem. – An Asian J. 2019, 14, 2802–2805.

[56] Stierle, A.; Streitel, R.; Nolte, P.; Vlad, A.; Costina, I.; Marsman, M.; Kresse, G.; Lundgren, E.; Andersen, J. N.; Franchy, R.; Dosch, H. Real Time Observation of Ultrathin Epitaxial Oxide Growth during Alloy Oxidation. New J. Phys. 2007, 9 (100).

[57] Sun, C.; Li, H.; Chen, L. Nanostructured Ceria-Based Materials: Synthesis, Properties, and Applications. Energy Environ. Sci. 2012, 5 (9), 8475–8505.

[58] Campbell, C. T.; Peden, C. H. F. Oxygen Vacancies and Catalysis on Ceria Surfaces. Science. 2005, 309 (5735), 713–714.

[59] Yang, J.; Xie, N.; Zhang, J.; Fan, W.; Huang, Y.; Tong, Y. Defect Engineering Enhances the Charge Separation of CeO_2 Nanorods toward Photocatalytic Methyl Blue Oxidation. Nanomaterials 2020, 10 (11), 1–12.

[60] Skorodumova, N. V.; Simak, S. I.; Lundqvist, B. I.; Abrikosov, I. A.; Johansson, B. Quantum Origin of the Oxygen Storage Capability of Ceria. Phys. Rev. Lett. 2002, 89 (16), 166601/1-166601/4.

[61] Deshpande, S.; Patil, S.; Kuchibhatla, S. V.; Seal, S. Size Dependency Variation in Lattice Parameter and Valency States in Nanocrystalline Cerium Oxide. Appl. Phys. Lett. 2005, 87 (13), 133113.

[62] Hao, X.; Yoko, A.; Chen, C.; Inoue, K.; Saito, M.; Seong, G.; Takami, S.; Adschiri, T.; Ikuhara, Y. Atomic-Scale Valence State Distribution Inside Ultrafine CeO_2 Nanocubes and Its Size Dependence. Small 2018, 14 (42), 1–8.

[63] Zhang, Y. C.; Li, Z.; Zhang, L.; Pan, L.; Zhang, X.; Wang, L.; Fazal-e-Aleem; Zou, J. J. Role of Oxygen Vacancies in Photocatalytic Water Oxidation on Ceria Oxide: Experiment and DFT Studies. Appl. Catal. B Environ. 2018, 224, 101–108.

[64] Li, Y.; Wei, Z.; Gao, F.; Kovarik, L.; Baylon, R. A. L.; Peden, C. H. F.; Wang, Y. Effect of Oxygen Defects on the Catalytic Performance of VO_x/CeO_2 Catalysts for Oxidative Dehydrogenation of Methanol. ACS Catal. 2015, 5 (5), 3006–3012.

[65] Chavhan, M. P.; Som, S.; Lu, C. H. Size-Controlled Ceria Nanocubes Obtained via Hydrothermal Route for Electrochemical Capacitors. Mater. Lett. 2019, 257, 126598.

[66] Tsunekawa, S.; Ishikawa, K.; Li, Z. Q.; Kawazoe, Y.; Kasuya, A. Origin of Anomalous Lattice Expansion in Oxide Nanoparticles. Phys. Rev. Lett. 2000, 85 (16), 3440–3443.

[67] Chiang, Y. M.; Lavik, E. B.; Kosacki, I.; Tuller, H. L.; Ying, J. Y. Defect and Transport Properties of Nanocrystalline CeO_{2-X}. Appl. Phys. Lett. 1996, 69 (2), 185–187.

[68] Zhou, X. D.; Huebner, W.; Anderson, H. U. Room-Temperature Homogeneous Nucleation Synthesis and Thermal Stability of Nanometer Single Crystal CeO_2. Appl. Phys. Lett. 2002, 80 (20), 3814–3816.

[69] Tang, Y.; Zhang, H.; Cui, L.; Ouyang, C.; Shi, S.; Tang, W.; Li, H.; Lee, J. S.; Chen, L. First-Principles Investigation on Redox Properties of M -Doped CeO_2 (M=Mn,Pr,Sn,Zr). Phys. Rev. B - Condens. Matter Mater. Phys. 2010, 82 (12), 1–9.

[70] Coduri, M.; Checchia, S.; Longhi, M.; Ceresoli, D.; Scavini, M. Rare Earth Doped Ceria: The Complex Connection between Structure and Properties. Front. Chem. 2018, 6 (OCT), 1–23.

[71] Andersson, D. A.; Simak, S. I.; Skorodumova, N. V.; Abrikosov, I. A.; Johansson, B. Optimization of Ionic Conductivity in Doped Ceria. Proc. Natl. Acad. Sci. U. S. A. 2006, 103 (10), 3518–3521.

[72] Akita, T.; Tanaka, K.; Kohyama, M. TEM and HAADF-STEM Study of the Structure of Au Nano-Particles on CeO_2. J. Mater. Sci. 2008, 43 (11), 3917–3922.

[73] Luches, P.; Giordano, L.; Grillo, V.; Gazzadi, G. C.; Prada, S.; Campanini, M.; Bertoni, G.; Magen, C.; Pagliuca, F. Atomic Scale Structure and Reduction of Cerium Oxide at the Interface with Platinum. 2015, 1–10.

[74] Liu, H. H.; Wang, Y.; Jia, A. P.; Wang, S. Y.; Luo, M. F.; Lu, J. Q. Oxygen Vacancy Promoted CO Oxidation over Pt/CeO_2 Catalysts: A Reaction at $Pt\text{-}CeO_2$ Interface. Appl. Surf. Sci. 2014, 314, 725–734.

[75] Xu, C.; Wu, Y.; Li, S.; Zhou, J.; Chen, J.; Jiang, M.; Zhao, H.; Qin, G. Engineering the Epitaxial Interface of $Pt\text{-}CeO_2$ by Surface Redox Reaction Guided Nucleation for Low Temperature CO Oxidation. J. Mater. Sci. Technol. 2020, 40, 39–46.

[76] Koettgen, J.; Grieshammer, S.; Hein, P.; Grope, B. O. H.; Nakayama, M.; Martin, M. Understanding the Ionic Conductivity Maximum in Doped Ceria: Trapping and Blocking. Phys. Chem. Chem. Phys. 2018, 20 (21), 14291–14321.

[77] Janek, J.; Martin, M.; Becker, K. D. Physical Chemistry of Solids–The Science behind Materials Engineering. Phys. Chem. Chem. Phys. 2009, 11 (17), 3010.

[78] Gerhardt, R.; Nowick, A. S. Grain-Boundary Effect in Ceria Doped with Trivalent Cations: I, Electrical Measurements. 1986, 69 (9).

[79] Badwal, S. P. S.; Rajendran, S. Effect of Micro- and Nano-Structures on the Properties of Ionic Conductors. Solid State Ionics 1994, 70–71 (PART 1), 83–95.

[80] Maier, J. Ionic Conduction in Space Charge Regions. Prog. Solid State Chem. 1995, 23 (3), 171–263.

[81] Fabbri, E.; Pergolesi, D.; Traversa, E. Ionic Conductivity in Oxide Heterostructures: The Role of Interfaces. Sci. Technol. Adv. Mater. 2010, 11 (5).

[82] Leon, C.; Santamaria, J.; Boukamp, B. A. Oxide Interfaces with Enhanced Ion Conductivity. MRS Bull. 2013, 38 (12), 1056–1063.

[83] Pennycook, T. J.; Beck, M. J.; Varga, K.; Varela, M.; Pennycook, S. J.; Pantelides, S. T. Origin of Colossal Ionic Conductivity in Oxide Multilayers: Interface Induced Sublattice Disorder. Phys. Rev. Lett. 2010, 104 (11), 1–4.

[84] Hsieh, Y. H.; Liou, J. M.; Huang, B. C.; Liang, C. W.; He, Q.; Zhan, Q.; Chiu, Y. P.; Chen, Y. C.; Chu, Y. H. Local Conduction at the $BiFeO_3$-$CoFe_2O_4$ Tubular Oxide Interface. Adv. Mater. 2012, 24 (33), 4564–4568.

[85] Peters, A.; Korte, C.; Hesse, D.; Zakharov, N.; Janek, J. Ionic Conductivity and Activation Energy for Oxygen Ion Transport in Superlattices - The Multilayer System CSZ (ZrO_2 + CaO) / Al_2O_3. Solid State Ionics 2007, 178 (1–2), 67–76.

[86] Kilner, J. A. Ionic Conductors: Feel the Strain. Nat. Mater. 2008, 7 (11), 838–839.

[87] Korte, C.; Schichtel, N.; Hesse, D.; Janek, J. Influence of Interface Structure on Mass Transport in Phase Boundaries between Different Ionic Materials: Experimental Studies and Formal Considerations. Monatshefte fur Chemie 2009, 140 (9), 1069–1080.

[88] Lee, S.; Zhang, W.; Khatkhatay, F.; Jia, Q.; Wang, H.; Macmanus-Driscoll, J. L. Strain Tuning and Strong Enhancement of Ionic Conductivity in $SrZrO_3$-RE_2O_3 (RE = Sm, Eu, Gd, Dy, and Er) Nanocomposite Films. Adv. Funct. Mater. 2015, 25 (27), 4328–4333.

[89] Maier, Joachim. Defect chemistry and ion transport in nanostructured materials: Part II. Aspects of nanoionics. Solid State Ionics. 2003, 157(1-4), 327-334.

[90] Tschöpe, A.; Sommer, E.; Birringer, R. Grain Size-Dependent Electrical Conductivity of Polycrystalline Cerium Oxide. I. Experiments. Solid State Ionics 2001, 139 (3–4), 255–265.

[91] Zhang, X.; Xie, J.; Shi, F.; Lin, D.; Liu, Y.; Liu, W.; Pei, A.; Gong, Y.; Wang, H.; Liu, K.; Xiang, Y.; Cui, Y. Vertically Aligned and Continuous Nanoscale Ceramic-Polymer Interfaces in Composite Solid Polymer Electrolytes for Enhanced Ionic Conductivity. Nano Lett. 2018, 18 (6), 3829–3838.

[92] Sun, J.; Liao, X.; Minor, A. M.; Balsara, N. P.; Zuckermann, R. N. Morphology-Conductivity Relationship in Crystalline and Amorphous Sequence-Defined Peptoid Block Copolymer Electrolytes. J. Am. Chem. Soc. 2014, 136 (42), 14990–14997.

[93] Inceoglu, S.; Rojas, A. A.; Devaux, D.; Chen, X. C.; Stone, G. M.; Balsara, N. P. Morphology-Conductivity Relationship of Single-Ion-Conducting Block Copolymer Electrolytes for Lithium Batteries. ACS Macro Lett. 2014, 3 (6), 510–514.

[94] Liu, W.; Lee, S. W.; Lin, D.; Shi, F.; Wang, S.; Sendek, A. D.; Cui, Y. Enhancing Ionic Conductivity in Composite Polymer Electrolytes with Well-Aligned Ceramic Nanowires. Nat. Energy 2017, 2 (5), 1–7.

[95] Liu, W.; Liu, N.; Sun, J.; Hsu, P. C.; Li, Y.; Lee, H. W.; Cui, Y. Ionic Conductivity Enhancement of Polymer Electrolytes with Ceramic Nanowire Fillers. Nano Lett. 2015, 15 (4), 2740–2745.

[96] Choi, J. H.; Ye, Y.; Elabd, Y. A.; Winey, K. I. Network Structure and Strong Microphase Separation for High Ion Conductivity in Polymerized Ionic Liquid Block Copolymers. Macromolecules 2013, 46 (13), 5290–5300.

[97] Kasson, P. M.; Zomorodian, A.; Park, S.; Singhal, N.; Guibas, L. J.; Pande, V. S. Persistent Voids: A New Structural Metric for Membrane Fusion. Bioinformatics 2007, 23 (14), 1753–1759.

[98] Xia, K.; Wei, G.-W. Persistent Homology Analysis of Protein Structure, Flexibility and Folding. Int J Number Method Biomed Eng. 2014, 30 (8), 814–844.

[99] Saggar, M.; Sporns, O.; Gonzalez-Castillo, J.; Bandettini, P. A.; Carlsson, G.; Glover, G.; Reiss, A. L. Towards a New Approach to Reveal Dynamical Organization of the Brain Using Topological Data Analysis. Nat. Commun. 2018, 9 (1), 1–14.

[100] Nielson, J. L.; Paquette, J.; Liu, A. W.; Guandique, C. F.; Tovar, C. A.; Inoue, T.; Irvine, K. A.; Gensel, J. C.; Kloke, J.; Petrossian, T. C.; Lum, P. Y.; Carlsson, G. E.; Manley, G. T.; Young, W.; Beattie, M. S.; Bresnahan, J. C.; Ferguson, A. R. Topological Data Analysis for Discovery in Preclinical Spinal Cord Injury and Traumatic Brain Injury. Nat. Commun. 2015, 6(1), 1-12.

[101] Hiraoka, Y.; Nakamura, T.; Hirata, A.; Escolar, E. G.; Matsue, K.; Nishiura, Y. Hierarchical Structures of Amorphous Solids Characterized by Persistent Homology. Proc. Natl. Acad. Sci. U. S. A. 2016, 113 (26), 7035–7040.

[102] Wanner, T.; Fuller, E. R.; Saylor, D. M. Homology Metrics for Microstructure Response Fields in Polycrystals. Acta Mater. 2010, 58 (1), 102–110.

[103] Gameiro, M.; Mischaikow, K.; Wanner, T. Evolution of Pattern Complexity in the Cahn-Hilliard Theory of Phase Separation. Acta Mater. 2005, 53 (3), 693–704.

[104] Ishida, M.; Kida, K.; Mizobe, K.; Nakane, K. Relation between the Betti Number of Fatigue Fracture Surfaces and Stress Intensity Factors of Low Carbon Steel (JIS, S45C). Adv. Mater. Res. 2015, 1102, 59–63.

[105] Wanner, T.; Fuller, E. R.; Saylor, D. M. Homology Metrics for Microstructure Response Fields in Polycrystals. Acta Mater. 2010, 58 (1), 102–110.

[106] Nakane, K.; Tsuchihashi, Y.; Matsuura, N. A Simple Mathematical Model Utilizing Topological Invariants for Automatic Detection of Tumor Areas in Digital Tissue Images. Diagn. Pathol. 2013, 8 (Suppl 1), 1–4.

[107] Hansen, N.; Adams, D. O.; Fullwood, D. T. Quantitative Methods for Correlating Dispersion and Electrical Conductivity in Conductor-Polymer Nanostrand Composites. Compos. Part A Appl. Sci. Manuf. 2012, 43 (11), 1939–1946.

[108] Teramoto, T.; Kamiya, T.; Sakurai, T.; Kanaya, F. Betti Number Ratios as Quantitative Indices for Bone Morphometry in Three Dimensions. Comput. Methods Programs Biomed. 2018, 162, 93–98.

[109] Friedrich, J. M. Quantitative Methods for Three-Dimensional Comparison and Petrographic Description of Chondrites. Comput. Geosci. 2008, 34 (12), 1926–1935.

[110] Hiraoka, Y.; Nakamura, T.; Hirata, A.; Escolar, E. G.; Matsue, K.; Nishiura, Y. Hierarchical Structures of Amorphous Solids Characterized by Persistent Homology. Proc. Natl. Acad. Sci. U. S. A. 2016, 113 (26), 7035–7040.

[111] Hirata, A.; Wada, T.; Obayashi, I.; Hiraoka, Y. Structural Changes during Glass Formation Extracted by Computational Homology with Machine Learning. Commun. Mater. 2020, 1 (1), 1–4.

[112] Townsend, J.; Micucci, C. P.; Hymel, J. H.; Maroulas, V.; Vogiatzis, K. D. Representation of Molecular Structures with Persistent Homology for Machine Learning Applications in Chemistry. Nat. Commun. 2020, 11 (1), 1–9.

[113] Oyama, A.; Hiraoka, Y.; Obayashi, I.; Saikawa, Y.; Furui, S.; Shiraishi, K.; Kumagai, S.; Hayashi, T.; Kotoku, J. Hepatic Tumor Classification Using Texture and Topology Analysis of Non-Contrast-Enhanced Three-Dimensional T1-Weighted MR Images with a Radiomics Approach. Sci. Rep. 2019, 9 (1), 2–11.

[114] Kimura, M.; Obayashi, I.; Takeichi, Y.; Murao, R.; Hiraoka, Y. Non-Empirical Identification of Trigger Sites in Heterogeneous Processes Using Persistent Homology. Sci. Rep. 2018, 8 (1), 1–9.

Chapter 2 Experimental procedure

The experiment part of this study comprises four parts: sample preparation, structure analysis, homological analysis, and ionic conductivity measurement. The target materials are Pt/CeO_2 nanocomposites (NCs) from Pt_5Ce alloy by oxidation-induced phase separation behavior. Figure 2.1 illustrates the whole experimental flow and lists the basic conditions used for some experiments. For the sample preparation, Pt_5Ce NCs were prepared by oxidizing the Pt_5Ce alloy, and composites with different structures were achieved by changing the temperature and syngas ratio. The composites were thinned to slices by the focused-ion beam (FIB) for TEM investigation. X-ray powder diffraction and TEM are used for phase identification and nanostructural analysis. Specifically, EELS, and 3D tomography in TEM were applied for the 2D structural observation, $Pt–CeO_2$ interface characterization, and 3D structural visualization, respectively. Two homology concepts, Betti numbers (β_i) and persistence diagram, were applied to quantitative describe the TEM-observed structures. The ionic conductivity was measured by impedance spectroscopy (IS). The theory and detailed information about each procedure is introduced in the following sections.

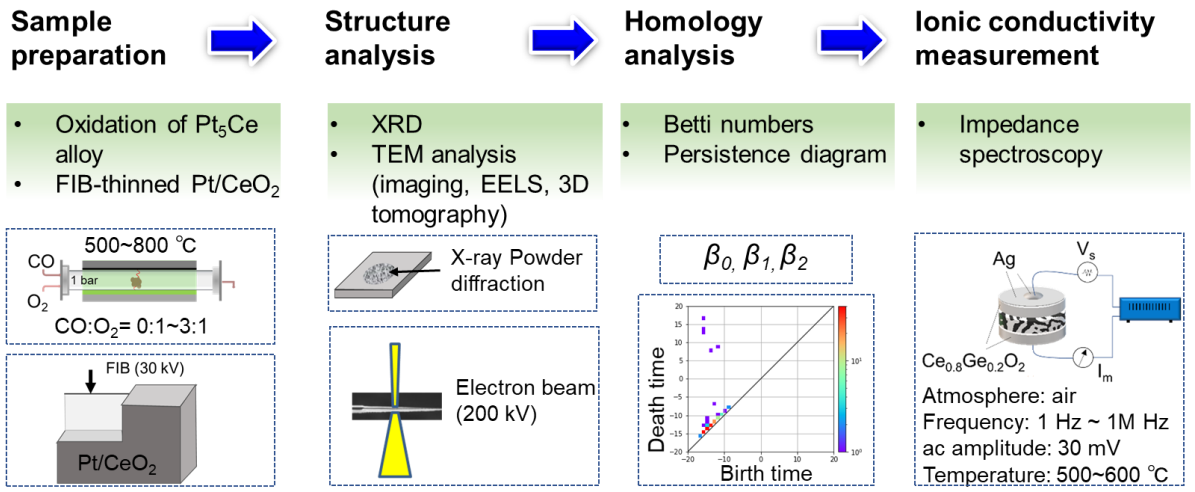

Figure 2.1. Schematic of experiment procedures applied in this work. It includes four main parts: sample preparation, structure analysis, homology analysis and ionic conductivity measurement. The basic conditions for some tests are listed in the figure.

2.1 Preparation of metal/oxide nanocomposites

2.1.1 Sample synthesis

The Pt/CeO_2 NCs with diverse textures were prepared by oxidizing the binary Pt_5Ce alloys. Figure 2.2 shows the schematic of the Pt/CeO_2 NCs preparation processes. A total of 3g Pt and Ce mixture elemental powders were weighed in a fixed atomic ratio (5:1) (Table 2.1). The precursor (Pt_5Ce alloys) were made by the typical arc-melting method. In a chamber filled with Ar gas, the heat is produced by arc melting the Pt and

Ce metals on the Cu base to form a hemispherical bulk alloy (~6 mm diameter). Two kinds of alloys, powders, and pellets were shaped by grinding and polishing the bulk alloy, respectively. The particle sizes of the powders range from 50 to 60 μm. The pellets for ionic conductivity measurement were ~5 mm in diameter and 2 mm in height. Afterwards, the Pt/CeO_2 NCs were formed after annealing the two kinds of alloys in the reactive gas environment. The annealing conditions were changed to generate different configurations of Pt/CeO_2 NCs.

Table 2.1 summarizes the various Pt/CeO_2 NCs used herein. In Chapter 3, FIB-thinned and powder Pt_5Ce alloys were prepared. They were annealed at a low temperature of 400 ℃ with different duration to track the phase separation behavior. Different Pt/CeO_2 powder and bulk samples by changing the syngas ratio were prepared in Chapter 4. The annealing temperature and duration were kept constant at 600 ℃ and 12 h, respectively. In Chapter 5, the annealing temperature was changed from 500 ℃ to 800 ℃ to prepare the powder and bulk NCs, while maintaning the same syngas ratio (2:1) and duration (12 h).

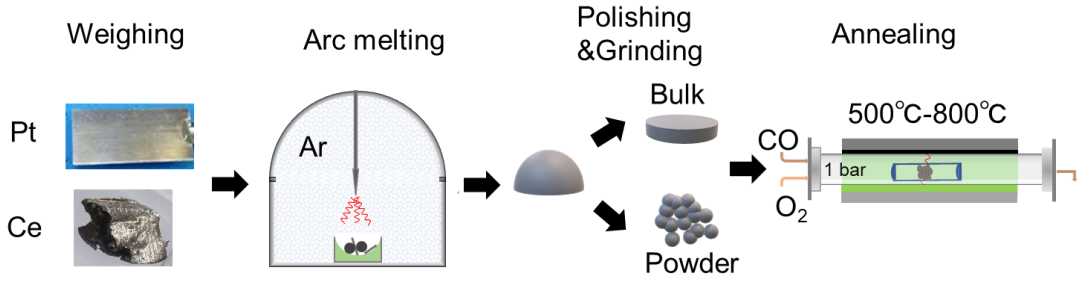

Figure 2.2 Schematic diagram of Pt/CeO_2 NCs production procedures.

Table 2.1. Various Pt/CeO_2 NCs prepared from Pt_5Ce alloy by changing the annealing conditions

	Chapter	Weight ratio(g) (Pt: Ce)	Type of alloys	Syngas ratio ($CO:O_2$)	Annealing temperature (℃)	Duration
1	Chapter 3	2.62:0.38	FIB-thinned slice	2:1	400	10 min
2			Powder	2:1	400	30 min
3			Powder	2:1	400	12 h
4	Chapter 4		Powder, bulk	0:1	600	12 h
5			Powder, bulk	1:1	600	12 h
6			Powder, bulk	2:1	600	12 h
7			Powder, bulk	3:1	600	12 h
8	Chapter 5		Powder, bulk	2:1	500	12 h
9			Powder, bulk	2:1	600	12 h
10			Powder, bulk	2:1	700	12 h
11			Powder, bulk	2:1	800	12 h

2.1.2 TEM specimen preparation by FIB thinning

FIB is a technique for sputtering the material surface and imaging the material using ion beams, usually gallium ions (Ga^+). Arbitrary nanostructures can be made after the FIB thinning. Figure 2.3a illustrates the FIB principle. A finely focused beam of Ga^+ ions operated at a high beam current was used for milling the sample because the high-energy Ga^+ removes the target material by sputtering. The higher the beam current, the less the thinning time and the poorer the achievable resolution and milling precision. As the interaction between Ga+ and the target material increases, secondary ions (i^+ or i^-), neutral atoms (n^0), and secondary electrons (e^-) would be generated above the surface. In contrast, the sputtered ions or secondary electrons caused by the interaction can be used for imaging. Also, damage to the material's surface is inevitable during the FIB milling. The higher the beam current, the deeper the damage on the material surface. Therefore, a decrease in current is necessary as the sample thickness degrades. Even when using a low beam current for imaging, the long-time processing required until the sample preparation is completed has severe damage on the surface seen in the projection direction. To solve the problem, specific material (usually C or Pt) can be deposited on the projection surface via chemical vapor deposition when a gas (C_8H_8, $C_9H_{16}Pt$) is introduced to the chamber. The protection layer also plays a vital role in controlling the sample thickness during milling.

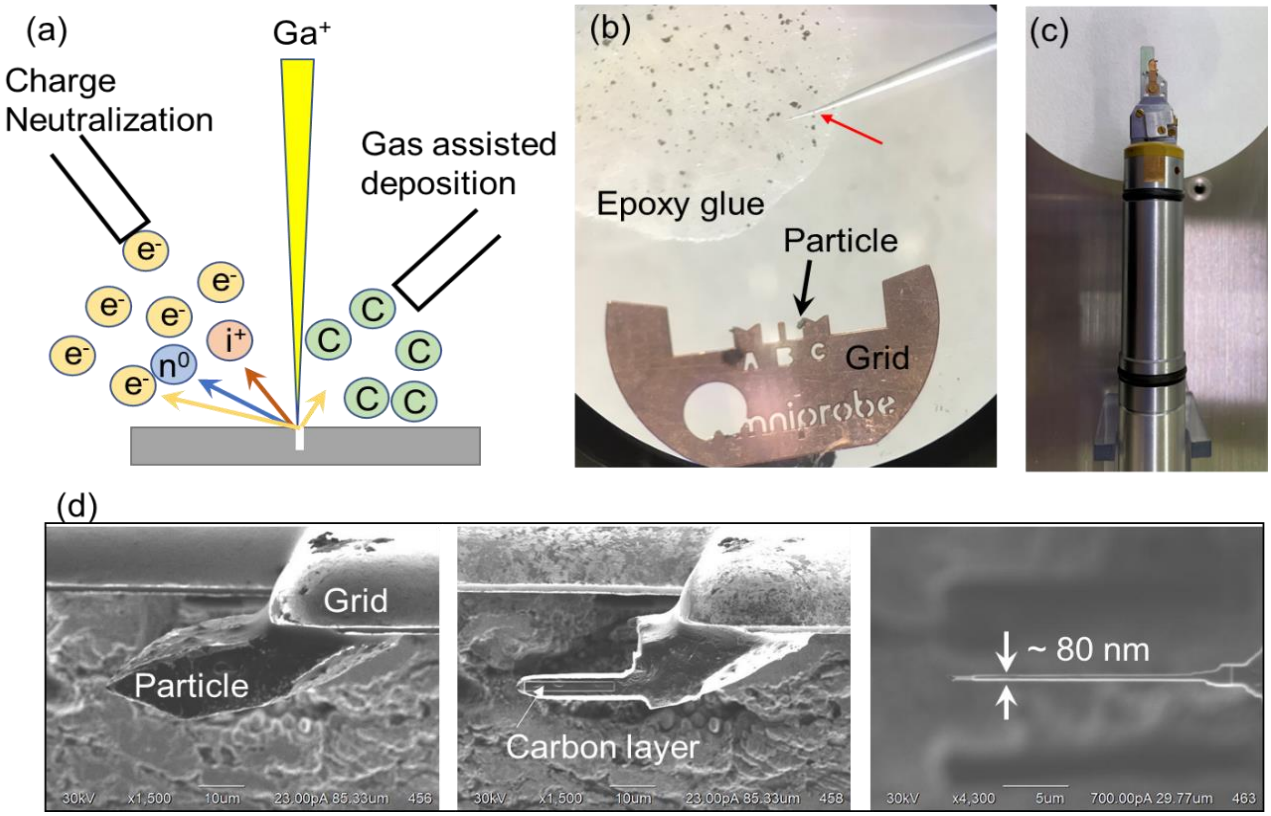

Figure 2.3. TEM specimen prepared by FIB. (a) Schematic diagram of FIB. (b) Cu grid for supporting the Pt_5Ce particles. (c) Image of the grid on the stage of the FIB holder. (d) FIB processing, including the carbon protective layer deposition and thinning by Ga+.

To thin the Pt/CeO_2 NCs powders to a thin slice for TEM observation in many cases, a grid (Figure 2.3b) with a 3-mm diameter to support the powder sample in the TEM holder is necessary. Powders with a 30-μm size can be transferred by a toothbrush marked by the red arrow in Fig 2.3a and then attached to one of the three posts using the Gatan G2 epoxy glue, which includes the resin and hardener in the ratio of 7:1. After confirming that the particle has been successfully attached to the post (black arrow in Figure 2.3b), the grid fixed in the holder was transported to the FIB chamber for thinning. Figure 2.3c shows the holder for the FIB system, which can also be used for a TEM system. Figure 2.3d shows different sample stages during the FIB milling (JEM-9320FIB, JEOL, Japan). Next, a suitable particle size was chosen for the thinning process. A rectangle frame of 10 μm × 2 μm on the particle surface is chosen for C deposition. The Ga^+ beam operated at 30 kV voltage was used to thin the sample. As shown in the middle panel of Figure 2.3d, the parts above and below the deposited area are removed with a large current (~10 nA). Then, a beam with a relatively lower current of 1 nA thins the deposited part to 1 μm. Furthermore, a 700-pA beam was used for thinning the sample until 300 nm. Afterward, the beam current was decreased to 200 pA for the 200-nm thick sample. Next, the 100-pA beam was used on the sample with <80-nm thickness (right panel of Figure 2.3d). A beam with a current of 30 pA and voltage of 5 kV was used for damage cleaning. Finally, the TEM specimens with a thickness of ~50 nm were made and transferred to the TEM system for structural characterization.

2.2 Structural characterization techniques

2.2.1 X-ray diffraction analysis

X-ray diffraction (XRD) analysis is a technique for identifying the chemical composition and crystallographic structure of a material. Figure 2.4a shows powder diffractometers with the Bragg–Brentano geometry. The incident angle (ω) is between the X-ray source and the sample. The diffracted angle (2θ) is between the incident beam and the detector. ω is always half of 2θ. For the powder XRD analysis, the sample is fixed, while the X-ray tube and detector rotate at θ°/min and 2θ°/min, respectively. The diffraction pattern occurs when X-ray is coherently scattered by the long-range orderly periodic array of atoms in a crystal,

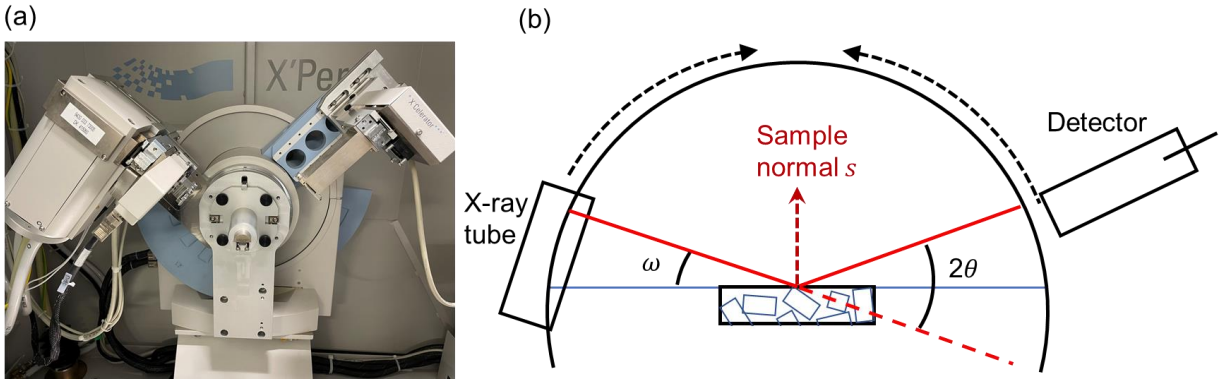

Figure 2.4. (a) Powder diffractometers using the Bragg-Brentano geometry. (b) Principle of powder XRD analysis.

producing constructive interference at specific angles. It is a product of the unique crystal structure of a material and does not work for amorphous materials. The diffraction angles are determined by the distance between parallel planes of atoms according to Bragg's law: $\lambda = 2d_{hkl}sin\theta$, where d_{hkl} is the spacing of the crystal plane (*hkl*). The intensity of the obtained diffraction is determined by the arrangement of atoms in the entire crystals, and the relative intensity reflects the preferable arrangement of atoms on a certain plane. The diffraction vector (S) bisecting the angle between the incident and scattered beam is always normal to the surface of powder samples. Different from a single crystal specimen, which produces only one family of peaks in the diffraction pattern, a powder sample produces all possible diffraction peaks.

A Panalytical X'PERT PRO X-ray diffractometer with a Cu $K_{\alpha 1}$ source; λ = 0.154056 nm was used for the XRD analysis (Figure 2.4b). With the sample fixed, the X-ray tube and the detector rotate at $5°/min$ and $10°/min$, respectively. Using the powder diffraction pattern, the components were identified, and the relative amounts of each phase, the crystallization degree, and the sample orientation were analyzed.

2.2.2 Transmission electron microscopy

TEM is an indispensable analysis tool in material science due to its extraordinary abilities to provide atomic-scale structural, phase, and crystallographic data [1-3]. TEM imaging is a technique to form an image by collecting electrons transmitted through a specimen. Owing to the smaller de Broglie wavelength of the electrons' beam, TEM allows imaging with a significantly higher resolution than light microscopes, even capturing a single column of atoms. Accelerated electrons reach the material surface and then interact with the specimen. The interactions include elastic and inelastic scattering. The transmitted electrons contain the physical and chemical information of the specimen due to the wave-particle duality of electrons. transmitted

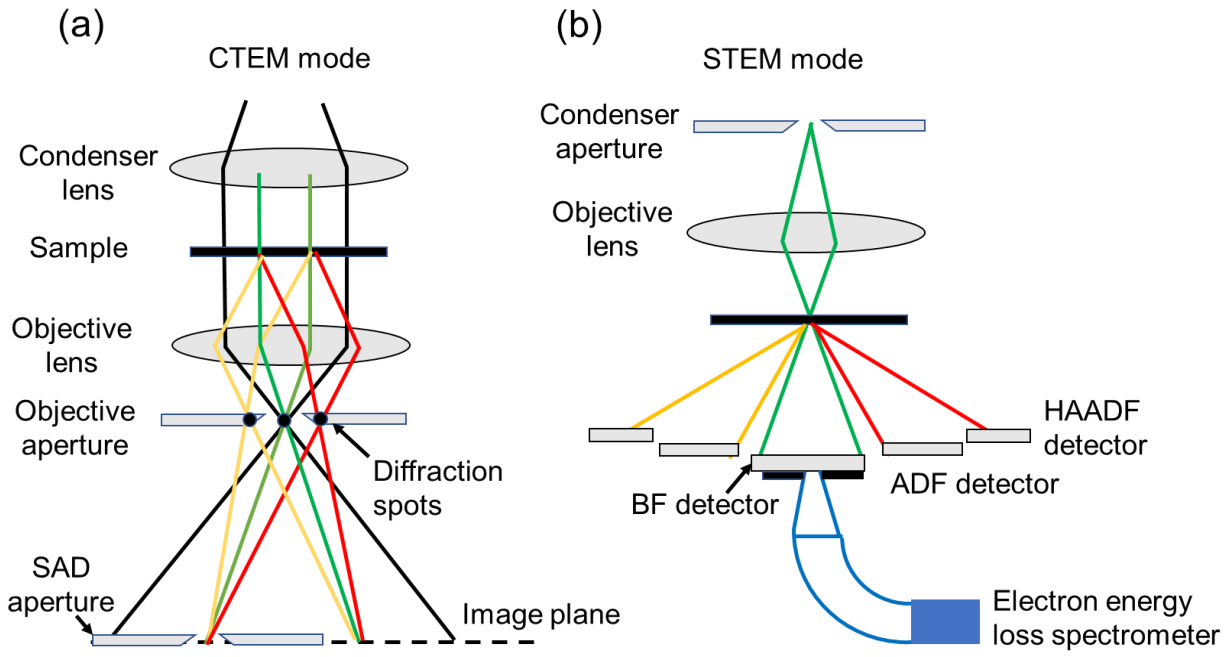

Figure 2.5. (a) Schematic of (a) CTEM mode, and (b) STEM mode.

electrons flow through the vacuum and electromagnetic lenses and are then detected by the charge coupled device (CCD) for various structural analyses. Figure 2.5 shows the illuminating system of two modes in TEM: conventional TEM (CTEM) mode with a parallel beam and scanning TEM (STEM) mode with a convergent beam reaching the sample.

2.2.2.1 Transmission electron microscopy imaging

TEM imaging and selected area electron diffraction (SAED) are operated in the CTEM mode in Figure 2.5a. Electrons are transmitted from the specimen and transported through the objective lens of a TEM microscope to form a diffraction pattern (DP) and an image at the back-focal and image planes, respectively. Therefore, a DP was projected on the CCD by adjusting the imaging-system lenses so that the back-focal plane acts as the object plane for the intermediate lens and projects an image by adjusting the intermediate lens so that the image plane is the object plane. DP helps identify the phase structure or orientation relationship (OR) with other phases. High-resolution TEM (HRTEM) images provide information about the atoms' arrangement in the crystal and the interfacial connection of the different crystals. The TEM images contain complementary diffraction contrast, and the image contrast varies with the focus condition for HRTEM.

Figure 2.5b shows that the STEM mode was used for the STEM imaging. Different detectors in the STEM mode collect the transmitted electrons scattered at different angles. Both annular dark-filed (ADF) and high-angle ADF (HAADF) detectors are disks with holes in their center. However, the disk diameter and the hole of the HAADF detector generally with 80–240-mrad are >> that of the ADF detector. The measured contrast in the ADF images mainly results from electrons diffracted in crystalline areas. However, it is superimposed by incoherent Rutherford scattering, resulting in a mass-thickness contrast to distinguish different phases directly. Since the electrons scattered at higher angles are much more caused by the incoherent Rutherford scattering, atomic number-dependent contrast (Z contrast) is achieved in HAADF images. Projected atomic scaled points with different brightness can be intuitively and directly interpreted by the difference in weight and number of certain atom columns. In addition to the experimental HAADF–STEM imaging, simulations were conducted using Dr. probe software [4] to evaluate the atomic column in the acquired image. It applies the multislice method [5] to calculate the quasi-elastic forward scattering of the incident high-energy electron probes by the sample.

Energy dispersive spectroscopy (EDS) captures and analyzes the characteristic X-rays generated from the sample when its intrinsic electron structure is impacted by a beam of electrons. Excitation and relaxation of the electrons in the sample generate X-rays, which have discrete energies determined by the orbital structure of each element present in the sample. Therefore, the EDS analysis can determine the elemental composition of the sample. EDS mapping is typically done in the STEM mode based on compiling extremely specific elemental composition data across an area of a sample, called local elemental analysis. It visualizes the elemental distribution in the selected area, where different colors represent different elements.

To understand the phase separation mechanism in binary alloys and characterize the Pt–CeO_2 NCs' structures, several following TEM techniques were utilized herein. Owing to the large difference in the atomic mass between the Pt and CeO_2 phases, it is easy to distinguish the two phases using HAADF–STEM images. The elemental distribution characteristics in the NCs were also investigated using EDS mapping. HRTEM imaging and HAADF–STEM imaging were applied for atomic analysis, whereas SAED was used for structural analysis. Furthermore, EELS was used to investigate the valence state of the CeO_2 phase.

2.2.2.2 EELS technique

EELS is a viable method of obtaining chemical information and determining the distribution of light elements with high sensitivity and spatial resolution [6, 7]. When a beam of electrons inelastically interacts with a sample of typically <100-nm thickness, the transmitted electrons that lose their energy contain the sample information, such as chemical elements, stoichiometry, and electronic structure. The energy loss of the electrons is measured by the dispersive properties of a homogeneous magnetic field on the charged electrons in an electron energy loss spectrometer.

Two well-characterized oxides, CeO_2 and Ce_2O_3, can be formed after the oxidation of Ce. It is essential to study the valence state of the Ce-based phase since oxygen vacancy would be absent in the case of +3 in the CeO_2 phase, which plays importantly aids oxygen-ion transportation. The Ce-$M_{4,5}$ edges of CeO_2 in Figure 2.6a reflect the electronic transitions from the 3d to the 4f states (M_4 and M_5 correspond to the $3d_{3/2}$ to $4f_{5/2}$ and the $3d_{5/2}$ to $4f_{7/2}$ transitions) combined with the ligand hole effects [8]. The energy loss near edge structures (ELNES) of Ce-$M_{4,5}$ is valence sensitive, which can be utilized to obtain the spatially resolved chemical information of Ce-containing materials [9]. The concentration of the 3+ in the CeO_2 phase can be measured by the intensity ratio of the Ce-$M_{4,5}$ ELNES: M_5/M_4. Several methods have been proposed to calculate the M_5-

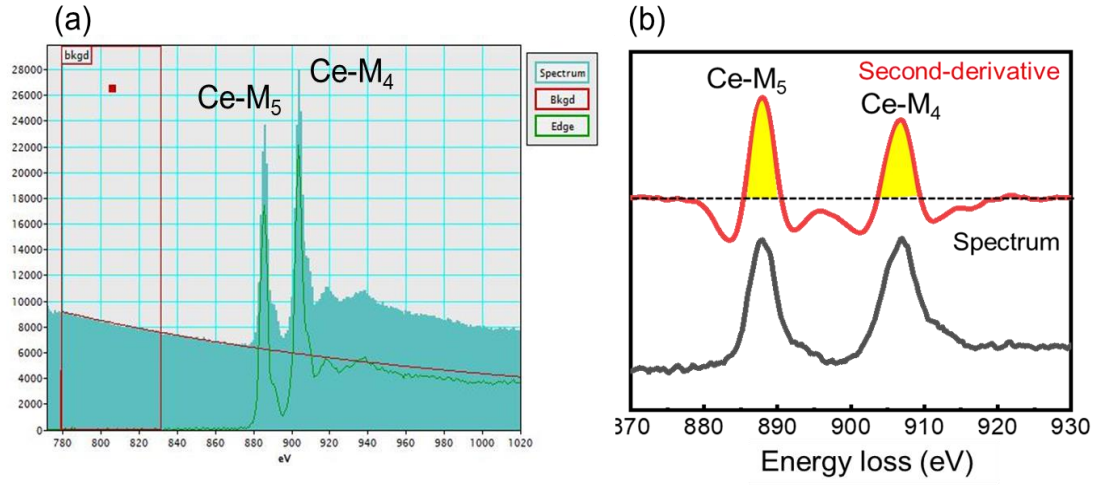

Figure 2.6 (a) EELS spectrum for Ce-M_4 and Ce-M_5 edges of standard CeO_2. (b) Second derivative method for calculation of the M_5/M_4. Acquired EELS spectra (gray) and corresponding second derivative spectra (red) in the range of the Ce-$M_{4,5}$ edge. M_5/M_4 was calculated by measuring the integrated area of the M_5 and M_4 peaks in the second derivative of the spectra, which are yellow-colored.

to-M_4 ratio, such as the second derivative of the spectra [10], multiple linear least squares fitting method [11], and the ratio of the peak value. The second derivative method was adopted herein because it is stable at different experimental resolutions and insensitive to the thickness variation. Figure 2.6b explains that Ce-M_5/M_4 was determined by measuring the positive part of the Ce-M_5 and Ce-M_4 peaks in the second derivate spectra, which were yellow-colored.

2.2.2.3 Electron tomography

Since the first study of the 3D reconstruction of biological macromolecules using electron microscopy in 1968 by de Rosier and Klug [12], electron tomography (ET) has been developed to be a well-established technique for different materials with mature reconstruction techniques. Owing to the limitation of the projected 2D images, information in the depth direction of the sample gives us wider insight into the material's structure. For crystalline nanomaterials, ET based on HAADF imaging is most suitable and reveals the 3D structure because of its compositional sensitivity.

The tomographic reconstruction is based on the Radon transformation, which was introduced in Radon's paper of 1917 [13]. It defines the mapping of a function $f(x, y)$, describing a real space object, by a projection or line integral through f along all possible lines L with unit length ds so that $Rf = \int_L f(x, y)ds$. Given the transformation nature, the structure of the object $f(x, y)$ can be reconstructed from projection Rf using the

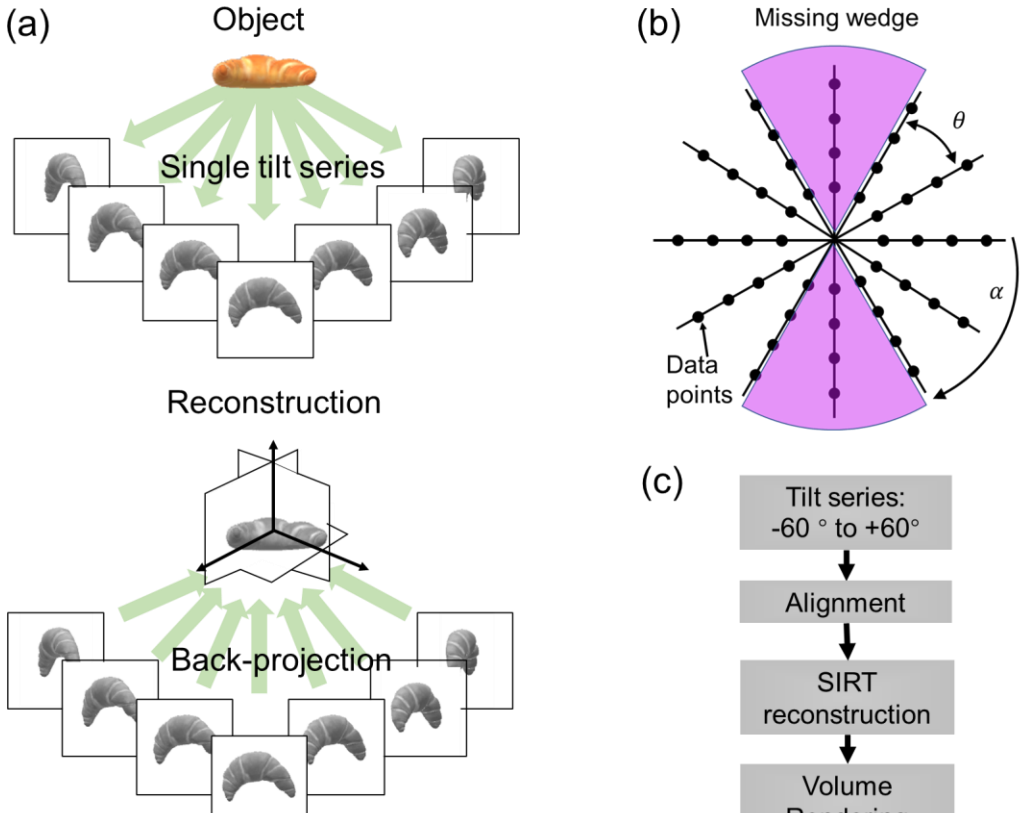

Figure 2.7 (a) Schematic of the electron tomography technique with the back-projection method. (b) Fourier representation of the object by a single tilt series of images. (c) Processes for 3D reconstruction and visualization.

inverse Radon transform. A general way to consider the projection of an object is to use a back-projection method (BJP), which is based on smearing out each image acquired in a tilt series back into a 3D space at the angle of the original projection. As shown in Figure 2.7a, using a sufficient number of images by tilting the sample with different angles, the superposition of all the back-projected rays generates the original object. This kind of direct back projection always results in the blurred structure because of an apparent enhancement of low frequencies and fine special detail reconstructed poorly (Figure 2.7b). Although the frequency sampling in each image plane is uniform, a higher data density near the center of the transformed space leads to the under-sampling of the high-frequency information. To solve this problem, weighted back projection (WBPJ) and simultaneous iterative reconstruction technique (SIRT) were developed to improve the reconstruction quality. Using a weighting filter to correct the uneven sampling and further iterative technique to improve the signal-to-noise ratio, the SIRT algorithm was reported to produce reconstructions that retain the highest fidelity, especially at high noise levels comparable with BPJ and WBJP [14].

Figure 2.7c displays the 3D reconstruction procedure applied herein. First, 61 tilt series images of the same area of interest with a 2° interval ranging from −60° to +60° were acquired in the HAADF–STEM mode using a plate-like specimen. Secondly, automatic and manual alignments with the cross-correction method were successively performed in the Digital Micrograph software (Gatan, America) throughout the tilt series. Before the reconstruction, the optimal orientation and position of the tilt axis were identified until only the minor arcs attached to the features in the reconstructed test plane. Then, a subregion with a certain number of N slices containing the useful data was chosen to launch a 3D reconstruction. Since SIRT can minimize the missing wedge effect at the cost of longer processing time, SIRT was selected as a reconstruction algorithm. The material's 3D structure was finally visualized using the Avizo software (Thermo Fisher Scientific, America) [15].

2.3 Homology analysis

Homology is an important technique that allows one to draw conclusions about the global properties of spaces and maps from local computations. In mathematics, topology is concerned with the properties of a geometric object that are preserved under continuous deformations, such as expansions, contractions, and twisting. If an object X can be topologically transformed into another object Y, then X and Y can be identified in the homological sense. Typically, a coffee cup and a ring donut are equivalent in the homology group because they contain the same connected components and 1D hole, enabling the topological transformation.

Homology computes many types of complexes, including Vietoris–Rips, simplicial complex, and cubical complex. Different data formats can be used for computational homology projects, such as point clouds and binary images based on the simplicial and cubical complexes, respectively. Herein, the input data is the binarized STEM images. Therefore, this subsection explains the computation process for digital images. Besides, two kinds of homology representations were introduced: Betti numbers and PDs.

2.3.1 Binarization of STEM images

Binarization is the conversion of grayscale images (i.e., STEM images) into black–white images, which contain the gray value (Gy) of pixels, either 0 or 255. The schematic of the binarization is shown in Figure 2.8a, where the Gy of each pixel is expressed. The pixels greater than the threshold are converted into white (Gy = 255), otherwise they are converted to black (Gy = 0). Two main types of binarization methods exist for obtaining binary images: global and adaptive thresholding. In basic global thresholding, a single value is set based on the histogram for all pixels in the image. The success of this technique strongly depends on how well the histogram can be partitioned, such as bimodal histograms. Concerning other kinds of histograms, such as those from the contrast images with uneven backgrounds, single-value thresholding does not work. To address such situations, adaptive thresholding by dividing an image into subimages and thresholding each pixel depending on its location is a useful approach. Figure 2.8b shows the difference between the global- and adaptive-thresholding methods.

Generally, the basic global threshold T is calculated as follows: 1). The image's histogram is calculated, and an initial estimate for T is selected; 2). The average gray values of pixels in the initial two segmented parts (T1 and T2) are computed; 3). A new threshold value T with a mean value of T1 and T2 is computed. 4). Steps 2 and 3 are repeated until the difference in successive iterations is < a predefined limited T_{∞}. Several optimal global thresholding methods were developed, such as Otsu's and MaxEntropy methods. For the adaptive thresholding, depending on the threshold to be calculated, the mean and Gaussian thresholding are frequently used. The threshold value is the mean of the neighborhood area minus the constant (C) for the former case, and a Gaussian-weighted sum of the neighborhood values minus C. Two parameters must be determined: block size and C. Herein, Python with OpenCV library [16] was used to conduct the binarization of the background-removed STEM images. The following codes for global and Gaussian thresholding were used:

```
G1 = cv.threshold (image, 130, 255, cv.THRESH_BINARY)
G2 = cv.adaptiveThreshold (image, 255, cv.ADAPTIVE_THRESH_GAUSSIAN_C, \c.v.THRESH_BINARY, 3, 5)
```

After binarization, noises are inevitable because of the vague interface between the Pt and CeO_2 domains. The left panel of Figure 2.8c shows the magnified binary image. Obviously, some interface regions are noisy. To improve the binary image's quality, closing and opening are used to smooth contours. Closing results from the dilation followed by the object's erosion in the image with a black background. Some small black noises in the white parts can be removed by closing processing, and a small connection between two black parts is separated, as shown in the middle panel of Figure 2.8c. The opening is the reverse of closing, i.e., erosion followed by dilation. Using the opening treatment, the white dots in the black background were removed, and a small connection between two black parts was consolidated (right panel of Figure 2.8c).

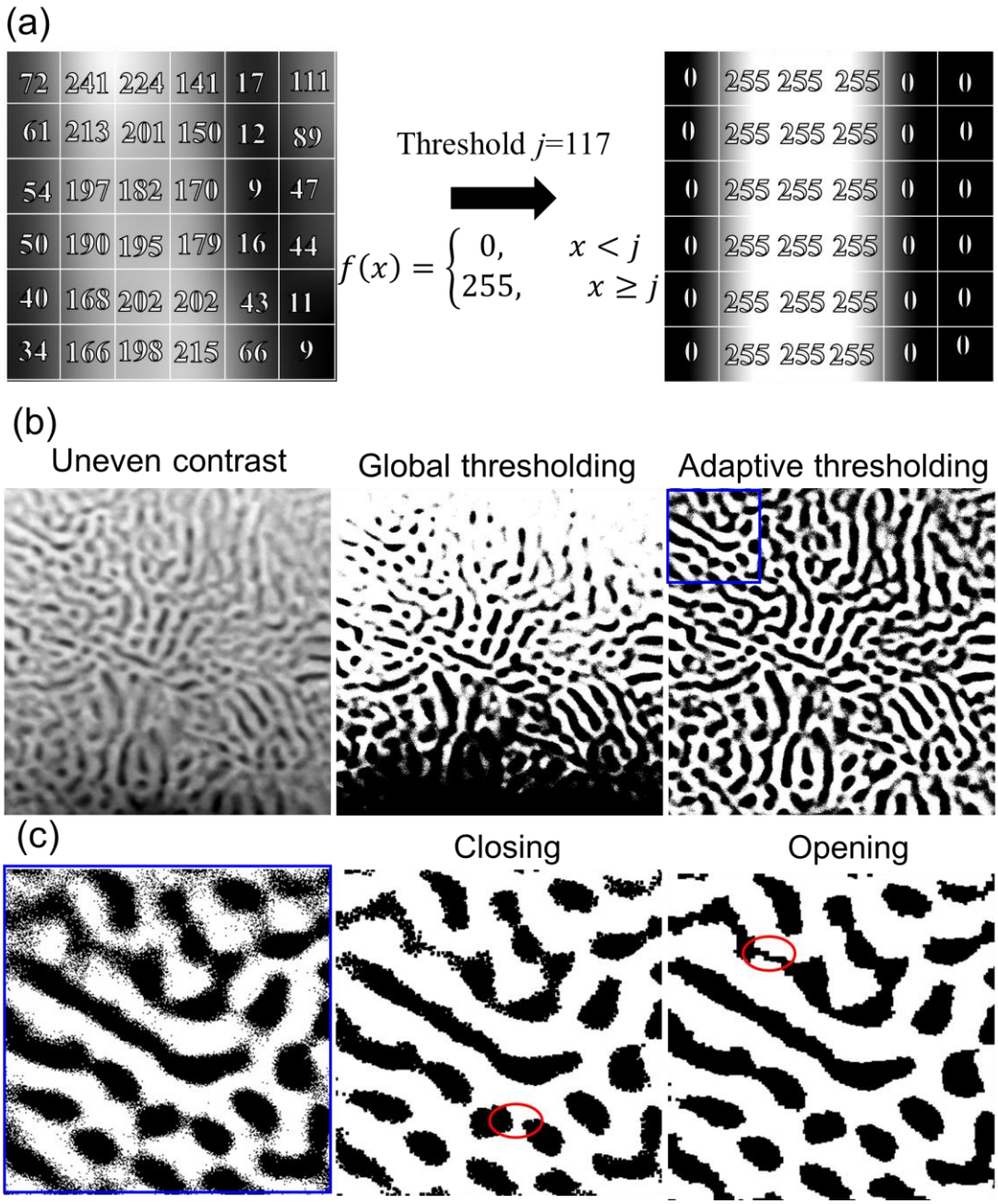

Figure 2.8. (a) Binarization algorism. (b) Difference between global and adaptive thresholding. (c) Post-processing: closing and opening for noise removal.

2.3.2 Calculation of Betti numbers

The nature of the homology is not to measure the size or shape of the structural feature, but to assign to a topological space an abelian group, i.e., topological complexity of given objects from the algebraic viewpoint. Specifically, it counts the number of connected components and encloses the regions contained by a geometric object, represented by Betti numbers (β_i). For simple objects, β_i can be counted manually, whereas for the objects with complicated shapes, computer calculation is more convenient and effective. Therefore, it is

necessary to understand the mathematical concepts of homology computation. Since the homology of images is based on the cubical complex, the cubical sets and their algebraic translations are introduced in this section.

Generally, a combinatorial object can be defined by vertices and edges for a graph, but it is insufficient to combinatorialize higher-dimensional topological space. Using cubes to build blocks for homology is useful for both lower- and higher-dimensional spaces. A union of elementary cubes representing a geometric object is fundamental for cubical homology. An elementary cube Q in the d-dimensional (dD) vector space $\mathbb{R}^d$ is a finite product of elementary intervals I_i (either a point $[l_i]$ or an interval $[l_j, I_{j+1}]$), i.e.,

$$Q = I_1 \times I_2 \times \cdots I_d \subset \mathbb{R}^d.$$

Figure 2.9 displays a variety of elementary cubes. The set of all elementary cubes is denoted by $\mathcal{K}$, while the set of all elementary cubes in $\mathbb{R}^d$ is denoted by $\mathcal{K}^d$, namely

$$\mathcal{K} := \bigcup_{d=1}^{\infty} \mathcal{K}^d.$$

Note that the cube $[1, 2] \subset \mathbb{R}$ differs from the cube $[1, 2] \times [1] \subset \mathbb{R}^2$ because they are subsets of different spaces, although they have the same position and shape. Therefore, the spatial dimension must be considered when comparing the objects. Two important definitions, the embedding number and the dimension of Q, are introduced and denoted by $embQ$ and $dim\ Q$, respectively. For $Q = I_1 \times I_2 \times \cdots I_d \subset \mathbb{R}^d$, $embQ := d$ and $dimQ$ is the number of intervals $[l_j, l_{j+1}]$. The set of k-dimensional (kD) elementary cubes is defined as $\mathcal{K}_k$ and let

$$\mathcal{K}_k := \{Q \in \mathcal{K} \mid dimQ = k\} \text{ and } \mathcal{K}_k^d := \mathcal{K}_k \cap \mathcal{K}^d.$$

The product of two elementary cubes, P and Q, is a new elementary object with the addition of the embedding number and the dimension, i.e.,

$$P \times Q := \mathcal{K}_{k+k'}^{d+d'}.$$

Note that generally, $P \times Q \neq Q \times P$. Thus, a cubical set X is the subset of $\mathbb{R}^d$ that can be written as a finite union of elementary cubes:

$$\mathcal{K}(X) := \{Q \in \mathcal{K} \mid Q \subset X\} and\ \mathcal{K}_k(X) := \{Q \in \mathcal{K}(X) \mid dimQ = k\}.$$

Specifically, the elements of $\mathcal{K}_0(X)$ are the vertices of X and the elements of $\mathcal{K}_{k1}(X)$ are the edges of X on a graph.

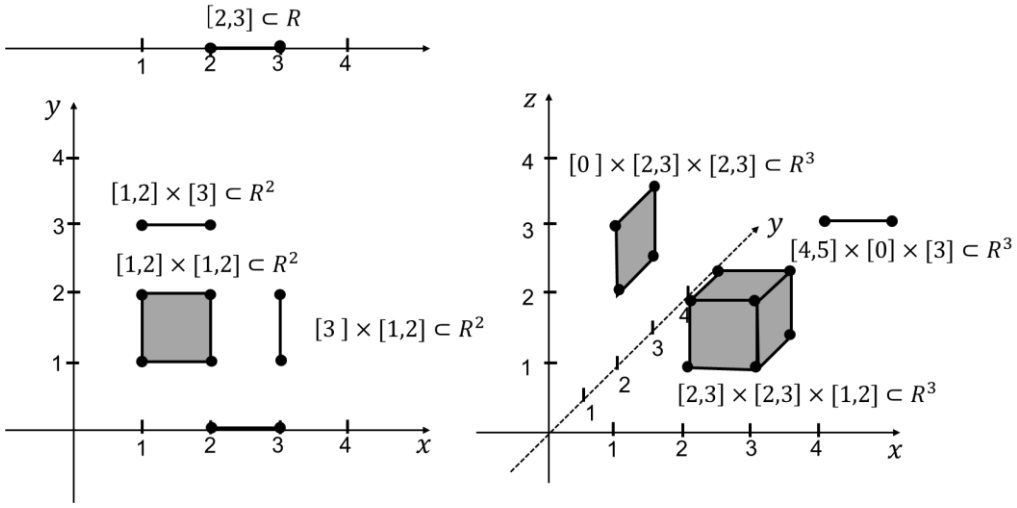

Figure 2.9. Elementary cubes in *R*, *R*^2, and *R*^3.

Once a cubical set X is constructed, translating geometric objects to algebraic ones is then essential to perform the homology calculation. An algebraic object $\hat{Q}$, also called an elementary k-chain, is identified to associate each elementary cube $Q \in \mathcal{K}_k^d$. The set of all elementary k-chains and all elementary chains are denoted by

$$\hat{\mathcal{K}}_k^d := \{\hat{Q} \mid Q \in \mathcal{K}_k^d\} \; and \; \hat{\mathcal{K}}_k^d := \bigcup_{k=0}^{\infty} \hat{\mathcal{K}}_k^d,$$

respectively. A characteristic function $\hat{Q} := \mathcal{K}_k^d \to \mathbb{Z}$ is defined by

$$\hat{Q}(P) := \begin{cases} 1 & if\ P = Q \\ 0 & otherwise \end{cases}$$

The sum of two elementary cubes $Q_1, Q_2 \in \mathcal{K}_k^d$ is then induced by

$$\left(\widehat{Q_1} + \widehat{Q_2}\right)(P) := \widehat{Q_1}(P) + \widehat{Q_2}(P) = \begin{cases} 2 & if\ Q_1 = Q_2 \; and \; P = Q_1 \\ 1 & if\ Q_1 \neq Q_2, and = Q_1 \; or \; P = Q_2 \\ 0 & otherwise \end{cases}$$

and the product of given $P \in \mathcal{K}_k^d$ and $Q \in \mathcal{K}_k^{d'}$ is given by $\hat{P} \lozenge \hat{Q} := \widehat{p \times Q}$. Let $\hat{Q} \in \mathcal{K}_k^d$, it can be the product of two elementary cubical chains $\hat{I}$ and $\hat{P}$ with $embI = 1$ and $embP = d - 1$ such that $\hat{Q} = \hat{I} \lozenge \hat{P}$. This decomposition is used in the definition of the following boundary maps. The set C_k^d was used to imply the set of all-chains and is written by

$$C_k^d := \left\{ \sum_{i=1}^{m} \alpha_i \widehat{Q_i} \mid \alpha_i \in \mathbb{Z}, \widehat{Q_i} \in \widehat{\mathcal{K}_k^d} \right\}.$$

The cubical boundary map is defined by $\partial_k : C_k^d \to C_{k-1}^d$. Take an elementary cube Q in 1 dimensional space (d=1) for example, $\partial_k \hat{Q} := 0$ if Q is a point $[l_i]$ and $\partial_k \hat{Q} := \widehat{[l+1]} - \widehat{[l]}$ if Q is an interval $[l_j, I_{j+1}]$. In the case of d>1, $\partial_k \hat{Q} := \partial_{k1} \hat{I} \lozenge \hat{P} + (-1)^{dim\hat{I}} \hat{I} \lozenge \partial_{k2} \hat{P}$, where $k_1 = dimI$ = 0 or 1 and $k_2 = dimP$. For all $k \geq 0$, $\partial_{k-1} \circ \partial_k = 0$, which means that a boundary does not have its boundary. The boundary operator has the same type for the cubical set X: $\partial_k^X : C_k(X) \to C_{k-1}(X)$. For the k-chian $z \in C_k(X)$, if $\partial_k z = 0$, z is called a

k-cycle, defined the kernel $ker\partial_k$; if there exist an element $c \in C_k(X)$ having the equation $\partial_c = z$, z is called a k-boundary, defined by the image $Im\partial_{k+1}$. The set of all k-cycles and k-boundaries in $C_k(X)$ are denoted by

$$ker\partial_k := Z_k(X) := \{z \in C_k(X) | \ \partial_k z = 0\} \subset C_k(X)$$

$$Im\partial_{k+1} := B_k(X) := \{z \in C_k(X) \mid z = \partial_c \ for\ some\ c \in C_{k+1}(X)\} \subset C_k(X),$$

respectively. The k-th cubical homology group of X is written by $H_k(X) := Z_k(X)/B_k(X)$ and the k-th Betti number of X is the rank of H_k. The relationship between Betti numbers and homology group is as follows: $H_k = \mathbb{Z}^{\beta_k}$ and $\beta_k = rankH_k = rankZ_k - rankB_k$. The Betti number counts the number of kD holes in X. Particularly, β_0 is the number of connected components, β_1 counts the number of tunnels or rings, and β_2 counts the number of cavities of X. Many homology computation software have been developed to apply the above algebra to calculate the Betti numbers. Herein, the software Chomp [17] was used.

2.3.3 Persistence diagram method

Persistent homology tracks the H_k elements as the scale parameters, such as distance and time, increase. Before computing the PD, an important item, filtration, must be known. Given a cubical complex $\mathcal{K}$, the filtration is a totally ordered set of subcomplexes $\mathcal{K}^i$ of $\mathcal{K}$, such that $\mathcal{K}^i \subseteq \mathcal{K}^j$ if $i \leq j$. With the increasing index i, successive complexes in the filtration maps $f^i: \mathcal{K}^i \to \mathcal{K}^{i+1}$ occur. A persistence complex is the sequence of chain complexes $\mathcal{K}^i$ connected by chain maps f^i. Similarly, when the scale parameter increases step by step of a cubical complex $\mathcal{K}$, the cubical complex correspondingly changes. The cubical complexes before and after the change are called X and Y, respectively. Consequently, the k-th persistent homology of the filtration maps: $H_k(X) \to H_k(Y)$, indicating whether the feature (kD hole) in X remains in Y or not. A pair of b_i and d_i describes the lifetime, including the burn (b_i) and death (d_i) times for a feature. All features in the cubical complex can be represented, thus the persistent homology can be decomposed by all pairs during the filtration, like $H_k(\mathcal{K}) \simeq \oplus_{i=1}^{P} I(b_i, d_i)$. The persistent diagram $D_k(\mathcal{K})$ is a multiset of (b_i, d_i) represented by a graph with the x and y axes as b_i and d_i, respectively.

Figure 2.10 displays the emergence and demise of the 0th persistent homology for a binary image (Figure 2.10a), i.e., the connected white components. Following the approach proposed in the paper [18], the numbers in the pixel represent the Manhattan distance (MD), where positive and negative numbers are assigned to the black and white pixels, respectively (Figure 2.10b). There are three pairs of homology filtration, two (−2, 1) and one (−3, ∞), as shown in Figure 2.10c. Figure 2.10d explains how the two pairs are identified. When the threshold for the MD is set to the largest negative number (−3), only one pixel marked by a red rectangle with −3 in the left panel is white, whereas other pixels with MD > −3 are black. When the threshold increases to −2, the white region expands because the surrounding pixels with MD = −2 become white. Additionally, the other two regions marked by red rectangles appear. With the threshold increases to 1, the three white regions merged into one large white area. In this case, two of the three regions are called death and the remaining one infinitely exists. Therefore, there are two pairs of (-2, 1) and one pair of (-3, ∞). Generally, all birth values are negative,

and the birth value or lifetime roughly indicates the shape of white phases in the original binary image. i.e., the longer the lifetime, the larger the distance between two close white phases. The larger the absolute birth value, the larger the white phases. Figure 2.11 shows a typical PD (see Figure 2.11b) obtained from the binary image of Pt-CeO_2 nanocomposite pattern (see Figure 2.11a) using the HomCloud software [19].

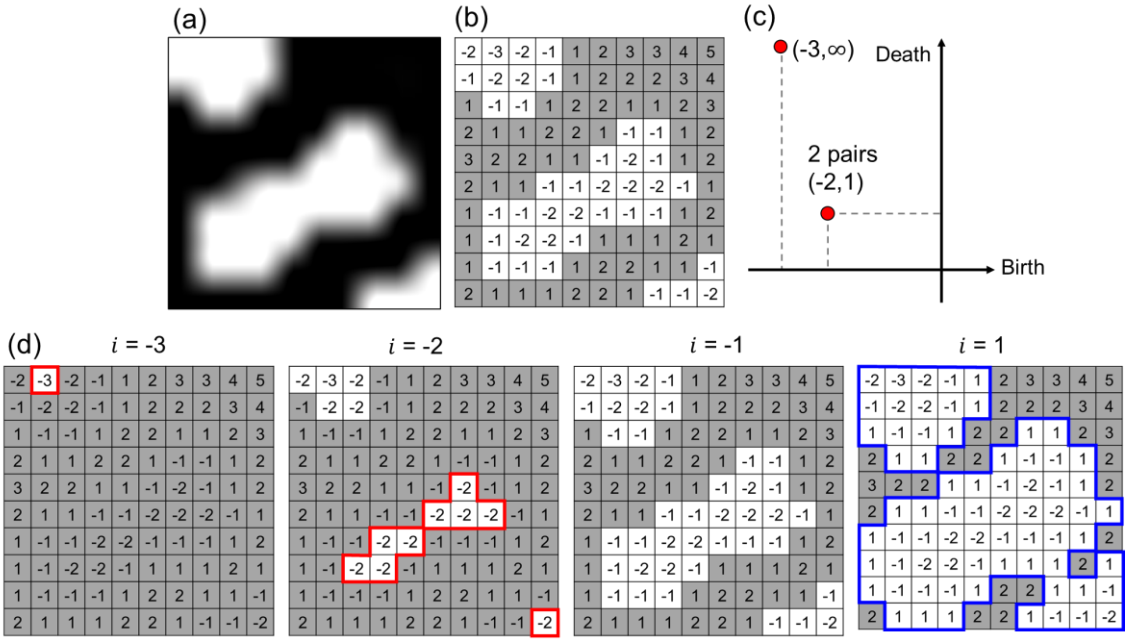

Figure 2.10. Illustration of persistence diagram for a binary image. (a) Original binary image. (b) Corresponding Manhattan distance in each pixel. Black and white regions are assigned to be positive, and negative, respectively. (c) Persistence diagram for the image in (a). (d) Evolution tracking with increasing Manhattan distance.

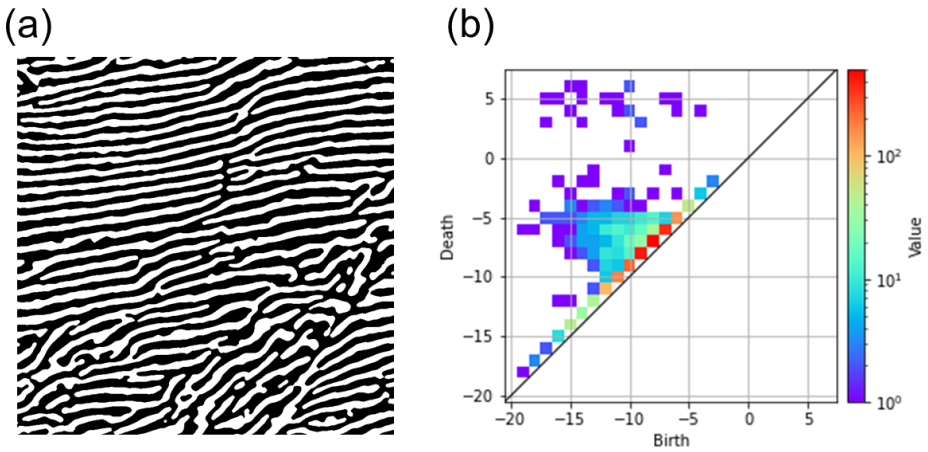

Figure 2.11. Typical persistence diagram for a binarized structure. (a) Binary image for a two-phase composite structure. (b) Corresponding persistence diagram.

2.4 Ionic conductivity measurement

IS is a technique for determining the frequency-dependent transfer function of a system and thus has been widely applied to interpret the hidden physical behavior of cells. The measured ionic conductivity is influenced by the nature of the material (composition, density, and microstructure), testing temperature, and pressure. The complex impedance method has been proven to have a high accuracy in measuring the ohmic conductivity of ceramic pellets [20]. It is measured at different frequencies or in a certain frequency range to investigate the response of the electrochemical system to the stimulus of an alternative current waveform (Figure 2.12a). The ratio of instant changes of voltage and current is the impedance of the system, which contains a magnitude $\frac{\Delta U}{\Delta I}$ and a phase shift ϕ. With Euler's relationship, it is possible to express the impedance as a complex function that includes two parts: the real and imaginary parts of the impedance. They show a different frequency dependency and therefore provide a comprehensive source of information. By varying the imposed alternating voltage frequency, the relationship between the real (ReZ) and imaginary (ImZ) parts in a certain frequency range can be obtained from the current response, which is plotted as a Nyquist impedance diagram (Figure 2.12b). Note that the imaginary part is negative, and each point on the Nyquist Plot is the impedance at a particular frequency. The impedance on the Nyquist Plot can be represented as a vector (arrow) of length $|Z|$, and the angle between the vector and the X-axis is called the phase angle arg Z. For the electrodes of SOFCs, the obtained Nyquist Plot usually comprises a series of suppressed semi-circles [21]. Each circle is related to a physical or chemical process, including membrane resistance losses, mass transfer, or oxygen reduction reaction kinetics in the target materials. Generally, circles at high frequencies originate from the oxygen transfer through the conductive phase of the composite, middle-frequency circles are caused by the GB effects, and electrode polarization can be seen at low frequencies. Sometimes, an ohmic resistance from the electrolyte appears in the high frequency before or between the circles. An important step in interpreting the diagram is building an equivalent circuit. A couple of resistance (R) and capacitance (C) forms a semicircle, and the resistance only results in a blank segment. Once R of the target material is determined, the conductivity (σ) and its temperature dependence can be plotted using the equation: $\sigma = d/RA$, where d is the pellet's height of the measured bulk sample and A is the pellet's surface area. The two parameters, such as the activation energy (E) and pre-exponential factor (σ_0), can then be induced following the Arrhenius equation: $\sigma T = \sigma_0 \exp(-E/kT)$.

The frequently used configuration for the IS measurement is mainly divided into two categories: three- and two-electrode four-wire setups. Herein, the two-electrode method was employed, and Figure 2.12c presents the schematic. Two CGO pellets sandwiched the Pt–CeO_2 NC to block the electron transportation through the composite, and Ag paste covers the CGO pellet to ensure proper current collection. Four wires connect to the IS measurement equipment. The symmetrical cell was kept at temperatures of 500°C–600°C in the air during the conductivity measurements, which were conducted over the frequency range of 1 Hz–1 MHz with a 30-mV applied peak-to-peak voltage.

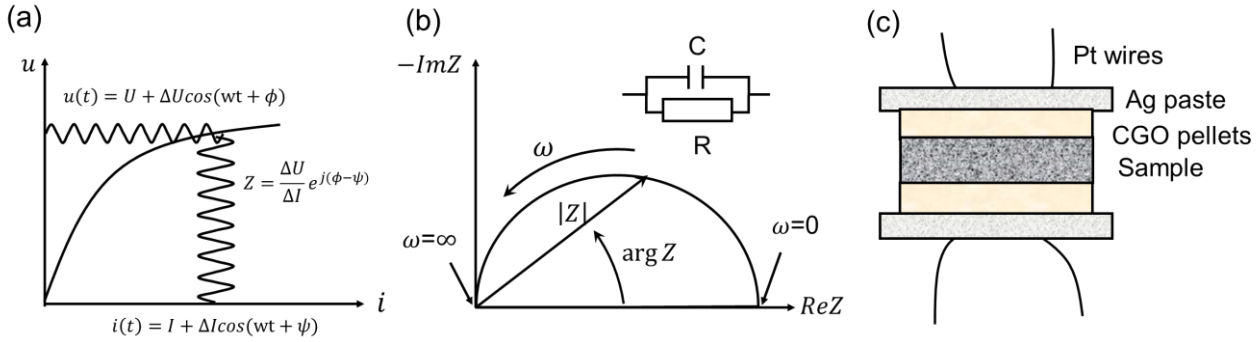

Figure 2.12. (a) Voltage–current curve obtained using IS. (b) Nyquist impedance diagram with the equivalent circuit model. (c) Two-electrode measurement.

References

[1] D.B. Williams, C.B. Carter, Transmission Electron Microscopy: A Textbook for Materials Science, second ed., Springer-Verlag, New York, 2009.

[2] Stephen J. Pennycook; Nellist, P. D. Scanning Transmission Electron Microscopy, Springer-Verlag, New York, 2011.

[3] P.W. Hawkes, J.C.H. Spence, Springer Handbook of Microscopy, Springer, Cham, Switzerland; 2019

[4] Barthel, J. Dr. Probe: A Software for High-Resolution STEM Image Simulation. Ultramicroscopy 2018, 193 (May), 1–11.

[5] Cowley, J. M.; Moodie, A. F. The scattering of electrons by atoms and crystals. I. A new theoretical approach. Acta Crystallographica, (1957), 10(10), 609-619.

[6] Egerton R. F. Electron Energy-Loss Spectroscopy in the Electron Microscope, Springer (US), 2011.

[7] Brydson, R.; Sauer, H.; Engel, W.; Zeitler, E. EELS as a Fingerprint of the Chemical Co-Ordination of Light Elements. Microsc. Microanal. Microstruct. 1991, 2 (2–3), 159–169.

[8] Turner, S.; Lazar, S.; Freitag, B.; Egoavil, R.; Verbeeck, J.; Put, S.; Strauven, Y.; Van Tendeloo, G. High Resolution Mapping of Surface Reduction in Ceria Nanoparticles. Nanoscale 2011, 3 (8), 3385–3390.

[9] Xu, H.; Wang, Y. Electron Energy-Loss Spectroscopy (EELS) Study of Oxidation States of Ce and U in Pyrochlore and Uraninite - Natural Analogues for Pu- and U-Bearing Waste Forms. J. Nucl. Mater. 1999, 265 (1–2), 117–123.

[10] Garvie, L. A. J.; Buseck, P. R. Determination of Ce^{4+}/Ce^{3+} in Electron-Beam-Damaged CeO2 by Electron Energy-Loss Spectroscopy. J. Phys. Chem. Solids 1999, 60 (12), 1943–1947.

[11] Song, K.; Schmid, H.; Srot, V.; Gilardi, E.; Gregori, G.; Du, K.; Maier, J.; Van Aken, P. A. Cerium Reduction at the Interface between Ceria and Yttria-Stabilised Zirconia and Implications for Interfacial Oxygen Non-Stoichiometry. APL Mater. 2014, 2 (3).

[12] De Rosier, D. J.; Klug, A. Reconstruction of Three Dimensional Fiber Structures from Orthogonal Projections. Nature 1968, 217, 130–134.

[13] Radon, J. On the determination of functions from their integrals along certain manifolds. Ber. Verh, Sachs Akad Wiss.,1917, 69, 262–277.

[14] Gilbert, P. Iterative Methods for the Three-Dimensional Reconstruction of an Object from Projections. J. Theor. Biol. 1972, 36 (1), 105–117.

[15] https://www.thermofisher.com/jp/ja/home/industrial/electron-microscopy/electron-microscopy-instruments-workflow-solutions/3d-visualization-analysis-software.html.

[16] OpenCV. https://opencv.org/.

[17] CHOMP: Computational homology project, http://chomp.rutgers.edu/.

[18] Obayashi, I.; Hiraoka, Y.; Kimura, M. Persistence Diagrams with Linear Machine Learning Models. J. Appl. Comput. Topol. 2018, 1 (3–4), 421–449.

[19] Homcloud. https://homcloud.dev/index.html.

[20] Winand, J. M.; Depireux, J. Measurement of Ionic Conductivity in Solid Electrolytes. Epl 1989, 8 (5), 447–452.

[21] Huang, Q. A.; Hui, R.; Wang, B.; Zhang, J. A Review of AC Impedance Modeling and Validation in SOFC Diagnosis. Electrochim. Acta 2007, 52 (28), 8144–8164.

Chapter 3 Growth mechanism of the phase separated Pt/CeO_2 nanocomposites

To prepare the Pt/CeO_2 nanocomposites with various structure for homology analysis, understanding the growth mechanism of the phase separated composites is important for structural engineering. By high resolution TEM analyzing the powder composites annealed for different duration, 30 min and 12 h, the phase separation behavior was declared. It involves the following steps: oxygen dissolution into the alloy causes special periodic compositional perturbation by atomic segregation, specifically, by local diffusion of Pt and Ce atoms. A striped pattern of Pt and CeO_2 with a 4–5 nm periodicity formed through phase transformation of the Pt-rich alloy and oxidation of the Ce-rich alloy, respectively. Notably, a fully epitaxial relationship between the Pt and CeO_2 phases was observed even in the initial stage. With continued annealing, the crystals rotated into an energetically favorable orientation with respect to the remaining $(111)Pt//(111)CeO_2$. The alloy oxidation and its resulting nanoscale phase-separation behavior was verified in ex-situ annealing experiment of an alloy specimen, which has been first thinned by a focused ion beam. Changing the oxygen partial pressure to the reaction interface may alter the orientation relationship between the hexagonal close-packed Pt_5Ce structure and face-centered cubic Pt/CeO_2 structure, thereby altering the growth direction of the separated phases. These findings provide us hints to tune the structures by changing the annealing conditions, which is useful for understanding the structure-property relationship of Pt/CeO_2 nanocomposites in the Chapters 4-6.

3.1 Introduction

Nanoscale heterostructures of noble metals (NM) and metal oxides (MO) are attractive with a variety of applications in catalysts [1, 2], photovoltaic [3] and electrode materials of fuel cells [4, 5]. Heterostructures at nanometer scale of two phases provide rich reaction active sites. Furthermore, the strong interaction of NMs with MO could contribute to specific performances than mono-component counterparts [6]. Considering the importance of tolerance capability and interaction at the interface, most researchers are dedicated to prepare high durable and high surface area configurations by numerous synthesis strategies, including Sol–gel methods [7], deposition–precipitation [8] and oxidation of bimetallic alloys [9–12]. The oxidation of bimetallic is an effective way to produce stable NM/MO heterostructures and complex structures can be engineered. For example, oxide supported noble metal nanoparticles of Au/NiO were synthesized by in situ phase separation of bimetallic nanoparticles [9]. Core-shell structures with Au core and in-oxide shell with high activity in CO_2 hydrogenation were formed by the oxidation of Au-In alloys [10]. Previous studies [13-15] have shown that the oxidation of binary alloys produces a topology-tailored structure of fibrous networks of NMs#TO, and it exhibited long-term stable catalytic on CO_2 reforming of methane [13]. However, much less studies focused

on the oxidation process of binary alloys, which is a powerful mechanism to produce nanoscale heterostructures.

Pt-CeO_2 system has been unceasingly investigated as catalysts in various field, such as CO oxidation, ethanol oxidation and fuel cells. Electron transfer from Pt to CeO_2 and oxygen vacancy formation at the interface were found to paly determinant roles for the high activity by first-principles study [16, 17] and experiment [18, 19]. Recently, different nanostructures of Pt/CeO_2 ranging from stripes to maze patterns were prepared and contributed to different ionic conductivities, which highlight the importance of the connective interface of Pt and CeO_2 domains [20]. It has been shown that different morphologies in the oxide precipitates of alloys arise from the competition at the oxide/alloy interface between the growth of existing particles and the nucleation of new particles [21]. Therefore, thorough understanding the oxidation induced phase separation behavior is important to control the geometry of heterostructures.

Here, I studied the annealing of Pt_5Ce alloys in the syngas of CO and O_2 at 400 ℃. Both FIB-thinned specimen's and bulky powder sample's oxidation under the same condition were analyzed to investigate the phase separation behavior. A combination of HRTEM and atomic-resolution HAADF–STEM techniques have been applied to understand the oxidation induced phase separation behavior. Moreover, orientation relationships among alloy precursor, Pt and CeO_2 phases were clarified. The oxidation processes in two samples are proved to be the same. Initially, Pt-rich and Ce-rich area were segregated with coherent relationship with Pt_5Ce alloy. Striped patterns of alternate crystalline Pt and CeO_2 phase were then formed with epitaxial relationship. Finally, the oxidation gives rise to network structure, whose framework is composed by polycrystalline Pt embedded by nanocrystalline CeO_2 with incoherent interfaces. However, the orientation relationship between hcp-structured Pt_5Ce alloy and fcc-structured Pt varies with the oxygen diffusion rate, which was deduced from the different orientation relationship in TEM specimen and bulk sample.

3.2 Experimental

3.2.1 Specimen preparation

Pt_5Ce alloy was prepared by arc melting of the elemental metals in a pure argon atmosphere. Alloy powders with an average particle size of 50 μm were then obtained by grinding. The alloy precursor was transferred to a reactive gas furnace (containing mixed CO and O_2 at a molecular ratio of 2:1) for phase separation. Two forms of the alloy, bulky powder and firstly FIB-thinned specimen were used for two different experiments. The schematic of the two experiments is shown in Figure 3.1. As shown in Figure 3.1a, the bulky powder alloys were first annealed for 30 min and 12 h to obtain partial and complete phase-separated structures, respectively. For the ex-situ experiment in Figure 3.1b, the firstly-FIB-thinned alloy specimen was prepared by FIB milling (JEOL JEM-9420FIB, Japan) of 30-KeV Ga ions and placed in TEM to observe the initial structure. The firstly-FIB- thinned specimen was then annealed for only 10 min at 400℃ to track its phase-separation behavior.

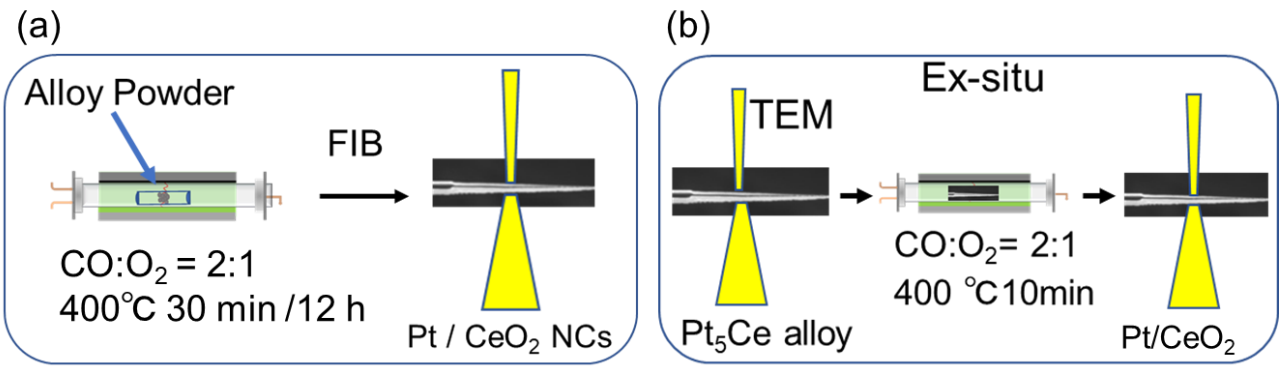

Figure 3.1. The illustration of the two experiments for the understanding of the phase separation behavior. (a) Powder alloy was used to annealing for 30 min and 12 h for the partially and completely phase separation. (b) Firstly-FIB-thinned specimen for the ex-situ experiment to track the phase separation process.

3.2.2 Transmission electron microscopy

The morphologies of the three kinds of specimens were investigated by a field emission microscope (JEOL JEM-2100F, Japan) operated at 200kV. The atomic analyses (HRTEM and HAADF-STEM) and energy dispersive X-ray spectroscopy (EDS) mapping of specimens were carried out in a JEOL JEM-200ARMF equipped with double Cs-correctors and a Schottky-filed emission gun. To highlight the lattice fringes in the atomic HAADF-STEM images, the images were processed by a smooth–filter which is freely available as a plug-in for the DigitalMicrograph **[**22**]**. The Fast Fourier transformation (FFT) patterns were also obtained using the DigitalMicrograph software package (Gatan, USA). The lattice strain maps were calculated from HAADF-STEM images by a geometric phase analysis (GPA) plug-in **[**23**]**. HAADF-STEM simulations were performed using the Dr. probe software **[**24**]**, implementing the multislice method to calculate the quasielastic forward scattering of the incident high-energy electron probes from the sample.

3.3 Results and discussion

3.3.1 Epitaxial relationship in the self-assembled Pt/CeO_2 nanocomposites

Phase-separation and self-assembly in oxidized Pt_5Ce alloy leads to a composite of Pt and CeO_2, as indicated by the XRD patterns in Figure 3.2. The EDS mapping for the composite is also analyzed and shown in Figure 3.3. It is clear that the bright-contrast phase of Pt alternates with the dark-contrast phase of CeO_2 forming an interwoven nanostructure. Atomic STEM characterizations of the Pt/CeO_2 nanocomposites annealed for 12h at 400℃ are shown in Figure 3.4. The average periodicity of approximately 50 stripe structures was 4.6 nm (see histogram in Figure 3.5a for details). To clarify the orientation relationship between the Pt and CeO_2 structures, the heterointerfaces between the two phases enclosed in boxes A and B in Figure 3.4a are magnified in Fig. 3.4b and 3.4c, respectively. As shown in Figure 3.4b, the Pt and CeO_2 crystals were

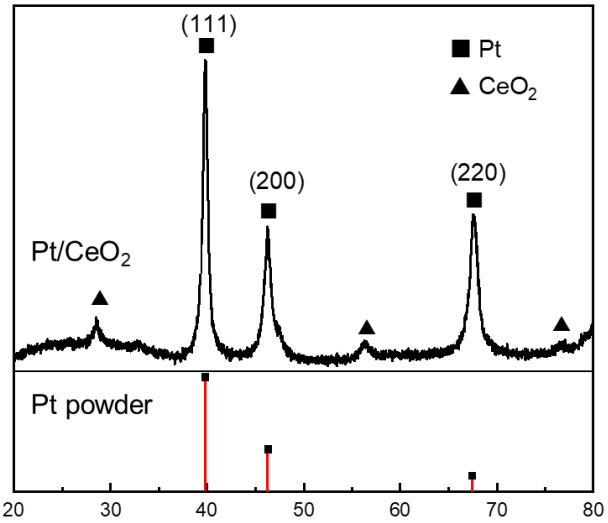

Figure 3.2. X-ray diffraction pattern of the Pt/CeO_2 composite and reference data of Pt metal, indicating the strong relative intensity of (220) plane.

exactly on the [110] zone axis but the interface was incommensurate. The angle between the (200) planes of Pt and CeO_2 was approximately 57°, and the (1-11)CeO_2 and (11-1)Pt planes were almost parallel. Figure 3.4c consolidates the parallel relationship between the (111) planes of Pt and CeO_2 crystals on different zone axis. Due to the large lattice misfit (~38 %), several edge dislocations were found at the heterointerface. However, the relationship was fully epitaxial along the direction of the [111] zone axis (see Figure 3.4d). The brightest spots (connected by red triangles in Figure 3.4d) were deduced as overlapped Pt and Ce atoms. More specifically, the calculated lattice-constant ratio between (111)CeO_2 and (111)Pt was 1.38, between the verified lattice constant ratio of 4:3 and 7:5 [25]. The lower and upper parts of Figure 3.4e present a structural model of the observed structure based on the calculated 4:3 CeO_2/Pt model and a simulated HAADF–STEM image along the [111] direction, respectively. The simulation results confirm that the Pt and Ce atoms overlapped at the brightest projection spots (enclosed by the dashed red circles in the model).

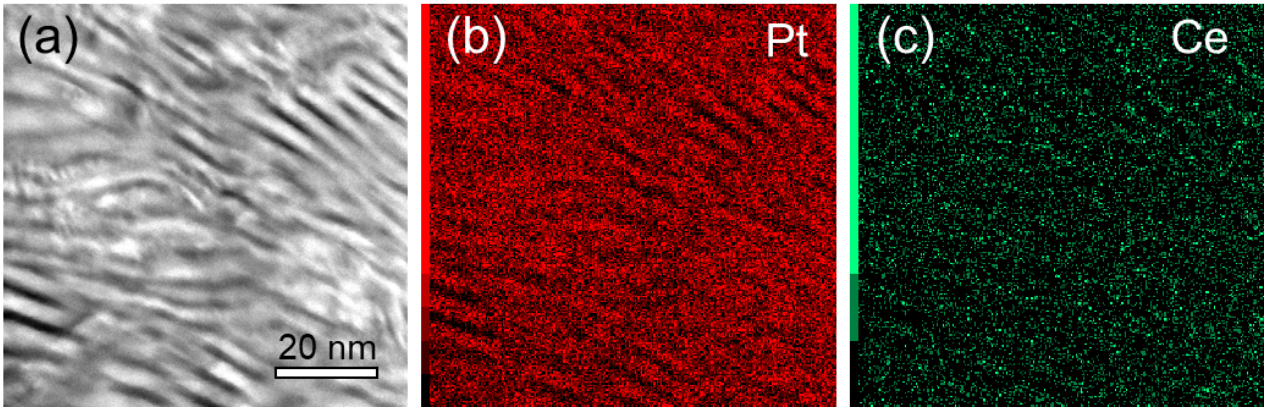

Figure 3.3. (a) HAADF–STEM image of Pt/CeO_2 nanocomposites annealed at 400℃ for 12 h. and corresponding element distribution mappings of (b) Pt and (c) Ce. It suggests the bright and dark phases in (a) are rich in Pt and Ce, respectively.

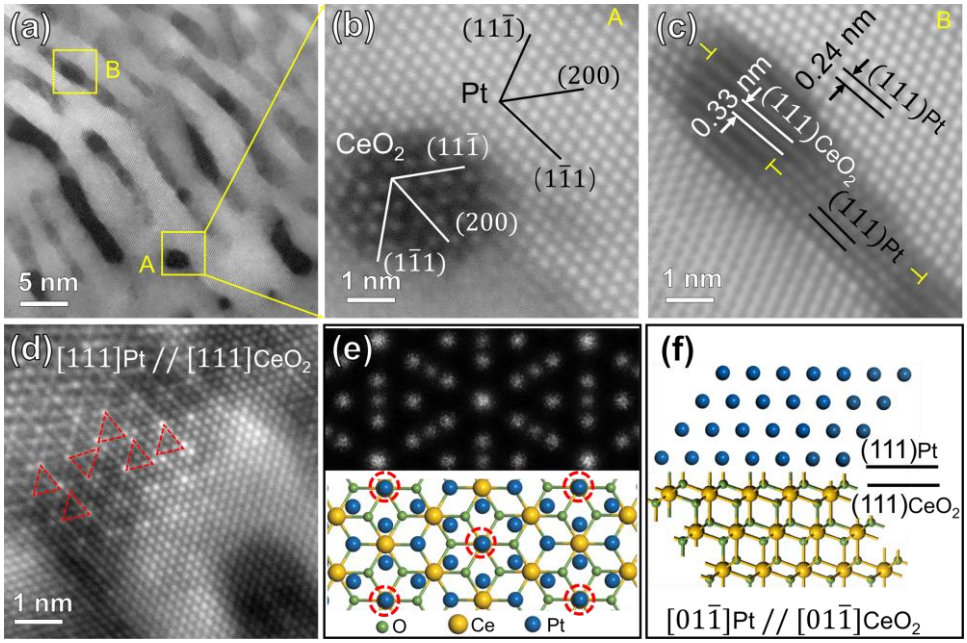

Figure 3.4. (a) HAADF–STEM image of the Pt/CeO_2 bulk sample annealed at 400°C for 12 h showing the completely separated Pt/CeO_2 composites. (b)–(c) Enlarged filtered HAADF–STEM images of the boxes in (a), indicating the incoherent relationship between Pt and CeO_2. (d) HAADF–STEM image of another site on the same sample showing the epitaxial relationship in the [111] zone axis. (e) Schematic of the 4:3 lattice structure of (111)CeO_2 on (111)Pt (lower view) and the corresponding simulated HAADF–STEM image (top view), revealing that the bright spots connected by red dashed triangles in (d) are produced by overlapped Pt and Ce atoms. (f) Side view along the [01-1] direction of the Pt/CeO_2 epitaxial interface, which has a 60° rotational relation with (111)Pt//(111)CeO_2.

Integrating the relationships observed in Figures 3.4b–d, the lattice-matching relationship between Pt and CeO_2 that maintains (111)Pt//(111)CeO_2 is a certain angle of rotation. From Figure 3.4d, the rotation angle was deduced as 60°, that is, the orientation relationship between Pt and CeO_2 is Pt(111)//CeO_2(111) 60°. This kind of rotated epitaxial relationship was already reported in thin-layers of Rh/CeO_2 [26], MoS_2/S [27, 28], etc., but firstly found in Pt/CeO_2 composites here. Owing to the sixfold symmetry axis of (111) planes, a 60° rotation of (111)Pt plane parallel to a (111)CeO_2 plane retains the epitaxial relationship, but other planes are crystallographically non-equivalent. Figure 3.4f illustrates the side view along [01-1] direction of the structure model in Fig. 3.4e. The atomic arrangement between Pt and CeO_2 matches that of Figure 3.4b. Since the fully epitaxial Pt(111)/CeO_2(111) and the epitaxial type of Pt(111)/CeO_2(111) 60° are much similar in the atomic arrangement at the metal-oxide interface perimeter that plays a central role in catalysis, no prominent difference would be expected on the performance.

3.3.2 Phase separation behavior during the oxidation of Pt_5Ce alloy

How the special epitaxial relationship of (111)Pt//(111)CeO_2 with a 60° rotation evolves in the self-assembled Pt/CeO_2 composites must be elucidated. For this purpose, I prepared a partially oxidized powder

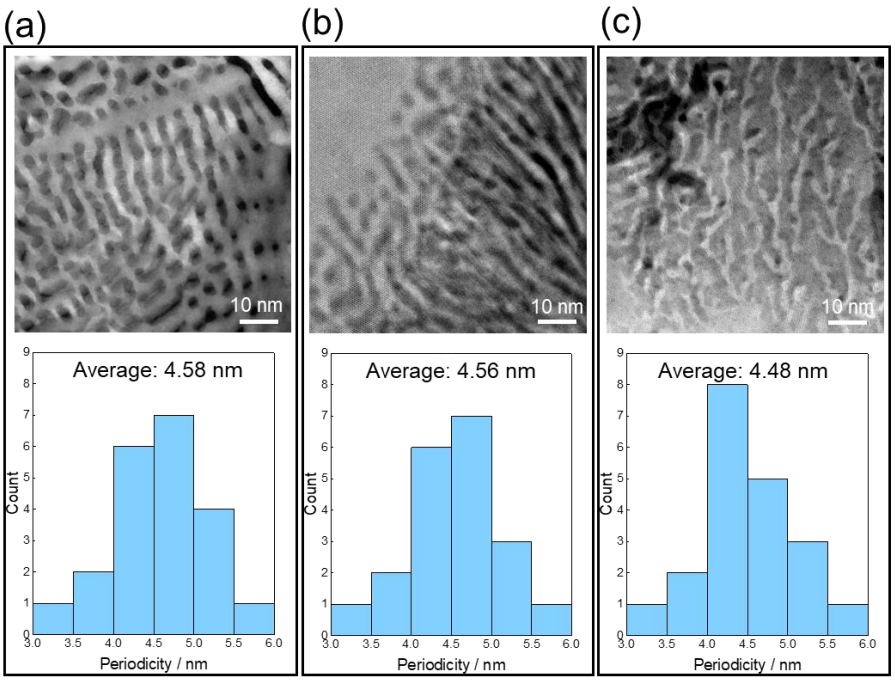

Figure 3.5. HAADF-STEM images and corresponding statistical data of stripes periodicity for bulky powder Pt/CeO_2 alloy annealed for (a) 12 h, (b) for 30 min, and (c) of firstly-FIB-thinned alloy annealed for 10 min.

specimen containing the reaction interface between the Pt_5Ce precursor and phase-separated Pt/CeO_2 nanocomposites. By analyzing the reaction interface structure, I can understand the early stage of the phase-separation behavior. Figure 3.6a displays HAADF–STEM image of the powder precursor heated for 30 minutes, projected along the [0001]Pt_5Ce direction. The reaction interface between the upper Pt_5Ce alloy and lower Pt/CeO_2 nanocomposites is marked by the black dashed line. The corresponding FFT images of two regions enclosed in the yellow-edged squares are shown on the right side of Figure 3.6a. These images clarify the different crystal structures of the alloy and nanocomposite. In the Pt_5Ce precursor, a periodical compositional contrast is visible within 10–20 nm from the interface. All spots in the FFT image were attributable to the Pt_5Ce structure, confirming the absence of precipitates; that is, the contrast was caused by atomic segregation. Meanwhile, the nanocomposites presented stripy patterns with alternating dark CeO_2 and bright Pt. The periodicity of the stripes was 4.6 nm, identical to that in the completely phase-separated nanocomposites. The statistical data are displayed in Figure 3.5b. It appears that the periodicity of the separated phase is independent of the annealing duration. Focusing on the near-interface region, one observes that CeO_2 stripes in the composites were connected with the dark-contrast phase in the precursor alloy. Moreover, the stripes were almost perpendicular to the reaction interface, indicating that the nanocomposites growth pointed toward the reaction interface (white arrows in the Fig. 3.6a). The Pt and CeO_2 structures viewed from the [-112] direction were identified by indexing the FFT patterns of the nanocomposites. Evidently, the Pt and CeO_2 grains shared a fully epitaxial relationship, unlike that of the completely oxidized sample [(111)Pt//(111)CeO_2 60°]. The orientation relationship between the Pt_5Ce alloy and self-assembled nanocomposites was derived as (1-100)Pt_5Ce//(220)Pt/CeO_2, [0001]Pt_5Ce//[-112]Pt/CeO_2. This result is the first observed orientation

relationship between hexagonal closest packed (hcp) and face-centered cubic (fcc) structures during a phase transformation. Another pronounced feature is the growth direction of the nanocomposites, which was parallel to the [110] direction. The fast growth rate of the (220) plane in [110] direction caused the preferential orientation of the Pt and CeO_2 phases in the composites, consistent with the XRD result (see Figure 3.2). In the XRD pattern, the relative intensity of the (220)Pt plane was much stronger than the referenced XRD powder data [JCPDS No. 04-0802].

To clarify the reaction interface structure between the Pt_5Ce alloy and Pt/CeO_2 nanocomposites, the HAADF–STEM image was magnified at the reaction interface. The image is displayed in Figure 3.6b. A hexagonal arrangement of atoms was projected along the [0001] zone axis in the Pt_5Ce structure. The reaction interface was uneven and facilitated phase separation in certain stages. The arrows indicate the terraces lying exactly on the (220) plane of the nanocomposite. Based on the above-described orientation relationship between the alloy and the precipitates, the atomistic structures of the phases were derived and are displayed in the right panel of Figure 3.6b. As shown in the structural model, the plane spacing of (11-20) in the alloy was approximately twice the plane spacings of (111) in the Pt precipitates. The lattice misfit of the (111) planes of fully epitaxial Pt and CeO_2 was calculated as 36 % against Pt crystal, similar to that of the completely oxidized sample.

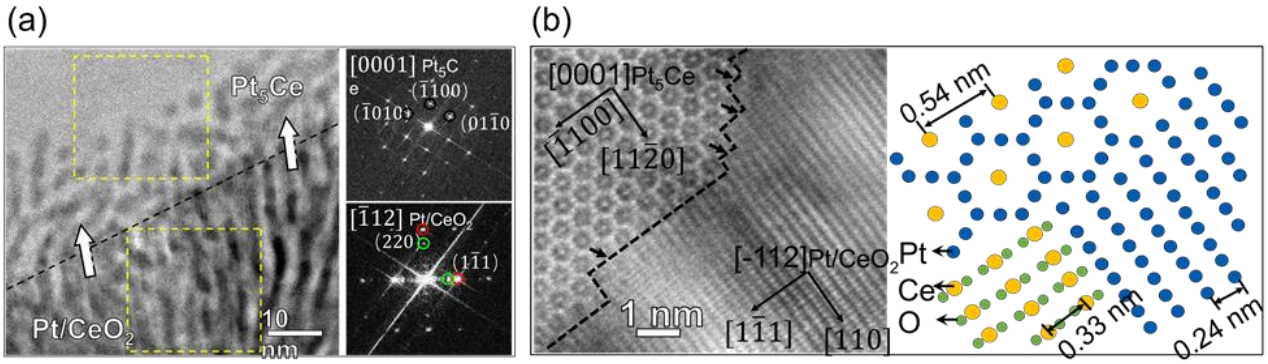

Figure 3.6. (a) HAADF–STEM image of the Pt/CeO_2 bulk sample annealed at 400°C for 30 min showing the interface area between the Pt_5Ce alloy and Pt/CeO_2 composites. The two FFT images were calculated in the areas within the yellow frames. In front of the dashed line, the contrast was caused by the atomic segregation. (b) Higher-magnification HAADF–STEM image at the reaction interface, showing the orientation relationship between the Pt_5Ce and Pt/CeO_2 composites. Right panel shows the corresponding structure model.

When alloys containing noble metals are oxidized, the noble metal phase separates from the oxide of the less noble metal. This phase separation is driven by the large discrepancy in the oxygen affinities of the noble and non-noble constituents [29]. Unlike nanoscale alloy particles [11], which form metal core-oxide shell structures when oxidized, the microcrystalline Pt–Ce alloy in the present study formed a spatially periodic striped pattern similar to a Turing pattern. Such periodic structures have been found in the oxidized alloys based on silver [30], nickel [31], and other metals undergoing internal oxidation. In this scenario, one alloy

component is selectively oxidized but cannot reach the surface quickly enough to form an oxide layer [32]. Alloy diffusion is thought to be negligibly slower than the inward oxygen movement, so the oxidation process is diffusion controlled [33]. The oxide in internal oxidation reactions can be spherical, facetted crystalline, dendritic, or some other shape [34]. In the striped structure observed here, the CeO_2 precipitates were constrained in their growth direction by the cerium and oxygen supplies. Consequently, the distance of oxygen diffusion to the immobile unreacted cerium was minimal, and the separated phase grew (on average) in the direction normal to the reaction interface. As oxygen must be transported through the CeO_2 phase to reach the reaction interface and Pt and Ce have different oxygen affinities, it was inferred that oxygen dissolution into the alloy contributed to atomic segregation in front of the reaction interface. CeO_2 and Pt phases were then epitaxially formed by oxidation of the Ce-rich alloy and transformation of the Pt-rich alloy, respectively. Moreover, the Pt-CeO_2 interface facilitated the oxygen diffusion from the surface to the inner Pt_5Ce alloy [44], thereby accelerating the oxidation process. The diffusion path of each element in the alloy and oxide is schematized in Figure 3.7. Owing to the low misfit between the (111) plane of Pt and the (11-20) plane in Pt_5Ce alloy, the phase transformation with the described orientation relationship, namely, (1-100)Pt_5Ce//(220)Pt/CeO_2, [0001]Pt_5Ce//[-112]Pt/CeO_2, beneficially minimizes the lattice strain. In contrast, the epitaxy (111) planes of Pt and CeO_2 are largely mismatched and cannot be solely compensated by inducing misfit dislocations. As the remaining lattice strain relaxes, the fully epitaxial relationship of Pt and CeO_2 at the early phase-separation stage should change to an epitaxial type of (111)Pt /(111)CeO_2 60° in the final stage.

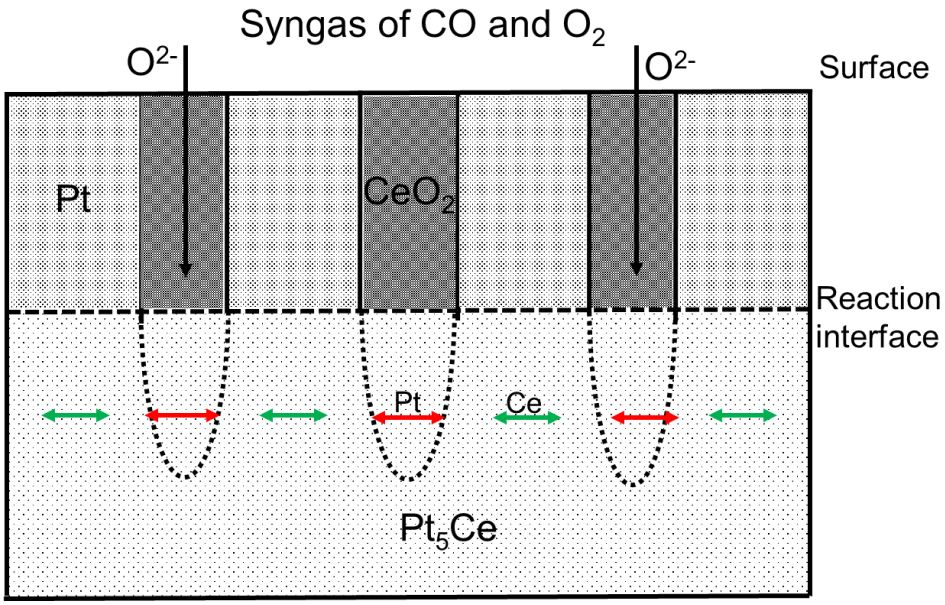

Figure 3.7. Schematic cross section of the diffusion paths in the Pt_5Ce alloy during phase separation. The vertical black arrows indicate the diffusion channel of oxygen from the surface. The diffusion paths of Pt and Ce atoms in front of the phase separation area were marked by red and green arrows, respectively.

3.3.3 Ex-situ experiment for tracking the phase-separation behavior

Although characterizing the samples prepared at different annealing times revealed the phase-separation behavior induced by oxidation, observing the whole process in a single sample would provide more conclusive results. For this purpose, I studied the phase-separation stages in an ex-situ experiment of the firstly-FIB-thinned alloy specimen. The ex-situ specimen was annealed for 10 min while the other synthesis conditions were those of the bulky powder sample.

Panels (a) and (b) of Figure 3.8 show the HAADF–STEM images and corresponding selected area electron diffraction (SEAD) patterns of the Pt_5Ce alloy precursor and the as-annealed alloy of the firstly-FIB-thinned specimen, respectively. The observed Pt_5Ce alloy precursor with about 300 x 300 nm^2 area presented a single hcp phase along the [0001] zone axis (Figure 3.8a) with no evidence of precipitates. After heating the initial Pt_5Ce alloy specimen ex situ to 400°C for 10 min, two interconnected phases with stripy patterns were continuously formed from the edge of the specimen (white and gray phases in the STEM image of Figure 3.8b). In a statistical analysis of the phase-separated region, the periodicity of the two-phase stripes was determined as 4.6 nm (see Figure 3.5c). The black arrows in Figure 3.8b indicate the growth direction of the striped structure. The stripes proceeded perpendicular to the alloy interface (dashed line in the figure). The SEAD pattern showed an additional two pairs of arc-shaped reflections. Based on the calculated diffraction distances, these reflections were indexed to diffractions of the (111) and (220) planes of the Pt and CeO_2 phases. The

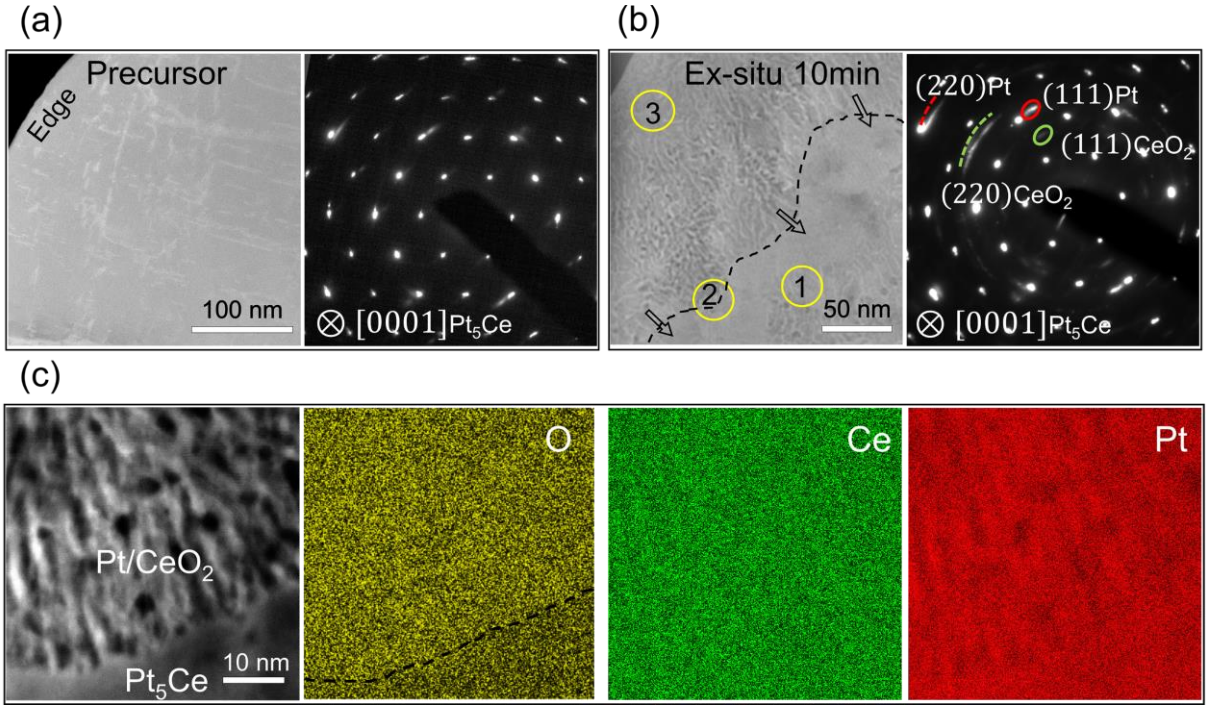

Figure 3.8. Characterization of nano-phase separation in Pt_5Ce alloy. HAADF–STEM images and corresponding SAED patterns along the [0001] Pt_5Ce zone axis of (a) Pt_5Ce alloy precursor and (b) the firstly-FIB-thinned specimen ex-situ annealed at 400°C for 10 min. (c) HAADF–STEM image of the interface area containing the alloy precursor and separated phases, and corresponding elemental maps of O, Ce and Pt.

positions of the diffraction spots suggest an almost-epitaxial relationship of the (111)Pt and (111)CeO_2 planes, but with a slight swing in the same direction. Figure 3.8c shows the elemental maps of the interface-contained regions. The concentrations of O atoms differed on both sides of the interface, suggesting an oxidation- induced phase separation. Within the phase-separated regions, the white and gray stripes were apparently rich in Pt and Ce, respectively, confirming that the phase-separated region is composed of Pt/CeO_2 composites.

As explained in subsection 3.3.2, oxidation of Pt_5Ce alloy produces not only a Ce metal oxide, but also an fcc structure of Pt metal, which emerges through a matrix phase transformation. Moreover, the (111) planes of Pt and CeO_2 shared a parallel relationship. A striped pattern with the same periodicity was observed both in the bulky powder sample and the firstly-FIB-thinned sample, suggesting that the metal atoms diffused laterally regardless of the sample geometry. In the present case, the absence of the oxide layer at the surface further verified the slow diffusion of alloy components and the resulting predominant oxidant diffusion. Because oxidation started at the surface and progressed inward, the front and back positions (marked as positions 1 and 3 in Figure 3.8b, respectively) at the interface should indicate the initial and late phase-separation stages, respectively. Therefore, to extract more information on the oxidation-induced phase-separation behavior, three regions at different separation stages (enclosed within the yellow-edged circles in Figure 3.8b) were further analyzed by HRTEM and HAADF–STEM.

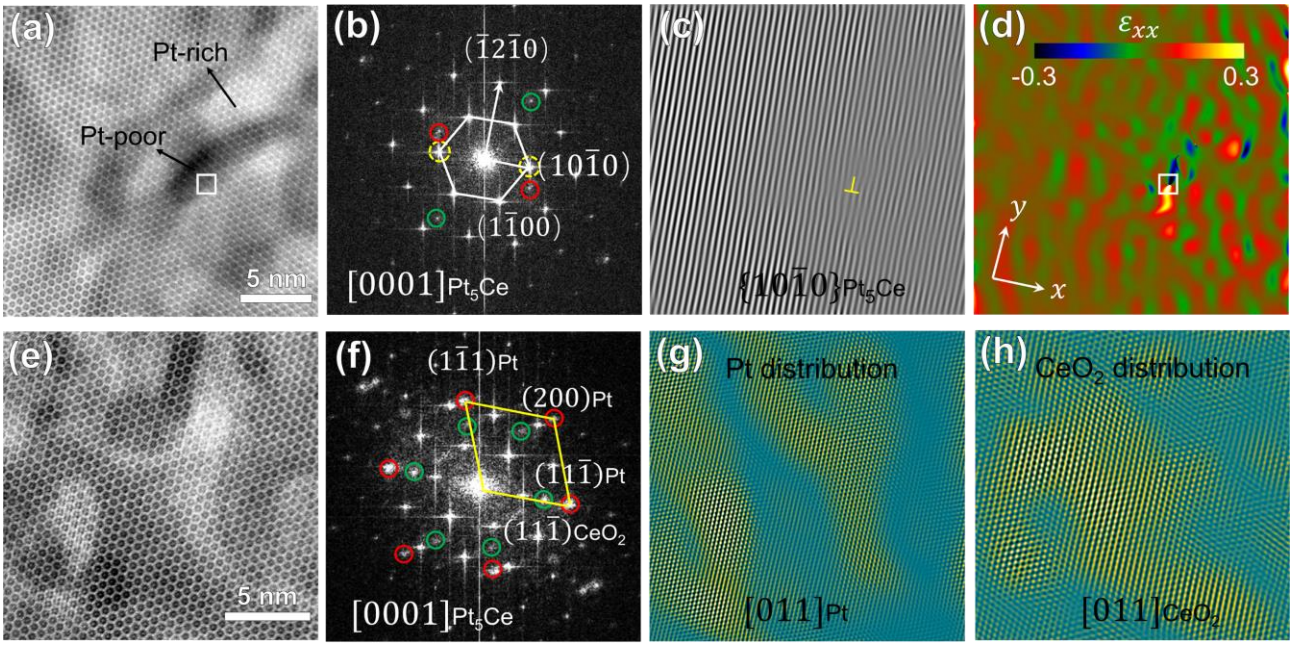

Figure 3.9. (a) HAADF–STEM image of the initial separation stage (region 1 in Figure 1[b]) showing atomic segregation along the [0001]Pt_5Ce axis, (b)FFT pattern of (a), (c) IFFT image of Pt_5Ce (10-10) extracted from (b) to highlight the lattice fringe image along {10-10}Pt_5Ce (yellow symbol indicates the edge dislocation), and (d) strain component ε_{xx} of (a) obtained in a GPA analysis: x ∥ [10-10]Pt_5Ce, y ∥ [1-210]Pt_5Ce. (e) HAADF–STEM image of another site in region 1 of panel 3.8(b), showing the Pt and CeO_2 crystals with a [0001]Pt_5Ce zone axis, and (f) corresponding FFT pattern (red- and green-edged circles enclose diffraction spots from the Pt and CeO_2 phases, respectively). (g) and (h) IFFT images displaying the Pt and CeO_2 distributions, obtained by extracting the six red circles and six green circles in (f), respectively.

Figure 3.9a is a HAADF–STEM image of the initial separation stage corresponding to Region 1 in Figure 3.8b. The Pt-rich and Pt-poor nanoclusters are distinguished by their Z-contrast intensities. Figure 3.9b displays the corresponding FFT patterns along the [0001] orientation of the Pt_5Ce alloy precursor. Besides the reflections of Pt_5Ce, two pairs of weak reflections suggested an ordering of the nanoclusters. The inverse-FFT (IFFT) patterns of both pairs of reflections confirmed their emergence in different regions (see Figure 3.10). The spots enclosed by the green- and red-edged circles in Figure 3.9b were identified as CeO_2 and Pt-rich alloys, respectively. After extracting the {10-10}Pt_5Ce reflections (enclosed by the yellow-edged circles in Figure 3.9b), an edge dislocation was identified in the {10-10} plane (Figure 3.9c). This dislocation resulted from lattice distortion and strain relaxation after component segregation, which would contract or expand the lattice. To visualize the degree of lattice distortion, the local lattice strain was mapped using GPA. Figure 3.9d shows the strain component ε_{xx} of Figure 3.9a. A small lattice strain appeared around the segregation areas. The obvious strain field around the edge dislocation implies a compressive strain in the Pt-poor nanoclusters and a tensile strain in the Pt-rich nanoclusters, which resulted from the larger atomic radius of the Ce atoms than the Pt atoms. The compositional contrast in Figure 3.9a at the same dislocation position (white-edged square) affirms this conclusion.

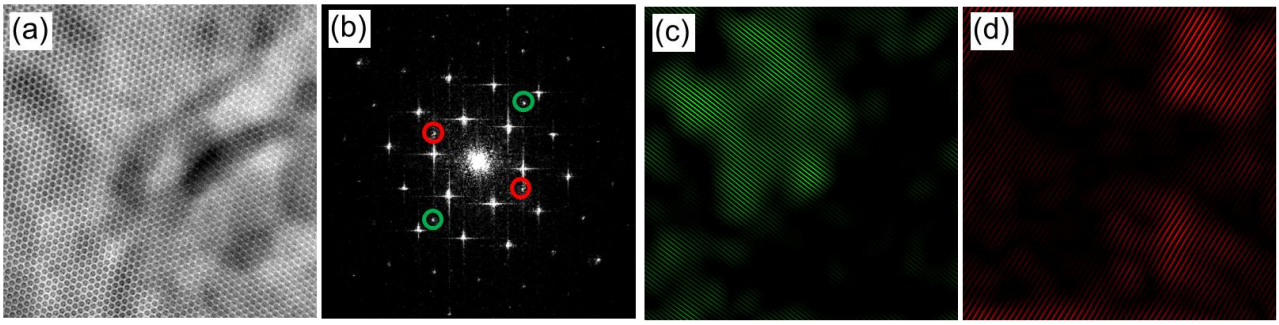

Figure 3.10. (a) HAADF-STEM image of Pt_5Ce alloy annealing for 400°C showing the segregation of Pt and Ce atoms. (b) Corresponding FFT image of (a). The IFFT patterns from green and red circles are shown in (c) and (d), respectively.

Figure 3.9e shows another HAADF–STEM image in Region 1 along the [0001]Pt_5Ce direction. The corresponding FFT pattern in Figure 3.8f demonstrates that Pt and CeO_2 crystals were formed in the Pt_5Ce alloy. In addition to the FFT spots of Pt_5Ce alloy, spots attributed to [011]Pt and [011]CeO_2 (enclosed within the red- and green-edged circles, respectively) were identified by calculating the interplanar spacings. Panels (g) and (h) of Figure 3.9 show the IFFT patterns determined from the Pt and CeO_2 spots in Figure 3.9f, illustrating the distributions of the Pt and CeO_2 phases, respectively. The patterns re-confirm that the bright and dark contrasts in HAADF–STEM in Figure 3.9e are related to the Pt and CeO_2 phases, respectively. As the oxidation process occurred after atomic segregation, it was inferred to be governed by inward diffusion of the dissolved oxygen. Moreover, stress in the atomic segregation area promoted the oxidation [35] and phase separation processes [36], accelerating the penetration into the phase-separation zone.

HRTEM images of the middle and late separation stages (Regions 2 and 3 in Figure 3.8(b)) are displayed in Figure 3.11. Figure 3.11a shows the interface area of Region 2, which contains both the Pt_5Ce alloy and the phase-separated Pt/CeO_2 composites in the $[0001]Pt_5Ce$ orientation. The growth direction of the Pt and CeO_2 stripes (indicated by the white arrows in Figure 3.11a) was explained earlier. In the corresponding FFT pattern (Figure 3.11b), the red and green-edged circles mark the Pt and CeO_2 spots, respectively. Clearly, the epitaxial relationship between Pt and CeO_2 was established in this separation stage. Moreover, the growth direction of the Pt/CeO_2 composites is consistent with the $[111]Pt/CeO_2$ direction. Considering the phase transformation of Pt_5Ce alloy with an hcp structure to Pt with an fcc structure, the orientation relationship between the two phases was obtained as $\{10\text{-}10\}Pt_5Ce//(1\text{-}11)Pt/CeO_2$, $[0001]Pt_5Ce//[011]Pt/CeO_2$, which differs from the typically reported phase relationship in Pt_5Ce surface alloy transformation, i.e., $\{0001\}Pt_5Ce//\{111\}$Pt.28 Figure 3.11c is an enlarged atomic STEM image of the region enclosed by the square in Figure 5(a). This image confirms the above-derived orientation relationships between the Pt_5Ce alloy and the Pt/CeO_2 composites. The atomic structure model of phase separation in this system is shown in Figure 3.11d. In the direction nearly normal to the growth direction of the precipitates, the lattice spacing of the (10-10) plane of the Pt_5Ce alloy was twice that of the (111) plane of Pt crystals. This perfect alignment favors phase separation. In the (111) planes, the ratio of the Pt to CeO_2 lattice vectors was 1.38 with an approximate misfit of 38%. Judging from the large misfit at the coherent interface, the epitaxial relationship between Pt and CeO_2 was probably unstable to further reactive heating.

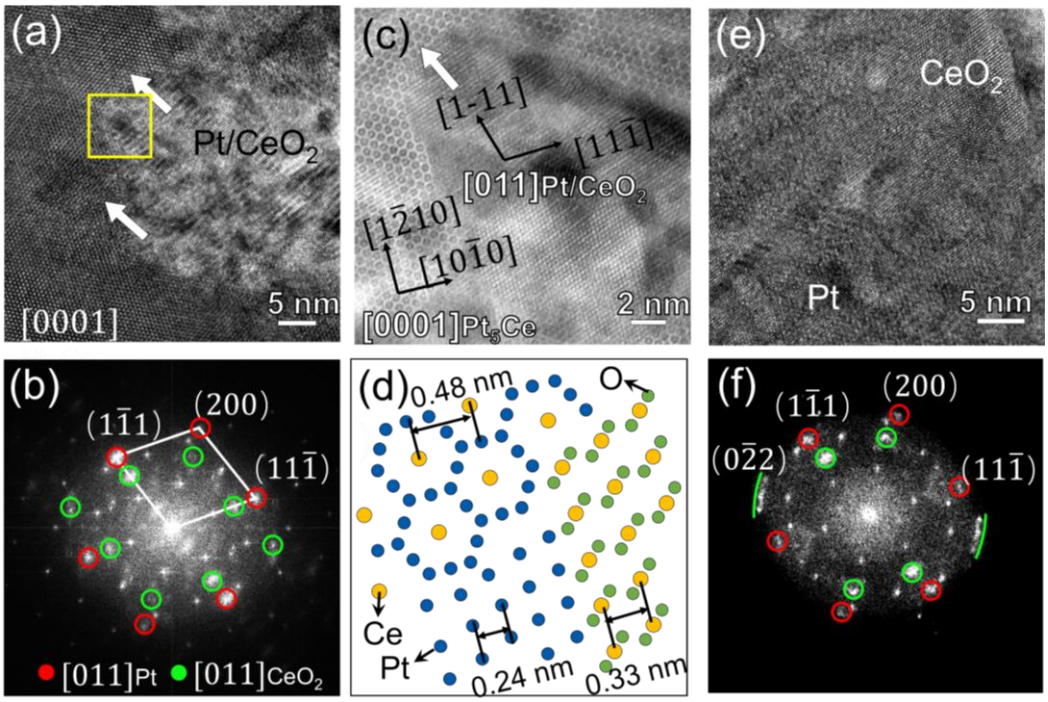

Figure 3.11. (a) HRTEM image with $[0001]Pt_5Ce$ zone axis and (b) corresponding FFT of the middle separation stage (region 2 in Fig. 3.8b) showing the interface area between Pt_5Ce alloy and Pt/CeO_2 composites. (c) HAADF–STEM image of the boxed area in (a), and (d) atomic structure model of each phase in the interface area. (e) HRTEM image along the $[0001]Pt_5Ce$ zone axis and corresponding FFT of the late separation stage (region 3).

In the late separation stage (close to the edge of the thinned specimen, indexed as region 3 in Figure .3.8b), the situation was somewhat different. The HRTEM image of this phase-separated area is shown in Figure 3.11e. The composite structure of Pt and CeO_2 is clearly visible. The corresponding FFT image is displayed in Figure 3.11f. Comparing the reflections in panels (b) and (f) of Figure 3.11, I find that some reflection spots developed arc shapes in the late separation stage and the CeO_2 crystals were shifted from the correct zone axis. The reflections from CeO_2(11-1) disappeared while those from (220) were stronger than those in the interface area. It was deduced that during the growth process, the CeO_2 crystals rotated through a small angle while the epitaxial relationship was retained on the (111) planes. Such rotational behavior is often found in largely mismatched metal–oxide heterointerface systems because it lowers the interface energy [37, 38]. Given the large misfit between the Pt and CeO_2 phases (38%), the crystal rotation was likely enforced by strain relaxation.

Based on the above results, the phase-separation behavior in the present samples was identical to that found in bulky powder samples and proceeded in three steps. In the first step, atomic segregation of Pt and Ce in the Pt_5Ce alloy because of their different oxygen affinity. As the oxygen continues to diffuse into the Ce-rich regions, the self-assembled Pt and CeO_2 stripy phases with a fully epitaxial relationship then become separated from the alloy during the early stage. Owing to the large misfit between the lattice constants of Pt and CeO_2 phases, the crystals with an initially commensurate interface tend to rotate along [111], and finally maintain the (111)Pt//(111)CeO_2 relation. The phase-separation behavior is schematized in Fig. 3.12. It should be noted that although stripy patterns of Pt and CeO_2 are kinetically favorable to minimize the oxygen diffusion distance to the immobile unreacted cerium, the stripes growth direction and the orientation relationship between the stripes and the precursor alloy should be energetically favorable because of the large internal surface area. Therefore, the preferred growth direction and orientation of stripes vary with the orientation of the precursor alloy and annealing temperature. Moreover, different growth directions ([110] and [111], respectively) and orientation relationships (see stereographic projections in Figure 3.13) in the bulky powder and firstly-FIB-thinned specimens indicate the influence of the oxygen partial pressure for the phase separation behavior. This is because oxygen can more easily reach the reaction interface on the surfaces of FIB-thinned samples than the inside bulky powder samples. The stripes were assumed to be oriented perpendicular to the growing interface between the alloy and Pt/CeO_2 precipitants; accordingly, the growth direction is closely related to the orientation relationship between Pt_5Ce and Pt/CeO_2.

3.4 Conclusion

Self-assembled epitaxial interfaces of Pt/CeO_2 nanocomposites were successfully formed by simple oxidation of Pt_5Ce alloy. Nanoscale stripy patterns of alternating Pt and CeO_2 phases were observed and an epitaxial interface between Pt and CeO_2 was identified on their (111) planes. Furthermore, the oxidation-induced phase-separation process in a partially oxidized sample was observed by atomic-scale TEM, and a verification experiment was performed by ex-situ annealing of a firstly-FIB-thinned TEM specimen. The oxygen partial pressure on the surface of the FIB-thinned specimen differed from that inside bulky powder

samples, affecting the growth direction of the stripes and the orientation relationship between the Pt_5Ce alloy and Pt/CeO_2 composites. These findings suggest that Pt/CeO_2 catalysts with an epitaxial interface can be economically prepared for fundamental research and practical applications. Furthermore, our results are expected to assist the structural design of metal–oxide nanocomposites. Consequently, Pt/CeO_2 nanocomposites with different structures can be prepared by changing the syngas ratio and annealing temperature, which are used for the following chapters to study the strucutre-propery relationship.

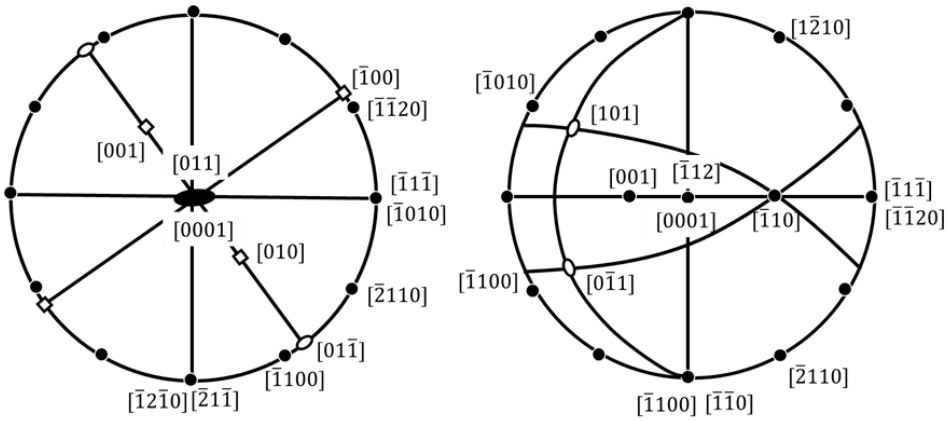

Figure 3.12. Schematic showing the formation of Pt/CeO_2 heterostructures through oxidation of Pt_5Ce alloy. The (111)Pt plane is parallel to (111)CeO_2 in the Pt/CeO_2 composites.

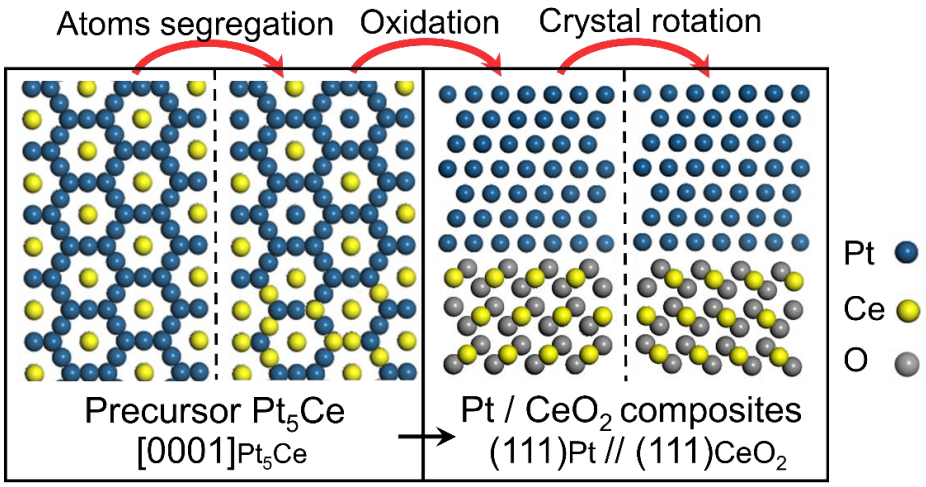

Figure 3.13. Stereographic projections showing the different orientation relationships between hcp-structured Pt_5Ce alloy and the fcc Pt phase in (a) the firstly-FIB-thinned specimen and (b) the bulky

References

[1] Bernal, S.; Calvino, J. J.; Cauqui, M. A.; Gatica, J. M.; Larese, C.; Pérez Omil, J. A.; Pintado, J. M. Some Recent Results on Metal/Support Interaction Effects in NM/CeO2 (NM: Noble Metal) Catalysts. Catal. Today 1999, 50 (2), 175–206.

[2] Li, G.; Tang, Z. Noble Metal Nanoparticle@metal Oxide Core/Yolk-Shell Nanostructures as Catalysts: Recent Progress and Perspective. Nanoscale 2014, 6 (8), 3995–4011.

[3] Liu, X.; Iocozzia, J.; Wang, Y.; Cui, X.; Chen, Y.; Zhao, S.; Li, Z.; Lin, Z. Noble Metal-Metal Oxide Nanohybrids with Tailored Nanostructures for Efficient Solar Energy Conversion, Photocatalysis and Environmental Remediation. Energy Environ. Sci. 2017, 10 (2), 402–434.

[4] Takahashi, M.; Mori, T.; Ye, F.; Vinu, A.; Kobayashi, H.; Drennan, J. Design of High-Quality Pt-CeO2 Composite Anodes Supported by Carbon Black for Direct Methanol Fuel Cell Application. J. Am. Ceram. Soc. 2007, 90 (4), 1291–1294.

[5] Lang, X.; Hirata, A.; Fujita, T.; Chen, M. Nanoporous Metal/Oxide Hybrid Electrodes for Electrochemical Supercapacitors. Nat. Nanotechnol. 2011, 6 (4), 232–236.

[6] Boudart, M. Catalysis by supported metals. Advances in catalysis. Academic Press, 1969, 20, 153-166.

[7] Damato, T. C.; de Oliveira, C. C. S.; Ando, R. A.; et al. A facile approach to TiO_2 colloidal spheres decorated with Au nanoparticles displaying well-defined sizes and uniform dispersion. Langmuir, 2013, 29(5), 1642-1649.

[8] Yan, W.; Mahurin, S. M.; Pan, Z.; Overbury, S. H.; Dai, S. Ultrastable Au Nanocatalyst Supported on Surface-Modified TiO_2 Nanocrystals. J. Am. Chem. Soc. 2005, 127 (30), 10480–10481.

[9] Zhou, S.; Yin, H.; Schwartz, V.; Wu, Z.; Mullins, D.; Eichhorn, B.; Overbury, S. H.; Dai, S. In Situ Phase Separation of NiAu Alloy Nanoparticles for Preparing Highly Active Au/NiO CO Oxidation Catalysts. ChemPhysChem 2008, 9 (17), 2475–2479.

[10] Endo, N.; Kameoka, S.; Tsai, A. P.; Hirata, T.; Nishimura, C. Preparation of Nano-Composited Catalyst from the Bulk Intermetallic Compound $AuZr_3$ with Hydrogen Absorption. Catal. Letters 2010, 139 (1–2), 67–71.

[11] Sutter, E. A.; Tong, X.; Jungjohann, K.; Sutter, P. W. Oxidation of Nanoscale Au-In Alloy Particles as a Possible Route toward Stable Au-Based Catalysts. Proc. Natl. Acad. Sci. U. S. A. 2013, 110 (26), 10519–10524.

[12] Sutter, P.; Tenney, S. A.; Ivars-Barcelo, F.; Wu, L.; Zhu, Y.; Sutter, E. Alloy Oxidation as a Route to Chemically Active Nanocomposites of Gold Atoms in a Reducible Oxide Matrix. Nanoscale Horizons 2016, 1 (3), 212–219.

[13] Tanabe, T.; Imai, T.; Tokunaga, T.; Arai, S.; Yamamoto, Y.; Ueda, S.; Ramesh, G. V.; Nagao, S.; Hirata, H.; Matsumoto, S. I.; Fujita, T.; Abe, H. Nanophase-Separated Ni_3Nb as an Automobile Exhaust Catalyst. Chem. Sci. 2017, 8 (5), 3374–3378.

[14] Imai, T.; Ueda, S.; Nagao, S.; Hirata, H.; Deepthi, K. R.; Abe, H. N_2O-Emission-Free Exhaust Remediation by Rh-NbO_x Nanocomposites Developed from Rh_3Nb Alloy Precursor. RSC Adv. 2017, 7 (16), 9628–9631.

[15] Shoji, S.; Peng, X.; Imai, T.; Murphin Kumar, P. S.; Higuchi, K.; Yamamoto, Y.; Tokunaga, T.; Arai, S.; Ueda, S.; Hashimoto, A.; Tsubaki, N.; Miyauchi, M.; Fujita, T.; Abe, H. Topologically Immobilized

Catalysis Centre for Long-Term Stable Carbon Dioxide Reforming of Methane. Chem. Sci. 2019, 10 (13), 3701–3705.

[16] Spiel, C.; Blaha, P.; Suchorski, Y. et al. CeO_2/Pt (111) interface studied using first-principles density functional theory calculations. Physical Review B. 2011, 84(4), 045412.

[17] Aranifard, S.; Ammal, S. C.; Heyden, A. On the Importance of the Associative Carboxyl Mechanism for the Water-Gas Shift Reaction at Pt/CeO_2 Interface Sites. J. Phys. Chem. C 2014, 118 (12), 6314–6323.

[18] Kalakkad, D.; Datye, A. K.; Robota, H. Interaction of Platinum and Ceria Probed by Transmission Electron Microscopy and Catalytic Reactivity. Appl. Catal. B, Environ. 1992, 1 (3), 191–219.

[19] Alayoglu, S.; An, K.; Melaet, G.; Chen, S.; Bernardi, F.; Wang, L. W.; Lindeman, A. E.; Musselwhite, N.; Guo, J.; Liu, Z.; Marcus, M. A.; Somorjai, G. A. Pt-Mediated Reversible Reduction and Expansion of CeO_2 in Pt Nanoparticle/Mesoporous CeO_2 Catalyst: In Situ X-Ray Spectroscopy and Diffraction Studies under Redox (H_2 and O_2) Atmospheres. J. Phys. Chem. C 2013, 117 (50), 26608–26616.

[20] Wen, Y.; Hashimoto, A.; Najib, A. S. B. M.; Hirata, A.; Abe, H. Topological Trends in Ionic Transport through Metal-Oxide Composites. Appl. Phys. Lett. 2021, 118, 054102.

[21] Stott, F. H.; Wood, G. C. Internal oxidation. Materials Science and Technology, 1988, 4(12), 1072-1078.

[22] Dave Mitchell's DigitalMicrograph™ Scripting Website. http://www.dmscripting.com/hrtem_filter.html.

[23] Useful Plugins and Scripts for DigitalMicrograph. https://www.physik.hu-berlin.de/en/sem/software/software_frwrtools.

[24] Barthel, J. Dr. Probe: A Software for High-Resolution STEM Image Simulation. Ultramicroscopy 2018, 193 (May), 1–11.

[25] Spiel, C.; Blaha, P.; Suchorski, Y.; Schwarz, K.; Rupprechter, G. CeO_2/Pt(111) Interface Studied Using First-Principles Density Functional Theory Calculations. Phys. Rev. B - Condens. Matter Mater. Phys. 2011, 84 (4), 1–11.

[26] Bernal, S.; Botana, F. J.; Calvino, J. J.; Cifredo, G. A.; Pe´rez-Omil, J. A.; Pintado, J. M. HREM Study of the Behaviour of a Rh/CeO_2 Catalyst under High Temperature Reducing and Oxidizing Conditions. Catal. Today 1995, 23 (3), 219–250.

[27] Ji, Q.; Kan, M.; Zhang, Y.; Guo, Y.; Ma, D.; Shi, J.; Sun, Q.; Chen, Q.; Zhang, Y.; Liu, Z. Unravelling Orientation Distribution and Merging Behavior of Monolayer MoS_2 Domains on Sapphire. Nano Lett. 2015, 15 (1), 198–205.

[28] Marzari, N.; Sanchez, O. L.; Kung, Y.; Krasnozhon, D.; Chen, M.; Bertolazzi, S.; Gillet, P.; Fontcuberta, A.; Radenovic, A.; Kis, A. Large-Area Epitaxial Monolayer MoS_2. ACS Nano 2015, 4 (4), 4611–4620.

[29] Wood, G. C.; Stott, F. H. Oxidation of Alloys. Mater. Sci. Technol. 1986, 3 (7), 519–530.

[30] Nguyen, T. D.; Zhang, J.; Young, D. J. Effect of Si on Corrosion of Fe-Cr and Fe-Cr-Ni Alloys in Wet CO_2 Gas. Corros. Sci. Technol. 2015, 14 (3), 127–131.

[31] Do, D. T. M.; Nanko, M. Internal Oxidation of Ni(Al) Solid Solution Zone Prepared by Pack Cementation of Pure Ni. Mater. Sci. Forum 2011, 696 (September), 384–388.

[32] Young, D. J. Diffusion in Internal Oxidation Reactions. Defect Diffus. Forum 2012, 323–325 (April 2012), 283–288.

[33] Stott, F. H.; Wood, G. C. Internal Oxidation. Mater. Sci. Technol. (United Kingdom) 1988, 4 (12), 1072–1078.

[34] Young, D. J. High Temperature Oxidation and Corrosion of Metals: Second Edition; 2008.

[35] Evans, H. E. Stress Effects in High Temperature Oxidation of Metals. Int. Mater. Rev. 1995, 40 (1), 1–40.

[36] Hong, D. H.; Lee, T. W.; Lim, S. H.; Kim, W. Y.; Hwang, S. K. Stress-Induced Hexagonal Close-Packed to Face-Centered Cubic Phase Transformation in Commercial-Purity Titanium under Cryogenic Plane-Strain Compression. Scr. Mater. 2013, 69 (5), 405–408.

[37] Matsunaga, K.; Sasaki, T.; Shibata, N.; Mizoguchi, T.; Yamamoto, T.; Ikuhara, Y. Bonding Nature of Metal/Oxide Incoherent Interfaces by First-Principles Calculations. Phys. Rev. B - Condens. Matter Mater. Phys. 2006, 74 (12), 2–9.

[38] Ernst, F. Metal-Oxide Interfaces. Mater. Sci. Eng. R 1995, 14 (3), 97–156.

Chapter 4 2D structure -ionic conductivity quantitative relationship of Pt/CeO_2 nanocomposites

Although ionic conductors have been thoroughly investigated, topological features of these materials' nanotextures have been surprisingly overlooked. To understand the importance of topological features, such as phase connectivities, to the oxygen ion conduction, different structures of materials are necessary. Based on the previous chapter on the phase separation behavior in the Pt_5Ce alloy, here I report fabrication of different metal-oxide nanocomposite consisting of intertwined phases of platinum (Pt) metal and oxygen-ion conductive cerium oxide (CeO_2), i.e., Pt/CeO_2 by changing the syngas ratio during the annealing. Sectional TEM observations coupled with topological analysis demonstrated that Pt/CeO_2 composites having different nanostructures can be classified with a topological measure that corresponds to the phase connectivity of CeO_2, namely the Betti number β_0, and another that corresponds to holes of the Pt phase, namely the Betti number β_1. The samples' oxygen ionic conductivity Pt/CeO_2 was measured at elevated temperatures in air by alternating current (AC) impedance spectroscopy. It was found that the nanostructure changed from a striped appearance to a maze-like appearance as the value of β_1/β_0 decreased. Both the activation energy E and pre-exponential factor $ln\sigma_0$ for the oxygen ionic conductivity was found to be independent of β_1 and exhibited linear, negative correlations to β_0. The topological connectivity of the ion-conductive CeO_2 phase, which was quantified with the Betti number β_0, was suitable as a descriptor to correlate the image data of nanostructures with their ionic transport properties.

4.1 Introduction

Ionic transport is a critical function for systems such as proton conductive polymers [1], and often governs the entire performance of batteries and/or fuel cells [2,3]. Most attempts to improve the ionic transport properties of a given conductor have relied on ion-hopping control between neighboring ionic sites [4,5]. Especially for inorganic conductors such as ionic conductive oxides, several experiments have been conducted using partial substitution of an ionic site with other ions having a different valence, in other words doping. This creates intrinsic oxygen vacancies and reduces the activation energy of ion hopping [6–8]. However, despite improving ionic transport, doping can significantly destabilize the mother phase [9]. Indeed, one of the most popular oxygen-ion (O_2-) conductors, cerium oxide (CeO_2), exhibits pronounced O_2- conductivity at elevated temperatures when tetravalent Ce^{4+} sites are partially substituted with trivalent Gd^{3+}, yet the mother phase can be retained if the Gd^{3+} is less than 30 at. % [10–12]. Excessive doping also introduces an ordering of the oxygen vacancies, leading to a reduction of ionic transport [12].

Much attention has been paid to ion-hopping control, but the effects of connectivity due to ionic conductive pathways have been surprisingly unexplored except for some pioneering research on polymer and

nanowire electrolytes for lithium-ion batteries [13–15]. This is despite the fact that ionic conductive pathways are expected to play a pivotal role in charge transport. Visual characterizations, such as sectional TEM, have been used extensively to design material textures at the nano- and micrometer scales. Yet these characterizations have not achieved to directly facilitate the desired control of conductive pathways. This is because of a lack of quantitative methodology that can extract information on the phase connectivity from image data.

Homology analysis has been developed as an advanced form of topology that deals not with measurable features such as lengths and/or angles but mostly with the connectivity of given objects. In recent years it has been applied to materials science [16–18]. Betti numbers, denoted β_i, derived from homology computations, are used to estimate the topological complexities of percolated structures in terms of their connectivity properties [18]. More specifically, β_0 gives the number of connected components (0 dimensional holes), β_1 gives the number of tunnels (1 dimensional holes) and β_i counts the number of holes of dimension i. Research has already been published on the microstructure-electrical conductivity relationships of conductor-insulator composites using Betti numbers [19,20].

I examined the correlation between the nanostructures and transport properties of ionic conductors, with the aim of controlling conductive pathways. I report here on sectional TEM observations, coupled with homology analysis.

A metal-oxide nanocomposite consisting of intertwined fibrous phases of metal and oxide, denoted NM/MO_x, was chosen for TEM-homology analysis because its nanotexture could be tuned by adjusting the preparation conditions [21]. Four Pt/CeO_2 composites with apparently very different nanostructures were analyzed. Impedance spectroscopy measurement revealed ionic transport properties indicative of the ionic conductive CeO_2 phase: the samples displayed a positive, linear correlation to the Betti number β_0, a homological measure that corresponds with the connectivity of ionic conductive CeO_2. It was demonstrated that a topological method based on Betti numbers could also be applied to understand the nanostructure-ionic conductivity relationship in metal-oxide nanocomposites.

4.2 Experimental

The schematic of the experiment process is shown in Figure 4.1. It includes the sample preparation, structure characterization, homological analysis and ionic conductivity measurement. Figure 4.1a shows the preparation of the bulk Pt/CeO_2 nanocomposites by the annealing of the Pt_5Ce alloy and the measurement of ionic conductivity by the impedance spectroscopy. Figure 4.1b illustrates the homology analysis of TEM images by counting the number of black domains (marked by light colors), β_0, and white holes (marked by red), β_0. Then the relationship between ionic conductivity and homological descriptors can be declared quantitatively. The details for the experiments are explained in the following subsections.

4.2.1 Sample preparation

Pt/CeO_2 composites powders were synthesized from crashed Pt_5Ce alloy powders, which acted as the precursor, by heat treatment at 600 ℃ for 12 h in a gas mixture of CO (2 vol% CO + Ar) and O_2 (1 vol% O_2 + Ar) at 60 sccm as the reduction and oxidation sources [22]. The gas ratio of CO to O_2 was varied to produce different composite nanostructures. The bulk composites for ionic conductivity measurements were prepared by directly heating the bulk Pt_5Ce alloy at 600 ℃ for 4 days. Referenced CeO_2 powders were prepared by heating commercial CeO_x at 800 ℃ in an oxygen gas stream to fully oxidize the Ce valence to +4.

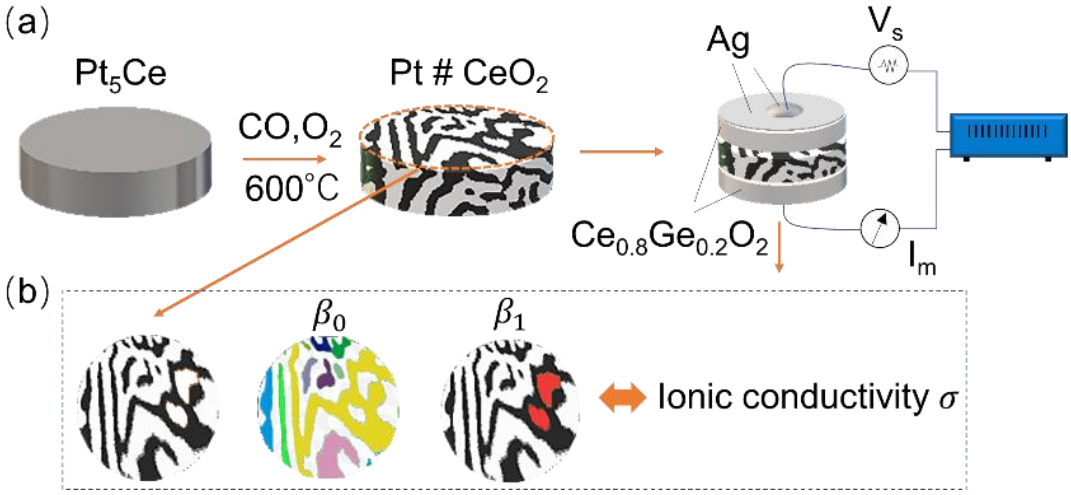

Figure 4. 0.1. Process for sample preparation and analysis. (a) Nanocomposites of Pt/CeO_2 were prepared from Pt_5Ce alloy by heat treatment in a reactive atmosphere at 600 ℃, followed by ionic conductivity measurements using AC impedance spectroscopy. (b) Nanostructures were identified by ADF-STEM imaging, then related to ionic conductivity by calculating topological invariants β_0 and β_1.

4.2.2 Structure characterization

XRD measurements were carried out on a Panalytical X'PERT PRO X-ray diffractometer by using the Kα radiation line of Cu. Hard X-ray photoemission spectroscopy (HAXPES) was performed using X-ray with a photon energy of 5.9493 keV) at the undulator beamline BL15XU of SPring-8, Japan. The HAXPES measurements were conducted at room temperature under UHV using a hemispherical electron energy analyzer (VG SCIENTA R4000). The total energy resolution was set to 220 meV. The binding energy was referenced to the Fermi edge of an Au thin film. A large thin area of the specimen was prepared for TEM observation by FIB milling, which provided an opportunity to observe the nanostructures of composites in different regions. First, a particle of ground composite ~20 μm across was glued to Cu grid. Then the particle was milled by Ga ions using a FIB system (JIB-4000, JEOL, Japan). A thin area with a thickness of ~80 nm was obtained for all composites. HRTEM studies were undertaken using a JEOL JEM-200ARMF microscope, with double Cs-correctors, operating at 200 kV. STEM images and energy-dispersive X-ray spectroscopy (EDX) elemental mapping were acquired with a JEM-2100F microscope (JEOL, Japan) equipped with a Schottky field emission

gun operated at 200 kV. Annular dark field (ADF)-STEM images of about 492×492 nm were acquired, then the background contrast eliminated using fast Fourier transform (FFT) in Gatan DigitalMicrograph software (see Fig. 4.2).

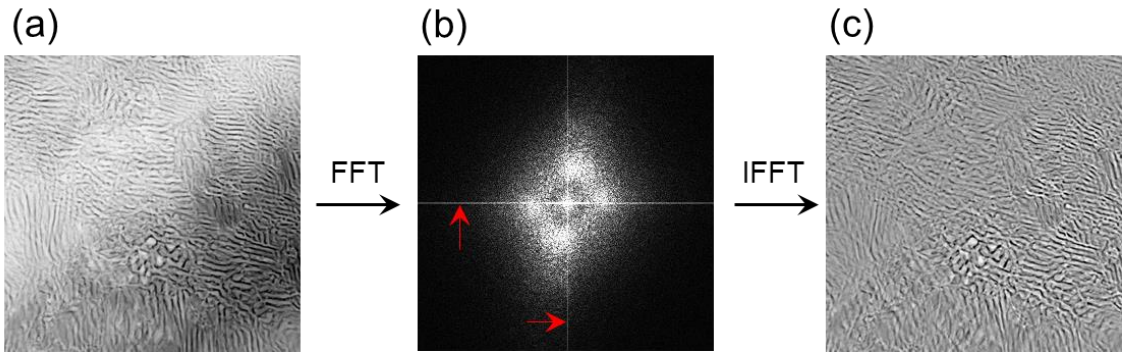

Figure 4.2. Background removal by fast Fourier transform (FFT). (a) Original STEM image with uneven background which was caused by non-uniform thickness because of FIB milling. (b) FFT patterns from original image. Two perpendicular lines indicated by arrows are the noise from the uneven background which needed to be filtered. (c) Background-removed image, which is the inverse fast Fourier transformed (IFFT) image of the filtered FFT patterns. IFFT restored the image with background contrast removed from the filted FFT image.

4.2.3 Homology analysis

CHomP software [23], which can compute topological properties for images and patterns, was used to compute the topological invariants. It requires binary images. The entire binarization process, including post-processing smoothing, was performed using OpenCV (an open-source computer vision library) in Python. First, all the ADF-STEM images were resized to 1024×1024 pixels by bilinear interpolation. Then an adaptive Gaussian thresholding algorithm was used to convert grayscale to binary images. The core of this algorithm is to set a threshold value for a pixel based on a certain small region (101 pixels in our case) around it, with the threshold value determined by a Gaussian-weighted sum of the neighboring values. There were blurred areas with low contrast, so a closing and opening process was applied to remove isolated small black and white noises, respectively, and a kernel size of 5×5 pixels was used (Fig. 4.3). After the optimized binary images were generated, Betti numbers were successfully calculated by CHomP based on homology theory to describe the geometric features of nanophase-separated composites.

4.2.4 Electrochemical measurements

To avoid electron transport in the composites, Pt/CeO_2 composites sandwiched between two $Ce_{0.8}Gd_{0.2}O_2$ (CGO) blocking electrodes were used to measure ionic conductivity using impedance spectroscopy (see Figure 4.1a) . Commercial CGO powder was pelletized under a uniaxial press at 20 MPa for 10 seconds. The CGO pellets were 7 mm diameter and 1 mm thickness. They were calcined in an oxygen atmosphere in a furnace at

850 ℃ for 12 h to be fully oxidized. One side of each CGO pellet was coated with a silver electrode to reduce the contact resistance. The sandwich structure of CGO/Pt/CeO_2/CGO cells were kept at a range of temperatures from 500 ℃ to 600 ℃ in air during conductivity measurement. Electrochemical measurements were conducted using a potentiostat/ galavanostat SP-150 system (Biologic, France) over the frequency range from 1 Hz to 1 MHz with an applied peak-to-peak voltage of 30 mV.

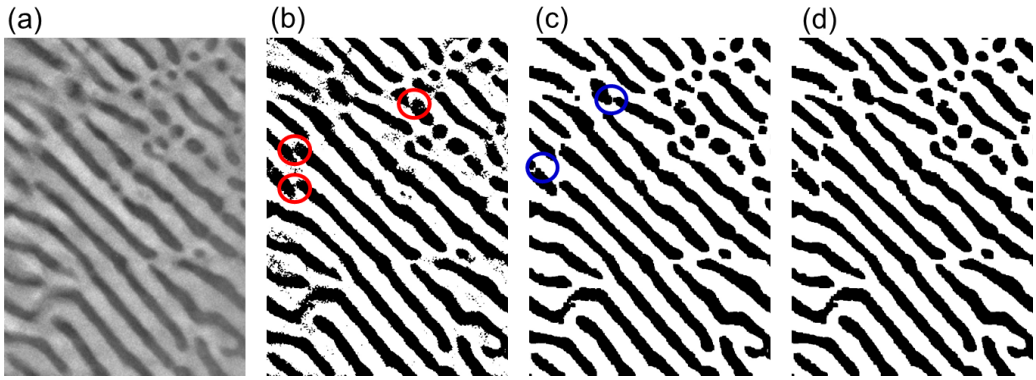

Figure 4.3. Binarization and post-processing of the background removal image. (a) The background-removed image by FFT; (b) corresponding binarization image using an adaptive Gaussian thresholding method; (c) closing, where unnecessary connections of black parts marked by red circles and black spots in (b) were removed; (d) opening, where gaps in black parts marked by blue circles in (c) were filled and white noise was removed. Note that the spot size to be removed was determined by the kernel set in the opening and closing process.

4.3 Results and discussion

4.3.1 Microstructure analysis

Four Pt/CeO_2 composites were prepared in different syngas ratios of CO and O_2 of 0:1, 1:1, 2:1, and 3:1, to form different nanostructures, denoted G01, G11, G21, and G31, respectively. XRD patterns of synthesized composites shown in Figure 4.4a illustrate that all the samples were composed of crystallized Pt and fluorite CeO_2, although the peaks of CeO_2 are weak because of the low fraction (~ 11wt%). It suggests that the Pt_5Ce alloys were completely transformed to the crystalized Pt and CeO_2 phases. No significant differences, in terms of peak positions and intensity ratio, were found in XRD of different samples, indicating the similar chemical composition regardless of the syngas ratio. The composites consist almost of Ce^{4+} species according to the Ce 3d core level HAXPES spectrum of G01, G21 and referenced CeO_2 in Figure 4.5, which suggests a low concentration of oxygen vacancies in the composites. HRTEM images of G21 and G01, as shown in Fig. 4.4b and Fig. 4.4c, respectively, display the alternating nanocrystals of Pt (dark contrast) and CeO_2 (bright contrast). The inset FFT patterns with sharp spots of bright phases marked by yellow boxes confirm good crystalline quality of cubic CeO_2 phase. Therefore, comparing with the transportation pathway through the interface, the effect of other structural features to the ionic conductivity should be negligible in this work.

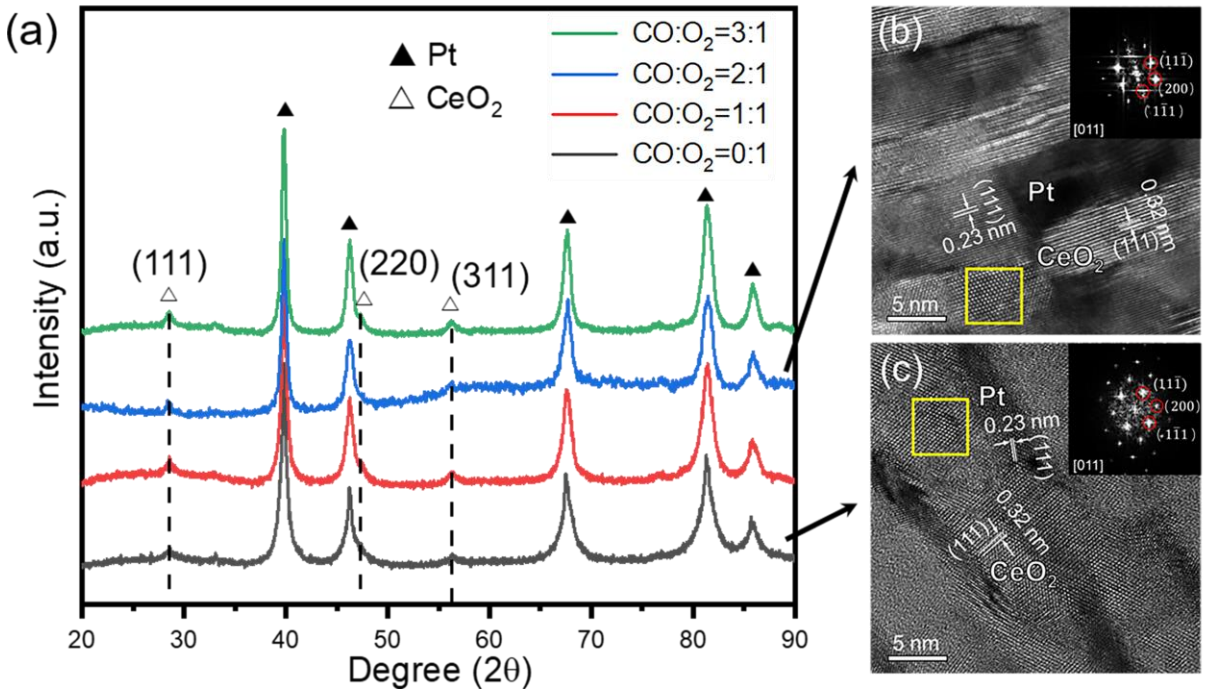

Figure 4.4. (a) XRD of Pt/CeO_2 composites prepared in different gas ratio of CO and O_2. HRTEM image of composites in the syngas ratio of (b) 2:1 (G21) and (c) 0:1 (G01).

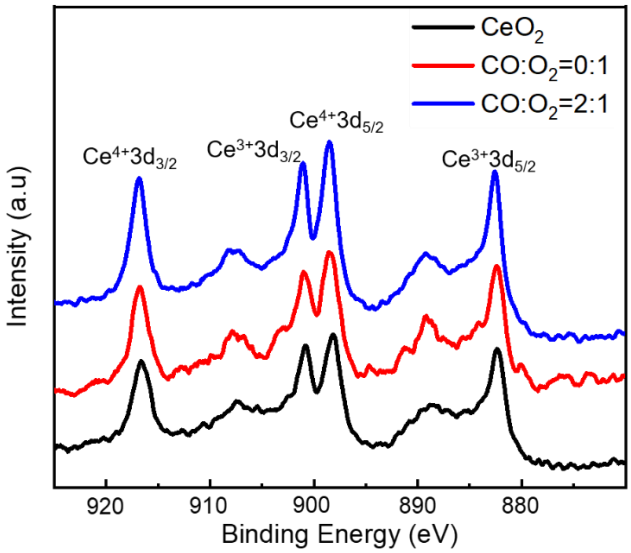

Figure 4.5. HAXPES profile of Pt/CeO_2 composites in the Ce 3d region. The peak positions and peak intensity ratios are the same regardless of the syngas ratio. The composites in the gas ratio of 0:1 (G01) and 2:1 (G21) consist almost of Ce^{4+} species according to the referenced CeO_2 spectrums, suggesting a low concentration of oxygen vacancies in the composites.

The same with that shown in Chapter 3, EDS mapping in Figure 4.6 shows the distribution of the Pt and CeO_2 with bright and dark contrast in the STEM image, respectively. Figures 4.7a–4.7d show typical background-removed ADF-STEM images of the four composites, suggesting similar homogenous periodic structures caused by nanophase separation. The nanostructure changed from a striped to a maze-like appearance as the O_2 partial pressure reduced. Another pronounced feature was the difference in the periodic

width of the pattern. G01 had the smallest-width patterns, while the other three samples (G11, G21, G31) have almost identical width scale patterns. The mean width over 200 white stripes in G01, G11, G21 and G31 was determined to be 5.1±0.9 nm, 6.4±2.1 nm, 6.3±1.3 nm, and 6.1±1.6 nm, respectively, while the width of CeO_2 stripes showed the opposite trend.

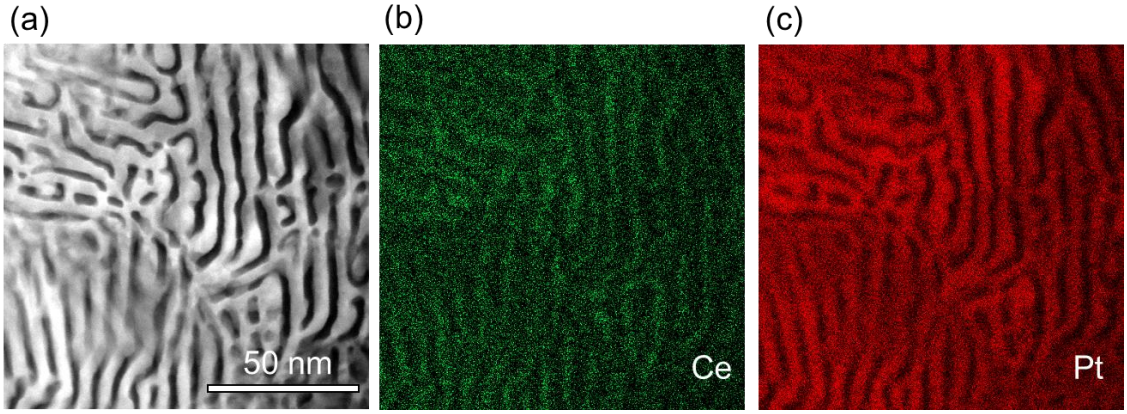

Figure 4.6. EDS mapping of the nanostructure of Pt/CeO_2 composites. (a) STEM image, (b) indicating the distribution of Ce, and (c) Pt. The results show that black and white components in (a) correspond to CeO_2 and Pt phases, respectively.

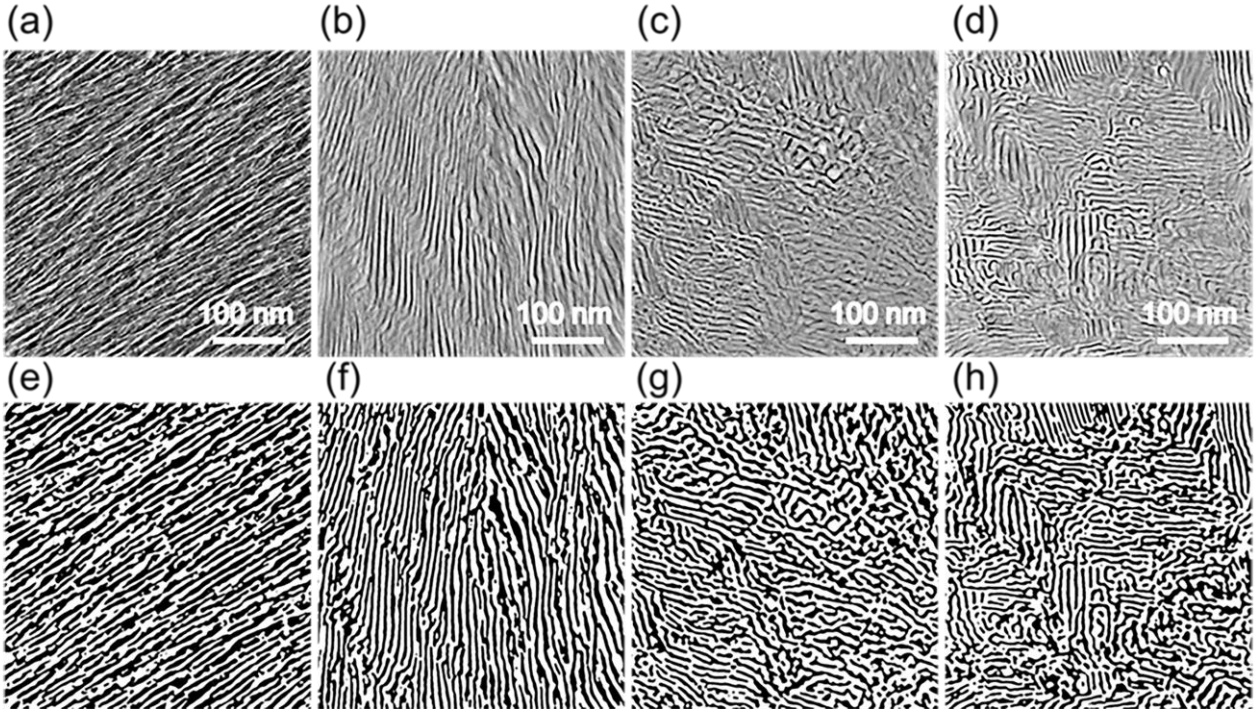

Figure 4.7. Pt/CeO_2 composite nanostructures fabricated with CO:O_2 gas ratios of 0:1 in (a) and (e); 1:1 (b) and (f); 2:1 (c) and (g); and 3:1 (d), (h). The upper row (a)–(d) shows the ADF-STEM images with background removed by FFT. The lower row (e)–(h) shows the corresponding binarized images using the adaptive thresholding method.

These phase-separated patterns closely resemble Turing patterns, which occur throughout nature [24,25], and are formed experimentally by reactive phase separation in polymer mixtures [26,27]. The reactive

diffusion model is widely used to explain the Turing pattern formation, and nanoscale Turing patterns are expected to form in the reaction-diffusion system with low diffusion properties [24]. In the present case, the reaction between Ce and O provides a strong driving force for reactive phase separation, and low mobility of Ce and Pt atoms is responsible for the nanoscale width of patterns. The presence of the CO syngas might facilitate the Pt atoms' diffusivity because of their high affinity to CO, and therefore increase the width of the Pt stripes. The transformation from stripes to maze patterns would be due to decreased reaction rates, as in the simulation results reported by Glotzer et al.,[26] where CO acting as inhibitor reduced both the O coverage of the reaction surface and the oxidation reaction rates. As a result, the length of stripe domains would be expected to decrease with increasing CO partial pressure.

Figures 4.7e–4.7f show the binarized images of the ADF-STEM images in Figs.4.7a-4.7d. They match the original "background removed" images well, though some low-contrast boundaries (caused by sample tilting) contain incorrect connection of Pt or CeO_2 phases. The white pixels of the binarized images were counted to give the area fractions for the Pt white phase, and the results showed that the four specimens contained the equivalent proportion of about 55% because of the same Pt_5Ce precursors. The discrepancy from the thermotical volume fraction of Pt (65%) might be owing to the partition of fuzzy interface. Also, substitutional Ce atoms in the Pt structure and substitutional Pt atoms in the CeO_2 structure would result in the actual density of Pt and CeO_2 phases, respectively, deviating from their theoretical values.

4.3.2 Homology results

The Betti numbers computed from the ADF-STEM images are shown in Fig. 4.8. Although the error bar of each sample is large, due to noisy and regional patterns from the images, the trends of averaged Betti numbers as the gas ratio changes can be identified. The averages were means, gathered from several regions of the samples.

The black curve with open square symbols in Fig. 4.8a indicates that G11 contained the lowest proportion of CeO_2 components, β_0, and this then increased with further increasing CO partial pressure against O_2. G01 and G11 had relatively low β_0 values because of the long and straight CeO_2 components (Figs. 4.7a and 4.7b). In other words, the lower value of β_0 means the higher connectivity of the CeO_2 phase. It is worth noting that G01 and G21 had almost identical β_0, despite their structures being quite different (Figs. 4.7e and 4.7g).

For the number of Pt holes, β_1, G01 had the highest value; it then slightly decreased with the increase in the fraction of CO in the reaction gas until G21, as shown in Fig. 4.8b. The heart of the topological method considers two objects to be equivalent if they can deform to each other by pulling and stretching, without breaking and tearing, regardless of their shape features. Even so, some metamorphosis methods from intrinsic topology, such as persistence diagrams [28], persistence images [29], and the ratio of β_1 to β_0 [30], reveal discrepancies in terms of shape features. Among them, the ratio of β_1 to β_0 was recently used to detect the contact density of a tumor and its aggregation status [30]. This was also calculated here to evaluate the shape difference, and the results are displayed as the blue curve with open circles in Fig. 4.8c. It can be seen that the

ratio β_1/β_0 decreased as the gas ratio increased, suggesting the contact density of CeO_2 decreased. In other words, the shape transformation from striped to maze corresponds to a decrease in Betti number ratio, β_1/β_0.

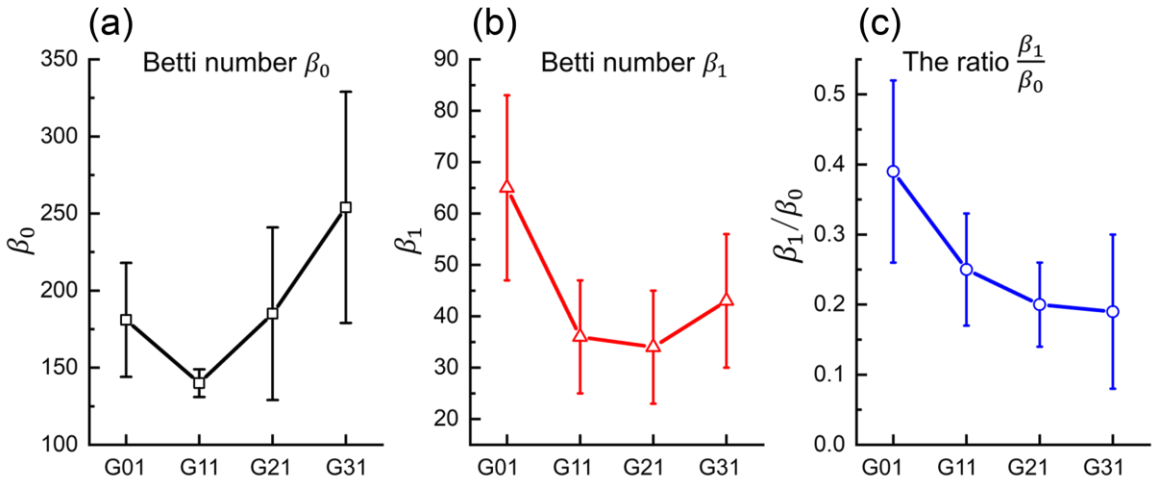

Figure 4.8. Betti numbers as a function of gas ratio CO to O_2. (a) Average number of CeO_2 components (β_0) represented by a black curve with open squares. (b) The number of Pt holes (β_1) represented by a red curve with open triangles. (c) The ratio of β_1 and β_0, shown by a blue curve with open circles.

4.3.3 Ionic conduction property

Figure 4.9 displays (a) Bode and (b) Nyquist plots of impedance spectra from the G11 composite measured at different temperatures, along with corresponding fits to an equivalent circuit. Impedance responses centered at the range from 10^2 Hz to 10^3 Hz and at ~10^6 Hz are temperature dependent. Imaginary resistance decreased and peak position shifted to higher frequencies with increasing temperature. In the Nyquist plots the impedance spectra consisted of two well-separated semicircles. The high-real resistance arc at lower frequency indicated a pronounced decrease in real resistance with increasing temperature.

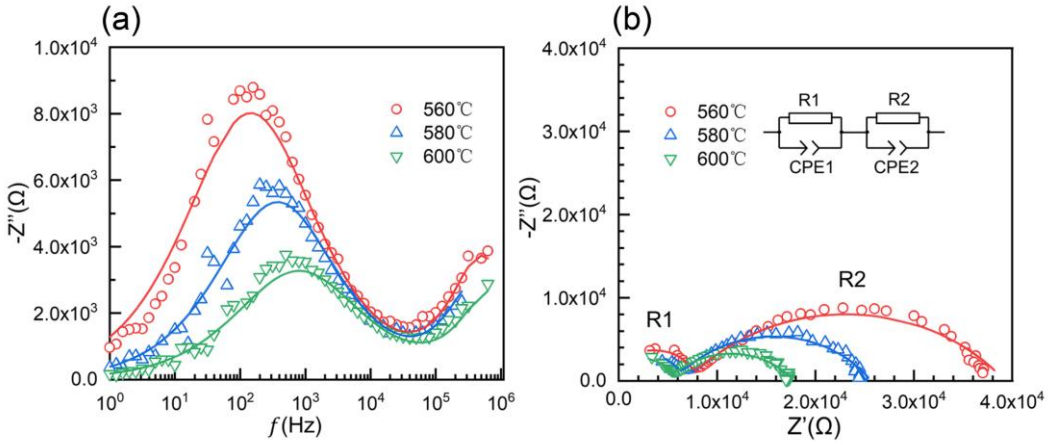

Figure 4.9. (a) Imaginary resistance of G11 versus frequency (Bode) plots of impedance spectra measured at 560, 580, and 600 ℃. (b) Imaginary versus real impedance (Nyquist) plots of the nanocomposite at different temperatures. The semicircle at higher frequencies is attributed to the CGO ionic electrodes, while at lower frequencies the Pt/CeO_2 composites contribute to the semicircle.

A less-marked dependence of syngas ratio for impedance is visible at higher frequencies. It was found that the resistivities R1 of the semicircle at higher frequencies measured on G11 at different temperatures were similar, and these were attributed to the response of CGO ionic electrodes. A single CGO pellet with Ag electrodes was then assembled to test the resistance, and the results coincided with R1 as shown in Fig. 4.10. Therefore, the impedance characteristics at low and high frequencies were ascribed to the sets of parallel combination of bulk resistance R and bulk capacitance CPE in Pt/CeO_2 and CGO, respectively. In Pt/CeO_2 composites, the RQ circuit originated from the bulk CeO_2 and the interface between the Pt and CeO_2, as explained by the transmission line model for Ni/YSZ composites [31]. In our case, the electronic transportation line was largely prohibited by the CGO ionic electrodes. In order to study the effect of structures on the conduction of O_2^- in bulk Pt/CeO_2, resistances R2 of the low frequency semicircle were extracted to calculate the ionic conductivity.

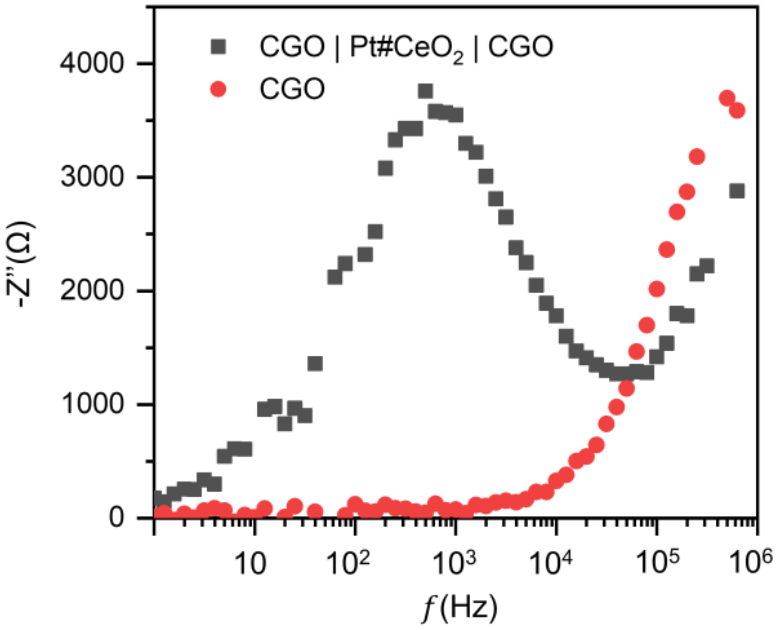

Figure 4.10. Bode plots of impedance spectra for CGO / Pt/CeO_2 / CGO and simple CGO system, suggesting the peak at high frequency represents CGO and low frequency corresponds to Pt/CeO_2.

Figure 4.11a shows the temperature dependence of ionic conductivity for Pt/CeO_2 composites as a function of the gas ratio of CO to O_2. The conductivity values σ' of these Pt/CeO_2 composites were calculated using the geometrical dimensions of thickness d, and cross-sectional area A, of the cylindrical block used for the impedance measurement, given by the following equation (4-1):

$$\sigma' = \frac{d}{R_2 A} \qquad (4\text{-}1)$$

Clearly, G11 showed the highest ionic conductance in the measured temperature range, followed by G01. When increasing the gas ratio of CO to O_2, the ionic conductivity decreases. This effect is larger at higher temperatures: for G01, it is about one order of magnitude higher than for G31. Hence, the advantage of a highly

connected CeO_2 phase with low β_0 can be seen. In general, the relationship between ionic conductivity and temperature for the metal/oxide composites follows the classical Arrhenius relationship:

$$ln(\sigma T) = ln\sigma_0 - \frac{E}{kT} \qquad (4\text{-}2)$$

where k is the Boltzmann constant, T is the absolute temperature, E is the activation energy, and $ln\sigma_0$ is a temperature-independent pre-exponential factor. According to the equation, the activation energy E and pre-exponential factor $ln\sigma_0$ were calculated from the fitted line in Fig. 4.11a. From Fig. 4.11b, both E and $ln\sigma_0$ have the same trend and decrease with the increasing gas ratio of CO to O_2, except for G01. The highest ionic conductivity of G11 at measured 500-600 ℃ temperatures is ascribed to the largest $ln\sigma_0$, while nanocomposites with lower E, such as G21 and G31, would facilitate oxygen ion hopping from one site to another one at lower temperature. Combining the calculated Betti numbers and ionic transport properties, it is interesting that the magnitude rankings of E and $ln\sigma_0$ are in contrast to the β_0 values shown in Fig. 4.8. Moreover, G01 and G21 with similar Betti number β_0 have almost the same E and $ln\sigma_0$, although the β_1 values are totally different. This implies that β_1, the number of Pt holes, has little influence on magnitude of E and $ln\sigma_0$. In other words, structures of high connectivity of the CeO_2 phase with low values of β_0 give rise to high values of activation energy E and pre-exponential factor $ln\sigma_0$, and they are independent of β_1.

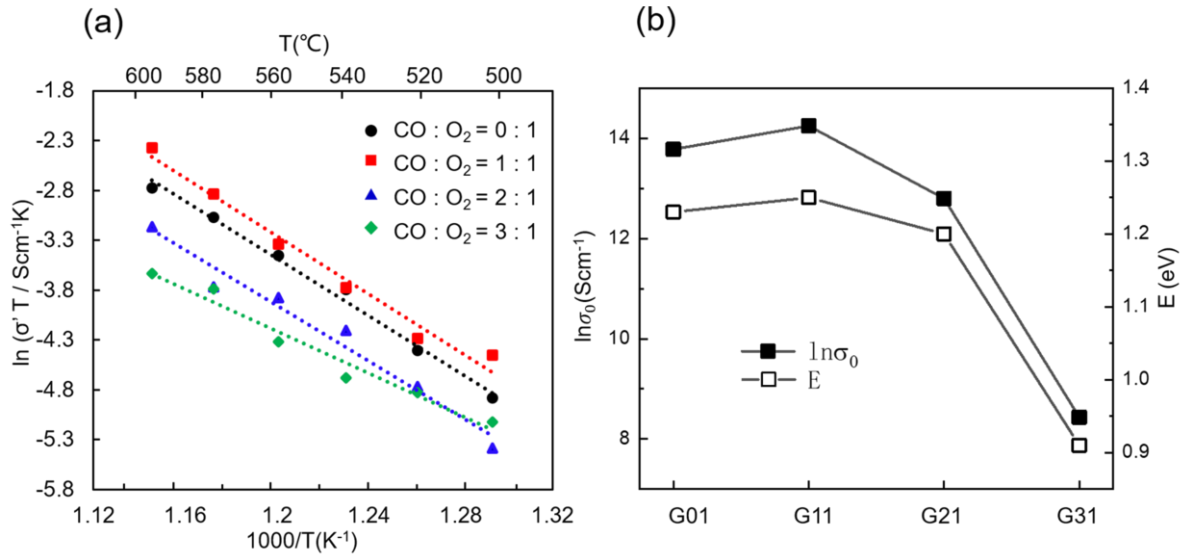

Figure 4.11. (a) Dependence of the ionic conductivity of Pt/CeO_2 composites versus inverse temperature. (b) Pre-factor $ln\sigma_0$ and activation energy E calculated from the fitting line as a function of the nanocomposites with different gas ratios.

Some previous papers indicated that the enhancement of conductivity by a network of ceramic phases is due to the long-range O_2^- transfer channel, which is better than the isolated nanoparticles [13,15]. A highly connected CeO_2 phase with lower β_0 in our case gives rise to a higher pre-exponential factor value, thus provides a faster O_2^- transportation pathway and improved ionic conductivity in the measured temperature range. Since the Pt phases are not conductive for oxygen ions, it is reasonable that β_1 contributes little to the

ionic transport properties. As we know, the pre-exponential factor $ln\sigma_0$ is determined by parameters such as hopping distance, carrier concentration, and entropy [5]. The activation energy is largely related to the bonding strength between oxygen and Ce ions. In addition, stress state and dislocations have significant impacts on the energy required for ion hopping [32]. Particularly for nanostructures of metal and ceramic with dissimilar structures, a high carrier concentration and enhanced mobility are thought to originate from the interface, as reported by many researchers [8,33]. Hence, the influence of the gas ratio is reflected not only in the interwoven structure of two phases but also in the crystallographic information from the interface, such as orientation, coherence, and so on.

4.4 Summary

In summary, Pt/CeO_2 nanocomposites with different structures via phase separation were prepared by changing the gas ratio of CO to O_2 during annealing. The nanostructures of Pt/CeO_2 composites were imaged by sectional TEM. Characterizations based on topological measurements, such as the number of CeO_2 components represented by Betti number β_0, and the number of Pt holes by Betti number β_1, were applied to relate the nanostructures to the oxygen ionic conductivity at 500-600 ℃ temperatures. It was demonstrated that β_1/β_0 can distinguish different structures from stripes to maze. Furthermore, the Betti number β_0 is directly proportional to the activation energy E and pre-exponential factor $ln\sigma_0$, which is decisive for ionic transportation, while the Betti number β_1 has little effect on the E and $ln\sigma_0$ values. Therefore, the Betti number β_0 acted as a descriptor to correlate the image data of nanostructures and their ionic transport properties. The topological approach developed in this report is not limited to a specific metal-oxide composite but can be extended to different systems including lithium-ion conductive polymers. Considering the limitation of projected 2D images with lacking depth information, more accurate 3D structural characterization such as tomography is necessary for better understanding the quantitative phase connectivity-ionic conductivity relationship by homological descriptors.

References

[1] Miyatake, K.; Chikashige, Y.; Watanabe, M. Novel Sulfonated Poly (Arylene Ether): A Proton Conductive Polymer Electrolyte Designed for Fuel Cells. Macromolecules 2003, 36 (26), 9691–9693.

[2] Omar, S.; Wachsman, E. D.; Nino, J. C. Higher Ionic Conductive Ceria-Based Electrolytes for Solid Oxide Fuel Cells. Appl. Phys. Lett. 2007, 91 (14), 89–92.

[3] Eames, C.; Frost, J. M.; Barnes, P. R. F.; O'Regan, B. C.; Walsh, A.; Islam, M. S. Ionic Transport in Hybrid Lead Iodide Perovskite Solar Cells. Nat. Commun. 2015, 6 (May), 1.

[4] Farrington, G. C.; Briant, J. L. Fast Ionic Transport in Solids. Science. 1979, 204 (4400), 1371–1379.

[5] Almond, D. P.; Duncan, G. K.; West, A. R. The Determination of Hopping Rates and Carrier Concentrations in Ionic Conductors by a New Analysis of Ac Conductivity. Solid State Ionics 1983, 8 (2), 159–164.

[6] Andersson, D. A.; Simak, S. I.; Skorodumova, N. V.; Abrikosov, I. A.; Johansson, B. Optimization of Ionic Conductivity in Doped Ceria. Proc. Natl. Acad. Sci. U. S. A. 2006, 103 (10), 3518–3521.

[7] Acharya, S. A.; Gaikwad, V. M.; Sathe, V.; Kulkarni, S. K. Influence of Gadolinium Doping on the Structure and Defects of Ceria under Fuel Cell Operating Temperature. Appl. Phys. Lett. 2014, 104 (11).

[8] Pergolesi, D.; Gilardi, E.; Fabbri, E.; Roddatis, V.; Harrington, G. F.; Lippert, T.; Kilner, J. A.; Traversa, E. Interface Effects on the Ionic Conductivity of Doped Ceria-Yttria-Stabilized Zirconia Heterostructures. ACS Appl. Mater. Interfaces 2018, 10 (16), 14160–14169.

[9] Koettgen, J.; Grieshammer, S.; Hein, P.; Grope, B. O. H.; Nakayama, M.; Martin, M. Understanding the Ionic Conductivity Maximum in Doped Ceria: Trapping and Blocking. Phys. Chem. Chem. Phys. 2018, 20 (21), 14291–14321.

[10] Etsell, T. H.; Flengas, S. N. The Electrical Properties of Solid Oxide Electrolytes. Chem. Rev. 1970, 70 (3), 339–376.

[11] Tianshu, Z.; Hing, P.; Huang, H.; Kilner, J. Ionic Conductivity in the CeO_2-Gd_2O_3 System ($0.05 \leqslant Gd/Ce \leqslant 0.4$) Prepared by Oxalate Coprecipitation. Solid State Ionics 2002, 148 (3–4), 567–573.

[12] Ou, D. R.; Mori, T.; Ye, F.; Kobayashi, T.; Zou, J.; Auchterlonie, G.; Drennan, J. Oxygen Vacancy Ordering in Heavily Rare-Earth-Doped Ceria. Appl. Phys. Lett. 2006, 89 (17).

[13] Choi, J. H.; Ye, Y.; Elabd, Y. A.; Winey, K. I. Network Structure and Strong Microphase Separation for High Ion Conductivity in Polymerized Ionic Liquid Block Copolymers. Macromolecules 2013, 46 (13), 5290–5300.

[14] Lee, S.; Zhang, W.; Khatkhatay, F.; Wang, H.; Jia, Q.; Macmanus-Driscoll, J. L. Ionic Conductivity Increased by Two Orders of Magnitude in Micrometer-Thick Vertical Yttria-Stabilized ZrO_2 Nanocomposite Films. Nano Lett. 2015, 15 (11), 7362–7369.

[15] Liu, W.; Lee, S. W.; Lin, D.; Shi, F.; Wang, S.; Sendek, A. D.; Cui, Y. Enhancing Ionic Conductivity in Composite Polymer Electrolytes with Well-Aligned Ceramic Nanowires. Nat. Energy 2017, 2 (5), 1–7.

[16] Gameiro, M.; Mischaikow, K.; Wanner, T. Evolution of Pattern Complexity in the Cahn-Hilliard Theory of Phase Separation. Acta Mater. 2005, 53 (3), 693–704.

[17] Hiraoka, Y.; Nakamura, T.; Hirata, A.; Escolar, E. G.; Matsue, K.; Nishiura, Y. Hierarchical Structures of Amorphous Solids Characterized by Persistent Homology. Proc. Natl. Acad. Sci. U. S. A. 2016, 113 (26), 7035–7040.

[18] Hirata, A. Structural Analysis of Metallic Glasses with Computational Homology; Springer Japan, 2016.

[19] Reuteler, J.; Hütter, M.; Gauckler, L. J. Backbone of Conductivity in Two-Dimensional Metal-Insulator Composites. J. Appl. Phys. 2011, 110 (2), 024909.

[20] Hansen, N.; Adams, D. O.; Fullwood, D. T. Quantitative Methods for Correlating Dispersion and Electrical Conductivity in Conductor-Polymer Nanostrand Composites. Compos. Part A Appl. Sci. Manuf. 2012, 43 (11), 1939–1946.

[21] Liu, X.; Iocozzia, J.; Wang, Y.; Cui, X.; Chen, Y.; Zhao, S.; Li, Z.; Lin, Z. Noble Metal-Metal Oxide Nanohybrids with Tailored Nanostructures for Efficient Solar Energy Conversion, Photocatalysis and Environmental Remediation. Energy Environ. Sci. 2017, 10 (2), 402–434.

[22] Najib, A. S. B. M.; Peng, X.; Hashimoto, A.; Shoji, S.; Iida, T.; Bai, Y.; Abe, H. Mesoporous Rh Emerging from Nanophase‐separated Rh‐Y Alloy. Chem. – An Asian J. 2019, 14, 2802–2805.

[23] W. Kalies, P. Pilarczyk, Computational homology program. 2003. See http://chomp.rutgers.edu/Projects/Computational_Homology/OriginalCHomP/software/ for more information.

[24] Kondo, S.; Miura, T.; Turing, T. Reaction-Diffusion Model as a Framework for Understanding Biological Pattern Formation. Science 2010, 329 (September), 1616–1620.

[25] Blagodatski, A.; Sergeev, A.; Kryuchkov, M.; Lopatina, Y.; Katanaev, V. L. Diverse Set of Turing Nanopatterns Coat Corneae across Insect Lineages. Proc. Natl. Acad. Sci. U. S. A. 2015, 112 (34), 10750–10755.

[26] Glotzer, S. C.; Edmund A. Di Marzio, and Muthukumar. M. Reaction-Controlled Morphology of Phase-Separating Mixtures Sharon. Phys. Rev. Lett. 1995, 74 (11), 2304–2307.

[27] Miho, M.; Ohta, T. Morphology of Phase-Separating Binary Mixtures with Chemical Reaction. J. Phys. Soc. Japan 1997, 66 (9), 2715–2725.

[28] Obayashi, I.; Hiraoka, Y.; Kimura, M. Persistence Diagrams with Linear Machine Learning Models. J. Appl. Comput. Topol. 2018, 1 (3–4), 421–449.

[29] Adams, H.; Chepushtanova, S.; Emerson, T.; Hanson, E.; Kirby, M.; Motta, F.; Neville, R.; Peterson, C.; Shipman, P.; Ziegelmeier, L. Persistence Images: A Stable Vector Representation of Persistent Homology. J. Mach. Learn. Res. 2017, 18, 1–35.

[30] Nakane, K.; Tsuchihashi, Y.; Matsuura, N. A Simple Mathematical Model Utilizing Topological Invariants for Automatic Detection of Tumor Areas in Digital Tissue Images. Diagn. Pathol. 2013, 8 (Suppl 1), 1–4.

[31] Sonn, V.; Leonide, A.; Ivers-Tiffée, E. Combined Deconvolution and CNLS Fitting Approach Applied on the Impedance Response of Technical Ni/8YSZ Cermet Electrodes. J. Electrochem. Soc. 2008, 155 (7), B675.

[32] Feng, B.; Ishikawa, R.; Kumamoto, A.; Shibata, N.; Ikuhara, Y. Atomic Scale Origin of Enhanced Ionic Conductivity at Crystal Defects. Nano Lett. 2019, 19 (3), 2162–2168.

[33] Garcia-Barriocanal, J.; Rivera-Calzada, A.; Varela, M.; Sefrioui, Z.; Iborra, E.; Leon, C.; Pennycook, S. J.; Santamaria1, J. Colossal Ionic Conductivity at Interfaces of Epitaxial ZrO_2:Y_2O_3/$SrTiO_3$ Heterostructures. Science. 2008, 321, 676–681.

Chapter 5 3D structure-ionic conductivity quantitative relationship of Pt/CeO_2 nanocomposites

Homology analysis revealed a hidden correlation between the charge-transport properties and the 2D phase connectivities of metal-oxide nanocomposites in the previous chapter. To study the 3D phase connectivity-ionic conductivity relationship, a group of Pt/CeO_2 nanostructured composites with different nanotextures ranging from fibrous networks to lamellae were synthesized and identified by transmission electron tomography. The pre-exponential factor of the ionic conductivity of each nanocomposite showed a linear correlation with one of the homological invariants corresponding to the three-dimensional (3D) connectivity of the ion-conductive CeO_2 phase, i.e., 3D–β_0. The other descriptor for ionic transport, namely the activation energy, could not be rationally attributed to any of the Betti numbers, but correlated with the local crystallinity at the Pt/CeO_2 interface. These findings are helpful in the design of electrolytes or electrodes with high oxygen ionic conductivities for application in solid oxide fuel cells. Moreover, the homological approach proposed in this work can be extended to different nanocomposites, opening up an unexplored pathway for the rational design of nanocomposites based on the homological linkages between their 3D nanotextures and their resulting functionalities.

5.1 Introduction

Nanostructured composites have been extensively developed in recent years owing to their ability to access synergistic performances that cannot be achieved using the individual components alone [1–7]. For example, SOFCs, the electron is composed of Ni-CGO (gadolinia-doped ceria), a typical nanocomposite comprising catalytically active metals and ion-conductive oxides, which serve as promoters for fuel oxidation and as mediators of oxygen ions. The atomic arrangement [8, 9], the chemical status of each individual atom [10, 11], and even the electronic densities at single atomic sites [12, 13] have therefore been investigated to improve the functionalities of such nanocomposites. However, this atomistic information rarely allows the development of a good understanding of the correlation between the nanotexture and the material functionality of a nanocomposite. As a result, few traditional material's design has led to improved transport properties, where the charge carriers can travel through interconnected conduction paths over several micrometers.

Two-dimensional (2D) projection imaging through the use of TEM provides deep structural insights into the textures of nanocomposites over an atomic to micrometer range [14, 15]. However, 2D projection imaging by TEM is not sufficient for elucidation of the complicated three-dimensional (3D) textures, which are known to affect their material functionalities (e.g., mechanical strength or electric transport) [16–18]. In contrast, electron tomography (ET) is an emerging technology that allows direct access to 3D nanotextures. The ability to image 3D structures and obtain truly quantitative 3D data for such nanostructured materials provides good opportunities to establish structure-property relationships for nanocatalysts and polymers [19–23]. In particular,

ET using HAADF-STEM has been exclusively applied for the 3D characterization of crystalline materials because the image intensities are directly interpretable [20–24].

For the quantitative interpretation of 3D structures, algorithmic homology has been successfully applied in the materials science as a mathematical tool for the topological analysis of complicated structural features [25–27]. The use of a homological invariant, namely the Betti numbers, β_i (i = 0, 1, 2…), is especially efficient for quantifying the structures of porous materials and/or glass materials, thereby enabling the number of i-dimensional holes to be counted on a topological surface [28, 29]. Indeed, it was demonstrated based on TEM projection imaging that the spatial connectivity of the CeO_2 phase in a lamellar-textured Pt/CeO_2 nanocomposite can be quantitatively represented by the zeroth Betti number, β_0, and further, β_0 can act as a rational descriptor that correlates the oxygen ion conductivity and the topological features of the nanotexture [30].

Thus, I herein demonstrate identification of the complicated 3D textures of nanocomposites using advanced ET and their quantitative classification using the i-dimensional Betti numbers. For this purpose, a group of Pt/CeO_2 nanocomposites is synthesized as a model system by promoting nanophase separation of a precursor alloy, Pt_5Ce, while controlling the nanotexture. The nanotextures of the Pt/CeO_2 composites are reconstructed by HAADF-STEM tomography using scanning transmission electron microscope (STEM) and mathematical post-processing. The Betti numbers, β_i, are then computationally calculated from the tomographic data and are linked to the experimentally measured ionic transport properties of the nanocomposites, which are reflected by the pre-exponential factor,$ln\sigma_0$. Finally, the connectivity of the CeO_2 phase, which is represented by the β_0 value, is used to determine the total flow of the ionic current, whereas the flow rate, which is relate to the activation energy E via the ion hopping frequency, is mostly dominated by the local structure of the Pt/CeO_2 interface.

5.2 Experimental

5.2.1 Sample preparation

Four Pt_5Ce alloy ingots of equal weight were prepared by arc-melting of the elemental materials, Pt and Ce. The ingots were polished into the disk-like shapes. The Pt/CeO_2 composites were prepared by annealing the Pt_5Ce alloy a furnace in a mixture of CO and O_2 (2:1 ratio). Annealing temperatures of 500, 600, 700, and 800 °C was employed to prepare Pt/CeO_2 composites with different morphologies. Due to the low rate of oxidation at low temperature, a longer annealing time (i.e., 8 d) was required for the 500 °C sample to ensure that the reaction reached completion. For all other temperatures, an annealing time of 4 d was used. The weight gain for each of the four samples was calculated to be ~2.8%, indicating an almost fully phase-separated process. The crushed powders were used for XRD analysis and FIB milling to obtain a TEM specimen with a thickness of ~50 nm.

5.2.2 Characterization of the Pt/CeO_2 composites

XRD analysis was conducted for phase identification and crystal structure analyses. HRTEM images were acquired using a double aberration-corrected electron microscope (JEOL JEM-ARM200F, Japan) operated at 200 kV. Aberration-corrected STEM was conducted using a JEM-ARM 200F with a field emission gun and double correctors. For the HAADF images, the collection angle of the detector was 68–240 mrad. The EELS spectra were recorded using a Gatan Enfinium camera system with an energy spread ΔE of ≈ 0.25 eV. A low dose rate and a short acquisition time of 2 s were used for each box scan to avoid beam irradiation. Three regions, two interfaces, and the center of the CeO_2 phase were selected for EELS analysis. HAADF-STEM images showing the 2D projection of the composite structures were obtained using a JEM-2100F (JEOL, Japan) field-emission gun transmission electron microscope operated at 200 kV. Reconstruction of the 3D heterostructures was performed using the HAADF–STEM electron tomography technique using the JEM-2100F instrument. Data collection was carried out by tilting the specimen about a single axis using a Fischione high-tilt tomography holder, ranging from angles of -60° to +60° at a 2° tilt step. At each tilt angle, an image with a frame size of 1024×1024 was acquired. Since 61 projections were used for reconstruction, the total electron dose was estimated to be ~8.48×10^4 e/Å^2. By comparing the STEM images before and after the tomography process (see Figure 5.1), although it was apparent that nanoparticles precipitated on the CeO_2 phases, no significant changes were visible in terms of the shapes of Pt and CeO_2 domains, indicating the negligible effect of electron damage on the tomography results. Alignment of the image stack and tomographic reconstructions were performed using DigitalMicrograph software (Gatan, USA), and the reconstruction was conducted by the simultaneous iterative reconstruction (SIRT) technique [31]. For phase separation, intensity-based binarization and post-processing of each Z-slice image were performed using a global threshold in Python with OpenCV libraries. The 3D visualization was perfomed using Avizo software (Thermo Fisher Scientific, USA). The resulting tomogram was cropped to the region of interest, yielding dimensions of $150\times150\times15$ nm^3 for homology analysis.

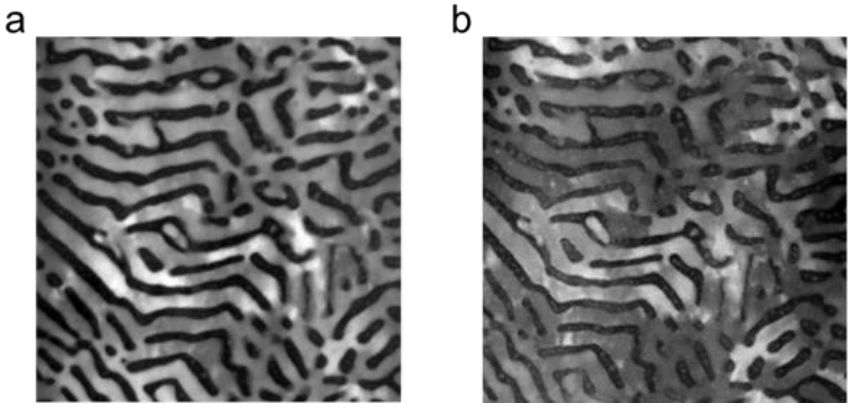

Figure 5.1 HAADF-STEM images of the sample NC600 (a) before, and (b) after tomography imaging. Although the electron beam during the tilt series affected the local structure of the dark CeO_2 phase, but the shape of the CeO_2 domains remains the same as before the tomography.

5.2.3 Homology analysis

To quantify the topology of each composite, their topological invariants, i.e., their Betti numbers, were obtained from both 2D projected STEM images and 3D tomographic structural data were measured. For the analysis of the 2D images, the averaged Betti numbers from three projection images were calculated from the binary image, which was obtained by adaptive Gaussian thresholding from the background-removed STEM image. The image processing process and its corresponding details areas those described in our previous work [30]. In addition, β_0 was computed as a function of the global threshold for the grayscale images to identify the structural feature, known as the Betti curve [32]. For the 3D structural data, segregation into two phases was performed by interactive binarization. The threshold value, that is 130, was determined by comparing the origin and binarized yz sectional plane of the 3D structure, as shown in Figure 5.2. The selected CeO_2 phases are marked by black domains, indicating the suitability of the threshold value. Label analysis was conducted to highlight the separated CeO_2 domains. The connected domains were marked using the same color, although it should be noted different shades of the same color may represent the different domains. We used volume rendering to clearly visualize the 3D structure, where only the CeO_2 phases with Pt phases were invisible. To output a series of 2D binary images for chomp analysis, a segmentation process was used to assign colored CeO_2 domains in black and the invisible Pt phase in white color. The processes used for extraction of the CeO_2 phases and homology analysis are illustrated in Figure 5.3. A text file recording the coordinates (x, y, z) of each 3D structure was obtained from the tomogram and was used to calculate the Betti numbers in Chomp software [33]. With the exception of the selected size of 150×150×15 nm^3 shown in Figures 4e–4h, different

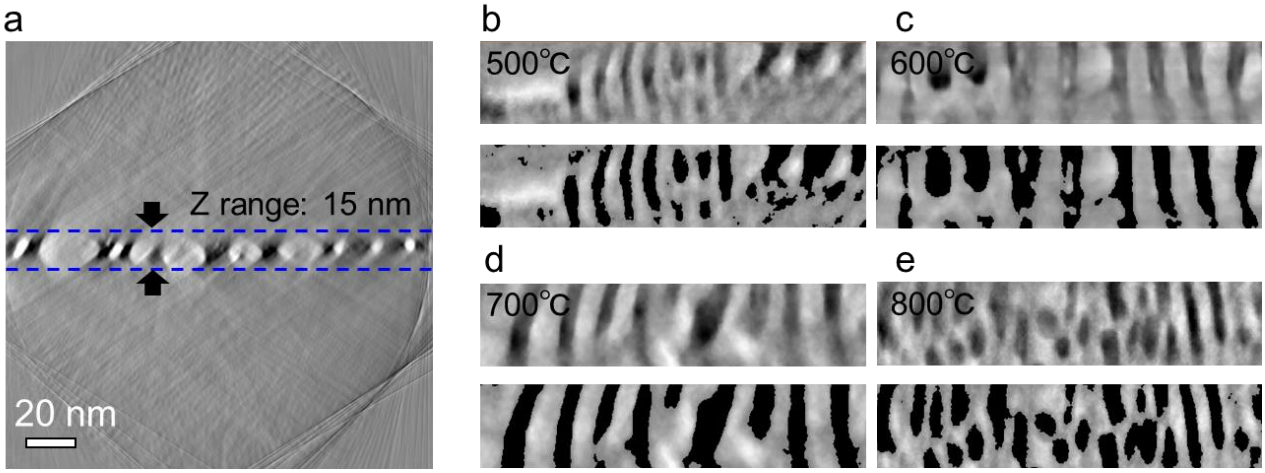

Figure 5.2. (a) Side view of the structure for reconstruction in the NC600, indicating a narrow thickness range (< 15 nm) for 3D reconstruction. Selection of the thresholding value (of 130) for the extraction of the CeO_2 phase. The yz sectional plane (up) and corresponding binarized image (bottom) of the 3D structure for the Pt/CeO_2 composite which was prepared by the annealing at (b) 500 °C, (c) 600 °C, (d) 700 °C and (e) 800 °C. The thickness of the displayed area is 15 nm. The extracted CeO_2 phases were marked by black color and the rest parts are the Pt phase in the bottom binarized image.

sizes were selected by changing the thickness and surface area to exclude the influence of the selected area on the homology analysis results.

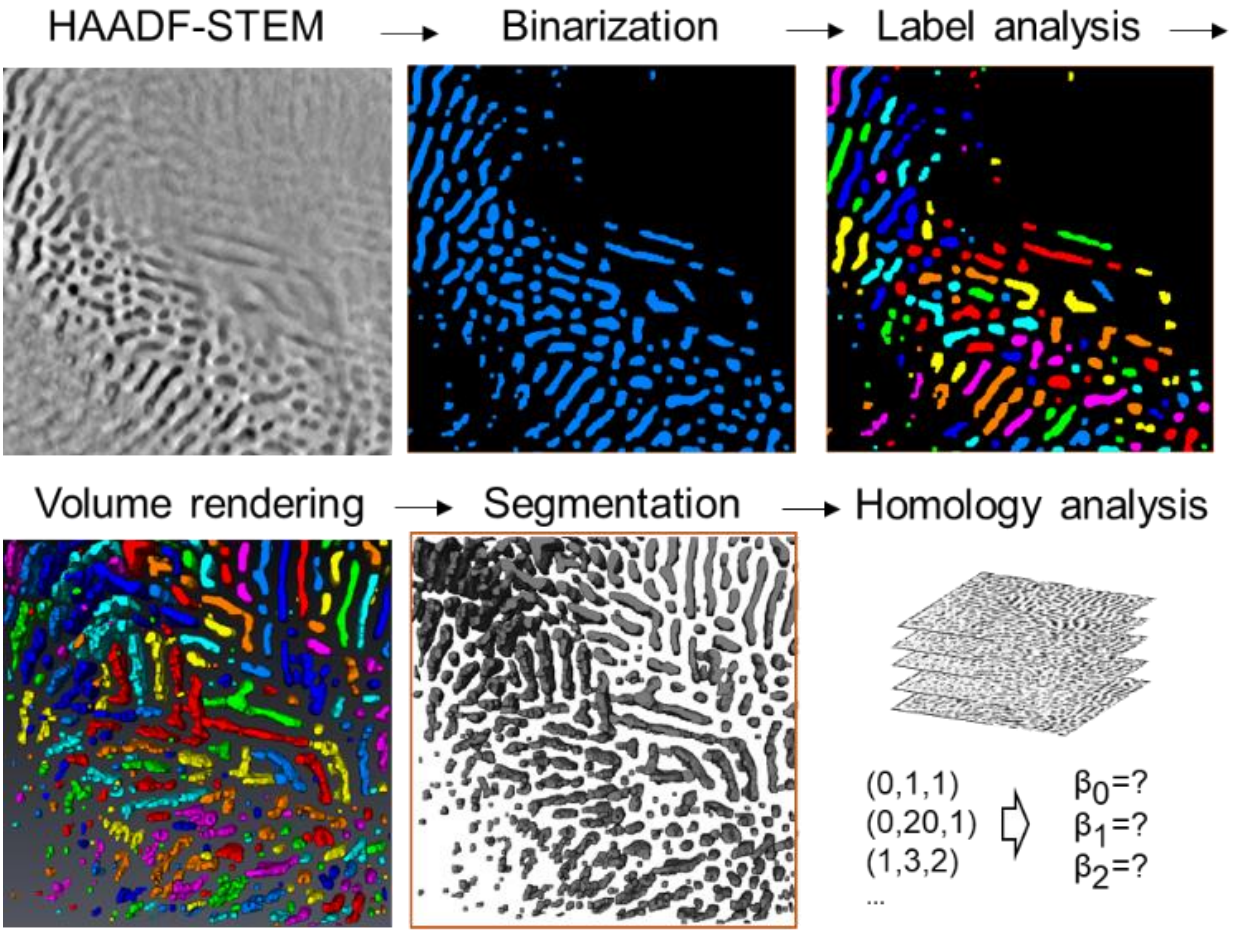

Figure 5.3. Pre-processing and homology analysis for the 3D structure. The reconstructed 3D structure of the Pt/CeO_2 nanocomposite obtained from the tomography images was initially binarized to extract the black CeO_2 phases. The separated CeO_2 domain are labeled using different colors. The 3D shapes of the CeO_2 phases were visualized by volume rendering. Subsequently, the composite was segmented into black CeO_2 and white Pt. A series of binary images were generated in the thickness direction to calculate the Betti numbers using Chomp software.

5.2.4 Ionic conductivity measurement

The ionic conductivity of each sample was investigated using impedance spectroscopy (SP-150, Biologic, Japan) described previously [30]. The frequency employed ranged from 1 Hz to 1M Hz, and all experiments were carried out under air. The ingot samples were placed between the CGO pellets to exclude the electronic current. Ag paste was used to cover one side of each pellet to form an electrode (see Figure 5.4a). The testing temperature was set from 500 °C to 600 °C. Fitting of the obtained impedance spectra with the corresponding equivalent circuit model was performed using the EIS Spectrum Analyser software [34].

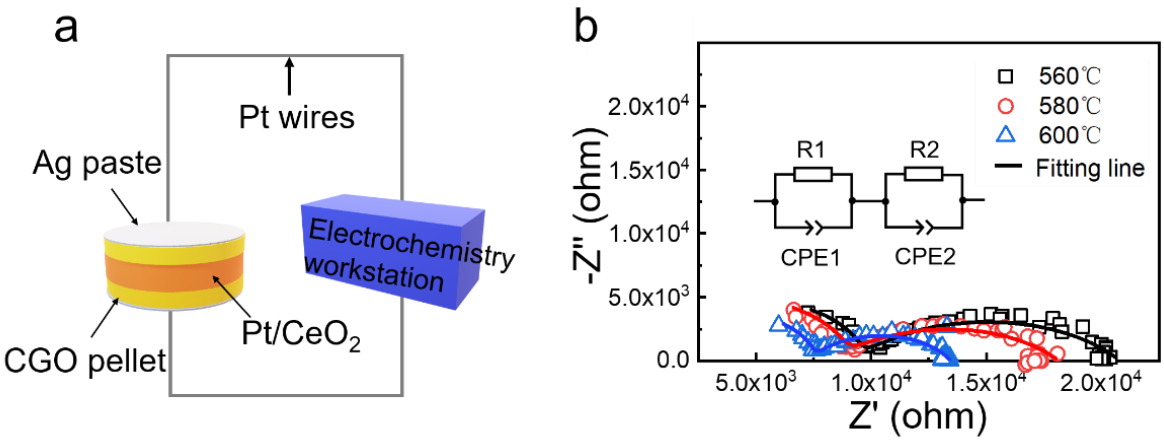

Figure 5.4. Schematic illustration of the ionic conductivity measurements for the Pt/CeO_2 composites based on the AC impedance spectroscopy method. (b) Experimental and fitting impedance spectra for the Pt/CeO_2 composites annealed at 800 °C; these spectra were recorded at different measurement temperatures. The equivalent circuit with two pairs of resistance R and a constant phase element (CPE) is shown in the inset. The Pt/CeO_2 composites contribute to the low frequency impedance response.

5.3 Results and discussion

5.3.1 Local structure analysis

Figure 5.5a shows a section high-angle annular dark-field (HAADF)-STEM image of a typical nanotexture in Pt/CeO_2 nanocomposites, which was prepared by annealing a Pt_5Ce alloy in a stream of carbon monoxide (CO) and oxygen (O_2) at 600 ^oC to promote spontaneous phase separation from the precursor Pt_5Ce alloy to the nanocomposite. According to the energy-dispersive X-ray spectroscopy (EDS) mapping shown in Figures 5.5b–5.5d, the black and white contrasting areas in Fig. 5.5a correspond to the CeO_2 and Pt phases, respectively. Figures 5.5e–5.5h show the high-resolution TEM (HRTEM) images of the nanocomposite in the vicinity of the Pt- and CeO_2 interface, which were prepared by annealing the same precursor alloy at 500, 600, 700, and 800 ^oC, respectively (hereafter denoted as NC500, NC600, NC700 and NC800, respectively). Computationally calculated FFT patterns are shown in the right-hand corners of the corresponding images. As indicated, the lattice parameters of the Pt and CeO_2 phases in all the samples were calculated as 0.39 and 0.54 nm, respectively. However, upon increasing the annealing temperature, the interface changed from a disordered phase to a highly epitaxial crystallized region. The sharpness of both Pt and CeO_2 peaks in the X-ray diffraction (XRD) patterns showed an increasing trend with the increase in the annealing temperature (see Figure 5.6). The full-width at half-maximum (FWHM) values of the Pt(111) peaks for the four samples are listed in Table 5.1, while FWHM of CeO_2 peaks are too weak to measure. The increased peak sharpness clearly shows the increased degree of crystallinity. For a nanoscale heterostructure, the interface between the metal and the oxide is thought to be the main pathway of oxygen transportation, since the low packing density and

rich structural defects at the interface contribute to a low activation energy for oxygen hopping [35, 36]. Furthermore, disordered interfaces with more defects than epitaxial interfaces are more conductive to oxygen ion transport [37, 38].

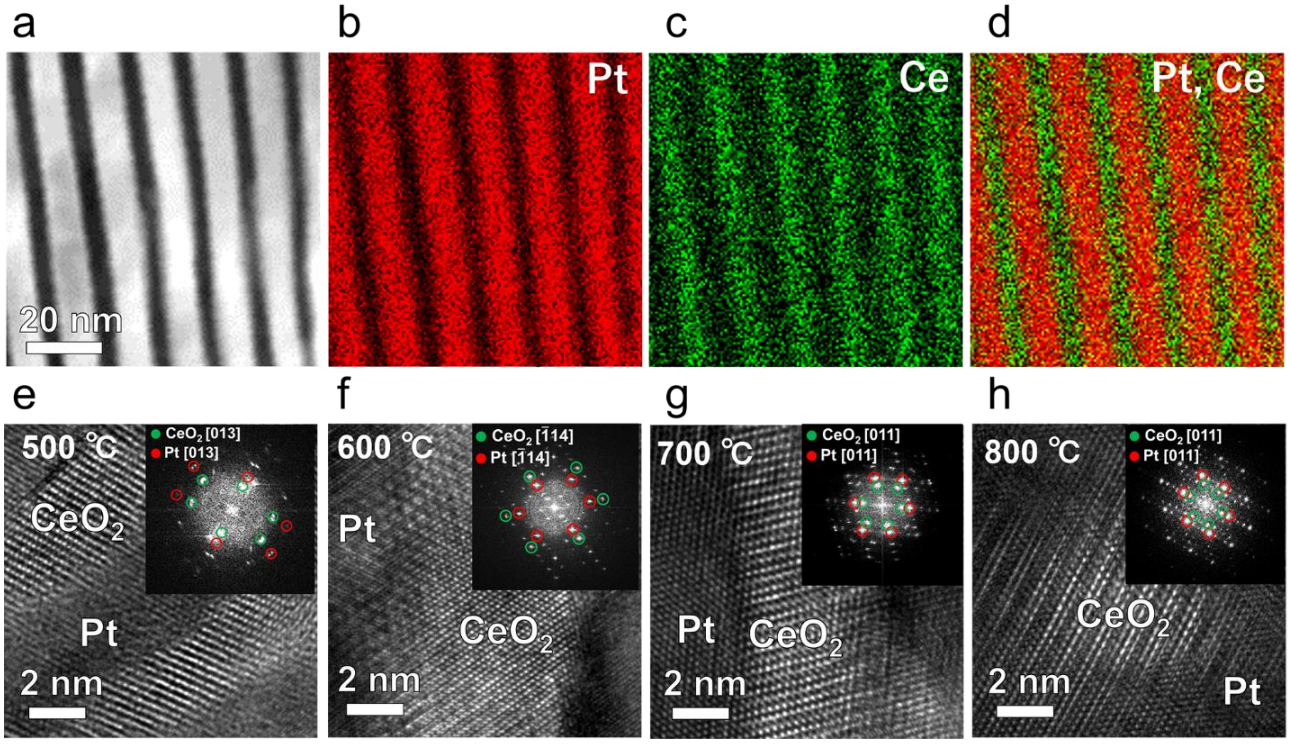

Figure 5.5. (a) HAADF-STEM image of the Pt/CeO_2 nanocomposite. The corresponding EDS mapping images show the elemental distributions of (b) Pt, (c) Ce, and (d) their overlap. HRTEM images for the Pt/CeO_2 composites prepared by annealing at (e) 500 °C, (f) 600 °C, (g) 700 °C and (h) 800 °C. The insets on the upper right are the corresponding FFT patterns from the HRTEM images, showing the crystalline degrees and epitaxial relationships between the Pt and CeO_2 phases.

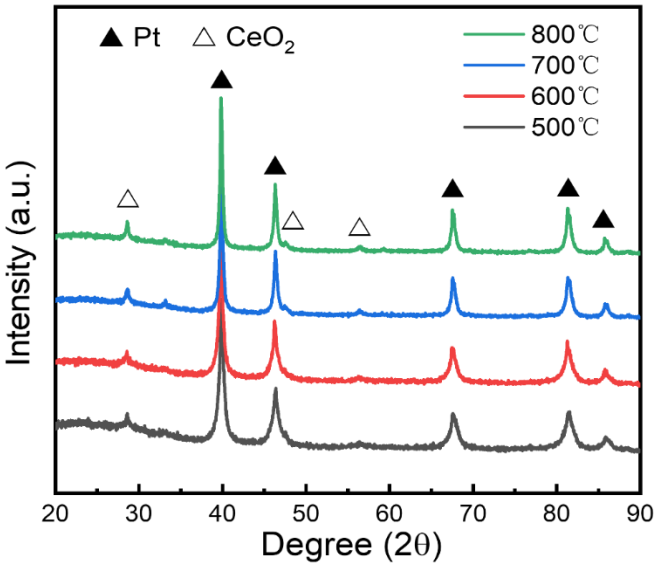

Figure 5.6. XRD patterns of the Pt/CeO_2 composites annealed at different temperatures ranging from 500 °C to 800 °C. Only two phases, Pt and CeO_2 were identified for the various composites.

Table 5.1. Integrated information for the four Pt/CeO_2 nanocomposites prepared using different annealing temperatures.

Sample	XRD	STEM – CeO_2 domain			Homology analysis			Ionic conductivity	
Heating temp.	HMFW /Pt (111)	Width /nm	Shape	Surface area/nm^2	3D-β_0	3D-β_1	3D-β_2	$ln\sigma_0$ / $Scm^{-1}K$	E / eV
500 °C	0.73	2.7	Lamellar, particle	83121	322	31	1	6.4	0.74
600 °C	0.64	5.2	Lamellar	89548	216	68	5	12.8	1.20
700 °C	0.45	4.1	Lamellar	60350	143	27	0	14.8	1.24
800 °C	0.41	4.0	Network	171441	164	226	86	14.1	1.21

To further investigate the compositional or chemical nature at the interface between the Pt and CeO_2 phases, electron energy loss spectroscopy (EELS) analysis was conducted, as shown in Figure 5.7. More specifically, Figure 5.7a shows the HAADF-STEM image of the Pt/CeO_2 composites prepared at 700 °C, NC700. Three regions, including two interfaces and the center of the CeO_2 phase, were selected for measurement of the EELS spectra. The corresponding EELS spectra for the Ce-M edges are shown in Figure 5.7b together with those for standard Ce-containing materials, namely CeF_3 and CeO_2. The featured peaks are located at the same position in each case, i.e., ~ 885 eV (Ce-M_5) and ~903 eV (Ce-M_4), which are close to the

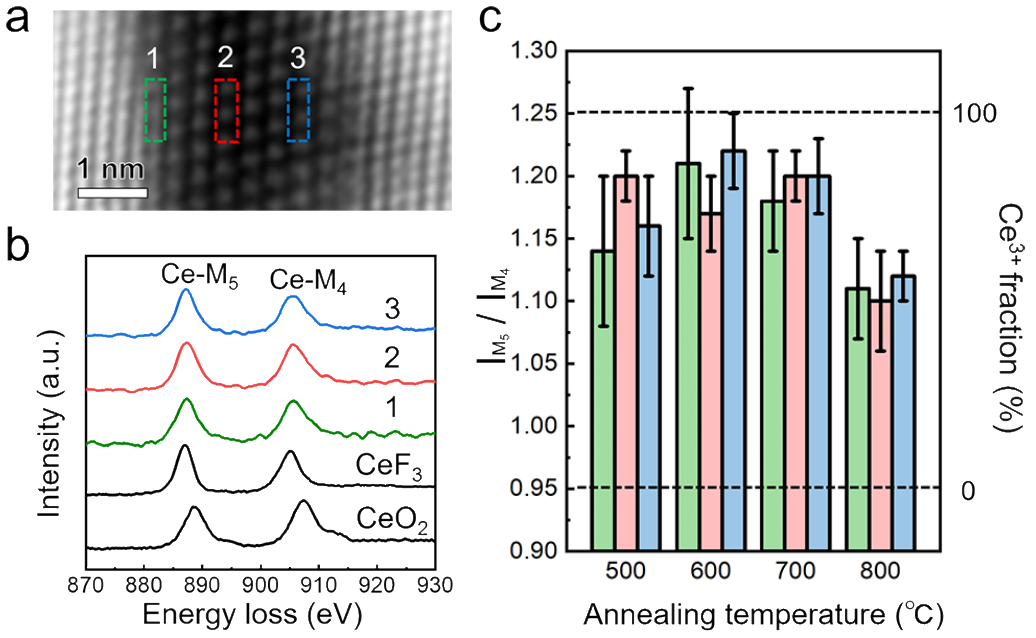

Figure 5.7. STEM-EELS detection of the cerium valence state distribution in the CeO_2 phase of the Pt/CeO_2 composite annealed at 700 °C. (a) Atomic structure of the CeO_2 phase. The dashed rectangles indicate the regions used for detection of the EELS spectra. (b) EELS spectra of the colored areas in (a), showing the ELNES of the Ce M_5 and M_4 edges. (c) The M_5/M_4 intensity ratios calculated from the positive part of the second derivative of the experimental spectra for the same three regions shown in part (a) for each sample.

peak positions of the CeF_3 reference spectra (886 eV and 905 eV, respectively). The valence state of Ce was then quantitively evaluated by calculating the M_5/M_4 edge ratio by the second derivative method, as illustrated in Figure 2.10. The same EELS process was conducted for the other samples, as shown in Figure 5.8. Figure 5.7c summarize the average M_5/M_4 ratios of the five CeO_2 precipitates for each sample area. The two broken lines in Figure 5.7c indicate the M_5/M_4 ratio for the reference CeO_2 (0.95) and CeF_3 materials (1.25). Importantly, all the samples showed similar valence states for the center Ce (red) and interface regions (green and blue), suggesting a homogenous distribution of Ce^{3+} in the CeO_2 nanophase comprising Pt/CeO_2. The averaged M_5/M_4 ratios for the whole CeO_2 phases of the NC500, NC600, NC700 and NC800 samples were calculated to be 1.17, 1.20, 1.20, and 1.11, respectively. The lower value obtained for the NC800 sample was attributed to lower concentration of Ce^{3+} compared to that present in the other three samples. A high concentration of Ce^{3+} represents rich oxygen vacancies in conducive CeO_2 phase, can facilitate oxygen ion transport to give a high pre-exponential factor $ln\sigma_0$ [39, 40]. An increased value for the pre-exponential factor is therefore considered to be related to an increased number of oxygen vacancies, and hence the NC800 sample is anticipated to have the lowest value of factor $ln\sigma_0$ from the local information obtained by EELS analysis. To confirm this assumption, we examined the temperature-dependent ionic conductivities of the nanocomposites using alternating-current (AC) impedance spectroscopy.

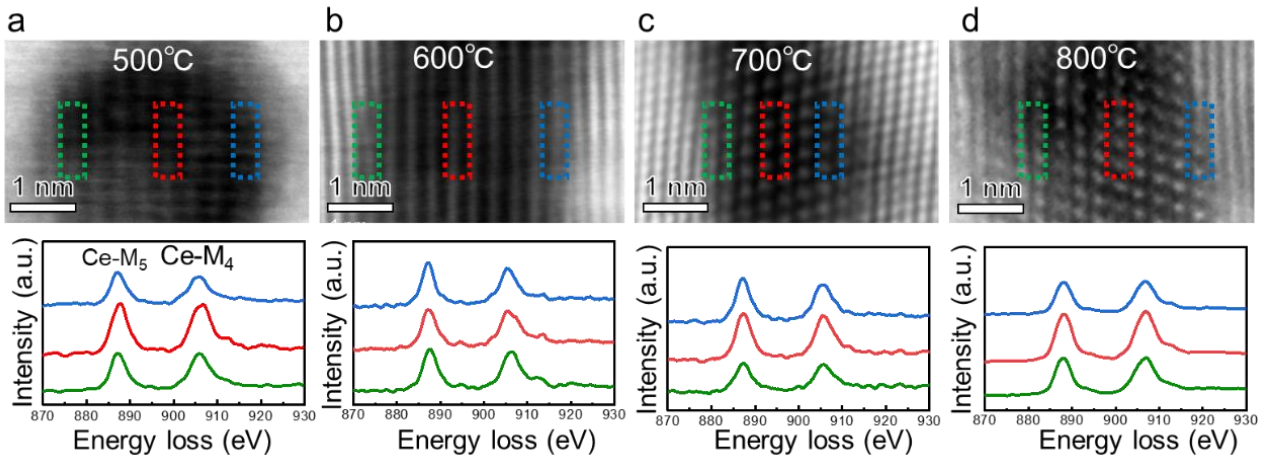

Figure 5.8. HAADF-STEM images and corresponding energy loss spectra for the Pt/CeO_2 composites annealed at (a) 500 °C, (b) 600 °C, (c) 700 °C and (d) 800 °C. The three regions marked by the different colors were selected for each sample to investigate the differences between the interface and the bulk center of the CeO_2 phase. The corresponding spectra are marked using the same color.

5.3.2 Ionic conductivities of the Pt/CeO_2 nanocomposites

The obtained AC impedance spectra showed two well-fitted semi-circles for the Pt/CeO_2 composites measured at various temperatures (Figure 5.4b). Signals in the high-frequency semicircle and low-frequency semicircle regions were ascribed to the CGO pellets and the Pt/CeO_2 composites, respectively. Each semicircle corresponds to the parallel combination of the bulk resistance and the bulk capacitance. Figure 5.9a displays the ionic conductance as a function of the annealing temperature for the Pt/CeO_2 samples, namely NC500, NC600, NC700 and NC800, wherein the conductivity was determined from the resistance R, surface area A and the thickness d of the Pt/CeO_2 composites according to the formula: $\sigma = d/RA$. The trendlines were fitted based on a linear equation and plotted with the corresponding color for each nanocomposite. It is clearly seen that NC800 and NC700 exhibit higher conductivities than NC600 and NC500. Using the Arrhenius plots, the activation energy E and the pre-exponential factor $ln\sigma_0$ were calculated and displayed in Figure 5.9b. Both E and $ln\sigma_0$ exhibit similar trends, where the magnitudes increase with an increase in the annealing temperature from NC500, NC600, and up to NC700, prior to slightly decreasing for the NC800 sample. Obviously, this result is not consistent with the trend anticipated from high-resolution TEM or EELS (see the red lines in Figure 5.9b inset). As mentioned above, for materials with the same components and configuration, the concentration of oxygen vacancies and the structural effect (i.e., the interface coherence) play important roles in determining the pre-factor value and the activation energy, respectively [37,39]. We have concluded that there should be the other unconsidered factor(s) than the local structural analyses, i.e., medium-range information ranging from 10 to 1000 nm as the transport pathway plays an important role determining in the ionic conductivity of a material [41–43].

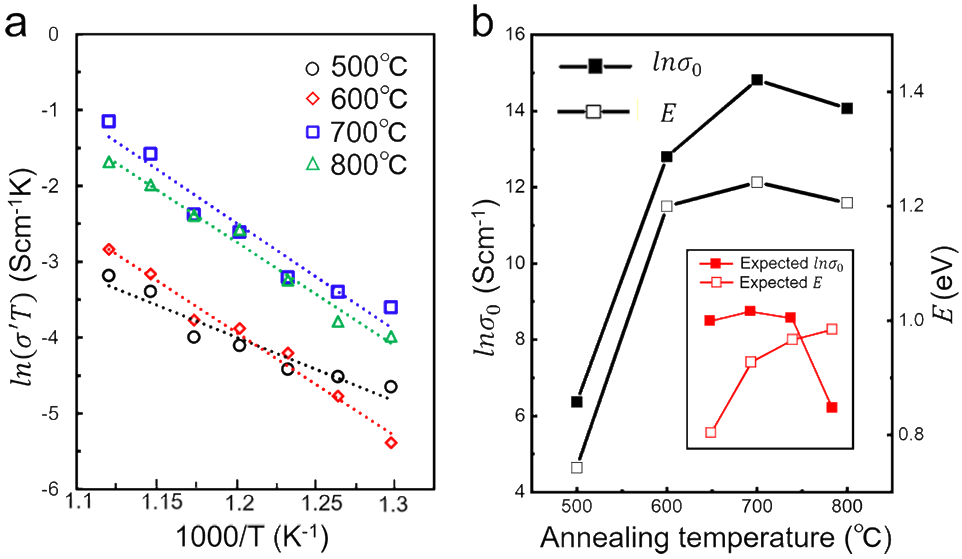

Figure 5.9. (a) Arrhenius plots (in the range of 500 to 600 °C) of the Pt/CeO_2 composites annealed at different temperatures. (b) Corresponding activation energies and pre-exponential factors for the oxygen ionic transportation deduced from the fitted Arrhenius plots. Red lines are the expected ionic conductivity parameter trends as a function of the annealing temperature.

5.3.3 Morphologies of the Pt/CeO_2 nanocomposites

Figures 5.10a–5.10d show the projection HAADF–STEM images of the Pt/CeO_2 composites of NC500, NC600, NC700 and NC800, respectively. For NC500 in Fig. 4a, short stripes and particle-like CeO_2 domains are visible as dark areas in the 2D projections. These stripes and particles of CeO_2 can be clearly observed on NC600 and NC700. Continuedly rising the annealing temperature up to 800 ^oC, the composite NC800 was fully covered with CeO_2 domains with small sizes (Fig. 5.10d). The widths of the CeO_2 phases for the various samples were therefore measured and the statistical results obtained from 200 domains are listed in Table 5.1. Note that gray-contrasted areas are recognized in some places in the STEM image of NC800 (the red arrows in Figure 5.10d inset), unlike the clearly contrasted images of NC500, NC600 or NC700. The gray-contrasted area in NC800 is rationally interpreted as an overlapped projection of the bright Pt- and dark CeO_2 phases along the incident electron beam. This gray-contrasted region most likely acts as a bridge connecting the two spatially separated CeO_2 domains.

Figures 5.10e–5.10h show the HAADF-STEM tomographs of the different CeO_2 phases comprising the Pt/CeO_2 nanocomposites. Visualizations from three different directions (front view, 30° rotation along the y axis, and side view) are displayed to provide a comprehensive understanding of the 3D structures. Due to the counterbalance between the thin area after high-angle tilt and the thick area needed for the integrity of the featured structure, the choice of thickness is important, especially for the focus-ion beam (FIB) slice that exhibits a high mass density. For the Pt/CeO_2 nanocomposites, the low inelastic mean free path (λ_{Pt}=82 nm) limits the thickness to < 40 nm for STEM tomography [44]. From the side view of the reconstruction on the central text plane in NC600 shown in Figure 5.2a, the structure with clear contrast is restricted in the thickness < 15 nm. Therefore, the thickness of the tomographs along the z-axis is determined to be 15 nm, although it is not enough to display the complete shape for some large domains. The colored areas represent mutually connected CeO_2 phases that are independent from the neighboring phases. As can be seen in Figure 5.10e, many small particles and short lamellae are distributed in the composites NC500. In contrast, Figures 4f and g show fewer particles and longer lamellae, as were observed in the 2D images (Figures 5.10b and 5.10c). Clearly, the CeO_2 lamellae in these three samples are evenly dispersed along the z axis, which have an almost depth-prolonged in shape from the corresponding 2D projection images shown in Figures 5.10a–c. In the case of the NC800 sample, the many isolated particle-like CeO_2 domains in Figure 5.10d are connected more deeply to form a network structure, as shown in Figure 5.10h. The extracted red CeO_2 component shown in the upper right-hand corner of Figure 5.10h clearly indicates that the three separated domains on the surface of the FIB-thinned specimen are connected by bridges (marked by black arrows). This is consistent with the prediction

that the two black CeO_2 domains in the 2D STEM image are possibly connected at greater depths, which can be called the "bridge effect". Generally, the resolution along the z-axis is significantly reduced (to ~ 2 nm) due to the "missing wedge" effect and the elongation factor during electron tomography. The distance between the two nearest CeO_2 domains in the 2D projection STEM image of NC800 is in the range of 3–4 nm, which is larger than the tomography resolution. Therefore, the bridge structures, rather than their artifacts could be properly detected. Moreover, since the same reconstruction method and conditions were applied to all samples, the quality of the reconstructed structures has a negligible effect on the comparative analysis. Only a few bridge structures can be observed in the NC500, NC600, and NC700 samples, which therefore supports the existence of bridge structures in NC800. The total surface areas of the CeO_2 domains were then calculated (Table 5.1), and it was found that the network structure of the 800 ^oC annealed NC800 sample possessed the highest surface area, followed by the samples annealed at 600 ^oC (NC600), 700 ^oC (NC700) and 500 ^oC (NC500).

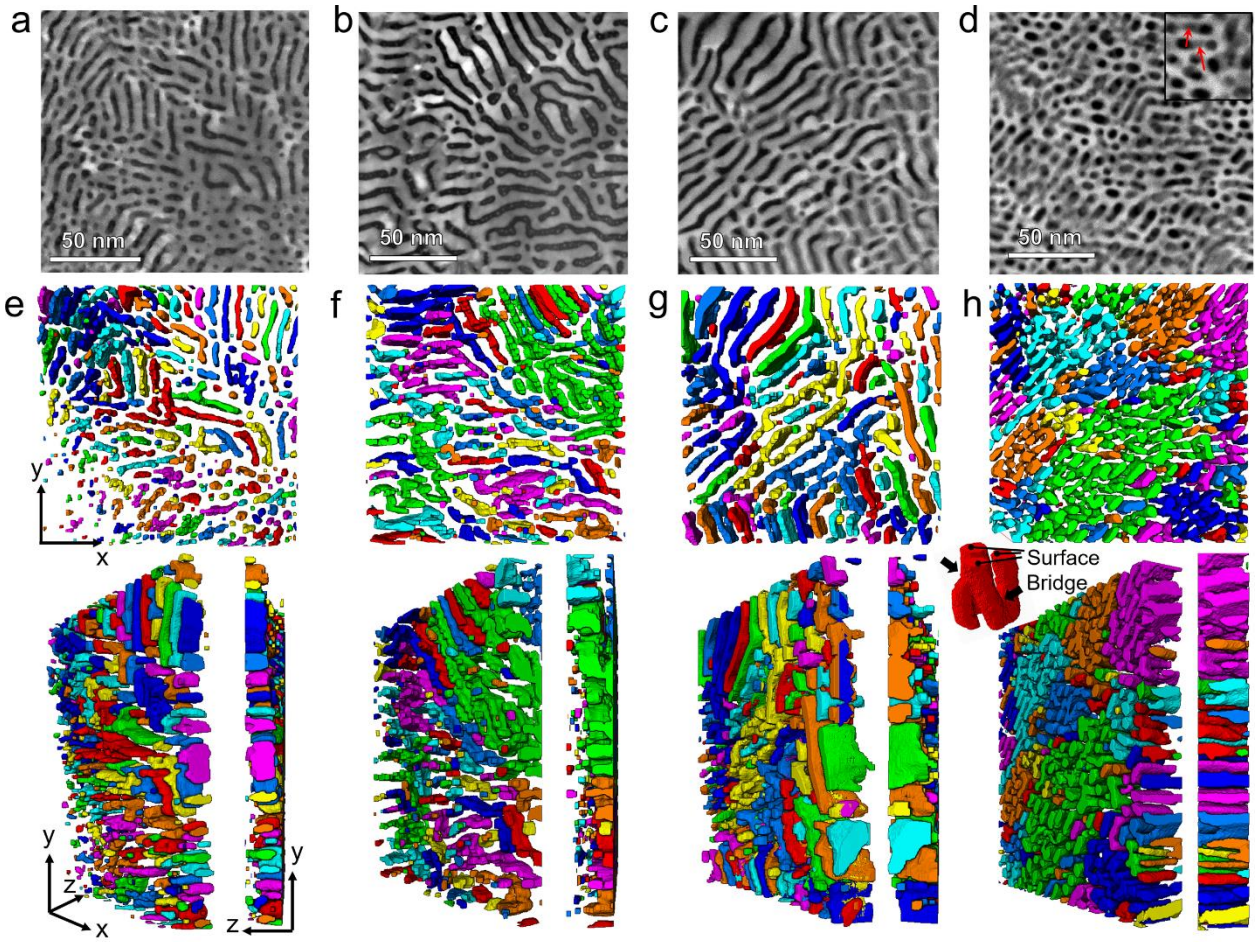

Figure 5.10. HAADF-STEM images of the Pt/CeO_2 nanocomposites annealed at (a) 500 °C, (b) 600 °C, (c) 700 °C and (d) 800 °C. (e)–(h) Reconstructed 3D structures of the different nanocomposites along three views, i.e., from the front, with 30° rotation along the y-axis, and from the side. These structures correspond to the 2D projection images shown in in the parts (a)–(d), respectively. The displayed size is 150 × 150 × 15 nm^3. The inset on the right-hand corner of (h) shows that the separated domains on the surface are connected by bridges, as marked by black arrows.

Self-assembled Pt/CeO_2 nanocomposites were then formed by oxidation of Pt_5Ce alloy to induce phase separation. The phase separation behavior in the Pt_5Ce alloy at low temperatures (400 °C) was previously studied by ex situ experiments carried out in our group [45]. In this case, the striped pattern was formed upon the diffusion of oxygen through the precipitate CeO_2 and further into the alloy with a minimized distance. The drastic change from the lamellar structure to the particle-like structure at 800 °C may therefore be attributed to the accelerated oxygen and metal diffusion rates, and so this variation in the phase-separation mechanism should therefore be considered.

5.3.4 Homological structure analysis

To quantitatively describe the homological nature of the nanocomposites, the Betti numbers, β_i, for the 2D projections and the 3D tomographic structures were computationally calculated. Considering the larger the area, the better for homology analysis, the 2D projections used for homology analysis are shown in Figures 5.11a–d rather than Figures 5.10a–d. The averaged Betti numbers from the three 2D projections for each sample are plotted in Figures 5.12a and b, where 2D–β_0 and 2D–β_1 represent the number of CeO_2 domains and enclosed Pt holes from the 2D projected STEM images, respectively. Figure 5.12a shows that the number of CeO_2 components (2D–β_0) decreased when the annealing temperature was increased from 500 to 700 ^oC

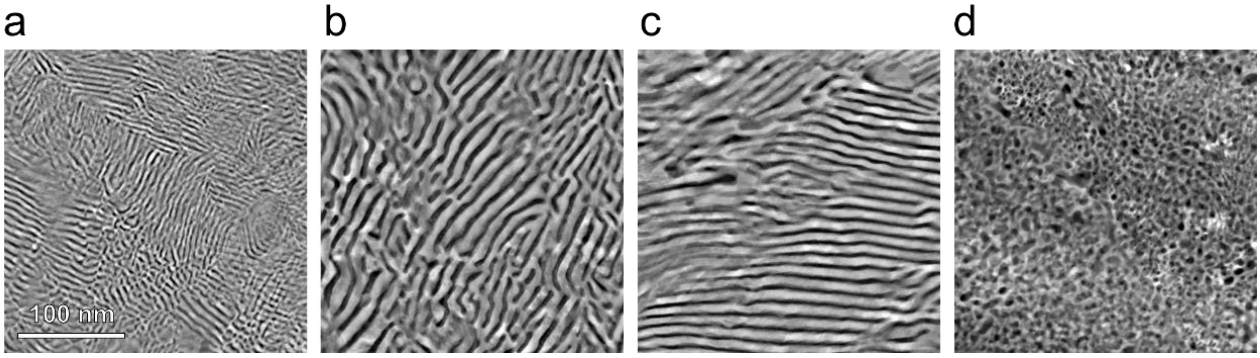

Figure 5.11. STEM images of the composites for 2D homology analysis. Samples annealed at different temperatures: (a) 500 °C, (b)600 °C, (c) 700 °C, and (d) 800 °C.

(see Figures 11a–c), and then increased to its highest value for the sample annealed at 800 ^oC. This is due to the increased volume fraction of the particle-like domain compared to the striped domain while keeping the total volume. Figure 5.12b shows that the NC600 and NC700 give the lowest 2D–β_1 values, while the NC500 and NC800 exhibit similar values. To identify the nanotexture from the topological view, the Betti numbers were plotted for each image as a function of the binarization threshold from the grayscale STEM image with background removal (Betti curves), which provided the specific characters for each pattern, as shown in Figure 5.12c. From the Betti curves, the growth and merger of the CeO_2 domains (2D–β_0) can be observed. The green curves for NC800 are characterized by smooth profile and sharp peaks. This was attributed to the fact that the transition interface and the dense small particles in the projection of the network structure are uniformly and quickly integrated with one another upon increasing the binarization threshold. The black curves for NC500

give large values of 2D–β_0, thereby indicating the presence of numerous randomly distributed mixtures of particles and short stripes. The long stripes in NC600 and NC700 (the red and blue curves, respectively) give rise to low values of 2D–β_0 and unobvious peaks. Thus, the Betti curves demonstrated the unique transient interface caused by the projection of 3D network structure in NC800.

For the displayed 3D tomographic structures given in Figures 5.10e–5.10h, the homology analysis results are shown in Figures 5.12d–5.12f. The colored CeO_2 domains were assigned to the dark-contrasted phase and the remaining invisible Pt area was assigned to the bright-contrasted phase. Figure 5.12d shows the 3D–β_0 trend representing the number of CeO_2 domains, while Figures 5.12e and 5.12f show the 3D–β_1 and 3D–β_2 results corresponding to the number of Pt channels (Pt domains running through the object or ting-shaped domains inside the object) and Pt cavities (Pt particles or stripes inside the object), respectively. Despite the fact that the β_0 has the same meaning in both the 2D projection images (Fig. 5.12a) and the 3D tomographs (Fig. 5.12d), it is interesting to note that the 3D–β_0 trends is different from that of 2D-β_0. More specifically,

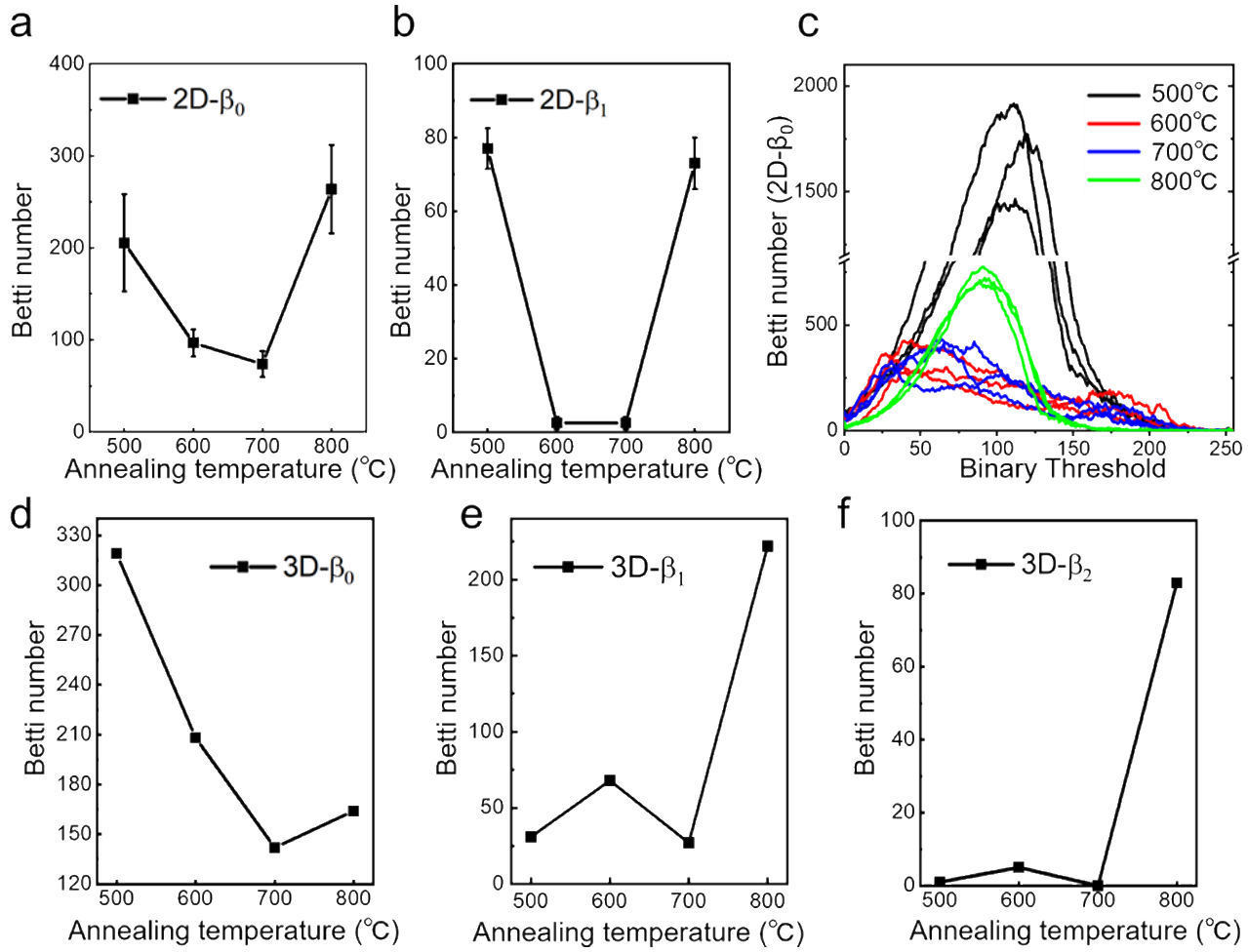

Figure 5.12. Betti numbers of the Pt/CeO_2 nanocomposites annealed at different temperatures. (a) 2D–β_0 and (b) 2D–β_1 calculated from the 2D projection image. (c) The plot of 2D–β_0 as a function of the binary threshold was used to identify the structural features for the various samples. (d) 3D–β_0, (e) 3D–β_1 and (f) 3D–β_2 as calculated from the reconstructed 3D structure.

the particle-like pattern in the 2D STEM image of NC800 exhibits the highest value of 2D–β_0, while a relatively lower value of 3D–β_0 was found for the 3D structure due to its 3D network structure that was poorly visualized by 2D projections. This difference can act as confirmation of the existence of bridge structures and the unsuitability of using 2D-β_0 to determine the network structure. As previously mentioned, the 2D images showed that the 3D CeO_2 structures in NC500, NC600 or NC700 samples tend to grow in the z-direction. In addition, the 3D–β_0 value decreased in an ascending order from NC500, NC600 and NC700 due to the presence of longer lamellae, which is consistent with the trend of 2D–β_0. Therefore, 2D projection is sufficient to describe the lamellar structures, while 3D reconstruction is necessary for network structure analysis (NC800). In contrast, the second lowest value of 3D–β_0 was obtained for NC800 with a network structure, and this value was only slightly higher than that of NC700 with a lamellae structure. In addition, for the Pt phases, no significant differences were found for 3D–β_1 and 3D–β_2 among the NC500, NC600 and NC700. The highest values of 3D–β_1 and 3D–β_2 were obtained for the network structure of the NC800, which indicates the presence of many Pt domains due to the strong phase separation behavior. As the nucleation-growth mechanism in the oxidation of Pt_5Ce alloy [37], the driving force for nucleation is strengthened at higher annealing temperature (i.e., up to 800 ^oC), leading to a high density of nuclei. Consequently, the CeO_2 nuclei grow and merge into a network structure separating the Pt phase. Based on the above 3D structural analysis, it is clear that the ionic conductivity parameters are strongly related to the 3D-β_0 because of their exactly inverse trends in the dependency of annealing temperature. Whereas, the parameters are independent of the 3D–β_1 and 3D–β_2 since NC500 and NC700, which are the same in the values of 3D–β_1 and 3D–β_2, have totally different values of $ln\sigma_0$ and E.

It is important to verify the validity of the reconstructed structure owing to its limited thickness. The homological nature of the 3D structure (β_0, β_1, and β_2) in the dependency of the thickness were investigated and shown in Figures 5.13a-c. The number of structural features, i.e., connected domains and holes, should be increased as the selected volume increases. Therefore, it is reasonable that the numbers of CeO_2 domains (3D-β_0) in NC500, NC600, and NC700 increase with the increased thickness because of the emergence of more new domains. While for NC800, 3D-β_0 slightly decreases when the thickness increased, indicating that some separated CeO_2 domains were connected in this thickness range and further confirming the "bridge effect" explained above. The 3D-β_1 and 3D-β_2 of the NC500 and NC700 are restricted in the very low value even for the 20 nm thickness, which can be explained that Pt phase is highly connected acting as a substrate. Upward trends of the 3D-β_1 for the NC600 and NC800 demonstrate the whole Pt substrate were divided by the CeO_2 precipitants. Moreover, increased 3D-β_2 for NC800 is the evidence of the Pt cavities separated by the network CeO_2 precipitants. It should be noted that when the NC600's structure thickness increase from 15 nm to 20 nm, misleading background information (i.e., the absence of features beyond the thickness of the sample, see Figure 5.2a) resulted the significant increase of the number of features. Thus, the 3D structure with 15 nm thickness is more reliable for the following discussion. Similarly, the positive relationships between the

selected area and the corresponding Betti numbers (see Figures 5.13d-f) proved the effectiveness of the reconstructed 3D structure.

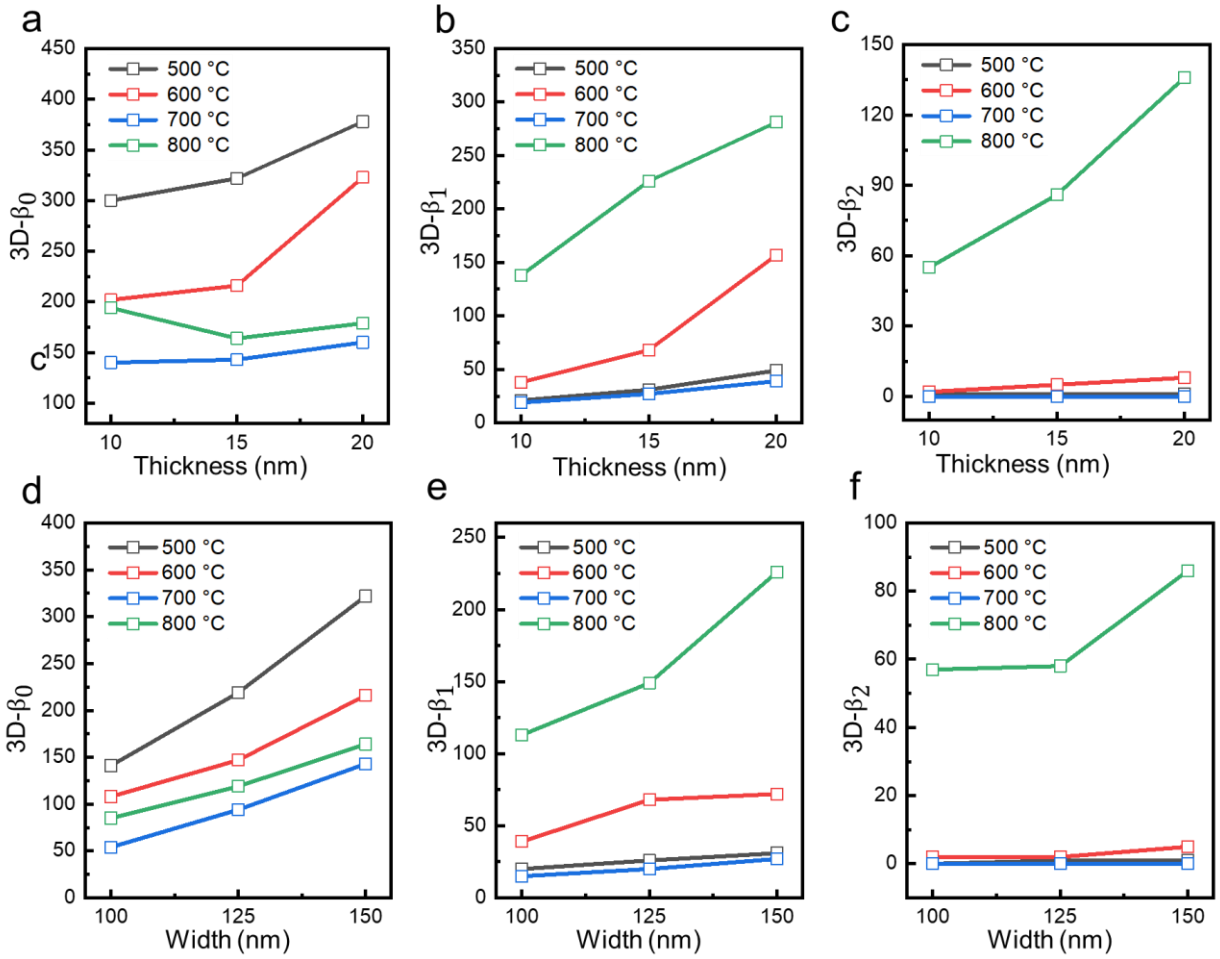

Figure 5.13. The influence of the 3D structural geometry of Pt/CeO_2 on the Betti numbers. The effect of thickness on the (a) 3D–β_0, (b) 3D–β_1, (c) 3D–β_2, and the effect of width on the (d) 3D–β_0, (e) 3D–β_1, (f) 3D–β_2. The structural width and thickness appear to have no influence on the zeroth Betti value as a function of the annealing temperature.

For the network structure, the hidden information in the thickness direction cannot be correctly displayed via the projected 2D image, and so interpretation of the structure is different from that of the reconstructed 3D structure. It is therefore necessary to employ the 3D tomographs to construct the structure-property relationship. To highlight the quantitative relationship between the 3D structure and the ionic conductivity, the dependency of both $ln\sigma_0$ and E on the 3D–β_0 (number of CeO_2 domains) was plotted in Figure 5.14. As indicated, the $ln\sigma_0$ value (green dots) has an approximate linear relationship with 3D–β_0, while the dependency of E (red dots) on the 3D–β_0 consisted of two linear curves having different slopes. The linear relationship between 3D–β_0 and $ln\sigma_0$ strongly suggests the decisive role of the topological connectivity of the CeO_2 phases as a conductive path for oxygen ions that ranged over hundreds of nanometers. The pre-exponential factor $ln\sigma_0$ is material-dependent, and is mainly affected by the hopping rate, the mobile ion concentration, and the ionic charge [46,

47]. Long stripes and network structures with highly connected ion transport pathways enable long-range transport for the increased magnitude of pre-exponential factor, $ln\sigma_0$ [48, 49]. Although the vacancy concentration varies slightly between the samples annealed at different temperatures, this has little influence on the value of the compared with the influence imparted by the conduction pathway.

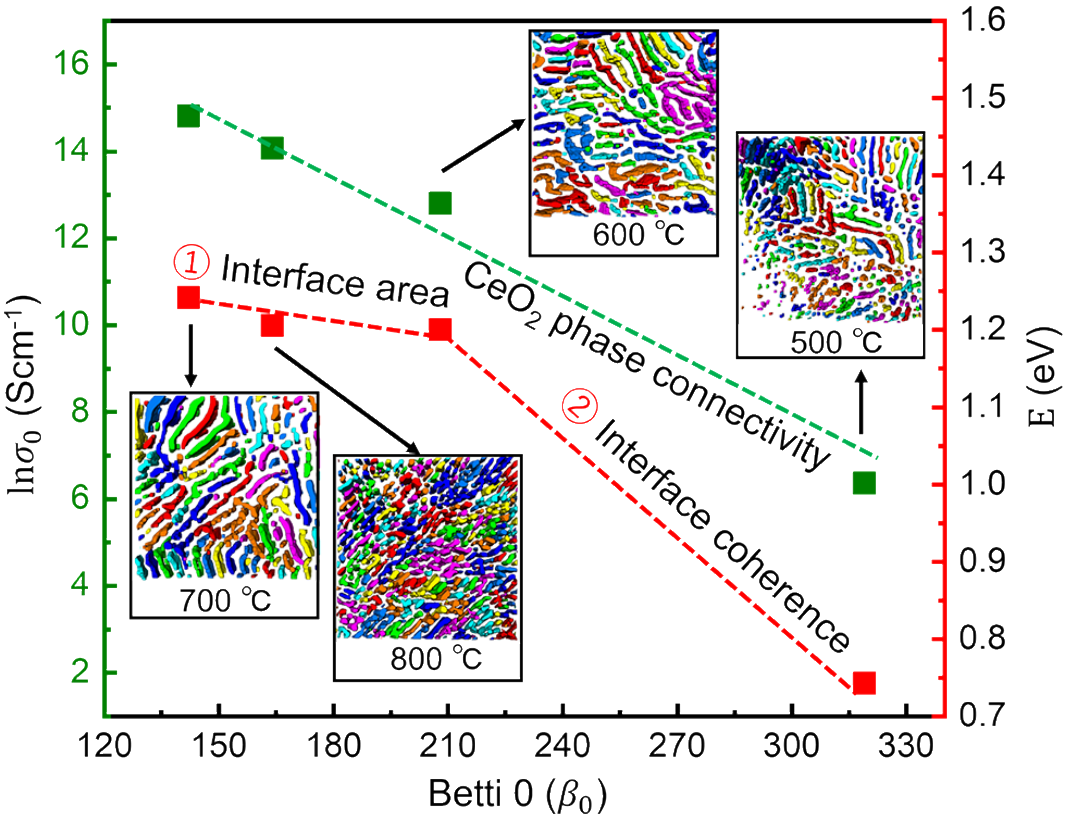

Figure 5.14. Quantitative relationship between the ionic conductivity parameters: Pre-exponential factor $ln\sigma_0$, activation energy E, and 3D–β_0. The green line indicating the trend of $ln\sigma_0$ demonstrates its strong dependence on the CeO_2 phase connectivity. The red polyline reveals two factors affecting the value of E, i.e., namely the interface coherence (steep slope) and the CeO_2 phase connectivity (gentle slope).

For fast ion transportation in the heterointerface, three factors are generally considered to affect the activation energy E, namely the interface structure, the interface area, and the space charge region [50–52]. More specifically, as explained above, compared with the epitaxial interface, partially amorphous interface regions with rich structural defects can significantly lower the activation energy. In the case of a similar semi-coherent interface, the residual strain field begins to influence E. Owing to a larger lattice misfit between the CeO_2 and Pt crystals, a certain degree of strain fields remains around the interface. The variation in the degree of the strain effect with the interface number therefore leads to a difference in the activation energy [46]. In addition, the activation energy can be lowered by increasing the interface area in the hetero-layered film [50, 53]. Based on our previous work, different Pt/CeO_2 nanocomposites with the same degree of crystallinity, a larger number of CeO_2 domains (2D–β_0), and a larger interface area gives rise to a lower value of E, indicating

the positive effects of the interface area on the oxygen ion transport [30]. This explains why the network structure with a large number of interfaces has a relatively lower activation energy. Furthermore, despite the fact that the space charge region in the interfacial region can affect the ionic conductivity, the region is limited to a Debye length, which is as small as several Å [51, 54]. This effect is pronounced only in materials with low interface concentrations [55], which is not the case for our self-assembled Pt/CeO_2 nanocomposites with rich interfaces.

5.4 Conclusion

To understand the relationship between the 3D structure and the ionic conductivity of self-assembled Pt/CeO_2 nanocomposites, different nanostructured composites were prepared by annealing Pt_5Ce at different temperatures. Upon increasing the temperature, an enhanced phase separation behavior was found to result in a transformation from a lamellar to a network structure with an improved crystalline degree at the interface. Due to the fact that 2D projected STEM is limited to depth information, 3D tomography is necessary to describe the actual morphology of the entangled network structure. Through the use of local structure analysis and phase connectivity, we found that one of the ionic conductivity parameters, i.e., the activation energy, was mainly affected by the local crystallinity at the Pt/CeO_2 interface, while another parameter, i.e., the pre-exponential factor was linearly influenced by the quantified CeO_2 phase connectivity, 3D–β_0. The homological structures of the Pt phase, including the 3D–β_1 and the 3D–β_2, have no effects on the ionic conductivity. Thus, one of homological descriptor, Betti numbers, can be acting as a bridge to connect the multidimensional structure and ionic conductivity of Pt/CeO_2 nanocomposites because of the importance of CeO_2 phase connectivity. And understanding the importance of the transportation pathway for ionic conductivity is helpful in the design of the solid-oxide fuel cell materials. We expected that the homological approach proposed herein could be extended to different nanocomposites, therefore opening up an unexplored pathway for the rational design of nanocomposites based on the homological linkage between nanotextures and functionalities.

In addition to understand the relationship between topological features, such as phase connecitvities, and properties of materials with the help of Betti numbers, the ablitiy to distinguish and classify different structures from a large amount of image data is another critical object for predicting the fianl property from a given structure. In that case, knowing the number of topological featuers is not enough because the geometry information is missing, which is also important to correctly describe an object. For this purpose, a more powerful tool, persistence diagram, should be needed for describing image data comprehensively, which will be discussed in the next chapter.

References

[1] Vaia, R. A.; Wagner, H. D. Framework for Nanocomposites. Mater. Today 2004, 7 (11), 32–37.

[2] Choi, S. M.; Awaji, H. Nanocomposites - A New Material Design Concept. Sci. Technol. Adv. Mater. 2005, 6 (1), 2–10.

[3] Yang, S. M.; Lee, S.; Jian, J.; Zhang, W.; Lu, P.; Jia, Q.; Wang, H.; Won Noh, T.; Kalinin, S. V.; MacManus-Driscoll, J. L. Strongly Enhanced Oxygen Ion Transport through Samarium-Doped CeO_2 Nanopillars in Nanocomposite Films. Nat. Commun. 2015, 6, 1–8.

[4] Ray, C.; Pal, T. Recent Advances of Metal-Metal Oxide Nanocomposites and Their Tailored Nanostructures in Numerous Catalytic Applications. J. Mater. Chem. A 2017, 5 (20), 9465–9487.

[5] Komarneni, S. Nanocornposites. 1992, 2 (12), 1219–1230.

[6] Pennycook, T. J.; Beck, M. J.; Varga, K.; Varela, M.; Pennycook, S. J.; Pantelides, S. T. Origin of Colossal Ionic Conductivity in Oxide Multilayers: Interface Induced Sublattice Disorder. Phys. Rev. Lett. 2010, 104 (11), 1–4.

[7] Puigdollers, A. R.; Schlexer, P.; Tosoni, S.; Pacchioni, G. Increasing Oxide Reducibility: The Role of Metal/Oxide Interfaces in the Formation of Oxygen Vacancies. ACS Catal. 2017, 7 (10), 6493–6513.

[8] Zhang, X.; Shen, Y.; Zhang, Q.; Gu, L.; Hu, Y.; Du, J.; Lin, Y.; Nan, C. W. Ultrahigh Energy Density of Polymer Nanocomposites Containing $BaTiO_3@TiO_2$ Nanofibers by Atomic-Scale Interface Engineering. Adv. Mater. 2015, 27 (5), 819–824.

[9] Gilardi, E.; Gregori, G.; Wang, Y.; Sigle, W.; Van Aken, P. A.; Maier, J. Interface Effects on the Ion Transport of Epitaxial $Y_2Zr_2O_7$ Films. ACS Appl. Mater. Interfaces 2017, 9 (32), 27257–27265.

[10] Pennycook, T. J.; Oxley, M. P.; Garcia-Barriocanal, J.; Bruno, F. Y.; Leon, C.; Santamaria, J.; Pantelides, S. T.; Varela, M.; Pennycook, S. J. Seeing Oxygen Disorder in YSZ/$SrTiO_3$ Colossal Ionic Conductor Heterostructures Using EELS. EPJ Appl. Phys. 2011, 54 (3), 1–11.

[11] Sato, Y. K.; Kuwauchi, Y.; Miyoshi, W.; Jinnai, H. Visualization of Chemical Bonding in a Silica-Filled Rubber Nanocomposite Using STEM-EELS. Sci. Rep. 2020, 10 (1), 1–8.

[12] Campbell, C. T. Catalyst-Support Interactions: Electronic Perturbations. Nat. Chem. 2012, 4 (8), 597–598.

[13] Gao, D.; Zhang, Y.; Zhou, Z.; Cai, F.; Zhao, X.; Huang, W.; Li, Y.; Zhu, J.; Liu, P.; Yang, F.; Wang, G.; Bao, X. Enhancing CO_2 Electroreduction with the Metal-Oxide Interface. J. Am. Chem. Soc. 2017, 139 (16), 5652–5655.

[14] Schaefer, D. W.; Justice, R. S. How Nano Are Nanocomposites? Macromolecules 2007, 40 (24), 8501–8517.

[15] Jancar, J.; Douglas, J. F.; Starr, F. W.; Kumar, S. K.; Cassagnau, P.; Lesser, A. J.; Sternstein, S. S.; Buehler, M. J. Current Issues in Research on Structure-Property Relationships in Polymer Nanocomposites. Polymer (Guildf). 2010, 51 (15), 3321–3343.

[16] Zavaliche, F.; Zheng, H.; Mohaddes-Ardabili, L.; Yang, S. Y.; Zhan, Q.; Shafer, P.; Reilly, E.; Chopdekar, R.; Jia, Y.; Wright, P.; Schlom, D. G.; Suzuki, Y.; Ramesh, R. Electric Field-Induced Magnetization Switching in Epitaxial Columnar Nanostructures. Nano Lett. 2005, 5 (9), 1793–1796.

[17] Chen, A.; Bi, Z.; Jia, Q.; Macmanus-Driscoll, J. L.; Wang, H. Microstructure, Vertical Strain Control and Tunable Functionalities in Self-Assembled, Vertically Aligned Nanocomposite Thin Films. Acta Mater. 2013, 61 (8), 2783–2792.

[18] Song, Y.; Chen, Y.; Xu, M.; Wang, W.; Zhang, Y.; Yang, G. A Cobalt-Free Multi-Phase Nanocomposite as Near-Ideal Cathode of Intermediate-Temperature Solid Oxide Fuel Cells Developed by Smart Self-Assembly. 2020, 1906979, 1–9.

[19] Jinnai, H.; Spontak, R. J. Transmission Electron Microtomography in Polymer Research. Polymer (Guildf). 2009, 50 (5), 1067–1087.

[20] Midgley, P. A.; Dunin-Borkowski, R. E. Electron Tomography and Holography in Materials Science. Nat. Mater. 2009, 8 (4), 271–280.

[21] Leary, R.; Midgley, P. A.; Thomas, J. M. Recent Advances in the Application of Electron Tomography to Materials Chemistry. Acc. Chem. Res. 2012, 45 (10), 1782–1791.

[22] Ercius, P.; Alaidi, O.; Rames, M. J.; Ren, G. Electron Tomography: A Three-Dimensional Analytic Tool for Hard and Soft Materials Research. Adv. Mater. 2015, 27 (38), 5638–5663.

[23] Zhou, J.; Yang, Y.; Ercius, P.; Miao, J. Atomic Electron Tomography in Three and Four Dimensions. MRS Bull. 2020, 45 (4), 290–297.

[24] Kübel, C.; Voigt, A.; Schoenmakers, R.; Otten, M.; Su, D.; Lee, T. C.; Carlsson, A.; Bradley, J. Recent Advances in Electron Tomography: TEM and HAADF-STEM Tomography for Materials Science and Semiconductor Applications. Microsc. Microanal. 2005, 11 (5), 378–400.

[25] Gameiro, M.; Mischaikow, K.; Wanner, T. Evolution of Pattern Complexity in the Cahn-Hilliard Theory of Phase Separation. Acta Mater. 2005, 53 (3), 693–704.

[26] Hansen, N.; Adams, D. O.; Fullwood, D. T. Quantitative Methods for Correlating Dispersion and Electrical Conductivity in Conductor-Polymer Nanostrand Composites. Compos. Part A Appl. Sci. Manuf. 2012, 43 (11), 1939–1946.

[27] Hirata, A.; Wada, T.; Obayashi, I.; Hiraoka, Y. Structural Changes during Glass Formation Extracted by Computational Homology with Machine Learning. Commun. Mater. 2020, 1 (1), 1–4.

[28] Wanner, T.; Fuller, E. R.; Saylor, D. M. Homology Metrics for Microstructure Response Fields in Polycrystals. Acta Mater. 2010, 58 (1), 102–110.

[29] Teramoto, T.; Kamiya, T.; Sakurai, T.; Kanaya, F. Betti Number Ratios as Quantitative Indices for Bone Morphometry in Three Dimensions. Comput. Methods Programs Biomed. 2018, 162, 93–98.

[30] Wen, Y.; Hashimoto, A.; Najib, A. S. B. M.; Hirata, A.; Abe, H. Topological Trends in Ionic Transport through Metal-Oxide Composites. Appl. Phys. Lett. 2021, 118 (5).

[31] Gilbert, P. Iterative Methods for the Three-Dimensional Reconstruction of an Object from Projections. J. Theor. Biol. 1972, 36 (1), 105–117.

[32] Chung, Y.-M.; Lawson, A. Persistence Curves: A Canonical Framework for Summarizing Persistence Diagrams. 2019, 1–31.

[33] Computation Homology Project (CHomp), http://conley3.rutgers.edu/.

[34] Bondarenko, A.; Ragoisha, G.; In Progress in Chemometrics Research, Pomerantsev A. L., Ed.; Nova Science Publishers: New York, 2005, pp. 89–102 (the program is available online at http://www.abc.chemistry.bsu.by/vi/analyser/)

[35] Kushima, A.; Yildiz, B. Oxygen Ion Diffusivity in Strained Yttria Stabilized Zirconia: Where Is the Fastest Strain? J. Mater. Chem. 2010, 20 (23), 4809–4819.

[36] Fabbri, E.; Pergolesi, D.; Traversa, E. Ionic Conductivity in Oxide Heterostructures: The Role of Interfaces. Sci. Technol. Adv. Mater. 2010, 11 (5).

[37] Peters, A.; Korte, C.; Hesse, D.; Zakharov, N.; Janek, J. Ionic Conductivity and Activation Energy for Oxygen Ion Transport in Superlattices - The Multilayer System CSZ (ZrO_2 + CaO) / Al_2O_3. Solid State Ionics. 2007, 178 (1–2), 67–76.

[38] Korte, C.; Keppner, J.; Peters, A.; Schichtel, N.; Aydin, H.; Janek, J. Coherency Strain and Its Effect on Ionic Conductivity and Diffusion in Solid Electrolytes - an Improved Model for Nanocrystalline Thin Films and a Review of Experimental Data. Phys. Chem. Chem. Phys. 2014, 16 (44), 24575–24591.

[39] Hojo, H.; Mizoguchi, T.; Ohta, H.; Findlay, S. D.; Shibata, N.; Yamamoto, T.; Ikuhara, Y. Atomic Structure of a CeO_2 Grain Boundary: The Role of Oxygen Vacancies. Nano Lett. 2010, 10 (11), 4668–4672.

[40] Turner, S.; Lazar, S.; Freitag, B.; Egoavil, R.; Verbeeck, J.; Put, S.; Strauven, Y.; Van Tendeloo, G. High Resolution Mapping of Surface Reduction in Ceria Nanoparticles. Nanoscale 2011, 3 (8), 3385–3390.

[41] Li, Y.; Hutchinson, T. P.; Kuang, X.; Slater, P. R.; Johnson, M. R.; Evans, I. R. Ionic Conductivity, Structure and Oxide Ion Migration Pathway in Fluorite-Based $Bi_8La_{10}O_{27}$. Chem. Mater. 2009, 21 (19), 4661–4668.

[42] Wang, Y.; Li, B.; Ji, J.; Zhong, W. H. Controlled Li+ Conduction Pathway to Achieve Enhanced Ionic Conductivity in Polymer Electrolytes. Journal of Power Sources. 2014, pp 452–459.

[43] Liu, W.; Lee, S. W.; Lin, D.; Shi, F.; Wang, S.; Sendek, A. D.; Cui, Y. Enhancing Ionic Conductivity in Composite Polymer Electrolytes with Well-Aligned Ceramic Nanowires. Nat. Energy 2017, 2 (5), 1–7.

[44] Iakoubovskii, K.; Mitsuishi, K.; Nakayama, Y.; Furuya, K. Mean Free Path of Inelastic Electron Scattering in Elemental Solids and Oxides Using Transmission Electron Microscopy: Atomic Number Dependent Oscillatory Behavior. Phys. Rev. B - Condens. Matter Mater. Phys. 2008, 77 (10), 1–7.

[45] WEN, Y.; Abe H.; Mitsuishi, K.; Hashimoto, A. Tracking the Emergence of Epitaxial Metal–oxide Interfaces from Precursor Alloys. Nanoscale 2021.

[46] Farrington, G. C.; Briant, J. L. Fast Ionic Transport in Solids. Science. 1979, 204 (4400), 1371–1379.

[47] Lee, S.; Zhang, W.; Khatkhatay, F.; Wang, H.; Jia, Q.; Macmanus-Driscoll, J. L. Ionic Conductivity Increased by Two Orders of Magnitude in Micrometer-Thick Vertical Yttria-Stabilized ZrO_2 Nanocomposite Films. Nano Lett. 2015, 15 (11), 7362–7369.

[48] Choi, J. H.; Ye, Y.; Elabd, Y. A.; Winey, K. I. Network Structure and Strong Microphase Separation for High Ion Conductivity in Polymerized Ionic Liquid Block Copolymers. Macromolecules 2013, 46 (13), 5290–5300.

[49] Liu, W.; Liu, N.; Sun, J.; Hsu, P. C.; Li, Y.; Lee, H. W.; Cui, Y. Ionic Conductivity Enhancement of Polymer Electrolytes with Ceramic Nanowire Fillers. Nano Lett. 2015, 15 (4), 2740–2745.

[50] Korte, C.; Peters, A.; Janek, J.; Hesse, D.; Zakharov, N. Ionic Conductivity and Activation Energy for Oxygen Ion Transport in Superlattices-the Semicoherent Multilayer System YSZ (ZrO_2 + 9.5 mol% Y_2O_3)/Y_2O_3. Phys. Chem. Chem. Phys. 2008, 10 (31), 4623–4635.

[51] Azad, S.; Marina, O. A.; Wang, C. M.; Saraf, L.; Shutthanandan, V.; McCready, D. E.; El-Azab, A.; Jaffe, J. E.; Engelhard, M. H.; Peden, C. H. F.; Thevuthasan, S. Nanoscale Effects on Ion Conductance of Layer-by-Layer Structures of Gadolinia-Doped Ceria and Zirconia. Appl. Phys. Lett. 2005, 86 (13), 1–3.

[52] Pergolesi, D.; Gilardi, E.; Fabbri, E.; Roddatis, V.; Harrington, G. F.; Lippert, T.; Kilner, J. A.; Traversa, E. Interface Effects on the Ionic Conductivity of Doped Ceria-Yttria-Stabilized Zirconia Heterostructures. ACS Appl. Mater. Interfaces 2018, 10 (16), 14160–14169.

[53] Fabbri, E.; Pergolesi, D.; Traversa, E. Ionic Conductivity in Oxide Heterostructures: The Role of Interfaces. Sci. Technol. Adv. Mater. 2010, 11 (5).

[54] Leon, C.; Santamaria, J.; Boukamp, B. A. Oxide Interfaces with Enhanced Ion Conductivity. MRS Bull. 2013, 38 (12), 1056–1063.

[55] Sun, L.; Marrocchelli, D.; Yildiz, B. Edge Dislocation Slows down Oxide Ion Diffusion in Doped CeO_2 by Segregation of Charged Defects. Nat. Commun. 2015, 6, 1–10.

Chapter 6 Structural description by persistence diagram

As mentioned in the previous chapters 4 and 5, the quantitative relationships between 2D or 3D structures in Pt/CeO_2 nanocomposites and their ionic conductivities can be identified using a homology descriptor, Betti numbers, considering the role of CeO_2 phase connectivity in material structure–property relationships. However, more detailed information about Pt/ CeO_2 nanostructures, such as the size and shape of CeO_2 domains, is required for in-depth structural classification. To obtain both homological and geometrical information about the structures, persistence diagram (PD), another homological tool, was used to represent each STEM image. It is proved that PDs can be used to characterize the Pt/CeO_2 structures observed by TEM imaging. The size and shape of the CeO_2 domains can be identified from the PDs. Besides, the combination of PDs and principal component analysis, a machine learning model, enabled us to perform structural classification. The application of the PDs to TEM imaging analysis paves the way for fast and convenient structural analysis.

6.1 Introduction

Metal/oxide nanocomposites with strong interfacial interactions have been immensely studied as catalysts and electrode materials because of their excellent chemical and physical properties [1,2]. Due to the importance of material configuration for the final composite performance, various nanocomposites structures were developed to optimize their properties. As a result, the investigation of structure-property relationships is of high interest for material design. Traditionally, geometric characterizations, such as size, density, and shape are used as structural descriptors. However, this approach fails to identify and differentiate minor differences among various structures, which may have different functionalities. Furthermore, the processing of large datasets become time-consuming and impractical.

Topological data analysis (TDA) is a powerful tool that has been employed in various research fields, such as medical biology [3-5], materials science [6-8], sensor and social networks [9, 10], and cosmic web [11], in the past decades due to its unique characteristics and efficiency. Unlike the traditional geometric measurements, TDA can be used to identify multidimensional topological intrinsic features known as homology groups or dimensional holes, including connected components (0-dimensional holes), loops or tunnels (1-dimensional holes), enclosed pores (3-dimensional features), and so on. These topological invariants are known as Betti numbers. Based on the most basic descriptors, this approach facilitates the differentiation between two complicated structures, as already discussed in Chapters 4 and 5. The important role of the connective components or crack holes in the functionality can be identified [12-14]. On the contrary, the total Betti numbers can give the whole information for static data with little geometric clues; thus, the information about where and how structural difference occur cannot be obtained. Persistent homology (PH) acts as a bridge between geometry and topology. PH tracks the appearance and disappearance of the homology groups through continuous filtration. Each homological feature is recorded with its birth time, b_i, (appearing) and death time,

d_i, (disappearing), and birth and death positions can be identified by reverse analysis. Therefore, PH provides invaluable structural information and has been used for the characterization of a biological structure [15], a magnetic domain structure [16], and amorphous material structures [8, 17], as well as image data analysis [18]. Furthermore, PH-based machine learning has been employed for the structural classification and prediction of even more complicated systems [19-22].

In our previous work [23, 24], the basic homology descriptor, Betti numbers, was applied to analyze the 2D and 3D structures of self-assembled Pt/CeO_2 nanocomposites, which were detected by scanning transmission electron microscopy (STEM) imaging and STEM tomography (Chapters 4 and 5), respectively. The quantitative relationship among the Betti number β_0, CeO_2 phase connectivity, and oxygen ion conductivity was established. As oxygen ions are transported along the interface with rich oxygen vacancies, the connectivity of the CeO_2 phase and the total interface area positively affect oxygen transportation. I applied PDs to visualize the topological features during filtration from the STEM images and study their relationship with the oxygen ion conductivity. Finally, the various structures obtained by changing the annealing conditions, gas ratio ($CO:O_2$), and temperature were classified by principal component analysis (PCA). The aim of this work was to evaluate whether PH can be used to correlate Pt/CeO_2 nanostructure with the ion transportation property.

6.2 Experimental

Figure 6.1 illustrates the processes used for the application of PH to the classification of various Pt/CeO_2 nanocomposites structures. All the structures obtained using various gas ratios and annealing temperatures were the same with those reported in Chapters 4 and 5. It includes structural image collection, PH analysis, and PCA. The details are explained in the following sections:

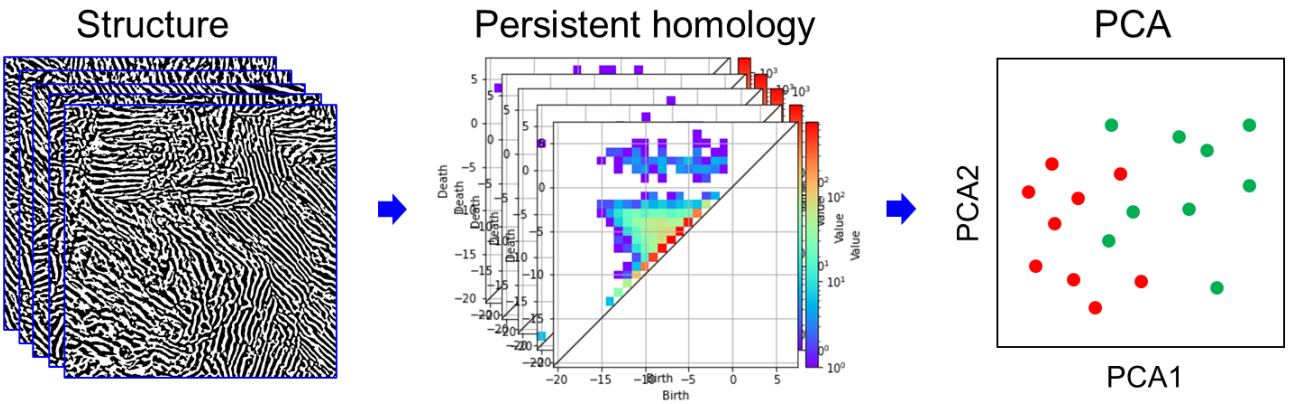

Figure 6.1. Classification of various structures in Pt/CeO_2 nanocomposites by combination of persistent homology and machine learning.

6.2.1 Structural images collection

Phase-separated Pt/CeO_2 nanocomposites were prepared by the annealing of the Pt_5Ce alloy. By changing the annealing temperature (500, 600, 700, and 800 ^oC) and syngas ratio ($CO:O_2$ = 0:1, 1:1, 2:1, and 3:1), different composites with various structures were obtained. The structures obtained using gas ratios of 0:1, 1:1, 2:1, and 3:1 were named as G01, G11, G21, and G31, respectively. The structures annealed at 500, 600, 700, and 800 ^oC were named as NC500, NC600, NC700, and NC800, respectively. They were characterized by STEM imaging (JEOL 2100F, Japan). Several images (4 from each gas ratio group and 7 from each temperature group) were selected, and all the images had the same size of 1024 pixel ×1024 pixel. The scale was 0.44 nm per pixel for the gas ratio groups and 0.34 per pixel for the temperature groups. Background subtraction was performed by filtering low-frequency signals in the FFT image. Due to the compositional contrast in the STEM images, Pt and CeO_2 phases were easily identified as the bright and dark regions, respectively. Binary images were then easily obtained using the Gaussian thresholding method.

6.2.2 Computational homology analysis

Persistence diagrams (PDs) were computed from binary images using the data analysis software "HomCloud" [25]. Each pixel in the binary image was assigned a value according to the Manhattan distance. The interested phase was (black) CeO_2, so black pixels were labeled with negative values, white pixels were labeled with positive values. The black pixels adjacent to white pixels were regarded as –1, while the white pixels adjacent to black pixels were regarded as +1. Through the filtration, that is, the increase in the value of the Manhattan distance, the growth and death of the black phase can be tracked. Owing to the role of CeO_2 phase connectivity in oxygen ion transportation, I focused on the 0-th homology. To compute the histograms from the PDs along the x- and y-axis, the targeted regions were clipped into squares in the range of [-25, 10] with a bin to be 36.

6.2.3 Principal component analysis

To apply machine learning models, the computed histograms were converted into the persistence image for vectorization [26]. As mentioned in the reference [27], the persistence image ρ for a PD $D = \{(b_i, d_i) \in \Delta: i = 1, \dots p)$ is defined by a function of space $\mathbb{R}^2$ as

$$\rho(x, y) = \sum_{i=1}^{p} \omega(b_i, d_i) \exp\left(-\frac{(b_i - x)^2 + (d_i - y)^2}{2\sigma^2}\right.$$

$$\omega(b, d) = \arctan\left(C(d - b)^p\right.$$

where $\rho(x, y)$ is a vector in $\mathbb{R}^2$ representing a PD, and $\omega(b, d)$ is a weight function. Here the variable parameters are C, p, and σ, and they were set to be (2.0, 0.5, 1.0), respectively, which are the same with those reported in reference [27]. The learned vectors were classified by PCA. Finally, for explicitly identifying the geometric structures of the critical areas on the diagram, inverse analyses of the pairs were conducted.

6.3 Results and discussion

6.3.1 Structures prepared by different annealing conditions

The annealing of the Pt_5Ce alloy in the syngas of CO and O_2 generates nanostructured Pt/CeO_2 composites. Changing the syngas ratio and the annealing temperature enables us to form nanocomposites with different nanostructures. The optimized binary images of various structures analyzed by STEM imaging are shown in Figure 6.2. Figures 6.2a–d show the binary images with different gas ratios (G01, G11, G21, and G31), and Figures 6.2e–h show those of different annealing temperatures (NC500, NC600, NC700, and NC800). To reveal the correlation between CeO_2 domains connectivity and the ionic conductivities of the Pt/CeO_2 nanocomposites, the average width of the CeO_2 phase (calculated from about 200 data points), the CeO_2- phase area fraction, and the number of black CeO_2 domains in various structures are summarized in Table 6.1.

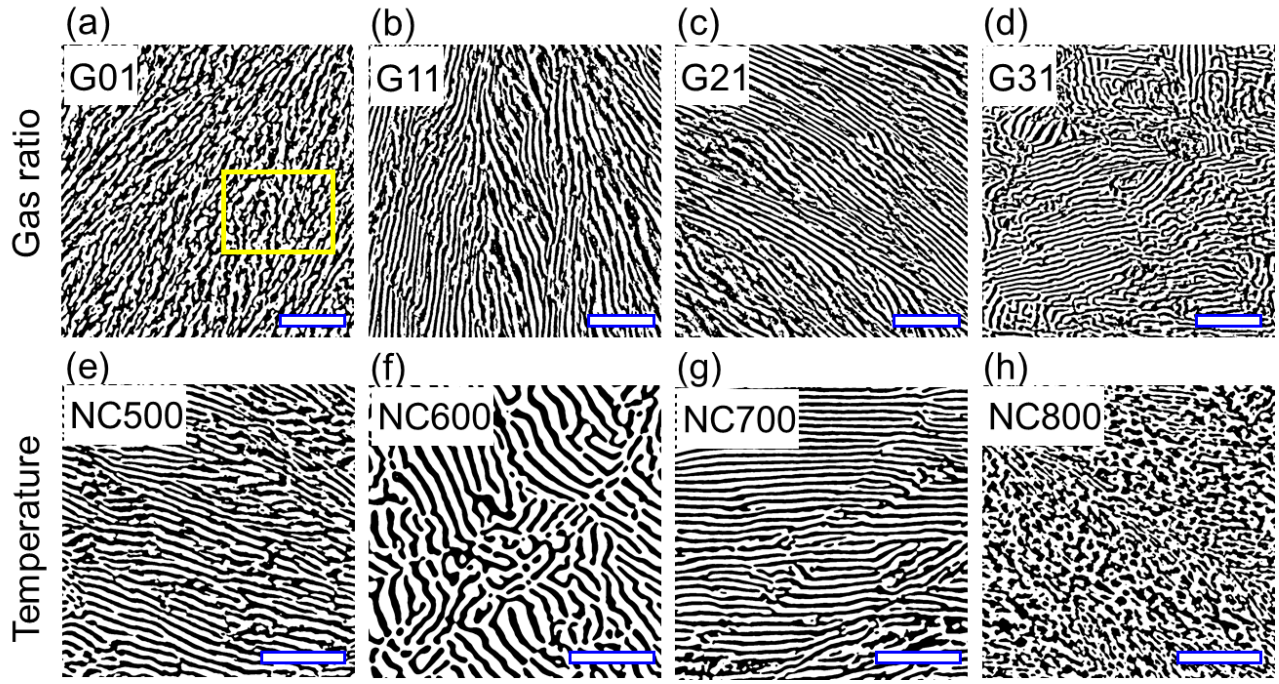

Figure 6.2. Binary images from the STEM images of different structures obtained by changing the syngas ratio ($CO:O_2$), (a) G01, (b) G11, (c) G21, and (d) G31, and the annealing temperature: (e) NC500, (f) NC600, (g) NC700, and (h) NC800. The scale bars are 100 nm for all images.

According to the phase separation mechanism described in Chapter 3, metal atom segregation in the precursor alloy and inward oxygen diffusion to react with the Ce-rich alloy resulting the formation of periodic striped patterns. As the same precursor Pt_5Ce was used, the fractions of the CeO_2 phase were nearly the same at 46% for all samples. The balance between segregation and oxidation determines the shape of precipitants. With the increased CO to O_2 ratio, that is, decreased oxygen partial pressure, the driving force for oxidation decreased giving more time for compositional segregation. Consequently, the length of the striped CeO_2 decreased, and its width decreased. However, owing to the minor difference in oxygen pressure, only slight differences were found in the structures. Almost all the structures featured long striped patterns, shorter stripes

were observed in G31, consisting with the theoretical results. With the increased annealing temperature, the phase separation process was strengthened. As mentioned in Chapter 5, the inward oxygen diffusion and Pt/Ce count diffusion accelerated at higher temperatures. At a lower temperature (500 ^{o}C), small particle-like CeO_2 domains and narrow stripes were formed, as shown in Figure 6.2e. With the further increase in the annealing temperature to 600 ^{o}C, larger islands and wider striped CeO_2 domains occurred because of the increased diffusion rate of metal atoms (Pt, Ce) in the alloy, as shown in Figure 6.2f. For NC700 (see Figure 6.2g), more but narrower stiped patterns were found compared with those of NC600 because of the significantly increased inward oxygen diffusion, which preventer metal atom diffusion at the oxidation interface. After a certain temperature (800 ^{o}C), the oxidation-induced striped patterns of Pt/CeO_2 nanocomposites transformed into a network structure because of the strong phase separation behavior, as shown in Figure 6.2h.

Table 6.1 Measured measured geometric and topological information of various structures

Sample	Width of CeO_2/nm	Width of CeO_2/pixel	Black-phase area/%	Betti number, β_0
G01	4.7± 1.1	10.7± 2.3	45.7± 2.4	198.8± 45.9
G11	5.2± 0.8	11.8± 1.8	46.8± 0.9	156.5± 50.7
G21	5.0± 0.9	11.4± 2.0	46.4± 0.9	199.3± 59.8
G31	4.9± 0.6	11.1± 1.4	45.8± 1.6	251.3± 48.6
NC500	2.7± 0.6	7.9± 2.0	47.8± 0.7	187.0± 75.0
NC600	5.2± 1.1	15.8± 3.2	45.2± 1.8	115.7± 50.6
NC700	4.1± 0.8	12.0± 2.4	47.0± 1.4	76.7± 19.6
NC800	3.4± 0.7	9.8± 2.0	47.0± 1.6	341.6± 89.6

6.3.2 Persistent homology analysis

The 0th PD allows tracking changes in CeO_2 domains in the filtration of the Manhattan distance, providing information about CeO_2 phase connectivity. For the computed birth–death pairs (b_i, d_i) in the 0th PD, the specific geometric structures of CeO_2 the phases can be predicted. To understand what type of information can be obtained from the PD, artificial images of black island-like domains having distinct sizes, densities, and connections were applied for PH computation. Figure 6.3 shows the birth–death pairs and their corresponding artificial structures. All the birth values are negative because of the negative Manhattan distance for black pixels, and all spots are located above the diagonal line since the death time d_i is always larger than the birth time b_i. Our PDs shown in Figure 6.1 had two distinct regions; thus, two PD regions were identified: the upside cloud region ($d_i > 0$), and the downside triangle region ($d_i < 0$). The difference between the two different regions in the PD is that the islands are isolated in the cloud region, whereas they are connected in the triangle region. In the cloud region, the more negative the birth time b_i is, the larger are the black islands; the higher the death time d_i is, the larger is the distance between the two nearest islands (distance between the two nearest

borders rather than the centers, marked by blue dashed arrows). In the triangle region, the islands (marked by green arrows) are connected by a bridge (marked by red arrows) to form a stripe structure. The birth time b_i represents the size of the islands, that is, the more negative b_i is, the larger are the islands and the cloud region. The death time d_i represents the size of the bridge, that is, the more negative d_i is, the larger are the bridges. More importantly, in the triangle region, the pairs far from the diagonal line, indicated by pink color, correspond to dumbbell-like structures consisting of two larger islands and a narrower bridge. In other words, the narrow bridges are noises that can be negligible compared to the islands with a relatively larger size. Notably, Betti number β_0 of the binary image measured (see Table 6.1), which is related to the ionic conductivity, can also be obtained from the PD. The total number of pairs in the cloud region ($N_{di>0}$) equals β_0.

Based on the above explanation, the pairs in the cloud region give the maximum width of islands and the distance between two islands, but not the shape of islands. On the contrary, the pairs in the triangle region give the shape of islands. Many pairs closing to the diagonal line indicate a stripy pattern. The domains become inhomogeneous in the direction further away from the diagonal line, which are composed of two relatively large domains and a narrow bridge. Usually, we use the width and length information to describe an object. As the birth time indicates the size of islands, the average birth time for all pairs in the PD gives us the average

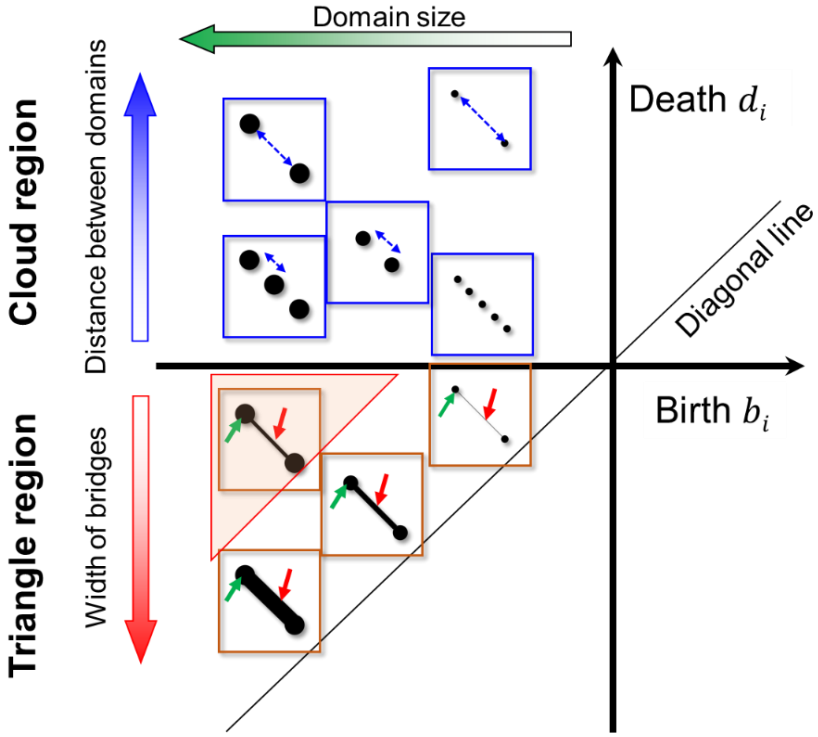

Figure 6.3. Typical geometric structure in the 0th persistence diagram. Two regions are separated: the cloud region and the triangle region. The blue arrows in the cloud region indicate the distance between two near black islands. The green and red arrows in the triangle region represent the black islands and the bridges between two black islands, respectively. The pink marked triangle covers the dumbbell-like islands where the bridges are noises that can be negligible.

width of islands. Based on the definition of the Manhattan distance, the width of an island equals twice the Manhattan distance, which is $W = 2b_{avg}$. Given the known total area of black domains, the average length information can be found by Length L= Area A/ width W. For an image displaying numerous islands, the average length $L_{avg} = A/(N \times 2b_{avg})$, where N is the number of isolated islands in the image. The number of islands should be equal to β_0, that is, number of pairs in the cloud region. However, the pairs in the triangle region far from the diagonal line correspond to the dumbbell-like structures, and the bridges can be negligible. In that case, the pairs located on the top left of the triangle region (marked by the pink area) should also contribute to the number of isolated islands. Therefore, $N = N_{di>0} + N_{marked}$, where N_{marked} is the number of pairs in the marked pink region. As a result, the average width and length of islands can be estimated from the PD.

6.3.3 Persistent homology for experimental STEM images

Figures 6.4a–d show the average (from four images) 0^{th} PD of the different structures obtained using various gas ratios. The bins of the histogram (PD) were set to 36 with each bin containing a birth–death pair corresponding to the CeO_2 domains, and the intensities of the pairs are indicated by the colors with high (resp. low) intensity by red (resp. violet). All the PDs had the characteristics of the cloud and triangle regions, indicating that these nanostructures contained isolated and connected islands, respectively. The intensity profiles along the x- and y- axes of PDs were plotted, as shown in Figures 6.4e–h and 6.4i–l, respectively. The

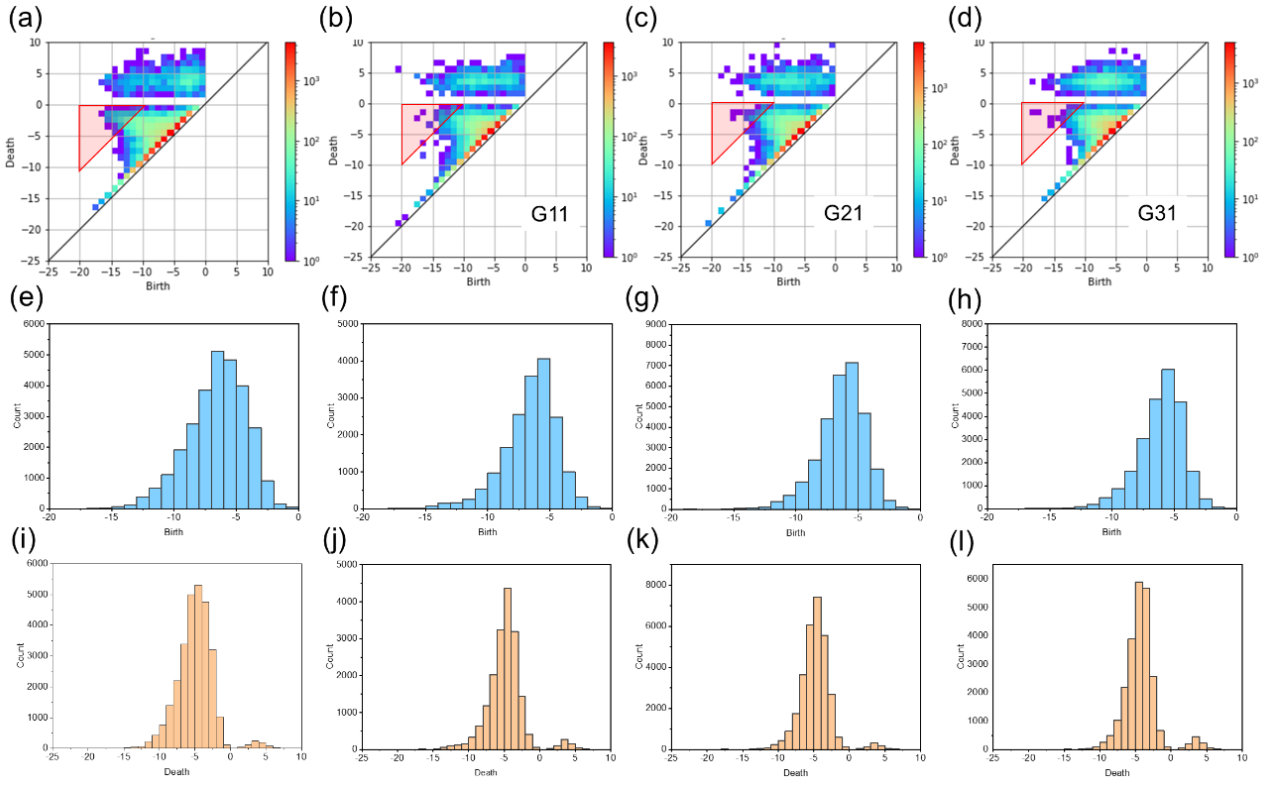

Figure 6.4. Summed 0^{th} PDs from the 4 images for (a) G01, (b) G11, (c) G21, and (d) G31. (e)–(h) Corresponding intensity profiles along the x-axis of the upside PDs. (i)-(l) Corresponding intensity profiles along the y-axis of the upside PDs.

dispersion along the horizonal direction of both regions decreased, and the vertical direction of the triangle region shrunk with the increased gas ratio. Minor difference was found in pair density in the triangle region, implying the similar features of the islands. As marked by the red triangles in Figures 6.4a-d, the pairs in the triangle region of G01 are much more than those in others, indicating the presence of many dumbbell-like domains in the G01 structure. Figure 6.5 shows the inverse analysis for the pairs in the pink-area that far from the diagonal line. Figure 6.5a shows the magnified image of the yellow rectangle area in Figure 6.3a, where red circles indicate the dumbbell-like structures. Figure 6.5b shows the corresponding pairs of the extracted dumbbell-like structures in PD, which are located in the red triangle shown in Figure 6.4a. Considering that the average birth time is close to 10, the marked regions for all PDs are determined to be the areas where d_i -b_i =10. It means that when the size difference between the bridge and the domains of the dumbbell-like islands is larger than 10 pixels, the bridges can be negligible.

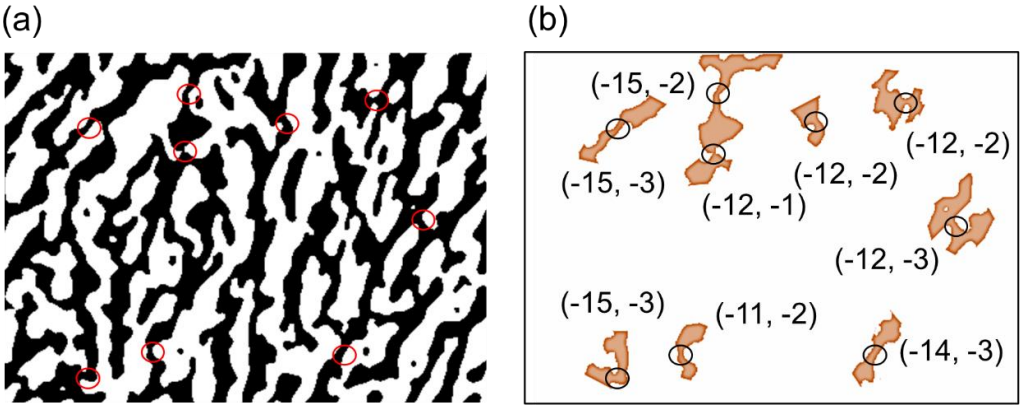

Figure 6.5. (a)Magnified image of the yellow area in Figure 6.3a. The red circles indicate the negligible bridges of the dumbbell-like domains. (b) Extracted dumbbell-like domains and corresponding homology pairs, which are located in the pink-marked area in Figure 6.4a.

For the structures obtained at different temperatures, the computed PDs are shown in Figures 6.6a–d. The difference of pairs density in the cloud region among different structures is large, in which the lowest and highest density was clearly seen in NC700 and NC800, respectively. The highest density in the marked region indicates the inhomogeneous domains in NC800. Similarly, the intensity profiles along the x- and y- axes of PDs are shown in Figures 6.6e–h and Figures 6.6i–l, respectively. The dispersion of both the cloud region and the triangle increased with the increased temperature.

To clearly identify the differences between the PDs, the average birth time for all regions b_{avg}, that is, the average width of islands, W_{avg}, the number of islands in the cloud region, $N_{di>0}$, and the number of islands in the marked region, N_{marked}, are listed in Table 6.2. The trends of $N_{di>0}$, which is β_0, are the same as those discussed in Chapters 5 and 6. Figures 6.7a and 6.7b show the twice b_{avg} and the statistical data of the domain width (in Table 6.1) of the structures obtained using different gas ratios and temperatures, respectively. Since no difference was found in the width of CeO_2 domains among the structures obtained using different gas ratios, it is difficult to describe the relationship between twice the average birth time $2b_{avg}$ and manual statistical data (see Figure 6.7a). Meanwhile, the average birth time $2b_{avg}$ represent the width of the CeO_2 phases as they share

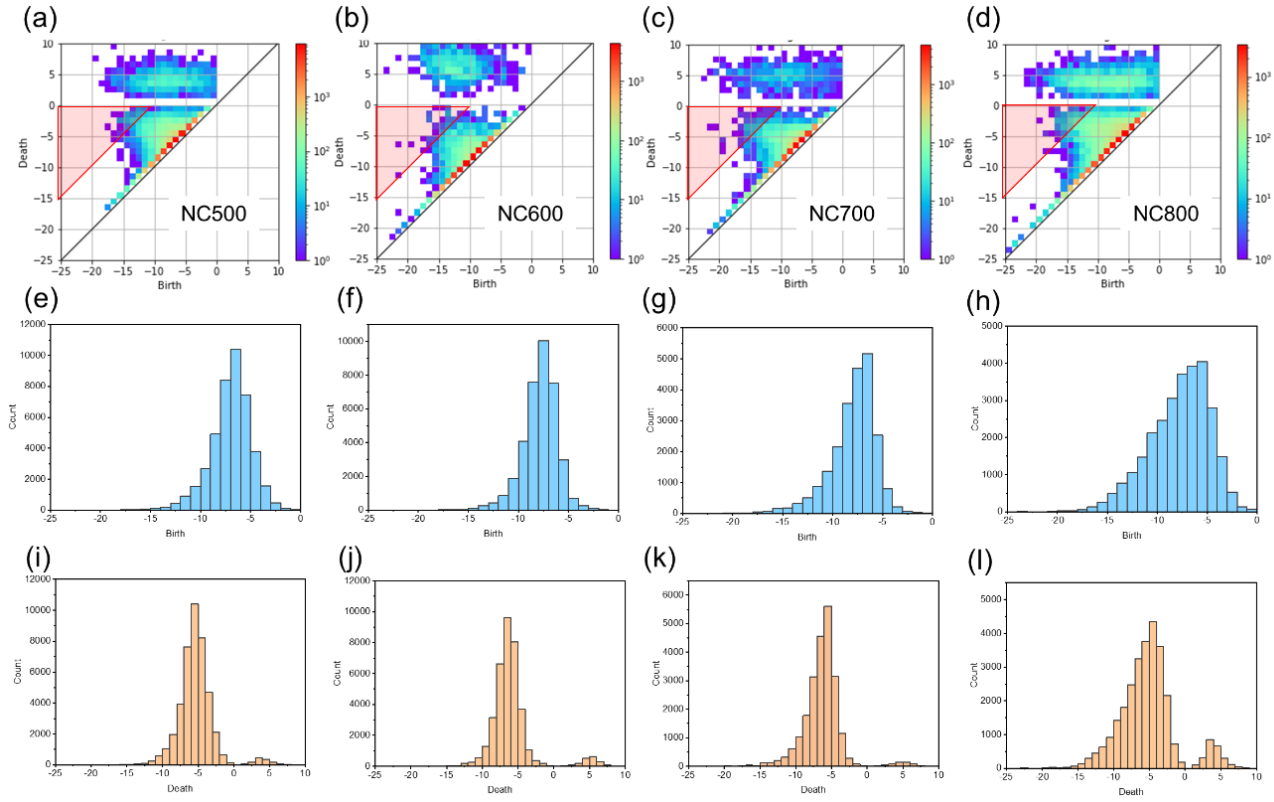

Figure 6.6. The summed 0th PDs from the 4 images for sample of (a) NC500, (b) GNC600, (c) NC700, and (d) NC800. (e)-(h) Corresponding intensity profiles along the x-axis of the upside PDs. (i)-(l) Corresponding intensity profiles along the x-axis of the upside PDs.

the same trend against temperature (see Figure 6.7b). Moreover, according to the difference between the $2b_{avg}$ and real data, the average birth time b_{avg} is actually 1 to 1.5 times the width of CeO_2 domains. Here we use $1.5b_{avg}$ representing the domain width. The high values of N_{marked} for G01 and NC800 means the several dumbbell-like structures in the structural images, which can be seen from Figure 6.2a. Since all the patterns were formed by the complete phase separation of the same alloy, Pt_5Ce, the area of the CeO_2 phase should be the same, which was assumed to be 46% according to the statistical data shown in Table 6.1. Therefore, the average length of domains can be obtained by: $L_{avg} = A/(N \times 1.5b_{avg})$. Noted that N is the sum of pairs from several images (4 for gas ratio group and 7 for temperature group). The results of calculated length value L_{avg} and the aspect ratio of the domains are shown in Table 6.2. G11 has a highest value, indicating the existence of long stripes in the pattern, which is consistent with the structures observed from STEM images (see Figure 6.2b). In contrast, the lowest value of L_{avg} (8.40) for NC800 suggests particle-like patterns, which can also be confirmed by Figure 6.2h. In other words, the application of PD to TEM images can not only give us the ionic conductivity-related β_0 but also enable us to extract the geometric information of the structures, such as the width and shape of domains. Moreover, it reduces time consumption compared to traditional statistical methods.

Table 6.2 Summarized statistical data of the persistence diagrams for various structures

Sample	Average birth time, b_{avg}/pixel	Pairs in the cloud region, $N_{di>0}$	Pairs in the marked region, N_{marked}	Average length, L_{avg}/pixel	Length/width ratio of CeO_2 domains
G01	-7.0± 2.3	795	187	187.1	17.82
G11	-7.1± 2.2	626	33	274.9	25.81
G21	-6.8± 2.0	797	29	229.0	22.45
G31	-6.6± 1.9	1005	17	190.7	19.26
NC500	-7.5± 2.1	1309	95	213.8	19.00
NC600	-10.7± 2.3	810	39	247.8	15.43
NC700	-8.5± 2.4	537	74	433.4	33.99
NC800	-8.3± 3.1	2391	201	104.6	8.40

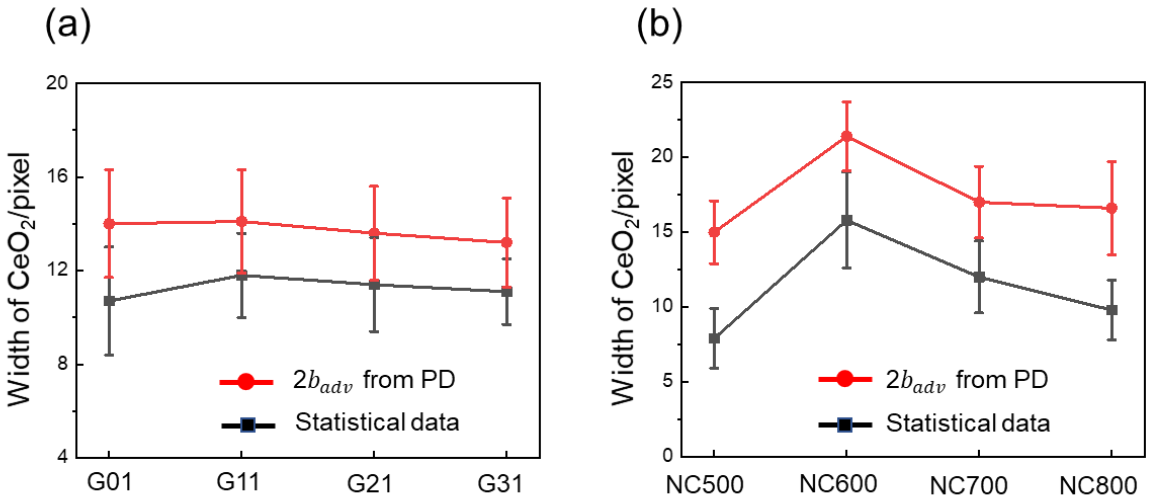

Figure 6.7. Comparison of twice the average birth time and the statistical data of CeO_2 domain width for the samples obtained using various (a) gas ratios, and (b) annealing temperatures.

6.3.4 Structural classification

Based on the feasibility of differentiating the structures using PD, we can further process and classify a large amount of data using machine learning models, which is promising for the structural prediction and designation of electrode materials.

The 0th PDs were vectorized using the persistence images, where the parameters were set to be σ = 2.0, C = 0.5 and p = 1.0 to classify different structures. Each TEM image corresponded to one persistent diagram and one vector in the space. After vectorization, persistence image vectors were projected into two-dimensional space for visualization. The results for different gas ratios and temperatures are shown in Figures 6.5a and 6.5b, respectively. The x- and y-axes represent the first and second principal component planes, respectively. The first principal components correlate with the gas ratio at a maximum degree, while the second principal components are independent of them at a minimum degree. Distinct colors are assigned to each annealing condition. Four groups in Figure 6.5a have characteristic differences from the persistence image vectors. Due to the small data for each sample (4 images per sample), it is difficult to classify them. For the different temperatures with increased data (15 images per sample) in Figure 6.5b, the location of each sample is different. Therefore, PH-based machine learning is suitable for the classification of TEM images of phase-separated Pt/CeO_2 nanocomposites. More data are required to improve the classification with clearer boundaries among different areas.

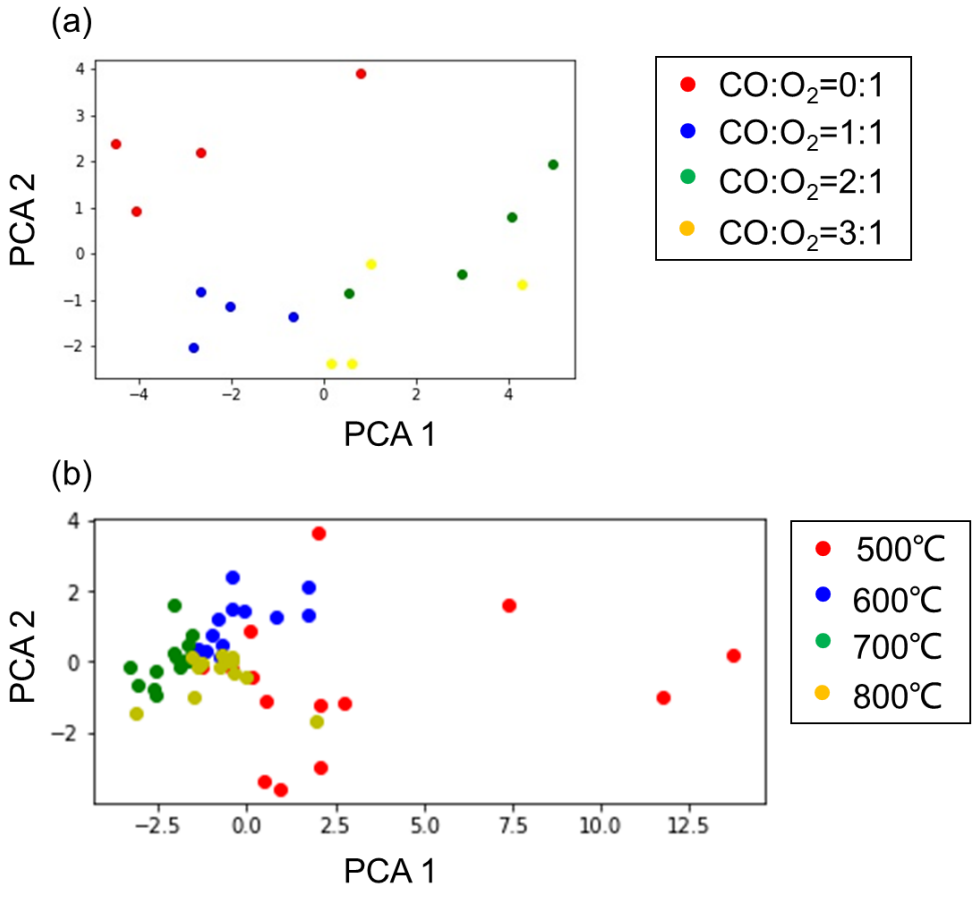

Figure 6.8. Projections of the persistence diagrams on the first and second principal component planes in PCA for various (a) gas ratios, and (b) annealing temperatures.

6.4 Conclusion

We applied applied persistence homology to analyze and classify Pt/CeO_2 nanostructures. Using PDs, not only the connectivity of the CeO_2 phase but also average width and length of the separated CeO_2 domains or islands were statistically obtained. The stripes and particle-like islands of CeO_2 were discerned according to the statistical data. Moreover, we showed that the combination of PH and PCA has the potential to classify different structures using machine learning. These findings can pave the way for an in-depth understanding of nanomaterials structure–property relationships based on the analysis of large datasets obtained from TEM imaging.

References

[1] Liu, X.; Iocozzia, J.; Wang, Y.; Cui, X.; Chen, Y.; Zhao, S.; Li, Z.; Lin, Z. Noble Metal-Metal Oxide Nanohybrids with Tailored Nanostructures for Efficient Solar Energy Conversion, Photocatalysis and Environmental Remediation. Energy Environ. Sci. 2017, 10 (2), 402–434.

[2] Jia, Q.; Ghoshal, S.; Li, J.; Liang, W.; Meng, G.; Che, H.; Zhang, S.; Ma, Z. F.; Mukerjee, S. Metal and Metal Oxide Interactions and Their Catalytic Consequences for Oxygen Reduction Reaction. J. Am. Chem. Soc. 2017, 139 (23), 7893–7903.

[3] Oyama, A.; Hiraoka, Y.; Obayashi, I.; Saikawa, Y.; Furui, S.; Shiraishi, K.; Kumagai, S.; Hayashi, T.; Kotoku, J. Hepatic Tumor Classification Using Texture and Topology Analysis of Non-Contrast-Enhanced Three-Dimensional T1-Weighted MR Images with a Radiomics Approach. Sci. Rep. 2019, 9 (1), 2–11.

[4] Li, L.; Cheng, W.-Y.; Glicksberg, B. S.; Gottesman, O.; Tamler, R.; Chen, R.; Bottinger, E. P.; Dudley, J. T. Identification of Type 2 Diabetes Subgroups through Topological Analysis of Patient Similarity. Sci. Transl. Med. 2015, 7 (311), 311ra174.

[5] Nielson, J. L.; Paquette, J.; Liu, A. W.; Guandique, C. F.; Tovar, C. A.; Inoue, T.; Irvine, K. A.; Gensel, J. C.; Kloke, J.; Petrossian, T. C.; Lum, P. Y.; Carlsson, G. E.; Manley, G. T.; Young, W.; Beattie, M. S.; Bresnahan, J. C.; Ferguson, A. R. Topological Data Analysis for Discovery in Preclinical Spinal Cord Injury and Traumatic Brain Injury. Nat. Commun. 2015, 6.

[6] Ushizima, D.; Morozov, D.; Weber, G. H.; Bianchi, A. G. C.; Sethian, J. A.; Bethel, E. W. Augmented Topological Descriptors of Pore Networks for Material Science. IEEE Trans. Vis. Comput. Graph. 2012, 18 (12), 2041–2050.

[7] Kramar, M.; Goullet, A.; Kondic, L.; Mischaikow, K. Persistence of Force Networks in Compressed Granular Media. Phys. Rev. E - Stat. Nonlinear, Soft Matter Phys. 2013, 87 (4), 1–8.

[8] Hiraoka, Y.; Nakamura, T.; Hirata, A.; Escolar, E. G.; Matsue, K.; Nishiura, Y. Hierarchical Structures of Amorphous Solids Characterized by Persistent Homology. Proc. Natl. Acad. Sci. U. S. A. 2016, 113 (26), 7035–7040.

[9] de Silva, V.; Ghrist, R. Coverage in Sensor Networks via Persistent Homology. Algebr. Geom. Topol. 2007, 7 (1), 339–358.

[10] Carstens, C. J.; Horadam, K. J. Persistent Homology of Collaboration Networks. Math. Probl. Eng. 2013, 2013.

[11] Wilding, G.; Nevenzeel, K.; van de Weygaert, R.; Vegter, G.; Pranav, P.; Jones, B. J. T.; Efstathiou, K.; Feldbrugge, J. Persistent Homology of the Cosmic Web – I. Hierarchical Topology in ΛCDM Cosmologies. Mon. Not. R. Astron. Soc. 2021, 507 (2), 2968–2990.

[12] Hansen, N.; Adams, D. O.; Fullwood, D. T. Quantitative Methods for Correlating Dispersion and Electrical Conductivity in Conductor-Polymer Nanostrand Composites. Compos. Part A Appl. Sci. Manuf. 2012, 43 (11), 1939–1946.

[13] Reuteler, J.; Hütter, M.; Gauckler, L. J. Backbone of Conductivity in Two-Dimensional Metal-Insulator Composites. J. Appl. Phys. 2011, 110 (2), 024909.

[14] Ishida, M.; Kida, K.; Mizobe, K.; Nakane, K. Relation between the Betti Number of Fatigue Fracture Surfaces and Stress Intensity Factors of Low Carbon Steel (JIS, S45C). Adv. Mater. Res. 2015, 1102, 59–63.

[15] Cang, Z.; Mu, L.; Wu, K.; Opron, K.; Xia, K.; Wei, G.-W. A Topological Approach for Protein Classification. Comput. Math. Biophys. 2018, 3 (1).

[16] Makarenko, I.; Shukurov, A.; Henderson, R.; Rodrigues, L. F. S.; Bushby, P.; Fletcher, A. Topological Signatures of Interstellar Magnetic Fields - I. Betti Numbers and Persistence Diagrams. Mon. Not. R. Astron. Soc. 2018, 475 (2), 1843–1858.

[17] Nakamura, T.; Hiraoka, Y.; Hirata, A.; Escolar, E. G.; Nishiura, Y. Persistent Homology and Many-Body Atomic Structure for Medium-Range Order in the Glass. Nanotechnology 2015, 26 (30).

[18] Suzuki, A.; Miyazawa, M.; Minto, J. M.; Tsuji, T.; Obayashi, I.; Hiraoka, Y.; Ito, T. Flow Estimation Solely from Image Data through Persistent Homology Analysis. Sci. Rep. 2021, 11 (1), 1–13.

[19] Pun, C. S.; Xia, K.; Lee, S. X. Persistent-Homology-Based Machine Learning and Its Applications -- A Survey. SSRN Electron. J. 2018, arxiv:1811.0025vl.

[20] Cang, Z.; Wei, G. W. Integration of Element Specific Persistent Homology and Machine Learning for Protein-Ligand Binding Affinity Prediction. Int. j. numer. method. biomed. eng. 2018, 34 (2), 1–17.

[21] Hirata, A.; Wada, T.; Obayashi, I.; Hiraoka, Y. Structural Changes during Glass Formation Extracted by Computational Homology with Machine Learning. Commun. Mater. 2020, 1 (1), 1–4.

[22] Cang, Z.; Mu, L.; Wei, G. W. Representability of Algebraic Topology for Biomolecules in Machine Learning Based Scoring and Virtual Screening; 2018; Vol. 14.

[23] Wen, Y.; Hashimoto, A.; Najib, A. S. B. M.; Hirata, A.; Abe, H. Topological Trends in Ionic Transport through Metal-Oxide Composites. Appl. Phys. Lett. 2021, 118, 054102.

[24] Wen, Y.; Abe, H.; Hirata, A.; Hashimoto, A. Correlation between the Charge-Transport Properties and the 3D-Phase Connectivities in Patterned Pt/CeO2 Nanostructured Composites: Implications for Solid-Oxide Fuel Cells. ACS Appl. Nano Mater. Under review.

[25] Homcloud: https://homcloud.dev/

[26] Adams, H.; Chepushtanova, S.; Emerson, T.; Hanson, E.; Kirby, M.; Motta, F.; Neville, R.; Peterson, C.; Shipman, P.; Ziegelmeier, L. Persistence Images: A Stable Vector Representation of Persistent Homology. J. Mach. Learn. Res. 2017, 18, 1–35.

[27] Obayashi, I.; Hiraoka, Y.; Kimura, M. Persistence Diagrams with Linear Machine Learning Models. J. Appl. Comput. Topol. 2018, 1 (3–4), 421–449.

Chapter 7 Summary and future work

7.1 Summary

TEM imaging is one of the most important characterization methods for materials nowadays because of the high-resolution (several Å), which provides rich physical and chemical information. It is indispensable for nanomaterials' structural analyses. The phase connectivity is important for transport properties, such as electronic conductivity and magnetism. Traditionally, the number, length, or diameter of the phases in the structure are obtained by manually measuring each component in the TEM images. However, it is time-consuming when the image data is large. Furthermore, it is difficult to give comparable quantitative information when different structures are complicated and difficult to distinguish. TDA is a fast-growing field and has recently been applied to materials science for analyzing structures from a topological viewpoint. A set of approaches in TDA give additional insight into the material's structure. Computational homology, a TDA tool, can discern different complicated structures quantitatively and process big data simultaneously. The phase connectivity can also be interpreted by the homology analysis.

The study aimed at applying TDA to TEM images of Pt/CeO_2-nanostructured composites. The main tasks completed herein are as follows:

- Application of Betti numbers as a suitable descriptor for the 2D phase connectivities of Pt/CeO_2 nanocomposites. (Chapter 4)
- Application of Betti numbers as a suitable descriptor for the 3D phase connectivities of Pt/CeO_2 nanocomposites. (Chapter 5)
- Classification of many TEM images showing the structure of Pt/CeO_2 nanocomposites by persistence diagram. (Chapter 6)

In chapter 3, the oxidation-inducing self-assembly phase separation process of the Pt_5Ce alloy was revealed at the atomic scale. Oxygen dissolution into the alloy causes special periodic compositional perturbation by atomic segregation, specifically, by local diffusion of Pt and Ce atoms. A striped pattern of Pt and CeO_2 forms through the phase transformation of the Pt-rich alloy and oxidation of the Ce-rich alloy, respectively. Notably, a fully epitaxial relationship between the Pt and CeO_2 phases was observed even in the initial stage. With continued annealing, the crystals rotate into an energetically favorable orientation with respect to the remaining $(111)Pt//(111)CeO_2$. The orientation relationship between the Pt_5Ce structure and Pt/CeO_2 structures, and the growth direction of the separated phases differe from the oxygen partial pressure. Therefore, the gas ratio of CO and O_2 and annealing temperature are important factors for tunning the structure of Pt/CeO_2 NCs because they influence the phase separation behavior. NCs with different structures prepared by changing these two factors are preconditions to study the structure–property relationship, which are used in the following experiments.

Chapter 4 studied the quantitative relationship between the structure and oxygen-ion transportation property by homology analysis. Different syngas ratios were applied for generating various structures. As the CO-to-O_2 gas ratio, increased, i.e., decreasing oxygen partial pressure, the interwoven two-phase structure changed from the striped to the maze pattern. No significant difference was found in the view of crystalline degree and valence state of Ce in CeO_2 phases from the XRD analysis and high-resolution TEM (HRTEM). Homology analysis on the STEM images showed that the structures in the sample with gas ratio of 1:1 has the lowest β_0 value followed by 0:1, 2:1, and 3:1. Thus, the maze pattern has a relatively lower connectedness than lamellae structures. The trends of β_1 differed from that of β_0. Through the measurement of the oxygen ionic conductivity by IS, the activation energy (E) and pre-exponential factor ($ln\sigma_0$) were deduced according to the Arrhenius equation. It was found that the trends of E and $ln\sigma_0$ are same and are negatively related to that of β_0, indicating the importance of the CeO_2 phase connectivity. The two samples: 0:1 and 2:1, with similar ionic conduction properties totally differed in terms of β_1, implying the little influence of the Pt phases on the property. As the oxygen ions mainly transport through the conductive CeO_2 phases, the highly connected CeO_2 phases provided a fast O^{2-} transportation pathway and thus improved the ionic conductivity in the measured temperature range. Therefore, β_0 can act as a suitable descriptor to correlate the structures and their ionic transport properties.

In addition to the 2D structures description performed by computational homology, the 3D structural analysis was applied because the 2D projection image sometimes cannot accurately convey the structural information. The structure–ionic conductivity quantitative relationship from a 3D viewpoint was investigated in Chapter 5. Various structures were obtained by changing the annealing temperature (from 500°C to 800°C), while maintaining the same gas ratio ($CO:O_2$ = 2:1). The crystalline degree increased as the annealing temperature increased from the XRD and HRTEM results. Besides, accelerated diffusion rates of metal atoms and oxygen ions at higher temperatures contributed to a wider and longer stripe pattern. Up to 800°C, the CeO_2 phases are small island-like domains. For samples annealed at 500°C, 600°C, and 700°C, each stripe just extended along the depth direction. However, at 800°C, isolated islands from the cross-sectional view are actually connected at certain depths, causing a 3D network structure. Consequently, the 2D-Betti numbers, especially β_0, could not correctly represent the connectivity of the CeO_2 phase for the network structure. Combing the results of the 3D homological structural description, Betti numbers, and ionic conductivity parameters (E and $ln\sigma_0$), it was demonstrated that the ionic conductivity relates to 3D-β_0. The homological structures of the Pt phase, including 3D-β_1 (number of Pt tunnels) and 3D-β_2 (number of enclosed Pt pores), do not affect the ionic conductivity. The value of $ln\sigma_0$ (green line) is linearly related to 3D-β_0. Concerning E, the crystalline degree and total interface area play additional roles for the low-temperature and high-temperature annealed samples, respectively. These findings give consolidated evidence that the connectivity of the CeO_2 phases significantly influences the oxygen-ion transportation in Pt–CeO_2 NCs.

As the connectivity of a structure can be quantitatively computed by homology, the classification of various structures is necessary for multiscale and large data. Chapter 6 applied persistent homology and

principal component analysis (PCA) to classify the different structures. Persistent homology tracks the change of CeO_2 phases in the filtration of the MD. The persistence diagram, a representer of persistent homology, described the shape of the structures. It was found that the persistence diagram contains much more information than traditional homology. The number of connected features (CeO_2 domains) and geometric information of the features can be obtained. Each binary image generated a persistence diagram, and each PD was vectorized by weighted persistent homology for the machine-learning model: PCA. Finally, Different structures with temperature or gas ratio as variables were classified by the PCA on persistence diagrams.

The conclusions about the application of homology on the TEM structural images of Pt/CeO_2 composites summarized above can be applied to other nanomaterials, especially for those materials in which phase connectivity influences the transportation of materials, such as magnetic and electrical properties. Long striped patterns or network structures with high connectivity are supposed to facilitate carries transportation and oxygen-ion conduction herein. Moreover, these findings pave ways for combining TEM techniques, such as diffraction pattern, EELS spectra, and atomic-resolution images combining with the homology for data differential and classification. Therefore, the combination of homology analysis and TEM is promising for material design, property prediction of materials in the future work.

7.2 Future work

The research work reported herein established the applicability of TDA, i.e., homology, for quantitatively describing phase connectivities and differentiating between different structures of $Pt–CeO_2$ NCs. However, this work is an open-ended project on using the homology method in materials science with several applications. The success achieved in this limited application reveals the potential for many more contributions to deal with various challenges. In the closing part of this study, a few potential research directions needing exploration in the near future are listed.

Big data collection

During the various structural classification, it is difficult to distinguish structures from small data accurately. A large amount of data for each sample is necessary to verify the suitability of homology methods with machine learning for structural description. However, the TEM specimen preparation is time-consuming; thus, the quality is difficult to guarantee. With the help of advanced FIB milling, such as machine-learning support and low-damage processing, good TEM specimens can be easily made, and thus plenty of TEM images were available. First, at least 50 STEM images for each sample are required for classification. Second, other types of patterns were prepared by combining different annealing temperatures and syngas ratios.

Homology analysis on the simulated structures

For a complementary understanding of the structure–ionic conductivity relationship, a diverse of structures needed to be analyzed. However, the structures obtained through experiments are very limited and time-consuming. More intriguing and complicated structures can be easily predicted through simulation using a suitable phase separation model. Based on the phase separation mechanism I revealed in Chapter 3, it is

possible to explore a reaction-diffusion model for simulating metal–oxide structures from binary alloy. Not only the Pt–CeO_2 nanostructures, but also other metal–oxide structures can be speculated. Applying the computational homology to the simulated structures, structures generated at in a certain condition can be easily discerned, Furthermore, it is expected to find an optimized structure with high oxygen-ion conductivity.

Homology analysis on atomic-resolution TEM images

Phase identification is vital for understanding phase transformation behavioral characteristics. Particularly, discerning the crystal structure from the disordered phases is also critical for the amorphous–crystal phase transition in alloys. Concerning the periodic and disordered arrangement of atoms in the crystal and amorphous phases, respectively, the different atomic arrangements can be distinguished by persistent homology. It is convenient to summarize what condition and when the transition will occur by large data analysis, such as *in situ* data. Moreover, identifying nanoparticles from the amorphous substrate using the persistent homology is worthy for *in situ* TEM imaging.

Hence, the powerful computational homology can traditionally provide geometric information from objects and quantitatively describe structures from multidimensional objects and efficiently process big data, which is critical for material design and property prediction of materials. The application of homology to TEM images is not constrained for Pt–CeO_2 NCs, but also for other nanostructured materials. It is expected to thrive in nanomaterials' structural analyses with the help of the interaction between TDA and TEM.

Publications

Scientific papers

1. **Wen, Y.**; Abe, H.; Hirata, A.; Hashimoto, A. Correlation between the Charge-Transport Properties and the 3D-Phase Connectivities in Patterned Pt/CeO_2 Nanostructured Composites: Implications for Solid-Oxide Fuel Cells. ACS Appl. Nano Mater. 2021, 4(12), 13602-13622.

2. **Wen, Y.**; Abe, H.; Mitsuishi, K.; Hashimoto, A. Tracking the Emergence of Epitaxial Metal–Oxide Interfaces from Precursor Alloys. Nanoscale 2021, 13, 18987–18995.

3. **Wen, Y.**; Hashimoto, A.; Najib, A. S. B. M.; Hirata, A.; Abe, H. Topological Trends in Ionic Transport through Metal-Oxide Composites. Appl. Phys. Lett. 2021, 118, 054102.

4. Ham, H.; Simanullang, W. F.; Kanda, Y.; **Wen, Y.**; Hashimoto, A.; Abe, H.; Shimizu, K.; Furukawa, S. Silica-Decoration Boosts Ni Catalysis for (De)Hydrogenation: Step-Abundant Nanostructures Stabilized by Silica. ChemCatChem 2021, 13 (5), 1306–1310.

Conference proceedings

1. **Wen, Y.**; Hashimoto, A. A.; Mohd Najib, A. S. Bin; Hirata, A.; Abe, H. Topological Analysis of Metal and Metal Oxide Hybrid Nanostructures. Microsc. Microanal. 2020, 26 (S2), 2096–2098.

2. **Wen, Y.**; Hashimoto, A.; Hirata, A.; Abe, H. Quantitative Analysis of 3D Structures in Metal-Oxide Composites. Microsc. Microanal. 2021, 27 (S1), 2974–2975.

3. **Wen, Y.**; Abe, H.; Hashimoto, A. Growth Mechanism of Periodic Nanopattern in Metal–Oxide Composites. Microsc. Microanal. 2021, 27 (S1), 2324–2325.

Conference presentations

Poster presentations

Wen, Y.; Hashimoto, A.; Najib A. S. B. M.; Hirata, A.; Abe, H. “Topological analysis of metal and metal oxide hybrid nanostructures” Microscopy & Microanalysis 2020, Online, Aug. 6, 2020.

Wen, Y.; Hashimoto, A.; Najib A. S. B. M.; Hirata, A.; Abe, H. “Probing the structure-property relationship of metal-oxide composites with homology analysis” The 63rd symposium of the Japanese society of Microscopy, Online, Nov. 20, 2020. (Award)

Wen, Y.; Abe, H.; Hashimoto, A. “TEM study on atomic-scale phase separation in binary alloys” The 77th annual meeting of the Japanese society of Microscopy, Tsukuba, Japan, Jun. 15, 2021.

Wen, Y.; Abe, H.; Hashimoto, A. “Growth mechanism of periodic nanopattern in metal-oxide composites” Microscopy & Microanalysis 2021, Online, Aug. 5, 2021.

Verbal presentations

Wen, Y.; Hashimoto, A.; Najib A. S. B. M.; Hirata, A.; Abe, H. “Identification of phase separated nanostructures by topological method” The 76th annual meeting of the Japanese society of Microscopy, Online, May 27, 2020.

Wen, Y.; Abe, H.; Hirata, A.; Hashimoto, A. “Topological analysis of metal/oxide composites in three dimensions” The 77th annual meeting of the Japanese society of Microscopy, Tsukuba, Japan, Jun. 14, 2021.

Wen, Y.; Abe, H.; Hashimoto, A. “Quantitative analysis of 3D structures in metal-oxide composites” Microscopy & Microanalysis 2021, Online, Aug. 5, 2021.

Wen, Y.; Abe, H.; Hirata, A.; Hashimoto, A. “Quantitative relationship between 3D structure-ionic conductivity by topological analysis” The 82nd JSAP Autumn Meeting 2021, Online, Sep. 11, 2021.

Acknowledgements

Foremost, I would like to express my deepest appreciation to my supervisor, Prof. Ayako Hashimoto, for the continuous support of my Ph.D study and research. Her guidance and advice carried me through all the stages of writing my project. I would also like to thank Dr. Kazutaka Mitsuishi of NIMS for letting me be a member of in-situ characterization group and giving brilliant comments for my work.

I would like to give my special thanks and gratitude to our project collaborator, Prof. Hideki Abe, who provided experimental support, taught me paper writing, and most importantly, the spirit of imagination! In addition, my sincere thanks go to Prof. Akihiko Hirata of Waseda Univ. for discussion about topological data analysis and suggestions for paper writing.

I respect and thank the committee members: Prof. Tomonobu Nakayama, Prof. Jie Tang and Prof. Hisanori Tanimoto for their valuable time on the thesis review, defense and insightful discussions.

I would like to acknowledge Dr. Sani, Ms. Misao Yamanaka, Dr. Xiaoguang Li, Mr. Wataru Yajima, and Ms. Ayumi Nakamura for experiments supporting and clerical work during the Ph.D. study.

I also acknowledge the Junior Researcher Assistantship of National Institute for Materials Sciences for the financial supports for my Ph.D. degree attainment, and Japan Science and Technology Agency for research projects in Ph.D. studies.

Last but not least, many thanks and deep gratitude to my boyfriend, Zehao Li, and my parents who accompany with me all the way for giving solid support for my life!